Durham E-Theses

Strange particle production by 4 Gev/c pions in deuterium

Christopher James Wagstaffe

How to cite:

Wagstaffe, Christopher James (1980) *Strange particle production by 4 Gev/c pions in deuterium.* Doctoral thesis, Durham University.

Use policy

STRANGE PARTICLE PRODUCTION

BY 4 GeV/c PIONS IN DEUTERIUM

A THESIS PRESENTED

BY

CHRISTOPHER JAMES WAGSTAFFE

for the

DEGREE OF DOCTOR OF PHILOSOPHY

AT THE

UNIVERSITY OF DURHAM

SEPTEMBER 1980

TO MY

PARENTS

ABSTRACT

This thesis presents an analysis of strange particle production in $\pi^+ d$ interactions at 4 GeV/c incident momentum. The experiment was carried out using the CERN 2-metre deuterium-filled bubble chamber and π^+ mesons originating from the CERN Proton Synchrotron. The film was analysed by three collaborating laboratories: Birmingham University, the Rutherford High Energy Laboratory (RHEL) and Durham University.

The channel cross-sections are evaluated from a total sample of about 22,000 events, particular attention being given to the resolution of ambiguous final states and to corrections for losses. The results are compared with those of existing data at higher and lower energies. Resonance production cross-sections are estimated for the well populated strange particle channels.

The differential cross-sections, hyperon polarisations and spin density matrix elements are determined for the two body and quasi-two body processes, and a complete amplitude analysis is carried out for the reaction $\pi^+ n \rightarrow K^{*+}(890)\Lambda^0$ from the correlated decay distributions of the $K^{*+}(890)$ and Λ^0. The results are interpreted in the framework of the Regge-pole model.

CONTENTS

LIST OF FIGURES

LIST OF TABLES

CHAPTER I

GENERAL BACKGROUND AND EXPERIMENTAL
CONSIDERATIONS

I.1 Introduction

Compared to the total cross-section, the production of strange

p articles by 4 GeV/c positive pions in deuterium takes place in about 7%

of the interactions and leads to visible strange particles in only about

half of these. Consequently in bubble chamber experiments running at

about one recorded event per frame of film, it is only with exposures of

the order of one million pictures that statistically worthwhile samples

of strange particle production can be obtained.

Kaon induced interactions will obviously provide better statistics

on strange particle production. However, the study of strangeness exchange

mechanisms and the strange particle decay modes of resonances with zero

strangeness requires data on πN collisions. In particular the strong

$K^*(890)$ and $\Sigma(1385)$ signals which are found to be present in the strange

particle samples enable the quasi-two body processes which involve the

production of these resonances to be studied, and a comparison with the

line reversed KN processes and SU(3) related reactions provides a very

rich testing ground for exchange model predictions.

I.1.1. Availability of data

The lack of data on strange p article production by pions is manifest

in the literature where information on cross-sections is relatively sparse

and that on differential cross-sections rare. A summary of the data

published since 1968 is given in table I.1 for beam momenta in the range

3-7 GeV/c. As can be seen deuterium interactions have been studied

TABLE I.1 SUMMARY OF LITERATURE ON πN → STRANGE PARTICLES SINCE 1968 (3-7 GeV/c)

Reference/Detector	Reaction/Channel	Momentum (GeV/c)	Events	Channel	Cross-sections Reaction	Differential	Density Matrix	Polarisation of Λ/Σ^0
I.1 Argonne-HBC	$\pi^+p \to \Sigma^+K^+$ $\Sigma^+K^+\pi^0$ $\Sigma^+K^0\pi^+$	5.4	74 580	Yes	Yes	Yes	Yes	Yes
I.2 Argonne-Spark Chamber	$\pi^+p \to \Sigma^+ K^0$	3-7	Not given	No	-	Yes	-	Yes
I.3 CERN - Spark Chamber	$\pi^-p \to K^0\Lambda/\Sigma^0$	6-11.2	Not given	Yes	-	Yes	-	No
I.4 Argonne-Spark Chamber	$\pi^+p \to K^+ \Sigma^+$ $K^+ \Sigma^+(1385)$	3,5,7.5	Not given	No	No	Yes	No	No
I.5 CERN - HBC	$\pi^-p \to K^0 \Lambda$ $K^0\Sigma^0$	3.9	590 83	Yes	-	Yes	-	Yes
I.6 BNL - HBC	$\pi^-p \to$ quasi two body	4.5 6	500K 200K (Frames)	Yes	Yes	Yes	Yes	Yes
I.7 CERN - HBC	$\pi^-p \to K^+\pi^-\Lambda$ $K^+\pi^-\Sigma^0$	3.9	616 322	Yes	Yes	Yes	Yes	No
I.8 CERN - HBC	$\pi^+p \to$ quasi two body	5	125K (Frames)	Yes	Yes	Yes	No	No
I.9 DBC	$\pi^+d \to K^+\Lambda\ p_s$ $K^+\Sigma^0\ p_s$	5.1	124	Yes	-	Yes	-	Yes
I.10 Argonne-Spark Chamber	$\pi^-p \to K^0\Lambda$ $K^0\Sigma^0$	3-6	∿ 40K (all momentum)	No	-	Yes	-	No
I.11 Argonne-Spark Chamber	$\pi^-p \to K^0 \Lambda$	5	3709	No	-	No	-	Yes
I.12 CERN- HBC	$\pi^-p \to K^+\pi^-\Lambda$ $K^+\pi^-\Sigma^0$	3.93	962 520	No	Yes	Yes	Yes	Yes
I.13 CERN - HBC	$\pi^-p \to A_2^- p$ $\hookrightarrow K^0_s K^-$	3.9	565 (All $K^0\bar{K}$)	Yes	Yes	Yes	Yes	--
I.14 Argonne-Spark Chamber	$\pi^-p \to K^-K^+ n$	6	∿16K	No	A_2,f	Yes	No	-
I.15 CERN - Spark Chamber	$\pi^-p \to K^0\Lambda$	5	∿25K	No	-	No	-	Yes
I.16 JINR - NBC	$\pi^-p \to$ strange particles	4.9	Not given	Yes	No	No	No	No
I.17 Argonne-Spark Chamber	$\pi^-p \to K^0 \Lambda$ $K^{*0}(890)\Lambda$ (backward production)	3-6	∿11K ∿ 5K	Yes	Yes	Yes	No	Yes

previously in only one experiment and that was of limited extent. Consequently the data presented in this thesis are largely new for deuterium, and the statistics are at least comparable to existing bubble chamber data on $\pi^- p$ interactions.

The resolution of ambiguous final states in samples of low statistics is known to be difficult. In the present work the selection criteria have been carefully determined in chapter II by simulating the ambiguities using Monte Carlo techniques. In addition the correction factors for geometrical losses related to the visibility of events have been calculated in chapter III. Although such losses are found to be small, they must be determined precisely if accurate values for the cross-sections are to be presented.

I.1.2 Resonance production and quasi-two body processes

For the more populated strange particle channels it is possible to estimate the contribution from any resonance production which may be present by fitting the relevant effective mass distributions with Breit-Wigner expressions plus phase space or by counting the number of events above background within the resonance mass band where statistics are low (see chapter IV). Where reaction (*) cross-sections are given in the literature, this is indicated in table I.1. In view of the limited statistics only the well-established resonances have been considered in the present work, although the evidence for exotic baryon resonances and for structure in the ($K\bar{K}\pi$) and ($K\pi\pi$) spectra is discussed towards the end of chapter IV.

(*) A reaction is a transition from the initial state to a final state consisting of particles or resonances produced directly by the interaction.

Two body and quasi-two body processes occurring at high energies are characterised by low four-momentum transfer. The interactions are said to be peripheral, and are therefore dominated by long range forces. In recent years the most successful model for describing such processes has been the Regge-pole theory. The evolution of Regge-poles was started by Regge and his collaborators in the late 1950's and developed from concepts in low energy potential scattering theory. It was demonstrated that the partial wave amplitudes considered as complex functions of both energy (E) and angular momentum have poles for integer values of the trajectory function, $\alpha(E)$. For positive integers the E-values are associated with bound states (E < O) or resonances (E > O) whose spin is given by $J = \alpha(E)$. In order to take into account the different effects of exchange forces for even and odd J, the concept of signature (τ) is introduced. The Regge trajectory links together poles with even spin ($\tau = +1$) or odd spin ($\tau = -1$) only. If two trajectories of opposite signature coincide the trajectories are said to be exchange degenerate, which enables certain predictions to be made about the hyperon polarisation and differential cross-section relations between line-reversed reactions (weak exchange degeneracy). If in addition the pole residues are identical the hyperon polarisation is predicted to be zero (strong exchange degeneracy).

To eliminate poles at unphysical values of angular momentum, the residues must vanish at negative right-signature values of α. If the residues for opposite-signature poles are exchange degenerate then this will produce a dip in the differential cross-section at the wrong-signature negative values of α for the partner pole. However, statistics are generally poor for large values of four-momentum transfer where the dips are predicted to occur, and no conclusive results are to be expected.

Conservation of angular momentum requires that amplitudes which change the overall helicity of the interaction must vanish at zero four-momentum transfer. This may produce a dip in the forward differential cross-section for reactions dominated by such processes. However, care must be taken to ensure that any geometrical losses which may produce spurious structure in the differential cross-section have been properly taken into account before any interpretation of the dips is made.

If only one trajectory is exchanged the coupling for the amplitude factorises into contributions from each vertex. The importance of this factorisation lies in the fact that the same coupling may occur in different reactions, or the couplings may be related by SU(3) symmetry. In some cases a comparison may be made by assuming one trajectory is dominant or by separating the effects of the different trajectories using the spin density matrix formalism (see section V.3). For example the known smallness of the $K\bar{\Sigma}N$ to $K\bar{\Lambda}N$ coupling ratio will mean that the unnatural parity exchange for $\pi^+ n \to K^{*+}(890)\Sigma^0$ will be considerably smaller than that for $\pi^+ n \to K^{*+}(890)\Lambda^0$ (see section V.4.2).

A more detailed description of the Regge-pole model is given in chapter V, where the predictions are compared with the data from this experiment and other related processes at a variety of beam momenta. As can be seen from table I.1, the lack of data on the spin density matrix and hyperon polarisations will put limitations on such a comparison.

I.1.3 Amplitude analysis

A considerable amount of information can be extracted from quasi-two body processes which involve the production of a vector meson and a hyperon with a subsequent parity violating decay. In the present experiment there are sufficient statistics to enable an amplitude analysis

of the reaction, $\pi^+ n \to K^{*+}(890) \Lambda^0$, to be carried out using the correlated decay distributions of the $K^{*+}(890)$ and Λ^0. The reaction is described by six amplitudes which may be determined, apart from two phase factors, without the use of polarised targets.

In chapter VI the joint density matrix for the reaction is determined and is used to construct the transversity amplitudes which are compared with those of the SU(3) related reaction $\bar{K}p \to \phi\Lambda^0$ at similar energy. In addition the hyperon polarisations arising from natural and unnatural parity exchange are calculated and compared with the results from the charge symmetric reaction at 3.93 GeV/c (ref. I.12) which has similar statistics.

I.1.4 Aims of the present experiment

The present experiment was set up in 1970 to study the interactions between a beam of 4 GeV/c positive pions and neutrons. Because it is not possible to produce free neutron targets, these have been provided by deuterons in a liquid deuterium filled bubble chamber. Since the deuteron consists of a neutron and a proton loosely bound together with a binding energy of 2.2 MeV, the neutron is free to a good approximation. Obviously interactions will also occur with the protons in the deuterium nuclei, so that some information may be obtained on $\pi^+ p$ collisions. Both types of collision are treated in the impulse approximation (appendix A) as though the spectator nucleon had taken no part in the interaction. Despite this simplification there are a number of problems associated with the use of deuterium since each nucleon is not a truly free target. These will be discussed in the following section.

The first stage of the work (see for example refs. I.18 and I.19) was concerned with the study of neutral meson states in the reaction,

$$\pi^+ d \to X^0 \, pp_s,$$

and in particular such states X^0/have a single neutral particle and so are
inaccessible to study in the charge symmetric reaction $\pi^- p \to X^0 n$.

The present work deals with the strange particle sample where there
are considerable advantages over the charge symmetric channels which con-
tain two visible neutral strange particles and an unseen neutral, and
which therefore have a very low detection probability.

This chapter contains a brief summary of the techniques used to
obtain the data together with a description of the scanning, measurement
and processing of events. Further details may be found in earlier work
on the experiment (refs. I.18 and I.19).

I.2 Problems associated with deuterium targets

The momentum distribution of the target neutron and its accompanying
proton within the deuterium nucleus (the Hulthen distribution - see
appendix A) will lead to variations in the centre of mass energy for the
interaction and also in the flux of target nucleons, depending on whether
the interacting nucleon was moving towards or away from the primary
particle.

In addition, because the neutron and proton are fairly close
together inside the deuteron, each may shadow the other from the primary
particle, and secondary interactions may occur between the spectator
nucleon and the other final state particles.

In the following sub-sections these problems are discussed in detail.

I.2.1 Indentification of the spectator

In some interactions the final state will include two candidates for
the spectator nucleon:

$$\text{e.g. } \pi^+ d \to K^0 \bar{K}^0 \, pp_s$$

By demanding the spectator momentum to be below 500 MeV/c this ambiguity

may be resolved in the majority of cases (see section II.2). However

for the small number of interactions which involve low 4-momentum

transfer to the target, both nucleons have momenta of the same order of

magnitude. In these cases the spectator is arbitrarily assigned to the

nucleon with the lower momentum. Monte Carlo simulations (see section

II.3) have shown that such an assignment is wrong in some 3% of the

cases.

I.2.2 Seen and unseen spectator proton events

Protons with momenta below ~ 85 MeV/c will not produce a visible

track in the liquid deuterium. From the Hulthen distribution this

implies that ~ 2/3 of the spectator protons will be unseen. In the

fitting of these events the unseen spectator proton is essentially

treated as a badly measured track in that it is assigned zero momentum

and an error consistent with the minimum observable momentum. The

fitting procedure then iterates the momentum and direction of the track

to the optimum values. The laboratory momentum and angular distributions

of the spectator protons are shown in figure I.1.for the channels

$$\pi^+ d \longrightarrow K^+ \Lambda^0 p_s \qquad \text{(4 constraint fit)}$$

$$\pi^+ d \longrightarrow K^+ \Lambda^0 \pi^0 p_s \qquad \text{(1 constraint fit)}$$

In both cases the momentum distribution for the seen spectator protons

is in good agreement with that predicted by Hulthen, indicating that

the interactions are well described by the impulse approximation. In

addition the seen spectator protons exhibit approximate angular isotropy.

The observed discrepancies for the unseen spectator proton 1C events

arise from the fact that both the π^0 and the spectator are missing. As
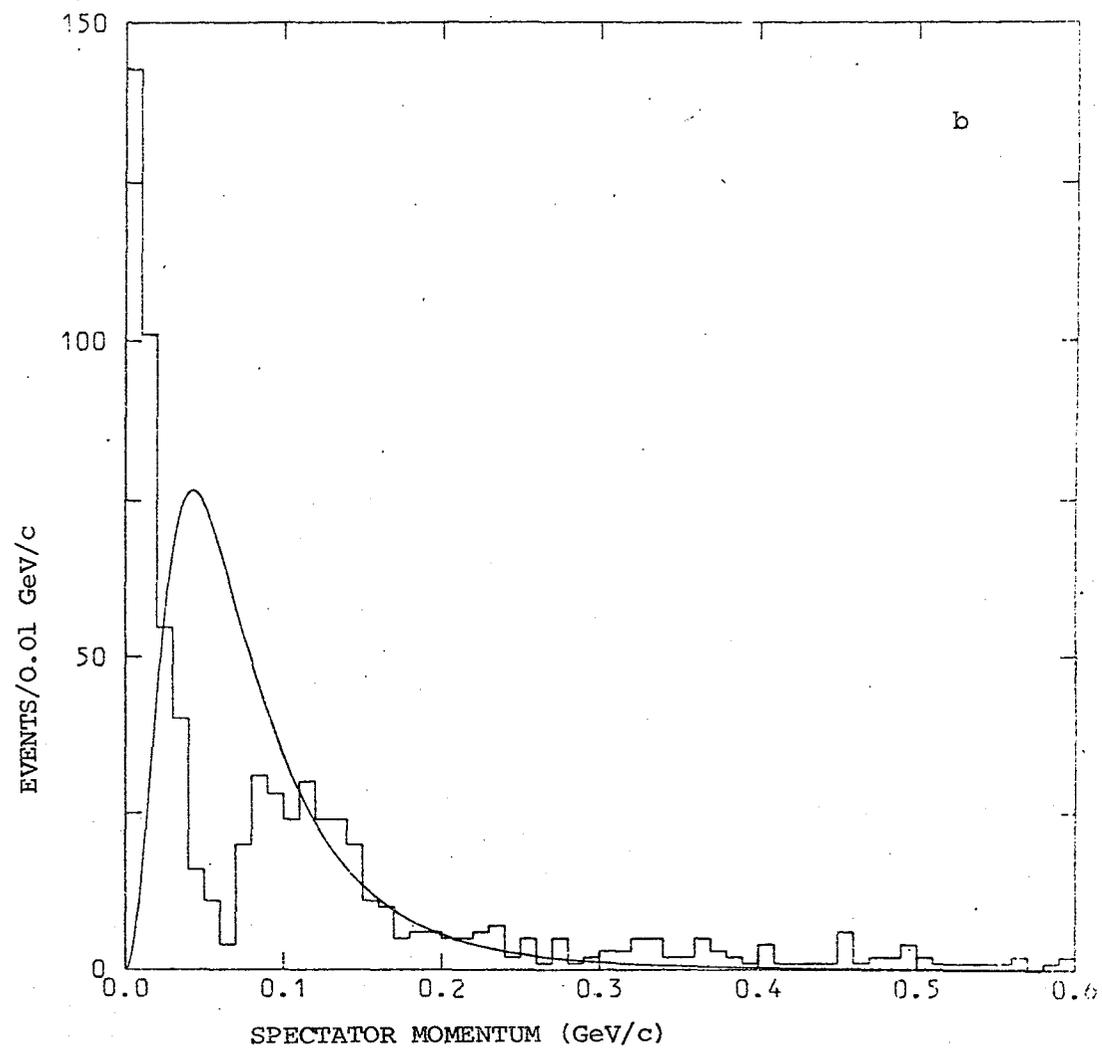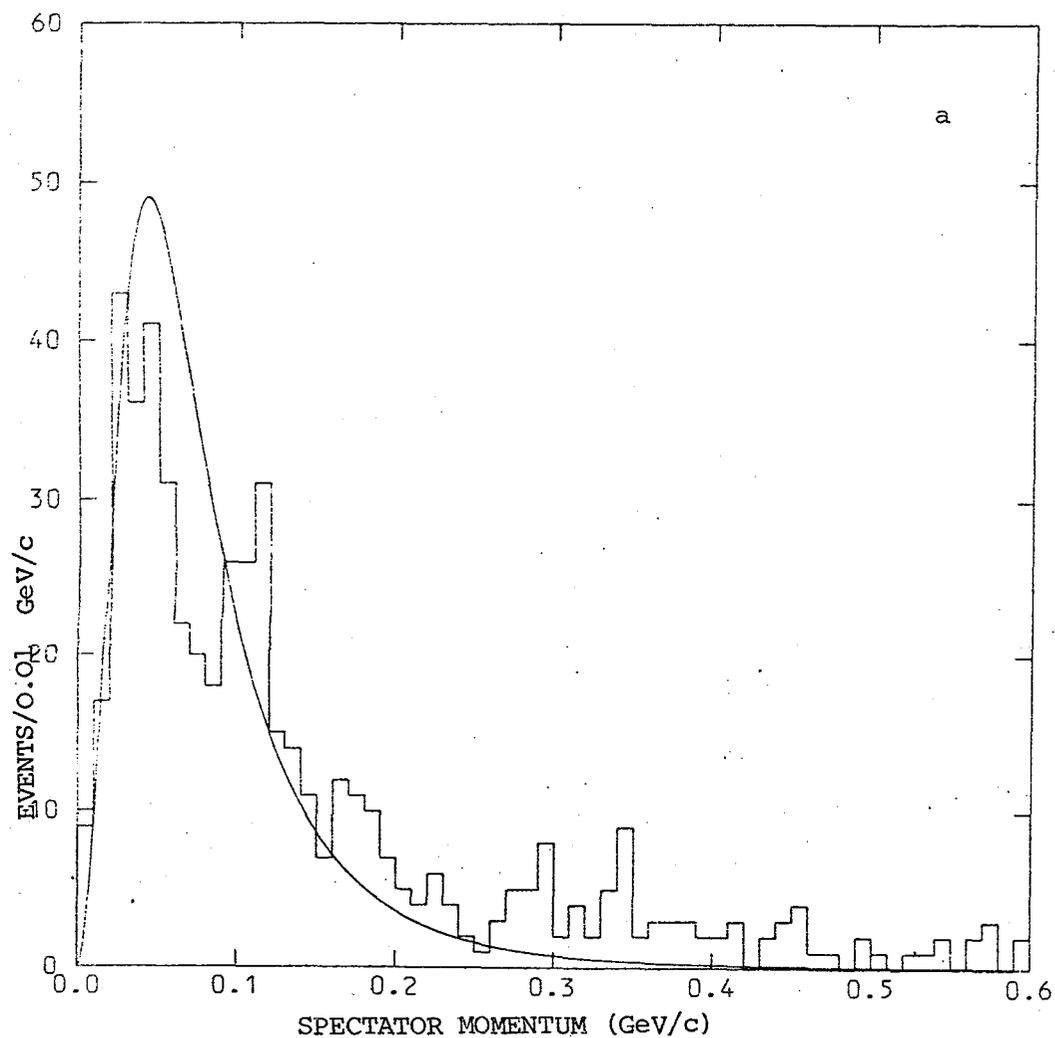
Fig. I.1 Spectator momentum distribution for the channels (a) $\pi^+ d \rightarrow K^+ \Lambda^0 p_s$ (b) $\pi^+ d \rightarrow K^+ \Lambda^0 \pi^0 p_s$. The curve represents the Hulthen distribution normalised to the total number of events.
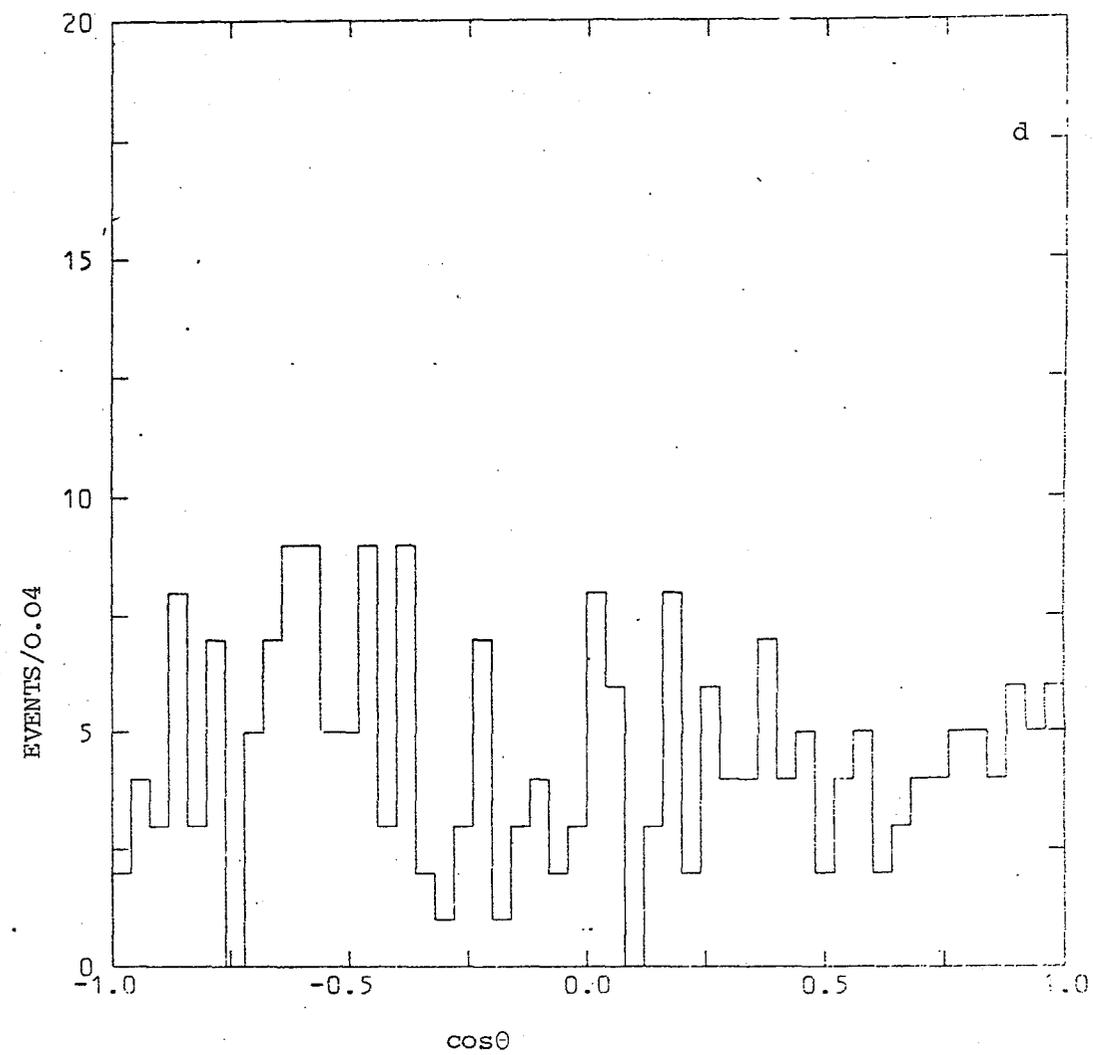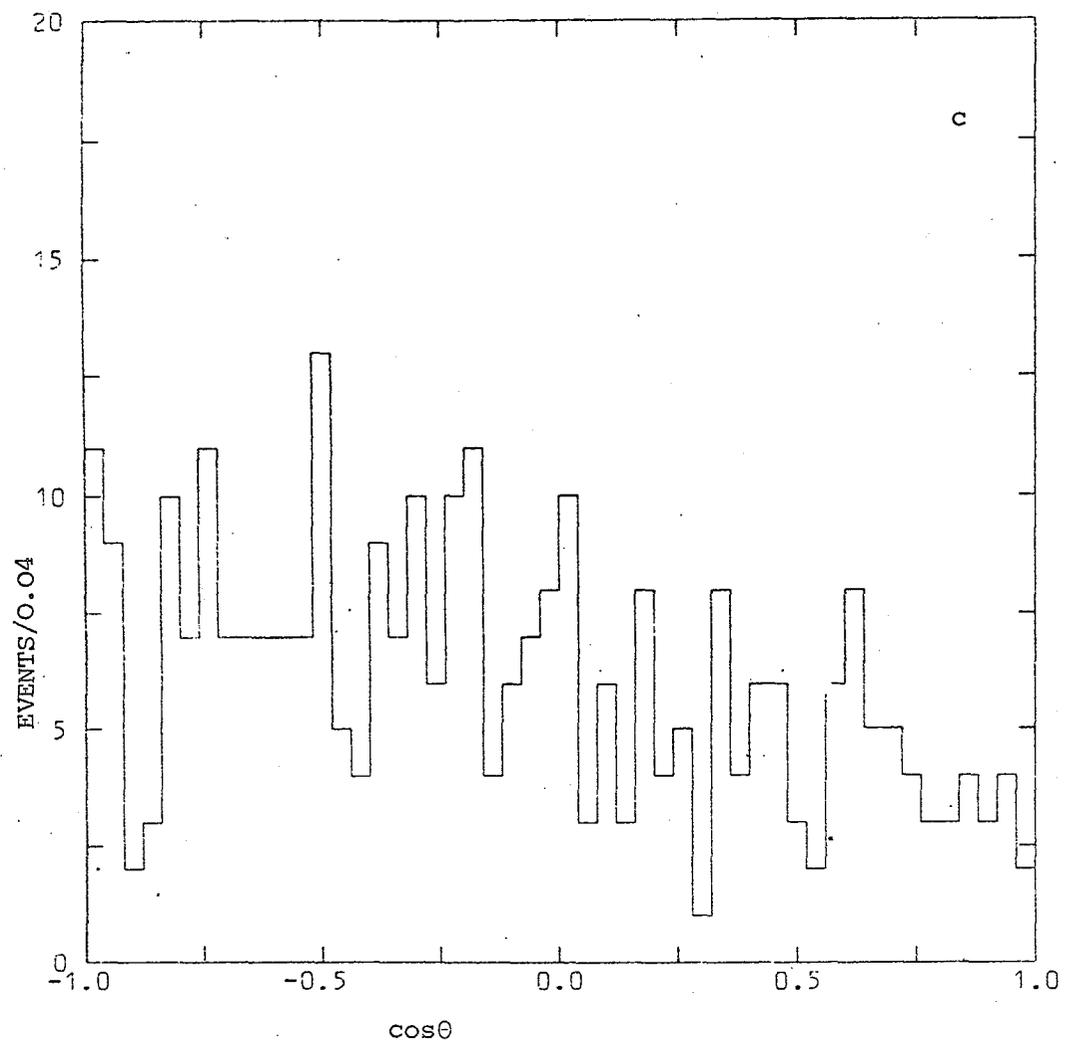
Fig. I.1 (cont)   Angular distributions with respect to the beam for (c) seen spectator and (d) unseen spectator in the channel $\pi^+ d \rightarrow K^+ \Lambda^o p_s$
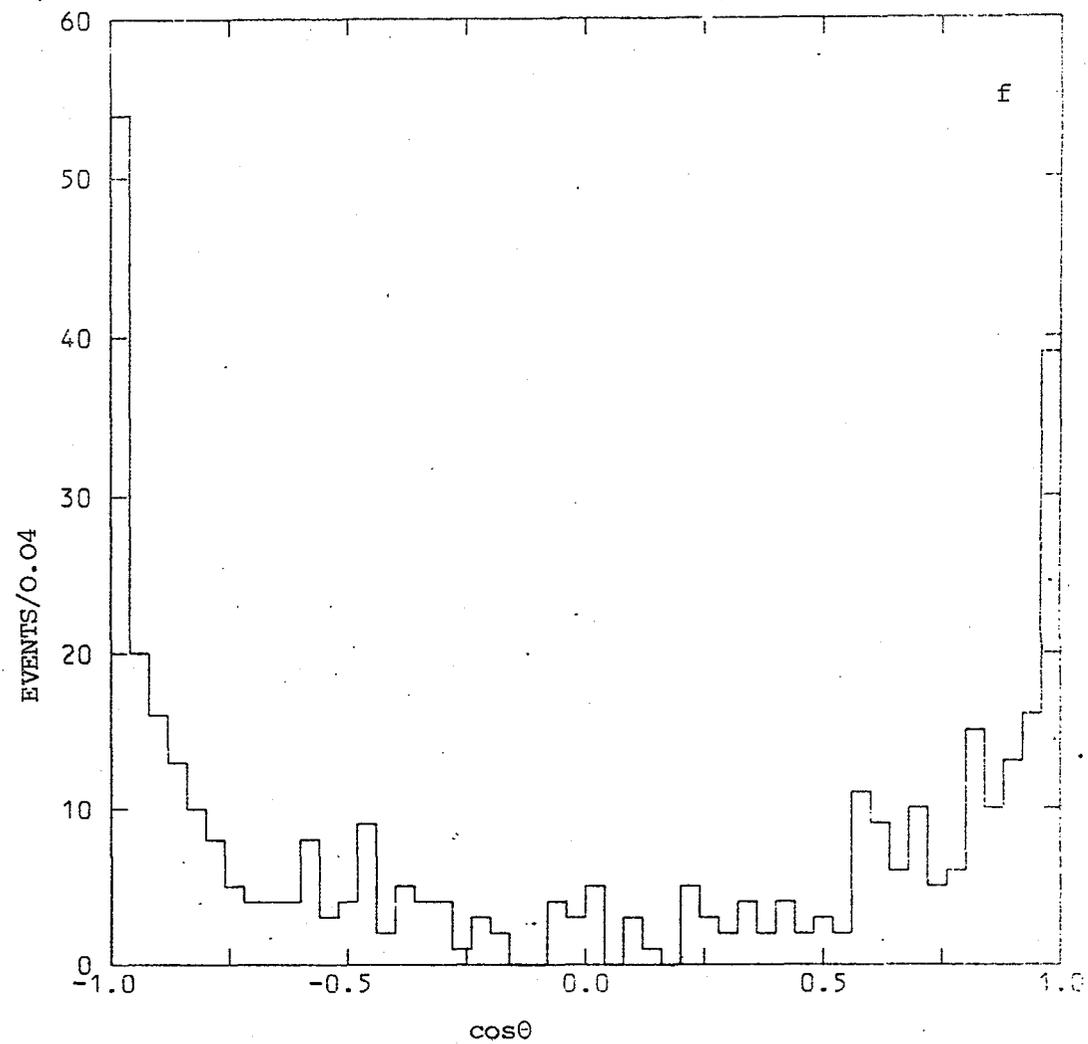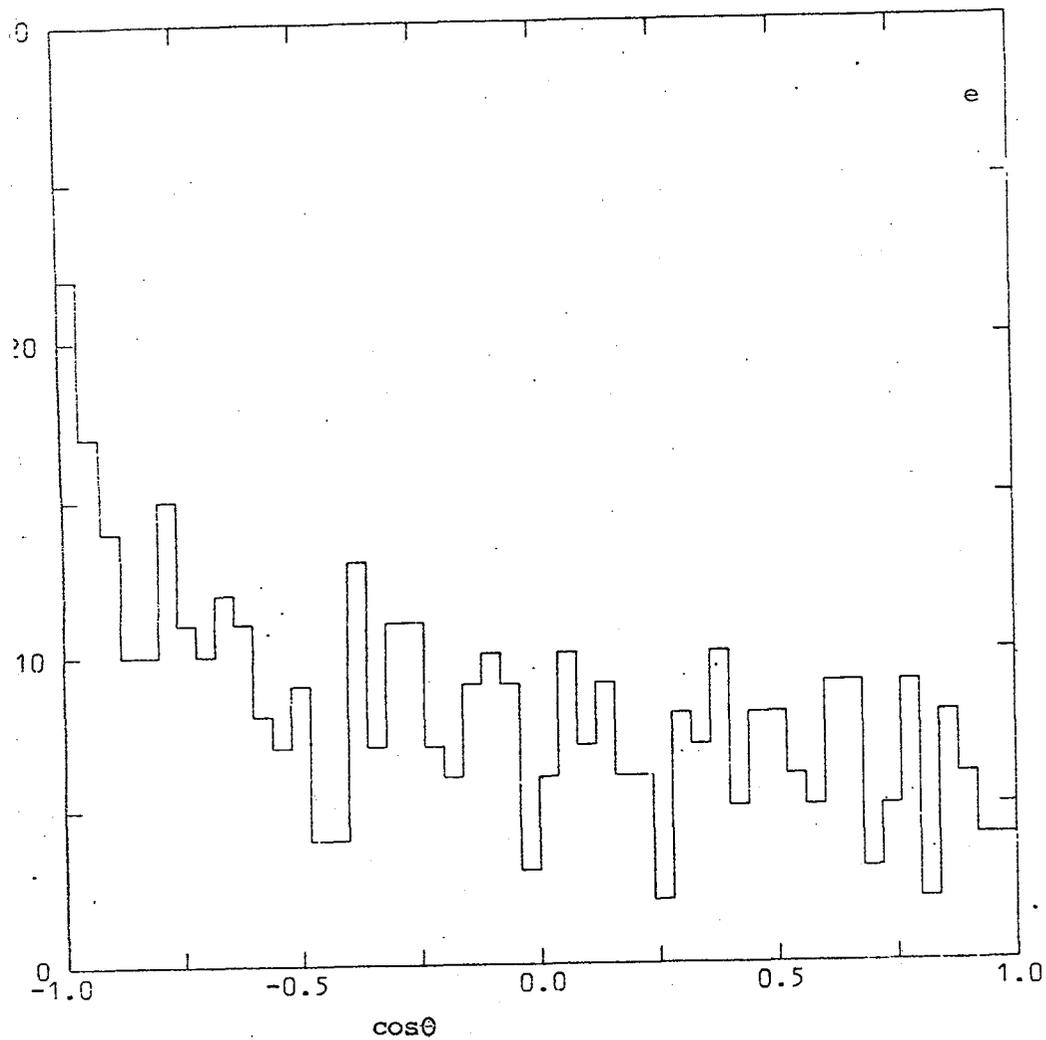
Fig. I.1 (Cont.) Angular distributions with respect to the beam for (e) seen spectator (f) unseen spectator in the channel $\pi^+ d \to K^+ \Lambda^0 \pi^0 p_s$

a result the spectator proton tends to be fitted along or in the

opposite direction to the missing π^{o} momentum producing the observed

forward-backward peaking. The fitting process tends to weight the

momentum in favour of the π^{o} so that the spectator momentum is under-

estimated. This produces a discontinuity in the momentum distribution

around 65 MeV/c.

In spite of the inaccuracies in fitting the unseen spectator proton

the fitting of the other tracks is not appreciably affected since the

spectator has only a small momentum vector.

Other effects which produce small variations from the expected

momentum and angular distributions of the spectator protons are discussed

in the following three sub-sections.

I.2.3 Variation in the centre of mass energy

For interactions involving a stationary target the variation in the

centre of mass energy arises purely from the small momentum bite of the

beam. However, for deuterium interactions the momentum distribution of

the target nucleon will produce a variation of some 10% of the mean

centre of mass energy. One consequence of this is that there will be no

single Dalitz or Goldhaber plot boundary to contain all the data (see

section IV.3).

I.2.4 Variation in the flux factor

Due to the momentum distribution of the target nucleons an asymmetry

exists in their flux depending on whether they are moving towards or

away from the primary particle. If the interaction were independent of

centre of mass energy then this asymmetry in the flux would result in a higher number of interactions where the target nucleon moves towards the beam than where the target nucleon moves away from the beam. Assuming that the target nucleon has a momentum equal and opposite to that of the spectator, the angular distribution for the spectator may be used to calculate the ratio of forward (f) to backward (b) target nucleons with respect to the beam. For the channel $\pi^+ d \rightarrow K^+ \Lambda^o p_s$ the ratio is

$$\frac{b}{f} = 0.82 \pm 0.07$$

Since b < f the cross-section must decrease with increasing centre of mass energy to reverse the asymmetry produced by the flux variation. Indeed this is found to be the case experimentally in section III.4.

I.2.5 Secondary scattering

In addition to the one step scattering amplitudes of the impulse approximation, the $\pi^+ d$ amplitude also includes multiple scattering terms. Furthermore there is a small probability of secondary scattering between the spectator and any one of the other final state particles. The cumulative effect of such processes can account for the observed excess of events in the high spectator momentum region. The majority of these events are removed by rejecting those spectators whose momentum is in excess of 500 MeV/c.

I.2.6. Shadowing effects

Mutual shadowing of the constituent nucleons implies that the total deuterium cross-section is less than the sum of the individual proton

and neutron cross-sections. The relationship between the cross-sections is given by (ref. I.20)

$$\sigma(\pi^+ d) = \sigma(\pi^+ n) + \sigma(\pi^+ p) - \frac{\sigma(\pi^+ n)\,\sigma(\pi^+ p)}{4\pi} <r^{-2}> \qquad \text{(I.1)}$$

where $<r^{-2}>$ denotes the mean inverse square nucleon separation. The value of $<r^{-2}>$ has been determined from existing cross-sections (ref. I.21) in deuterium and hydrogen with $\sigma(\pi^+ n)$ replaced by the charge symmetric $\sigma(\pi^- p)$. By interpolation the value of $<r^{-2}>$ at 4 GeV/c is $0.26\ fm^{-2}$. From equation (I.1) shadowing effects are estimated to reduce the individual nucleon cross-sections by some 3%.

I.3 Beam, chamber and exposure

The experiment was conducted at CERN and consisted of two exposures of approximately equal size, the first being 450K pictures and the second 400K pictures. The film was analysed by three collaborating laboratories: Birmingham University, the Rutherford High Energy Laboratory (RHEL) and Durham University.

An electrostatically separated beam (ref. I.22) of approximately 4 GeV/c π^+ mesons originating from the CERN Proton Synchrotron was injected into the 2-metre deuterium bubble chamber. The final particle momentum in the first exposure was 4.02 GeV/c with a momentum bite of 0.25%, and in the second exposure (3.94 $\pm$ 0.02) GeV/c. A plot of the beam momentum for both exposures is shown in figure I.2. Any contamination of the beam must be due to the four charged particles μ^+, K^+, p, d. However, the deuteron contamination is expected to be negligible at this energy using two RF separation cavities. Assuming the muon contamination is due to the pion decay $\pi^+ \longrightarrow \mu^+ + \nu$ within the distance of 7 metres

EVENTS/0.005 GeV/c

BEAM MOMENTUM (GeV/c)
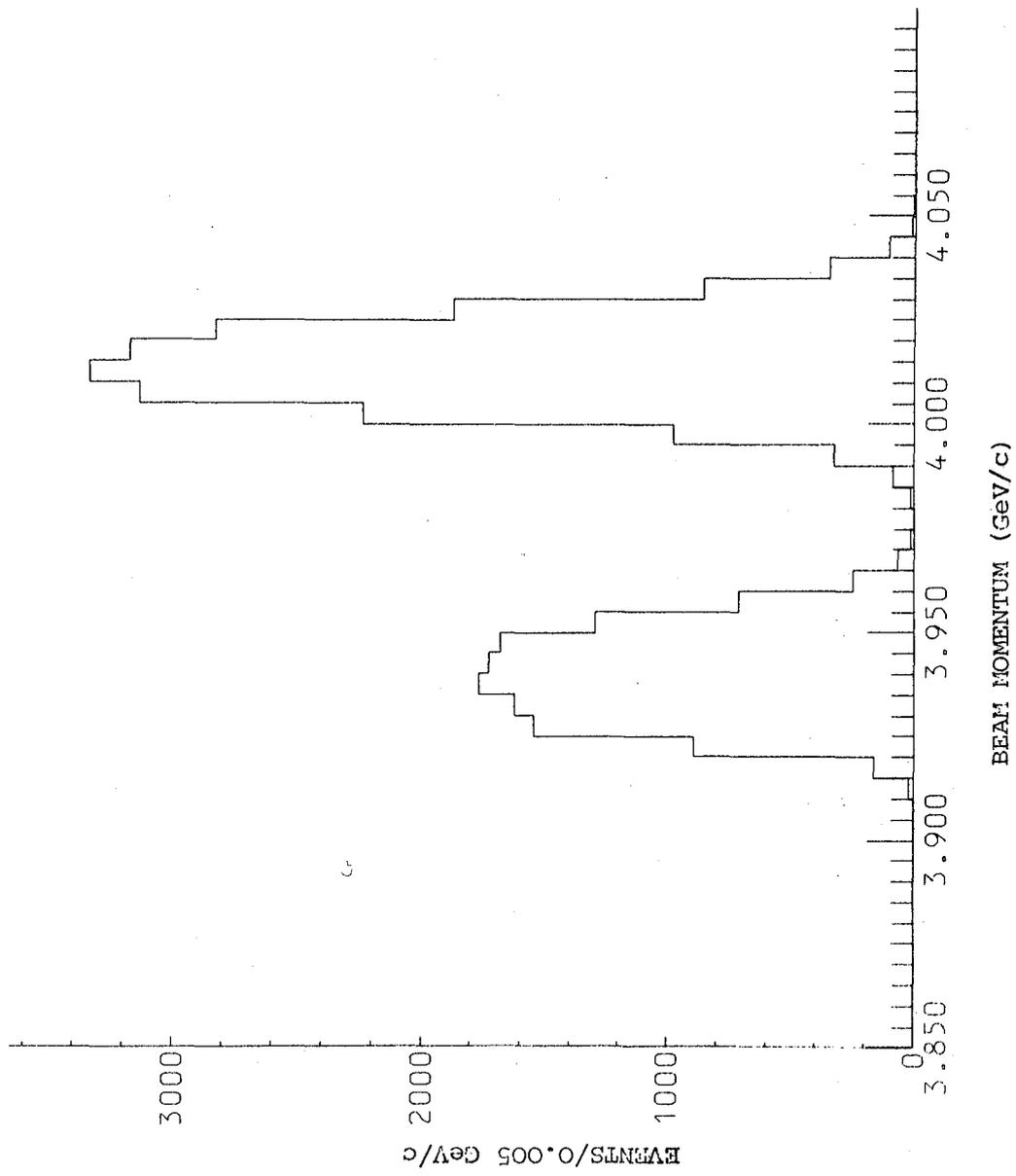
Fig. I.2

from the last collimator to the bubble chamber, the contamination is estimated to be (0.4 ± 0.1)% using the pion lifetime and momentum, and assuming that muons with momentum < 3.8 GeV/c will be "off-beam" (this corresponds to a difference in displacement of > 1.cm over 200 cm). The K^+ contamination was estimated from the number of decays $K^+ \rightarrow \pi^+ \pi^+ \pi^-$ which could be fitted to a sample of some 3000 3-pronged events. An upper limit of 1 event was found, giving an estimate of $<(0.5 \pm 0.1)$% for the contamination. The proton contamination was estimated by using a method of Gordon (ref. I.23). This relies on the two assumptions:

  (i) that the cross-sections

$$\frac{\sigma \ (\pi^+ d \ \rightarrow \ pp\pi^+ \pi^-)}{\sigma \ (\pi^+ d \ \rightarrow \ all)} = \frac{\sigma (pd \rightarrow ppp\pi^-)}{\sigma (pd \rightarrow all)}$$

and (ii) that the ratio of the probabilities

$$\frac{p \ (\text{spurious proton fit to a true pion beam})}{p \ (\text{spurious pion fit to a true proton beam})} = 2$$

which can be shown from Monte-Carlo simulations (see section II.3). The method yields a value of (4 ± 3)% for the proton contamination.

A schematic diagram of the bubble chamber is given in figure I.3. The approximate internal dimensions of the chamber are 200 x 51 x 60 cm. The liquid deuterium in this volume was kept at a temperature of $27^{\circ}K$ under a pressure of $6.3 \ kg/cm^2$. A pressure drop of $3.5 \ kg/cm^2$ was required to bring the liquid into a condition sensitive to bubble formation. The chamber was operated in its double pulsed mode with approximately 1/10 of a second between pictures and some 2 seconds between each double pulse. The sequence of operation is shown in figure I.4. During each pulse an average flux of about 12 beam particles was injected into the chamber. The trails of vapour bubbles formed along the paths of charged particles were photographed through the front chamber window by means of a triangular array of cameras with optical axes perpendicular to the window. The

2 METRE C.E.R.N. BUBBLE CHAMBER (HORIZONTAL SECTION)

FLASH UNITS

VACUUM TANK

MAGNET ARMATURES

LENSES

BEAM ENTRANCE

D_2

MAIN
MAGNET
COILS

CHAMBER GLASS

OUTER CHAMBER
(COLD TANK)

CAMERA PLATE

1m   0   1m

0   SCALE   2
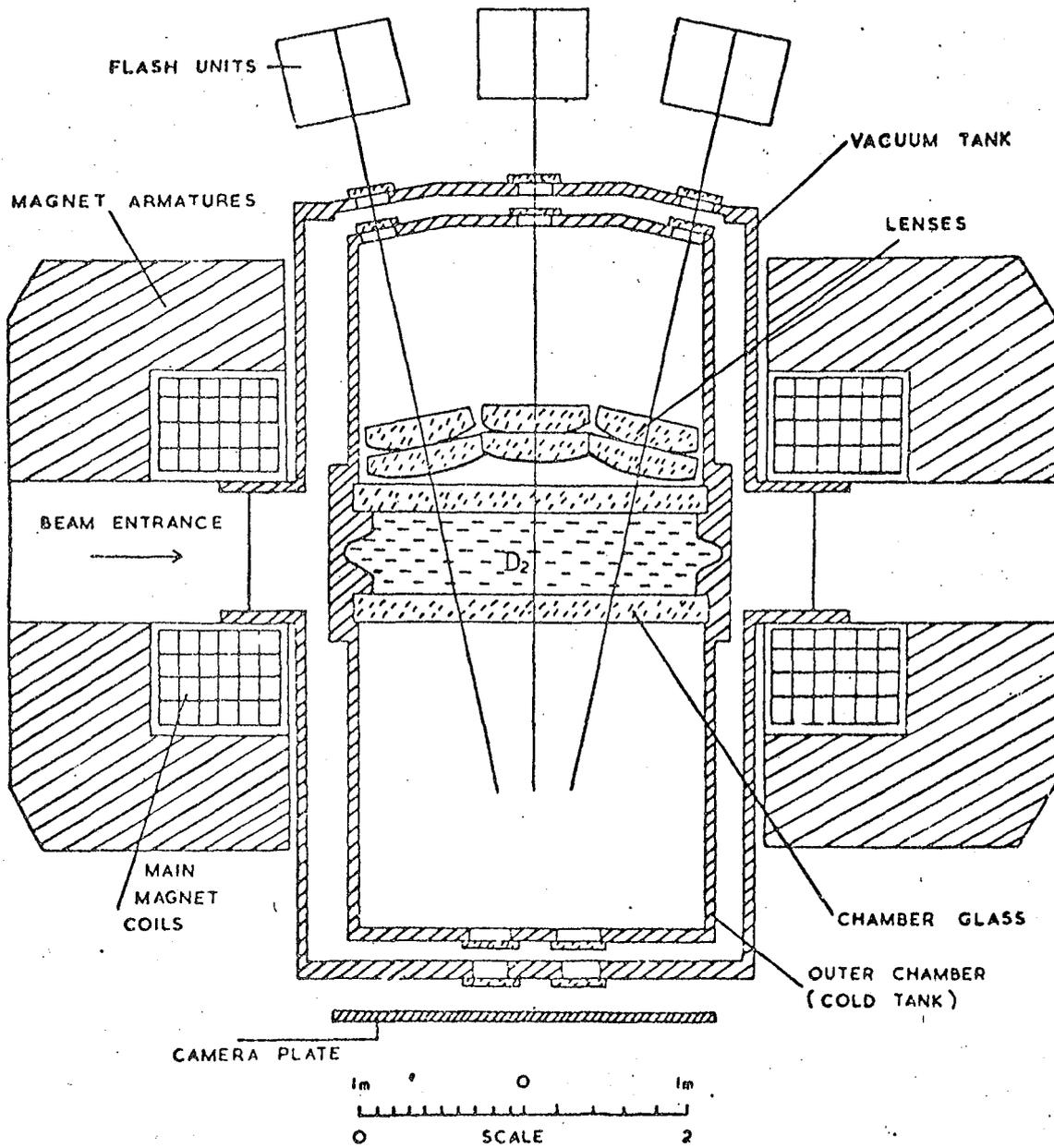
Fig. I.3
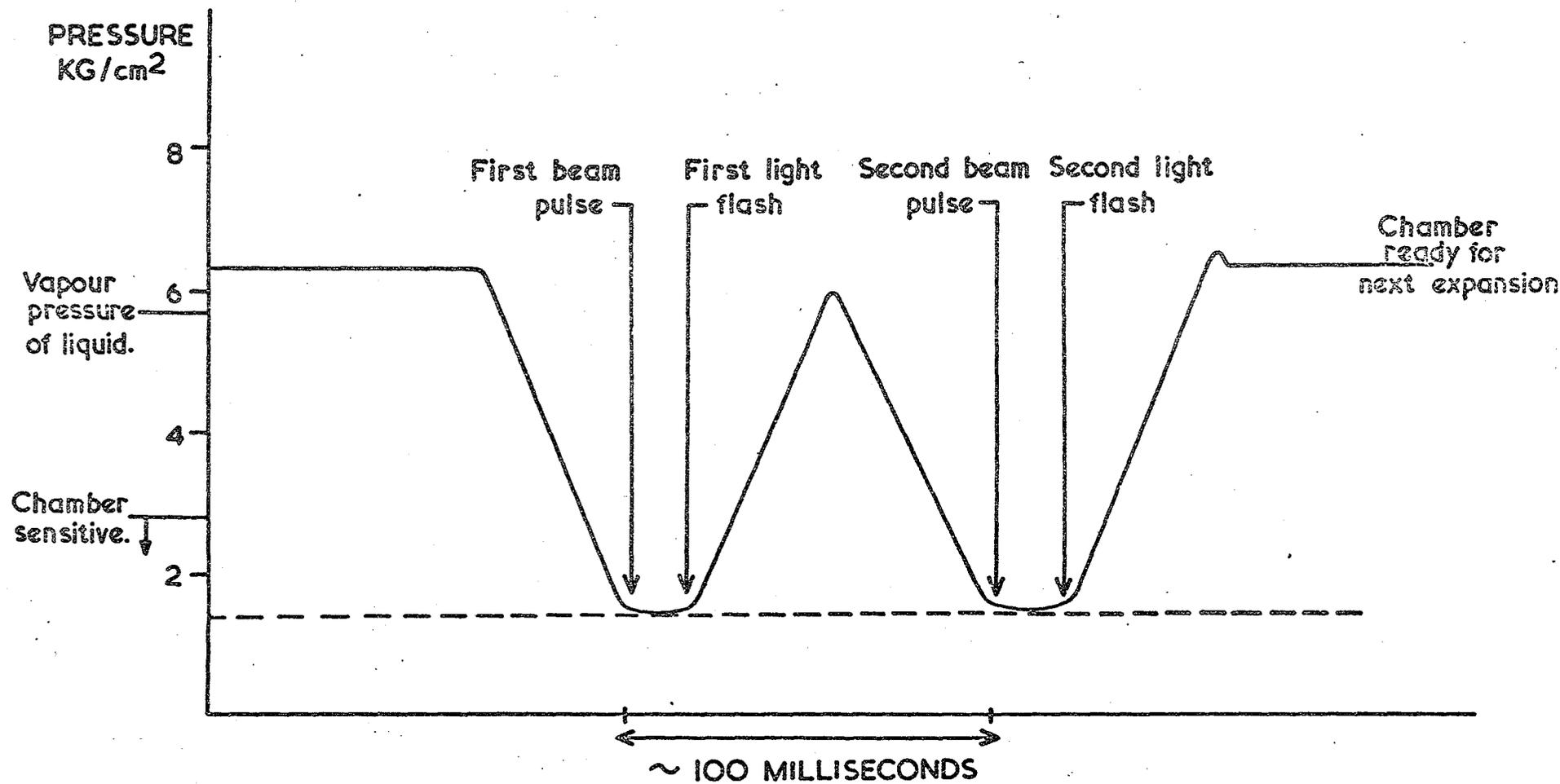
TYPICAL CURVE OF DOUBLE PULSE OF BUBBLE CHAMBER.

Fig. I.4

chamber was illuminated through the rear window by three monochromatic electron flash tubes. The light from these tubes was focussed in such a way that the cameras could only receive light scattered by the bubbles (dark field illumination). Fiducial marks were etched onto the front and rear windows for reference in the geometrical reconstruction of the events.

Surrounding the bubble chamber was a large electromagnet producing a nearly homogeneous magnetic field throughout the chamber volume. The magnetic field was perpendicular to the windows and had a central value of 17.5 Kgauss. Any variations in the field were mapped with an accuracy of about 1% of the central value so that corrections to the particle paths could be made in the kinematics reconstruction programme. Moving charged particles are forced to travel along a helix under the influence of the Lorentz force. The radius of curvature of the track projected onto a plane perpendicular to the field enables the momentum of the particle to be obtained:

$$ p = \frac{0.3\ H\ R}{\cos \lambda} $$

where p is the momentum in MeV/c,

H is the magnetic field in Kgauss,

R is the radius of curvature in cm,

and λ is the dip angle

I.4 Scanning and measurement

Events were recorded regardless of whether the interaction occurred on the target proton or the target neutron provided that one or more V^o particles were observed. A V^o is produced when a neutral strange particle

decays visibly in the chamber (i.e. Λ° or K°). If one of the charged secondaries from the interaction vertex displayed a kink, it was regarded as a possible decay of a charged, strange particle (i.e. $K^{\pm}$ or $\Sigma^{\pm}$) and measured as such. However, because of contamination from pion scatterings, events comprising one or more kinks but no V° particles were not measured. Consequently only a part of the total strange particle production has been considered.

The scanners were instructed to record events only if the inter-action took place within a fiducial volume of length 107 cm in the first exposure and 127 cm in the second exposure. However, for the purpose of calculating the topological cross-sections (section III.2), the length is reduced to 76 cm in order to remove edge effects and to provide a well-defined length for non-interacting beam tracks.

The scanning efficiencies for the different topologies were deter-mined from double scanning about one quarter of the total film. It has been assumed that all events within a topology have an equal probability of being seen. The scanning efficiency for scan i ($i = 1, 2$) is defined by

$$e_i = N_i/N$$

where N_i is the number of events found in scan i, and N is the unknown total number of events in the topology considered.

Consequently the number of events found in both scans is

$$N_{12} = e_1 e_2 N = e_1 N_2 = e_2 N_1$$

giving

$$e_1 = N_{12}/N_2$$

$$e_2 = N_{12}/N_1$$

The values of e_1 for the different topologies are listed in table I.2.

TABLE I.2

SCANNING EFFICIENCIES

Topology	Scanning efficiency (%)
2 prong + 1 neutral V	86 ± 2
2 prong + 2 neutral V's	97 ± 3
2 prong + 1 neutral V + 1 charged V	95 ± 4
4 prong + 1 neutral V	91 ± 2
4 prong + 2 neutral V's	100 ± 12
4 prong + 1 neutral V + 1 charged V	99 ± 7
6 prong + 1 neutral V	100 ± 4

The three views of each event were measured on the RHEL HPD1 automatic measuring machine, after pre-measurement using three image plane digitisers. Each digitiser measured the coordinates of interaction points, points on particle tracks and fiducial marks to an accuracy on the table of ˜25 μm so that the HPD would know approximately where the tracks of an event were to be found. The HPD also provides ionisation measurements from the relative bubble density of the tracks which are used to help resolve kinematic ambiguities (see chapter II).

I.5 The processing of events

A schematic flow diagram of the processing of events is shown in figure I.5. In this section the various stages from the HPD to the final data summary tape (DST) will be described.

After the HPD has digitised the tracks the results are converted into master points by the programme HAZE. On average one master point is produced for every 2.5 cm of track in real space. From such measurements the error on a reconstructed point in space is typically 30 μm in the (x, y) plane (perpendicular to the camera axis) and ˜300 μm in the z direction (parallel to the camera axis).

The three-dimensional reconstruction of events is achieved by using the Rutherford Laboratory programme GEOMETRY (ref. I.24). After allowing for optical distortion and film stretch, the programme reconstructs the event from the film coordinates of the master points, thereby calculating the vertex and centre of track values for the momentum, azimuthal and dip angles with their associated errors.

SCHEMATIC FLOW DIAGRAM FOR EVENTS
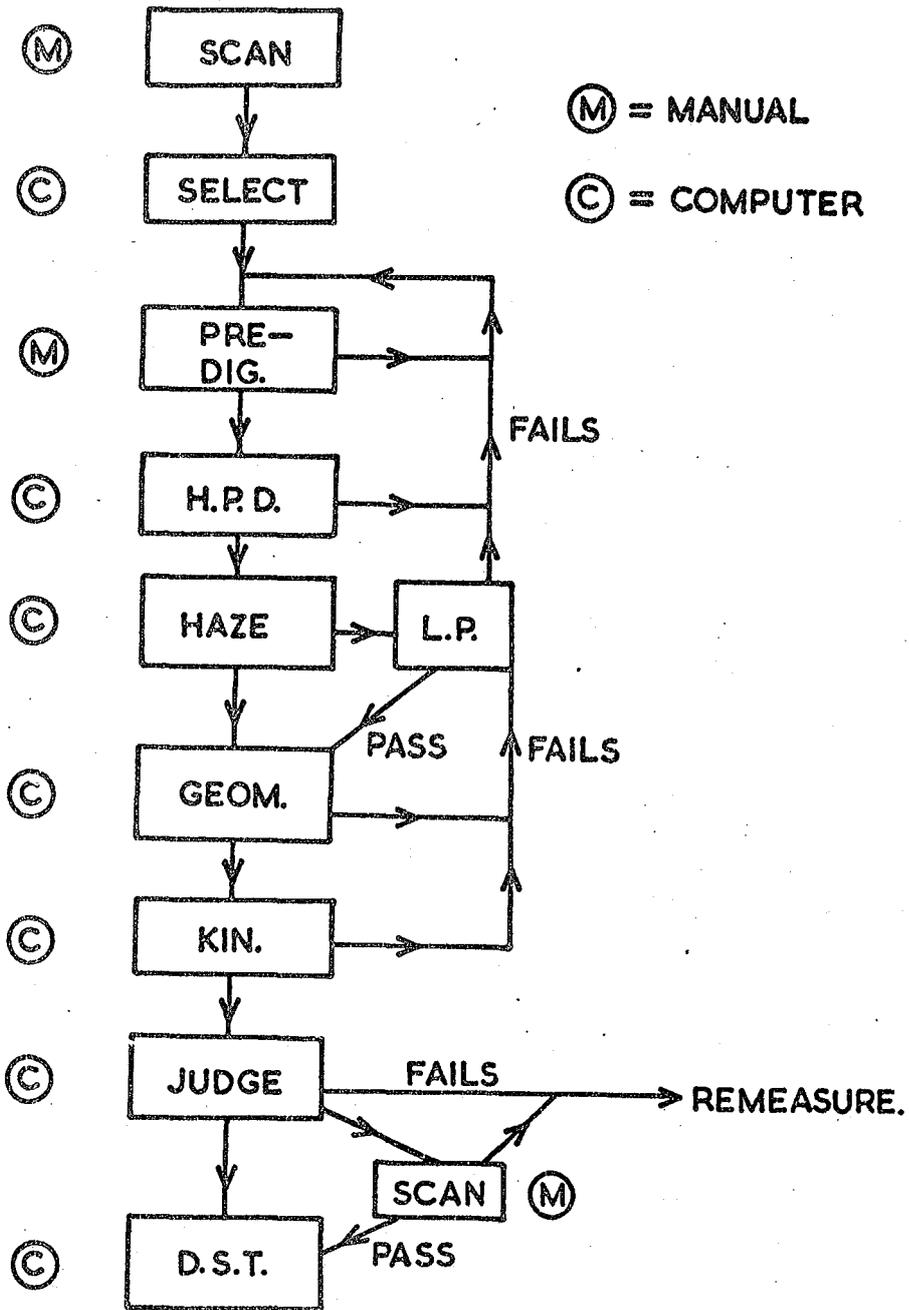
Fig. I.5

The light-pen is used to recover events which have failed geometrical reconstruction due to HAZE errors. For example a crossing track may be misinterpreted as being the correct one, or a scatter may occur on a track. The light-pen enables an on-line HAZE programme to be redirected by an operator to the correct track, or to be instructed to use only part of the available track length.

After geometrical reconstruction the events are fitted to a series of hypotheses using the KINEMATICS programme (ref. I.25). The χ^2 probability is calculated for each hypothesis. In addition the fitted values for the track momenta and directions are required to satisfy the four constraint equations which account for conservation of momentum and energy. The number of degrees of freedom for the fit is given by

ND = (number of measured quantities) - (number of free quantities)

The latter term is equal to the difference (number of measured quantities) - (number of constraints), so that ND is simply the number of constraints. If there are no missing neutral particles in the final state all four constraint equations can be used (4C fit). If however there is a missing neutral of known mass, the three momentum equations must be used to solve for the momentum, dip and azimuth of the missing particle, leaving the energy equation as the only constraint (1C fit). For two or more missing neutrals there are insufficient equations to solve for the number of particles and the event becomes a no-fit (OC fit), for which the χ^2 probability is undefined.

The number of hypotheses fitting an event can be reduced by rejecting those hypotheses for which the calculated ionisation for a secondary track differs by more than a predetermined amount from that measured by the HPD. The majority of such tests are carried out by the programme JUDGE (ref I.26) and only some 5% of the events need to be returned to the

scan table to estimate the ionisation by eye. Despite this there are still a considerable number of ambiguities which must be resolved by further selection criteria. These will be dealt with in chapter II. All successful fits to the events are written onto the final data summary tape.

The pass rate through the system from HPD to DST was ˜95%. Failed events have been at least twice through the analysing chain.

CHAPTER II

RESOLUTION OF AMBIGUITIES

II.1 Introduction

The limited precision of measurement means that often more than one

hypothesis is fitted to an event in KINEMATICS. In some cases the

resulting ambiguities may be resolved by demanding that the ionisation

predicted by KINEMATICS is compatible with that measured by the HPD (JUDGE

programme - section I.5). Where this is insufficient the event may be

re-examined on the scan-table by a physicist and judgement made where

possible. However for track momenta of > 1.3 GeV/c it becomes impossible

to distinguish the ionisation of a pion from that of a proton. For a

pion and a kaon, the corresponding limit is ~ 0.8 GeV/c. Consequently a

series of selection rules must be determined in order to resolve the

remaining ambiguities (on average about 2.5 hypotheses per event). Indeed

most of the analysis involved in the calculation of the strange·particle

cross-sections is concerned with establishing criteria to resolve the

ambiguous channels. This is known to be difficult for samples with low

statistics and consequently cross-sections have not been calculated for

channels containing fewer than about 15 events.

II.2 Basic selection rules

One approach in determining the selection criteria is to examine the

data for obvious experimental features which characterise a spurious fit.

This involves a comparison of experimental and predicted distributions.

Two obvious choices for such a comparison are the χ^2 probability distri-

bution, which should be isotropic provided the errors of measurement

have been estimated correctly, and the spectator momentum distribution,

which has been predicted by Hulthen and Sugaware (see appendix A). On

the basis of the comparison two preliminary selections have been made:

(i) The χ^2 probability $P(\chi^2)$, for the primary vertex fit is

required to exceed a prescribed minimum. This minumum was chosen as

follows:

number of constraints (at the primary vertex)	$P(\chi^2)$ min. (%)
1	5
2	0.1
4 (one associated V^o)	0.1
4 (two associated V^o's)	0.001

These values were decided by the examination of the probability distri-

butions such as those shown in figure II.1. The distributions are flat,

as expected, apart from the spike at low probability which is normally

interpreted as being due to contamination from spurious fits, and may be

removed by the appropriate probability selection. This is supported by

Monte Carlo simulations (see section II.3) where in general the spurious

fits do occur at low probability. For the more highly constrained fits

a lower minimum was chosen because (a) the spike occurred at lower

probability, and (b) there were fewer ambiguities in the low probability

region than for the less constrained fits. The loss of genuine fits

due to the probability selection may be corrected for by simple scaling,

assuming the distribution is flat. Obviously the only significant loss

is for those events in the one-constraint class, where a correction

factor of 1.05 must be applied to the total number of events finally

assigned to this class.

(ii) The fit is rejected if the spectator momentum is greater than

500 MeV/c. This is to avoid using the small number of events which have

involved a final state interaction with the spectator nucleon (see

section I.2.5), or where in a spurious fit the wrong track is selected

$\pi + d \to \to K^+ \Lambda^\circ p_s$

$\pi^+ d \to K^+ \Lambda^\circ \pi^\circ p_s$
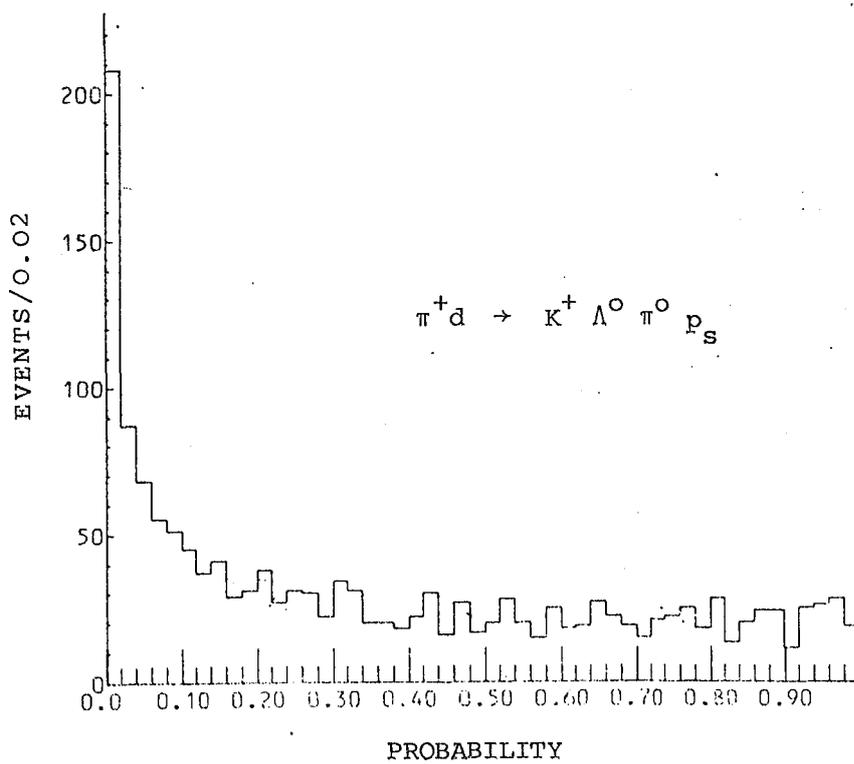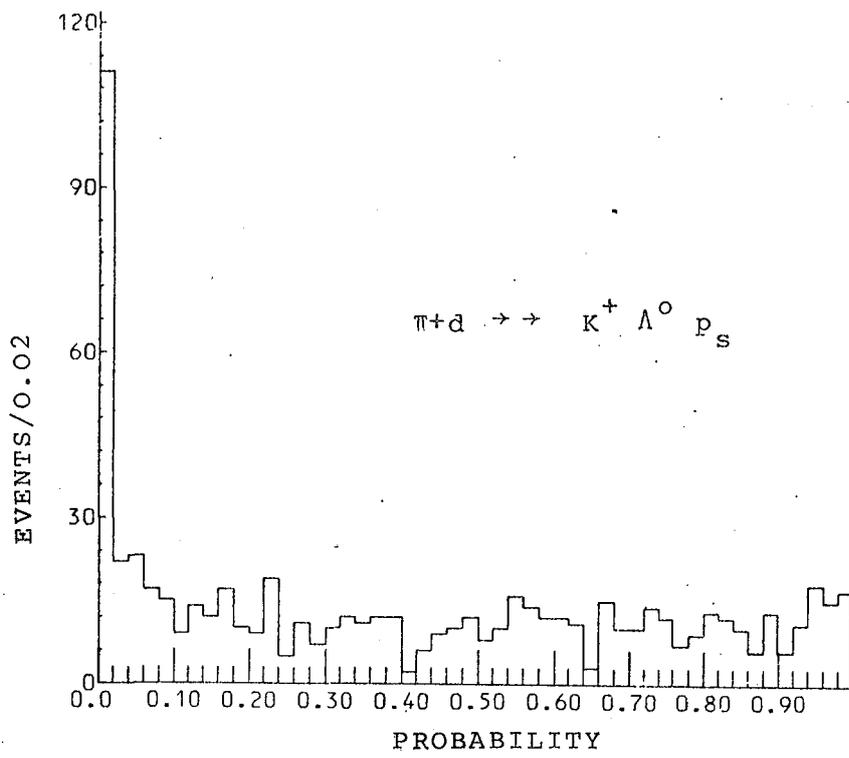
Fig. II.1 Single vertex probability distributions

as the spectator. In previous work on the experiment this maximum value

for the spectator momentum was taken to be 300 MeV/c (refs. I.18 and I.19).

However, in the strange particle sample ambiguities of this type mainly

arise when the spectator proton is fitted as a K^+, in which case

ionisation tests are usually sufficient to resolve the ambiguities below

a momentum of 500 MeV/c. The loss of genuine fits due to the spectator

momentum selection may be estimated from the Hulthen distribution and is

found to be negligible.

The above selection rules, in most cases, are not sufficient to

resolve completely the ambiguous channels. The remaining ambiguities

are shown in table II.1. Here the diagonal elements correspond to

unambiguous fits and the figures in brackets indicate the number of self-

ambiguities (i.e. all fits to the event pertain to the same channel, but

the individual track identities have been changed between ambiguities).

The off-diagonal elements indicate two-fold ambiguities. However in

some cases there may be more than two fits to the event. For example,

supposing an event is fitted with the following three hypotheses:

$$(1) \quad \pi^+ d \longrightarrow K^+ \Lambda^o_v \; p_s \qquad\qquad (*)$$

$$(2) \quad \pi^+ d \longrightarrow K^+ \Lambda^o_v \; p_s \; \pi^o$$

$$(3) \quad \pi^+ d \longrightarrow K^+ \Sigma^o_v \; p_s$$

then a two-fold ambiguity would be indicated between 1 and 2, between 2

and 3, and between 1 and 3. A similar argument holds for higher order

ambiguities. Ambiguities involving channels with two or more unseen

neutrals are not shown since no cross-sections have been calculated for

these channels. (The reasons for this are discussed in section II.3D).

(*) The sub-script v with Λ, Σ or K is used to indicate the decay was
visible within the bubble chamber. Σ^o_v denotes the decay $\Sigma^o \longrightarrow \Lambda^o_v \gamma$
The sub-script i stands for invisible decays.

TABLE II.1-AMBIGUITY MATRICES

Diagonal elements show the number of unambiguous fits. The figures in brackets give the number of self-ambiguities. Low populated channels (i.e. $\lesssim$ 15 events) are not shown.

Subscripts v and i imply that the V^o was seen or unseen respectively.

a)   2 PRONG + 1 NEUTRAL V

CHANNEL	$K^+ \Lambda^o_v p_s$	$K^+ \Lambda^o_v p_s \pi^o$	$K^+ \Lambda^o_v n_s \pi^+$	$K^+ \Sigma^o_v p_s$	$K^o_i \Lambda^o_v p_s \pi^+$	$K^o_v \Lambda^o_i p_s \pi^+$	$K^o_v K^o_i p p_s$	$K^o_v K^+ p n$	$K^o_v \Sigma^o_i p_s \pi^+$
$K^+ \Lambda^o_v p_s$	(0) 292	30	0	334	0	0	0	0	0
$K^+ \Lambda^o_v p_s \pi^o$	30	(0) 576	5	89	429	9	7	17	7
$K^+ \Lambda^o_v n_s \pi^+$	0	5	(119) 640	0	24	1	0	3	0
$K^+ \Sigma^o_v p_s$	334	89	0	(0) 106	2	0	0	0	0
$K^o_i \Lambda^o_v p_s \pi^+$	0	429	24	2	(0) 525	15	4	14	8
$K^o_v \Lambda^o_i p_s \pi^+$	0	9	1	0	15	(0) 124	36	164	165
$K^o_v K^o_i p p_s$	0	7	0	0	4	36	(0) 279	59	24
$K^o_v K^+ p n$	0	17	3	0	14	164	59	(13) 421	78
$K^o_v \Sigma^o_i p_s \pi^+$	0	5	0	0	8	165	24	78	(0) 116

CHANNEL	$K^+ \Lambda^o_v p_s \pi^+\pi^-$	$K^+ \Lambda^o_v p_s \pi^+\pi^-\pi^o$	$K^+ \Lambda^o_v n_s \pi^+\pi^+\pi^-$	$K^+ \Sigma^o_v p_s \pi^+\pi^-$	$K^o_i \Lambda^o_v p_s \pi^+\pi^+\pi^-$	$K^o_v \Lambda^o_i p_s \pi^+\pi^+\pi^-$	$K^o_v K^o_i pp_s \pi^+\pi^-$	$K^o_v K^+ pp_s \pi^-$	$K^o_v K^+ pp_s \pi^-\pi^o$	$K^o_v K^+ pn \pi^+\pi^-$	$K^o_v K^- pp_s \pi^+$	$K^o_v K^- pp_s \pi^+\pi^-$	$K^o_v K^- pn \pi^+\pi^+$	$K^o_v \Sigma^o_i p_s \pi^+\pi^+\pi^-$
$K^+ \Lambda^o_v p_s \pi^+\pi^-$	(131) 325	67	2	704	2	0	0	14	2	0	4	2	0	0
$K^+ \Lambda^o_v p_s \pi^+\pi^-\pi^o$	67	(55) 486	3	197	170	4	2	0	1	2	0	1	1	2
$K^+ \Lambda^o_v n_s \pi^+\pi^+\pi^-$	2	3	(23) 142	2	2	0	0	0	0	0	0	0	0	0
$K^+ \Sigma^o_v p_s \pi^+\pi^-$	704	197	2	(28) 127	2	0	0	9	1	0	4	1	0	0
$K^o_i \Lambda^o_v p_s \pi^+\pi^+\pi^-$	2	170	2	2	(0) 218	5	2	0	0	1	0	0	1	3
$K^o_v \Lambda^o_i p_s \pi^+\pi^+\pi^-$	0	4	0	0	5	(0) 33	8	0	0	54	0	1	29	45
$K^o_v K^o_i pp_s \pi^+\pi^-$	0	2	0	0	2	8	(0) 79	0	19	15	1	17	3	3
$K^o_v K^+ pp_s \pi^-$	14	0	0	9	0	0	0	(15) 185	4	0	57	0	0	0
$K^o_v K^+ pp_s \pi^-\pi^o$	2	1	0	1	0	0	19	4	(3) 76	1	1	5	0	0
$K^o_v K^+ pn \pi^+\pi^-$	0	2	0	0	1	54	15	0	1	(9) 120	0	3	26	18
$K^o_v K^- pp_s \pi^+$	4	0	0	4	0	0	1	57	1	0	(0) 245	3	0	0
$K^o_v K^- pp_s \pi^+\pi^-$	2	1	0	1	0	1	17	0	5	3	3	(1) 60	2	0
$K^o_v K^- pn \pi^+\pi^+$	0	1	0	0	1	29	3	0	0	26	0	2	(0) 93	11
$K^o_v \Sigma^o_i p_s \pi^+\pi^+\pi^-$	0	2	0	0	3	45	3	0	0	18	0	0	11	(0) 27

c) 2 PRONG + 2 NEUTRAL V's

CHANNEL	$K^0_v \Lambda^0_v p_s \pi^+$	$K^0_v \Lambda^0_v p_s \pi^+ \pi^0$	$K^0_v \Lambda^0_v n_s \pi^+ \pi^+$	$K^0_v \Sigma^0_v p_s \pi^+$	$K^0_v K^0_v pp_s$	$K^0_v K^0_v pp_s \pi^0$	$K^0_v K^0_v p n \pi^+$
$K^0_v \Lambda^0_v p_s \pi^+$	(o) 203	9	.9	135	5	0	3
$K^0_v \Lambda^0_v p_s \pi^+ \pi^0$	9	(1) 224	2	36	0	0	4
$K^0_v \Lambda^0_v n_s \pi^+ \pi^+$	9	4	(o) 158	0	0	0	1
$K^0_v \Sigma^0_v p_s \pi^+$	135	36	0	(o) 52	4	0	0
$K^0_v K^0_v pp_s$	5	0	0	4	(o) 123	0	5
$K^0_v K^0_v pp_s \pi^0$	0	0	0	0	0	(o) 54	2
$K^0_v K^0_v p n \pi^+$	3	4	1	0	5	2	(o) 165

d) 4 PRONG + 2 NEUTRAL V's

CHANNEL	$K^0_v \Lambda^0_v p_s \pi^+ \pi^+ \pi^-$	$K^0_v \Lambda^0_v p_s \pi^+ \pi^+ \pi^- \pi^0$	$K^0_v \Sigma^0_v p_s \pi^+ \pi^+ \pi^-$
$K^0_v \Lambda^0_v p_s \pi^+ \pi^+ \pi^-$	(o) 35	1	31
$K^0_v \Lambda^0_v p_s \pi^+ \pi^+ \pi^- \pi^0$	1	(o) 16	5
$K^0_v \Sigma^0_v p_s \pi^+ \pi^+ \pi^-$	31	5	(o) 4

e) 2 PRONG + 1 CHARGED V + 1 NEUTRAL V

CHANNEL	$K^0_v \Sigma^+ n_s \pi^+; \Sigma^+ \to p\pi^0$	$K^0_v \Sigma^+ n_s \pi^+; \Sigma^+ \to \pi^+ n$	$K^0_v \Sigma^+ p_s \pi^0; \Sigma^+ \to p\pi^0$	$K^0_v \Sigma^+ p_s \pi^0; \Sigma^+ \to \pi^+ n$
$K^0_v \Sigma^+ n_s \pi^+; \Sigma^+ \to p\pi^0$	(15) 48	0	0	0
$K^0_v \Sigma^+ n_s \pi^+; \Sigma^+ \to \pi^+ n$	0	(11) 99	0	0
$K^0_v \Sigma^+ p_s \pi^0; \Sigma^+ \to p\pi^0$	0	0	(2) 8	0
$K^0_v \Sigma^+ p_s \pi^0; \Sigma^+ \to \pi^+ n$	0	0	0	(1) 26

f) 4 PRONG + 1 CHARGED V + 1 NEUTRAL V

CHANNEL	$K^0_v \Sigma^-_v p_s \pi^+ \pi^+$	$K^0_v \Sigma^+ p_s \pi^+ \pi^-; \Sigma^+ \to p\pi^0$	$K^0_v \Sigma^+ p_s \pi^+ \pi^-; \Sigma^+ \to \pi^+ n$	$K^0_v \Sigma^+ p_s \pi^+ \pi^- \pi^0; \Sigma^+ \to p\pi^0$	$K^0_v \Sigma^+ p_s \pi^+ \pi^- \pi^0; \Sigma^+ \to \pi^+ n$
$K^0_v \Sigma^-_v p_s \pi^+ \pi^+$	(4) 55				
$K^0_v \Sigma^+ p_s \pi^+\pi^-; \Sigma^+ \to p\pi^0$		(9) 27	0	0	0
$K^0_v \Sigma^+ p_s \pi^+\pi^-; \Sigma^+ \to \pi^+ n$		0	(8) 32	0	1
$K^0_v \Sigma^+ p_s \pi^+\pi^-\pi^0; \Sigma^+ \to p\pi^0$		0	0	(1) 10	0
$K^0_v \Sigma^+ p_s \pi^+\pi^-\pi^0; \Sigma^+ \to \pi^+ n$		0	1	0	(5) 12

A blank signifies the ambiguity is not possible

II.3 Monte Carlo simulations

The measurements of strange particle channels have been simulated using Monte Carlo techniques (FAKE programme - ref. II.1). This requires a priori knowledge of the experimental momentum transfer and angular distributions which may be obtained from unambiguous real data. Although such data will not yield completely unbiased distributions, they will suffice for the purpose of the simulation since the formation of ambiguities was found to have little dependence on the momentum transfer and angular distributions of the simulated events. On the other hand care must be taken to ensure that realistic errors of measurement are used in the simulation since these will critically affect the formation of ambiguities. This may be done by ensuring that the stretch functions are distributed as Gaussian of unit width, and that the χ^2 probability distribution is flat, for correct fits to the simulated events. The stretch functions are defined as

$$S = \frac{(x_f - x_m)}{\sqrt{(\sigma_m^2 - \sigma_f^2)}}$$

where x_f and x_m are the fitted and measured quantities, and σ_f and σ_m are their respective errors. The quantities used in fitting an event are 1/momentum, tan (dip angle) and azimuthal angle. After passing the simulated events through KINEMATICS the probability of forming ambiguities and their characteristics may be determined. However, because of the above dependence on measurement errors no precise quantitative interpretation of the results has been made. In spite of this, the analysis of the simulated ambiguities does enable final selection criteria to be defined, with some idea of the resulting purity of the resolved channels. The criteria which have been adopted are as follows:

A.   Accept the highest constraint fit unless the ambiguity is of the 4C/2C

kind.

FAKE simulations show in all cases that whereas an all charged

event (4C fit) may be spuriously fitted with the same charged description

together with one unseen neutral particle (1C fit) the reverse is never

true. (i.e. the true 1C event is never fitted as a 4C event). In

general it is found that with an ambiguity the higher constraint fit is

the correct one. The 4C/2C ambiguity is an exception to this and is

considered in B. The rule is also found to be inadequate in resolving

1C/OC ambiguities for some channels. (A OC fit arises when there are

two or more unseen neutrals in the event). However any contamination of

the 1C fits from true OC events will in general manifest itself as a

tail on the missing mass squared distribution which may be easily

removed by demanding that the missing mass squared should be less than

a prescribed maximum. Two examples of 1C channels which have a

significantly high contamination from OC events are dealt with in

section II.4i).

B.   Events which involve an ambiguity between Λ^o_v and Σ^o_v (i.e. 4C/2C

ambiguities) may be resolved by using the decay properties of the

$\Sigma^o \rightarrow \Lambda^o \gamma$ decay. The method is similar to that of Butler (ref. II.2)

but has been modified in this experiment to accommodate the spectator

proton. The three main types of 4C/2C ambiguities occurring in the

strange particle sample are:

   (a) $\pi^+ d \rightarrow K^o_v \Lambda^o_v p_s$ or $K^+ \Sigma^o_v p_s$

   (b) $\pi^+ d \rightarrow K^o_v \Lambda^o_v p_s \pi^+$ or $K^o_v \Sigma^o_v p_s \pi^+$

and (c) $\pi^+ d \rightarrow K^+ \Lambda^o_v p_s \pi^+ \pi^-$ or $K^+ \Sigma^o_v p_s \pi^+ \pi^-$

   In each case the Σ^o_v has the subsequent decay:

$$\Sigma^o \rightarrow \Lambda^o \gamma$$

so that in the fitting process the $(\Lambda^0\gamma)$ effective mass must be constrained to that of the Σ^0. In the rest system of the true Σ^0, the decay cosine distribution of the emitted γ-ray should be isotropic. However, for the spuriously fitted Σ^0 FAKE simulations have shown a pronounced peaking of the γ-distribution in the direction of the outgoing mesonic system, M. (K^+, $K^0\pi^+$ and $K^+\pi^+\pi^-$ for (a), (b) and (c) respectively). Empirically the γ-distribution of the fitted Σ^0 events shows just this effect as can be seen from figure II.2. Here each event has been transformed into the Σ^0 rest system and the cosine of the angle, $\beta_M\gamma$, between M and the emitted γ-ray has been plotted separately for the three Σ^0-channels above. The hatched area corresponds to those Σ^0-fits which are not ambiguous with the Λ^0-channel. These are consistent with isotropy whereas the remaining (ambiguous) events are forward peaked. The explanation of this is that KINEMATICS will tend to fit spurious γ-rays predominantly in the direction of the other final state particles so as to best accommodate an increase in the energy/momentum of the γ by a corresponding decrease in the energy/momentum of the other outgoing particles. Consequently those ambiguities with cos $\beta_M\gamma$ >0.85 are assigned to the Λ^0-channel. The loss of geniune Σ^0-fits by this selection is corrected for by simple scaling, using the fact that the γ-distribution for those events finally assigned to the Σ^0-channel should be isotropic. The correction factors are shown in table II.2. FAKE simulations of (a) and (b) have shown that ~16% of the true Λ^0-channel is left spuriously fitted as Σ^0 after the above selection. However almost all of these Λ^0-events are characterised by an unseen spectator proton and therefore those Σ^0-fits with cos $\beta_{M\gamma}$ <0·85, accompanied by a <u>seen</u> spectator must be genuine Σ^0's. Consequently any Λ^0/Σ^0 ambiguity satisfying these criteria may be assigned to the Σ^0-channel. This is sufficient to resolve approximately 2/3 of the ambiguities of type (a) and (b).
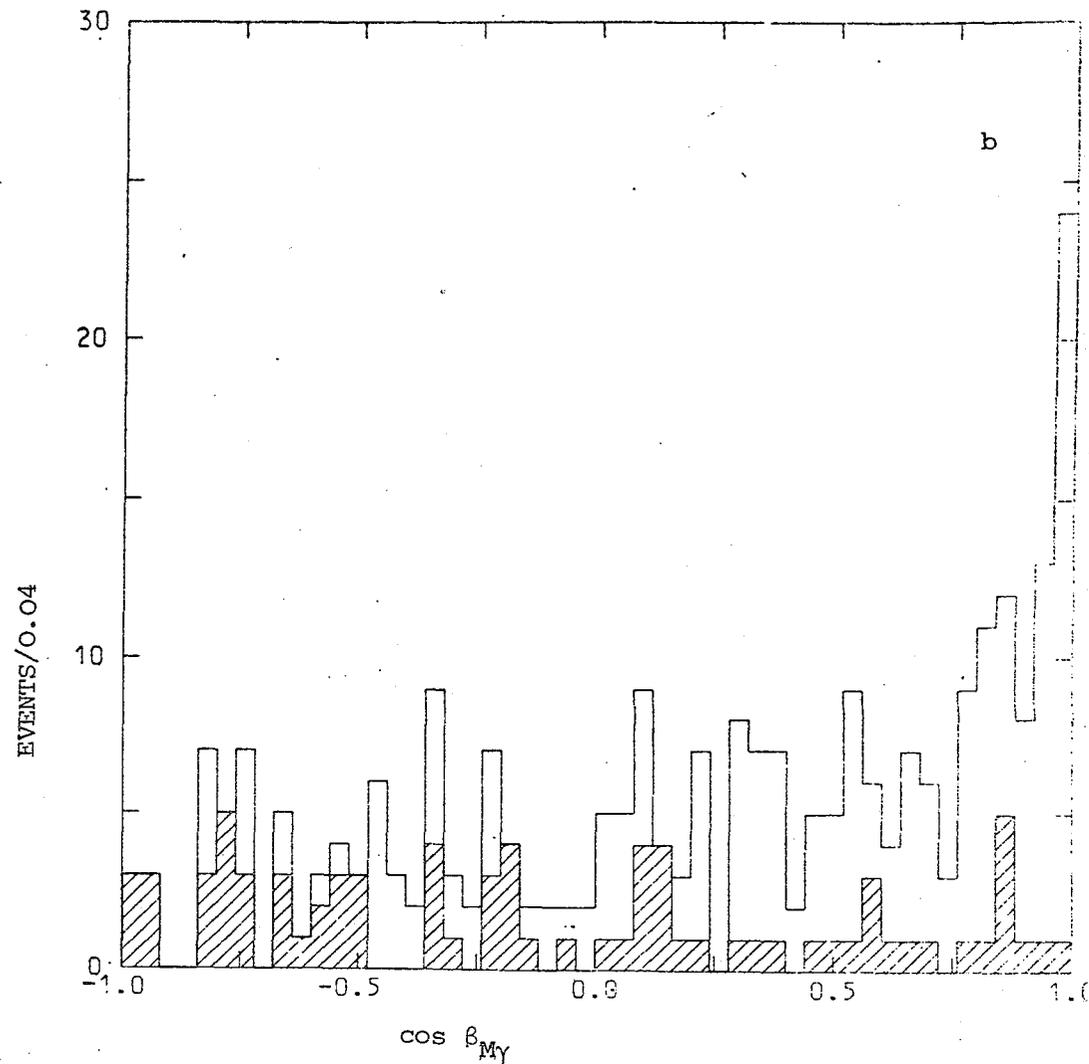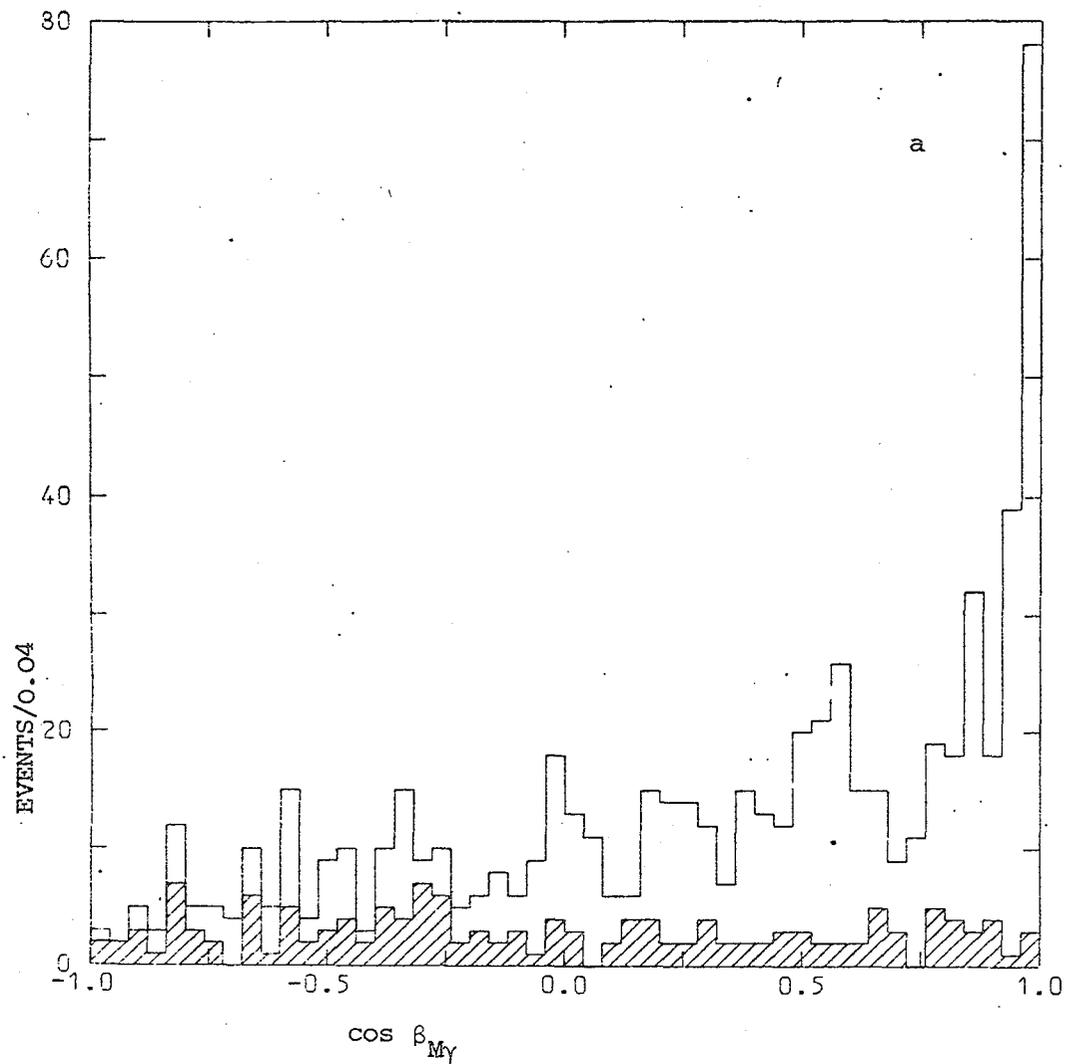
Fig. II.2 The γ-decay distributions for events fitting the channels (a) $\pi^+ d \rightarrow K^+ \Sigma^0 p_s$ (b) $K^0 \Sigma^0 \pi^+ p_s$. The hatched area corresponds to those events with no Λ^0/Σ^0 ambiguity.
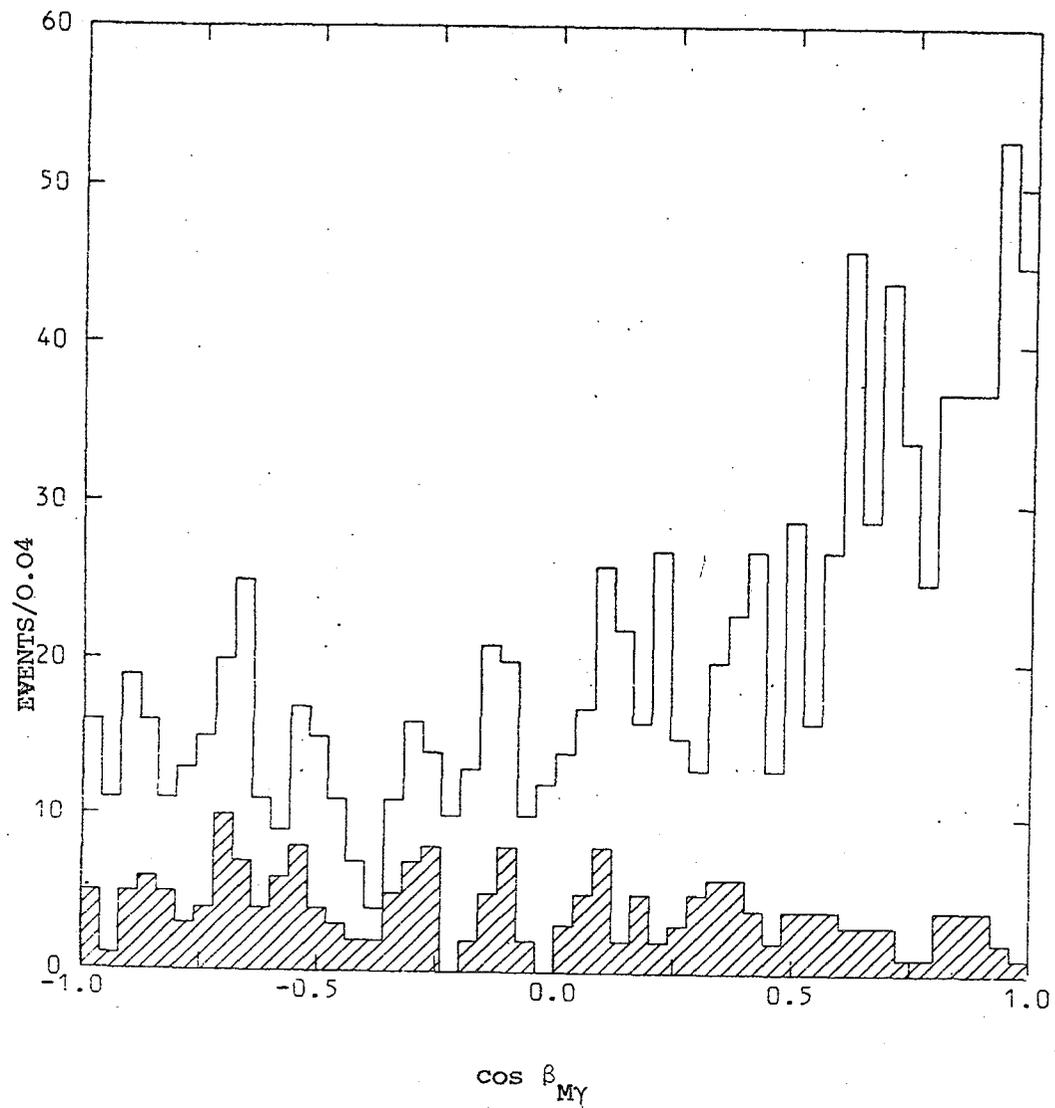
Fig. II.2 (c) The γ-distribution for events fitting the channel $\pi^+ d \to K^+ \Sigma^0 \pi^+ \pi^-$. The hatched area corresponds to those events with no Λ^0/Σ^0 ambiguity.

TABLE II.2

CORRECTION FACTORS FOR THE γ DECAY ANGLE

Channel	Correction factor
$\pi^+ d \rightarrow K^+ \Sigma^O p_s$	1.05
$\pi^+ d \rightarrow K^O \Sigma^O \pi^+ p_s$	1.06
$\pi^+ d \rightarrow K^+ \Sigma^O \pi^+ \pi^- p_s$	1.06

The remainder are resolved as in D below. As can be seen from figure II.2, the Υ-distribution for ambiguities of type (c) does not show the same pronounced peaking as for (a) and (b). This is because the high multiplicity of the final state provides the fitting process with more freedom to fake a spurious γ. However ~30% of the ambiguities may still be resolved by assigning those fits with $\cos\beta_{M\gamma} > 0.85$ to the Λ^o-channel, leaving the remainder to be resolved by rule D.

C. Accept a Λ^o-fit in preference to a K^o-fit. This arises from the kinematic limitation imposed on the Λ^o due to the large difference in masses of the secondary pion and proton which results in the proton always having momentum in excess of the negative pion momentum. Whereas the Λ^o can simulate the K^o, only for a restricted range of the positive pion momentum can the K^o simulate the Λ^o decay. As can be seen from table II.1 the number of V^o's ambiguous in this way is <5% of the total data.

D. The remaining ambiguities (normally about 13% of the total data) can be resolved by either of the following two methods:

   1. Accept the fit with the highest primary vertex probability.

   2. Divide the fits in the same proportions as unambiguous data.

As there is no significant difference in the results of either method, the first is used for simplicity, since it enables decisions to be made on an event-by-event basis. In some cases this method is statistically questionable, particularly when the χ^2 probability levels of the ambiguous hypotheses are not sufficiently different. In spite of this, the degree of purity for the resolved channels is estimated to be reasonably high (see section II.4). Moreover, the method is adequate for the purpose of channel cross-section calculations since, although a small number of events may be wrongly assigned, any contamination is largely balanced by a loss of genuine fits to other

channels. Consequently the precision of cross-section calculations is mainly determined from Poisson statistics, and there are no sizeable systematic errors. This is not the case for the estimation of resonance production when the identities of the particles forming the resonance are changed between the ambiguities[*]. Any loss of resonant signal is not compensated by contamination, since the contamination will in general be distributed over the whole of the kinematically allowed region of an effective mass combination rather than in any particular resonance region for a spuriously fitted channel. However if the fit is accepted only if the probability difference between the ambiguities is >10% the loss of resonant signal is greatly reduced. Although this is not as efficient in removing contamination, for the purpose of resonance production the contamination is largely removed by selecting events within the resonance mass band.

The most frequent use of rule D is to resolve ambiguous hypotheses of the same constraint class, especially the large number of 1C/1C ambiguities which occur in the strange particle sample. For the OC/OC ambiguities method 2 above is the only one available, since the χ^2 probability for a OC fit is not defined. However the small number of unambiguous events in this constraint class makes any accurate repartition of events extremely difficult. Consequently the OC channels have been left unresolved and no calculation of their cross-sections has been attempted.

Occasionally it may be possible to resolve an ambiguity by more than one of the above four rules. If this is the case then the order of priority is taken to be the order in which the rules are listed. For example an event may be ambiguous between the hypotheses:

---

[*] Resonance production is dealt with in detail in chapter IV.

(a) $\pi^+ d \rightarrow K^+ \Lambda^o_v p_s$ $p(\chi^2) = 0.53$ (4C fit)

and (b) $\pi^+ d \rightarrow K^+ \Lambda^o_v p_s \pi^o$ $p(\chi^2) = 0.71$ (1C fit)

On the basis of rule D hypothesis (b) would be accepted, but since

rule A takes priority the event must be assigned to hypothesis (a).

II.4   Quality of the data and selection rules

When the above selection criteria are applied to the events simulated

by FAKE 85-90% of these events are correctly placed in the resulting

reallocation to the various channels. It is assumed that these results

will apply to the real data. In addition several consistancy checks can

be made on the real data in some cases:

(i)   The missing mass squared distribution (MM^2) of a fitted neutral

particle should be symmetric around the squared mass value of the missing

neutral. Figure II.3 shows the MM^2 distribution for the following 1C

channels

(a) $\pi^+ d \rightarrow K^+ \Lambda^o_v p_s \pi^+ \pi^- \pi^o$

(b) $K^o_i \Lambda^o_v p_s \pi^+ \pi^+ \pi^-$

(c) $K^+ \Lambda^o_v p_s \pi^o$

(d) $K^o_i \Lambda^o_v p_s \pi^+$

The distributions for (a) and (b) are quite symmetric around the

squared mass value of their respective missing neutrals as is generally

the case for the 1C channels. However the distributions for (c) and

(d) are skewed towards higher mass values which is interpreted as being

due to contamination from multineutral channels with the same charged
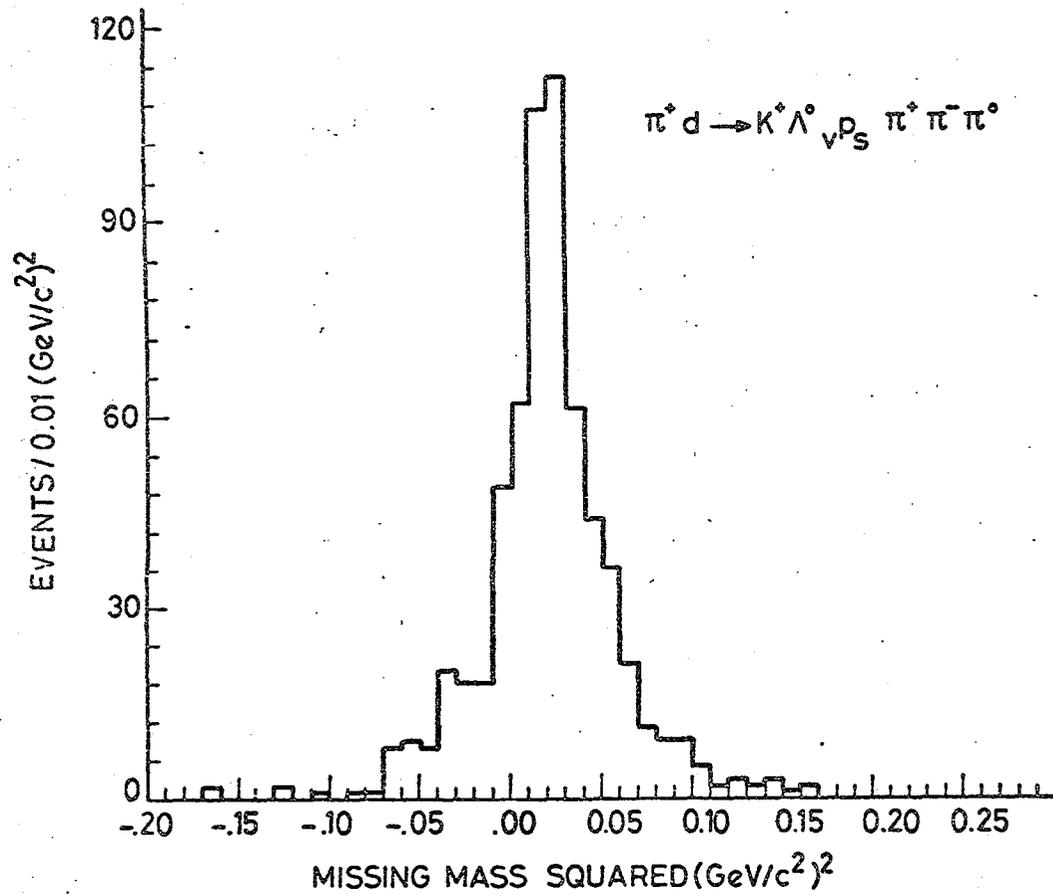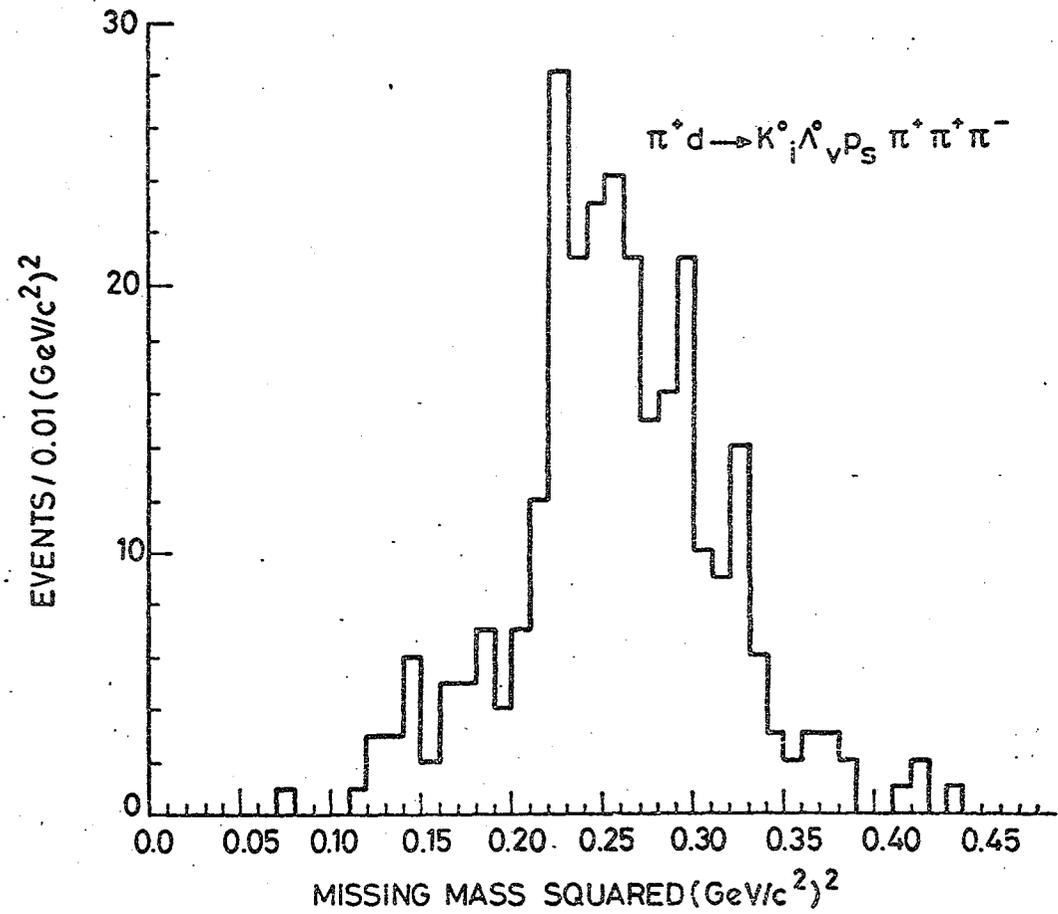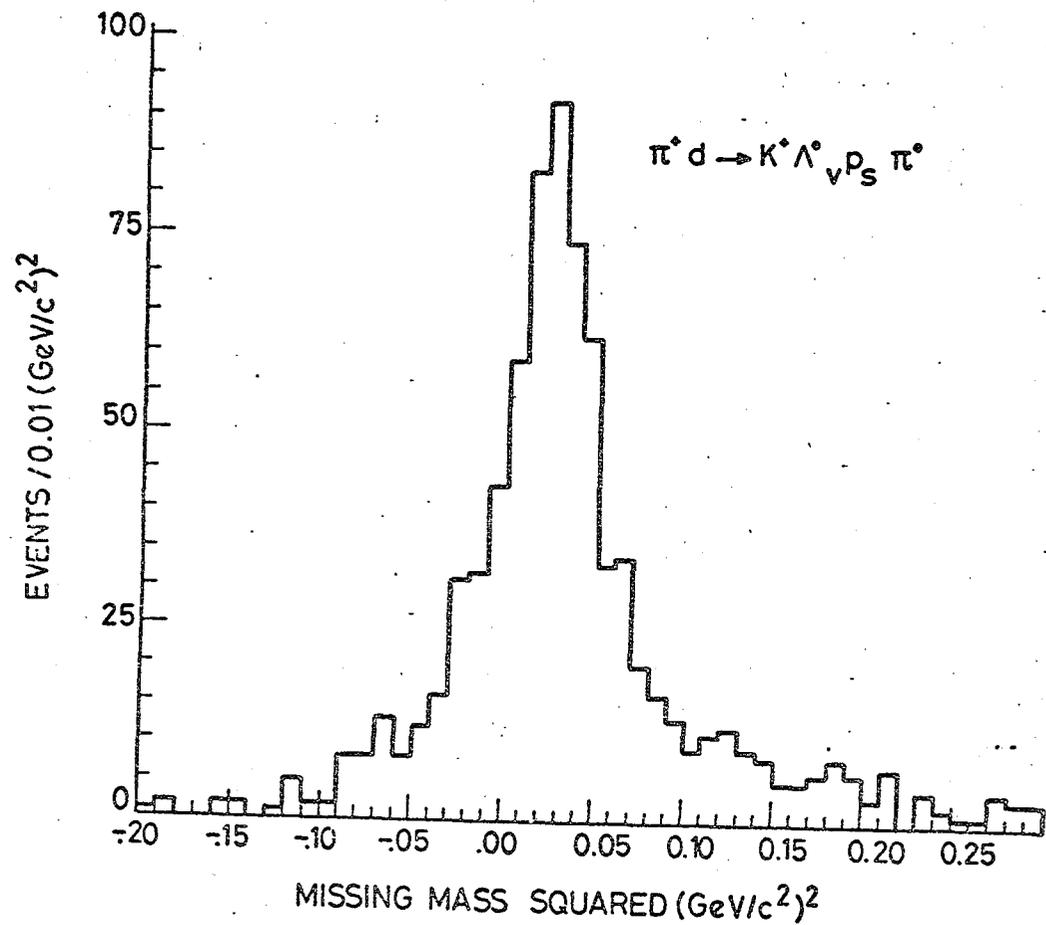
Fig.II.3

(c)
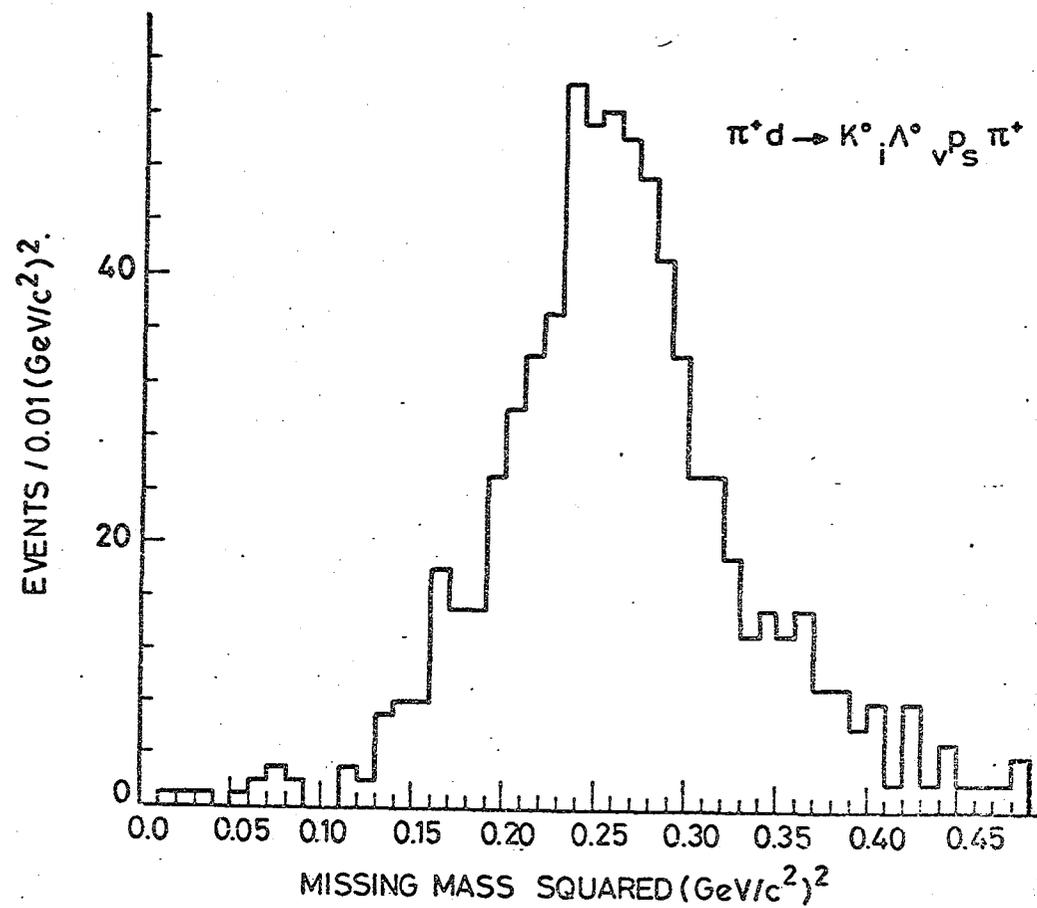
(d)

Fig. II.3 (cont.)

description (OC fits). The contamination is largely removed by rejecting

those events with $MM^2 > 0.15$ $(GeV/c^2)^2$ in (c) and $MM^2 > 0.35$ $(GeV/c^2)^2$

in (d). Any loss of genuine 1Cfits in this way may be estimated by a

comparison of the MM^2 distribution above and below the central value. No

significant loss is found for either channel.

(ii)   Interactions yielding two neutral strange particles will in general

be seen in different topologies depending on whether one or both particles

decay visibly. Obviously the ratio between the numbers of events in each

category can be predicted from the known branching ratios of the strange

particles into seen and unseen modes of decay (Ref. II.3) and may be com-

pared with observed values. This has been done in table II.3, where the

observed values include corrections for scanning efficiency and

geometrical losses (see section III.3.2 for a full discussion). The

agreement is good, which gives confidence in the selection rules defined

in section II.3. In particular it provides a useful check on the

resolution of the frequently occurring 1C/1C ambiguities by rule D using

the characteristics of the higher constrained samples.

(iii)   Where a channel exhibits strong resonance production, antichecks

may be made by inspecting the effective mass distributions of the rejected

fits to the channel. For example the channels:

$$(1) \quad \pi^+ d \rightarrow K^+ \Lambda^o_v p_s \pi^o$$

$$\text{and} \quad (2) \quad \pi^+ d \rightarrow K^o_i \Lambda^o_v p_s \pi^+$$
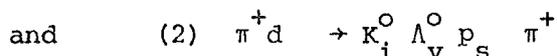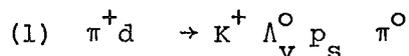
both show strong K^{*+} (890) production.

Figures II.4 (a) and (b) give the $(K\pi)^+$ effective mass distribution

for those fits rejected from channels (1) and (2) respectively due to the

existence of another 1C fit with a higher χ^2 probability level (rule D).

By way of comparison figures II.4 (c) and (d) give the $(K\pi)^+$ distributions

TABLE II.3

A COMPARISON OF OBSERVED AND PREDICTED RATIOS
FOR EVENTS IN THE SAME CHANNEL WITH ONE OR TWO
VISIBLE V^O's

Ratio	Observed	Predicted
$K^O_i \Lambda^O_v p_s \pi^+ / K^O_v \Lambda^O_i p_s \pi^+$	$3.47 \pm .29$	3.43
$K^O_i \Lambda^O_v p_s \pi^+ / K^O_v \Lambda^O_v p_s \pi^+$	$2.19 \pm .26$	1.92
$K^O_v \Lambda^O_i p_s \pi^+ / K^O_v \Lambda^O_v p_s \pi^+$	$0.63 \pm .09$	0.559
$K^O_v \Sigma^O_i p_s \pi^+ / K^O_v \Sigma^O_v p_s \pi^+$	$0.69 \pm .11$	0.559
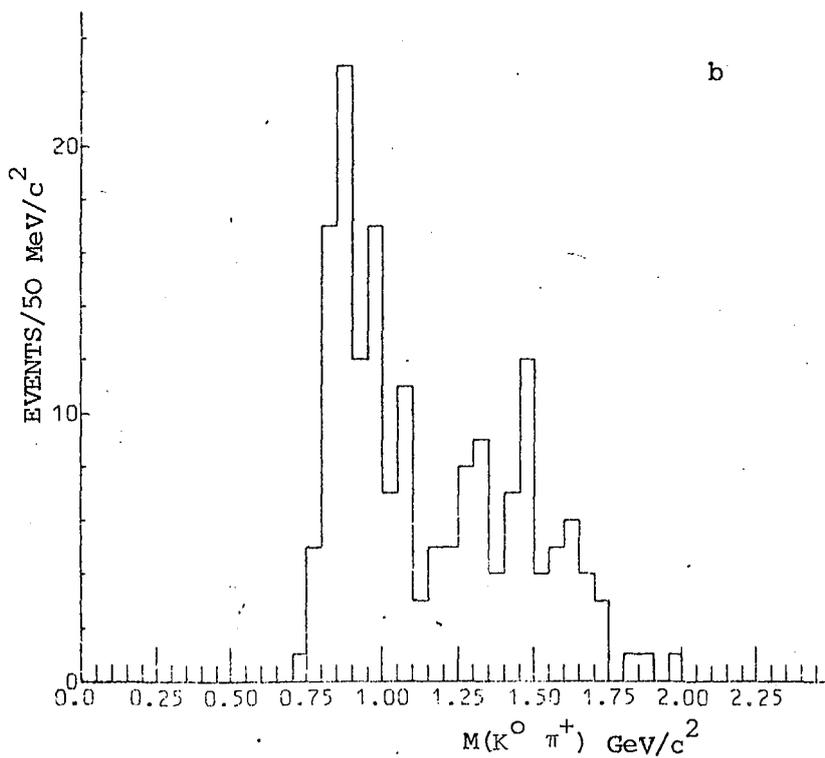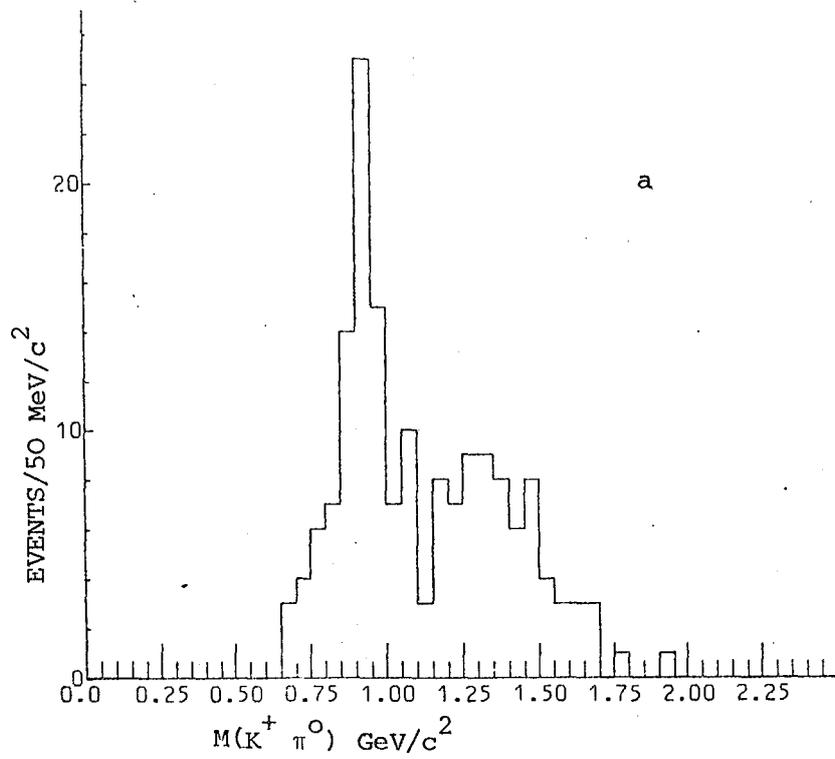
Fig. II.4 The $(K\pi)^+$ effective mass distributions for those events rejected by rule D from the channels (a) $\pi^+ d \rightarrow K^+ \Lambda_v^o \pi^o p_s$ (b) $\pi^+ d \rightarrow K_i^o \Lambda_v^o \pi^+ p_s$
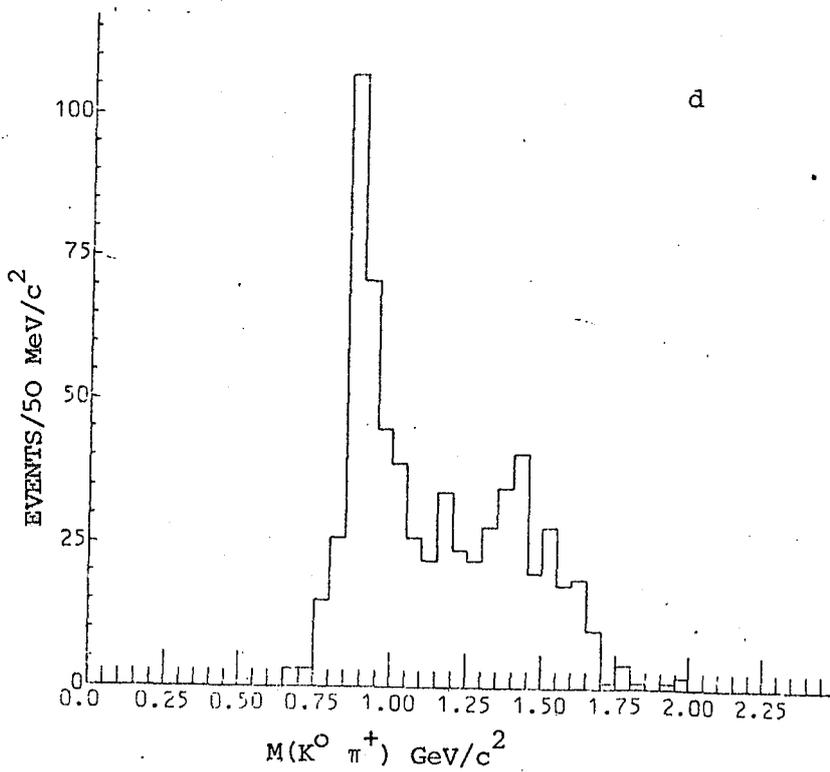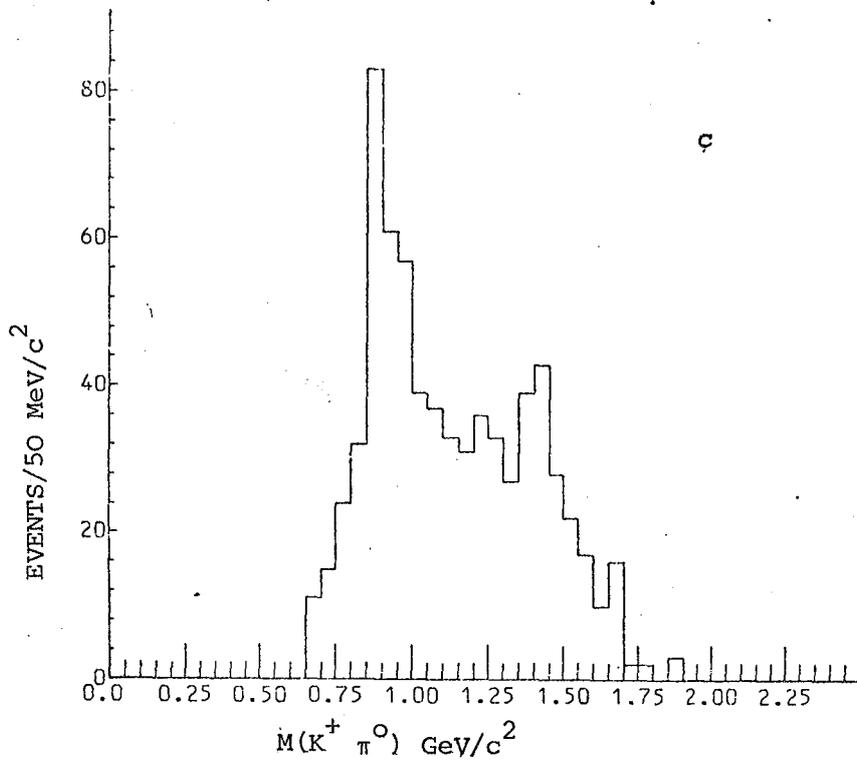
Fig. II.4 (Cont.) The (Kπ)[+] effective mass distributions for
events finally assigned to the channels.

(c) $\pi^+ d \rightarrow K^+ \Lambda_v^0 \pi^0 p_s$ (d) $\pi^+ d \rightarrow K_i^0 \Lambda_v^0 \pi^+ p_s$
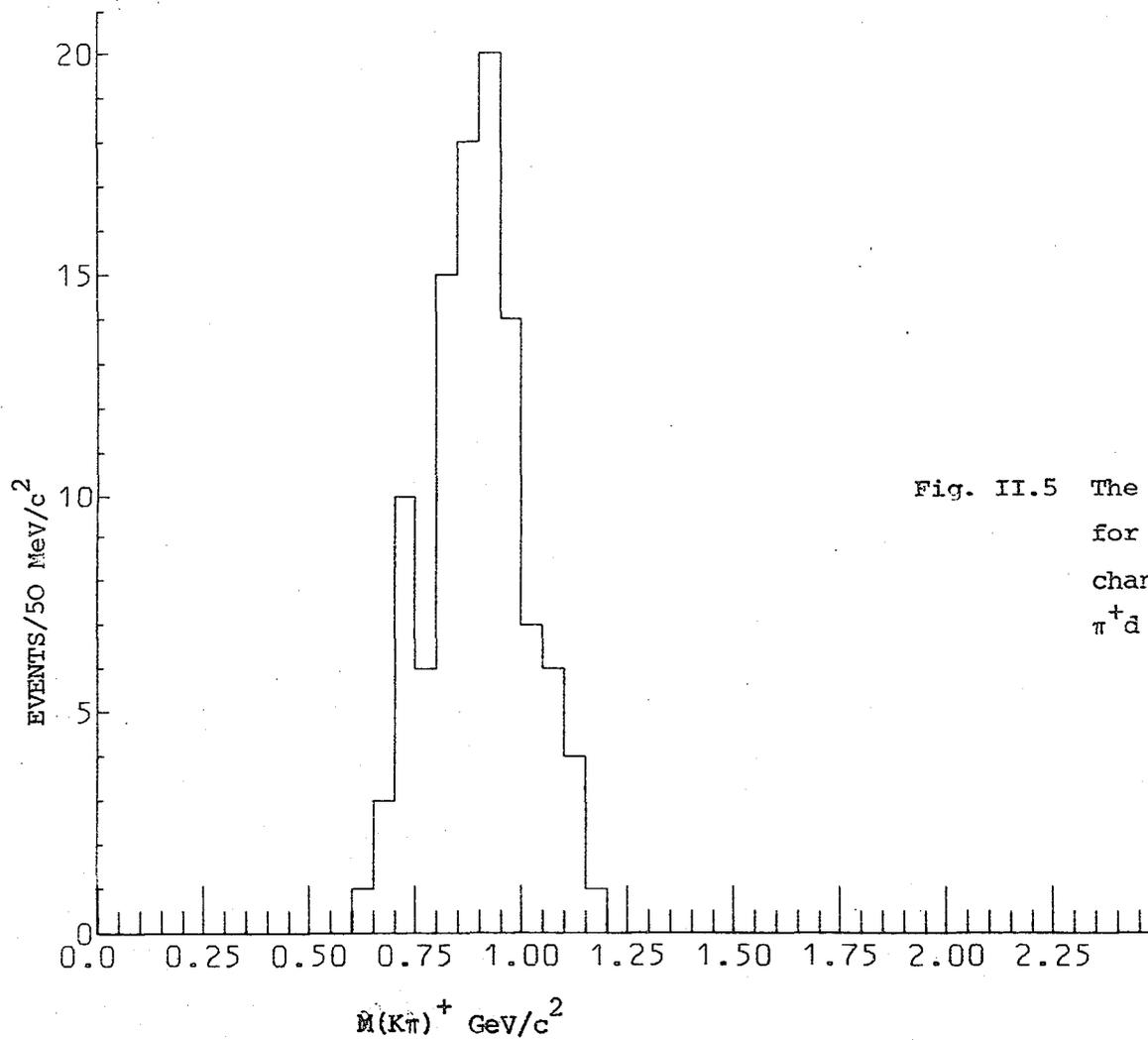
Fig. II.5 The $(K\pi)^+$ effective mass distribution for events rejected by rule D from the channels $\pi^+ d \rightarrow K^+ \Lambda_v^o \pi^o p_s$ and $\pi^+ d \rightarrow K_i^o \Lambda_v^o \pi^+ p_s$

for the accepted fits. Clearly the amount of resonance signal in (a)
and (b) is only about 15% of the amount in (c) and (d). Antichecks on
those 1C fits rejected by rule A are misleading, since FAKE simulations
have shown that true 4C events when fitted with either of the above 1C
channels will tend to produce a spurious peak near the threshold region
of the $(K\pi)^+$ effective mass distribution which may be misinterpreted as
$K^{*+}(890)$ signal. This is because the true 4C events have zero missing
mass and energy, so that a spurious missing neutral tends to be fitted
with near zero momentum. Consequently the effective mass of any particle
combination which includes the spurious neutral will in general be rather
low. Empirically this is found to be the case for those fits rejected
from the above channels by rule A, as can be seen from figure II.5. This
has important implications for the study of resonance production in 1C
channels where the resonance occurs near threshold. Care must be taken
to ensure that there is no significant 4C contamination which would
appear within the resonance mass band. Normally this contamination is
removed by rule A. However in some cases it may be that a true 4C event
has not provided an acceptable fit to the corresponding 4C hypothesis, so
that an unambiguous 1C fit is obtained. This could arise either because

    (a)   the χ^2 probability for the fit is below the prescribed minimum

           (see section II.2)

or   (b)   the fit has failed to converge.

    The problem is known as "4C-breakthrough" and has been considered in
detail by M. Dale (ref. I.19) for the channels,

$$\pi^+ d \rightarrow p \, p_s \, \pi^+ \, \pi^- \qquad (4C)$$

$$\text{and} \quad \pi^+ d \rightarrow p \, p_s \, \pi^+ \, \pi^- \, \pi^o \qquad (1C)$$

Initially it was estimated that a significant proportion of the 4C events fell into category (b). However, after the introduction of improved convergence criteria in the fitting routines of the KINEMATICS programme by D. J. Crennell (ref. II.4) the problem was largely removed. Moreover, in the FAKE simulations of the strange particle channels described in section II.3, it was found that less than 1% of the true 4C fits failed to converge when using the improved convergence criteria. In addition the low value of the minimum χ^2 probability level adopted in section II.2 for the 4C fits ensures that the number of events in category (a) is negligible.

(iv)   Some idea of the efficiency of $\Lambda^\circ/\Sigma^\circ$ separation by rule B may be obtained by inspecting the Σ° decay distribution $(\cos \beta_{M\gamma})$ for isotropy. Figure II.6 shows the distribution for those events which were finally assigned to the various Σ°-channels. It is compatible with isotropy apart from the gap above 0.85 due to the imposed selection.

(v)   Any substantial contamination of visible strange particle decays will in general distort the proper time distribution, τ, of the decaying particle. A comparison of the predicted and experimental distributions of τ will therefore provide a useful check on the purity of the fitted decay samples. This has been done in figure II.7 for the decays.

$$\Sigma^+ \to n\, \pi^+ \quad \text{and} \quad \Sigma^- \to n\, \pi^-$$
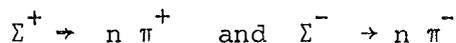
(The $\Sigma^+ \to p\pi^\circ$ decay mode is not used for reasons discussed in section III.3.1). The proper lifetime has been calculated from the expression,

$$\tau = \frac{mL}{pc}$$

where m = the rest of the decaying particle

p = the momentum of the decaying particle,

L = the decay length,

and   c = the speed of light $(3.00 \times 10^{10}$ cm sec$^{-1})$
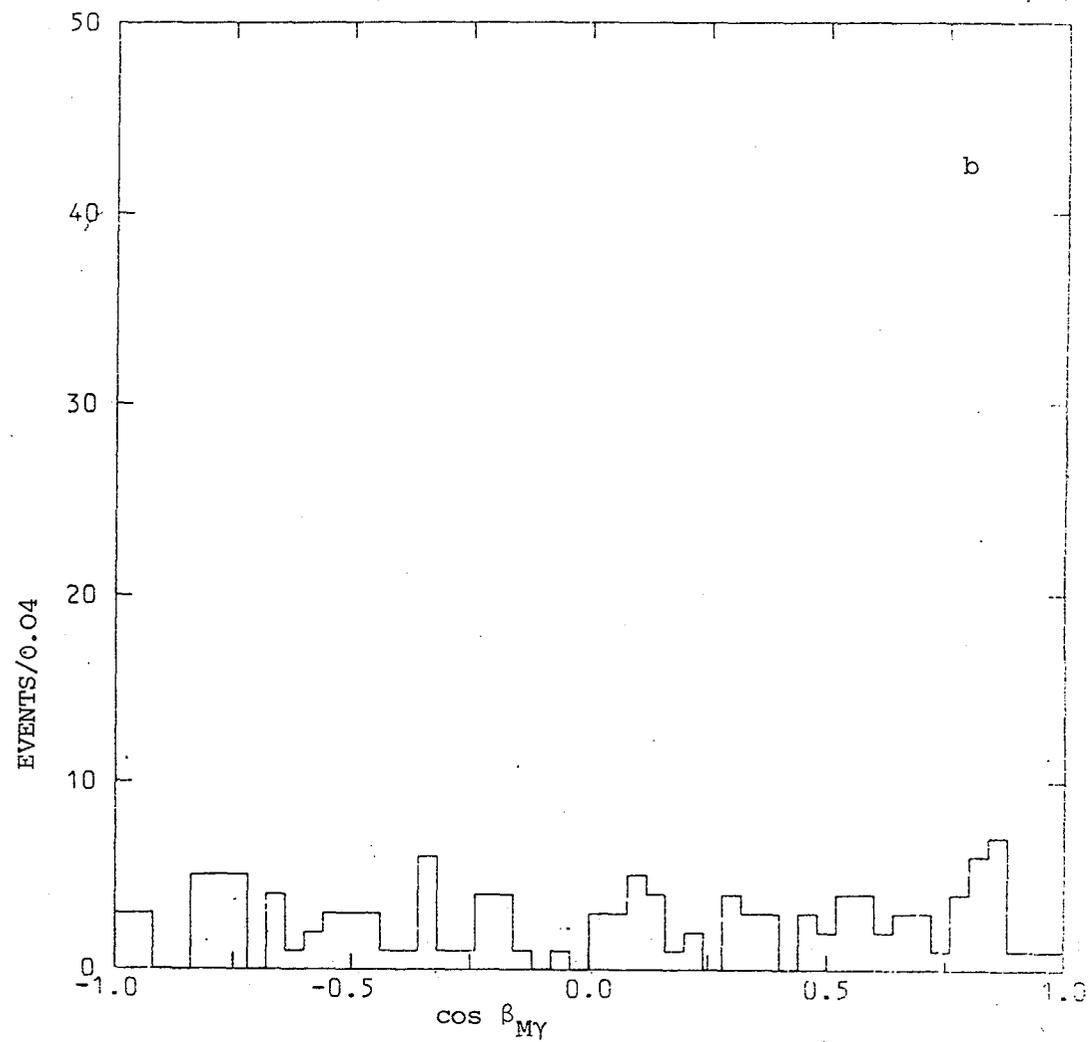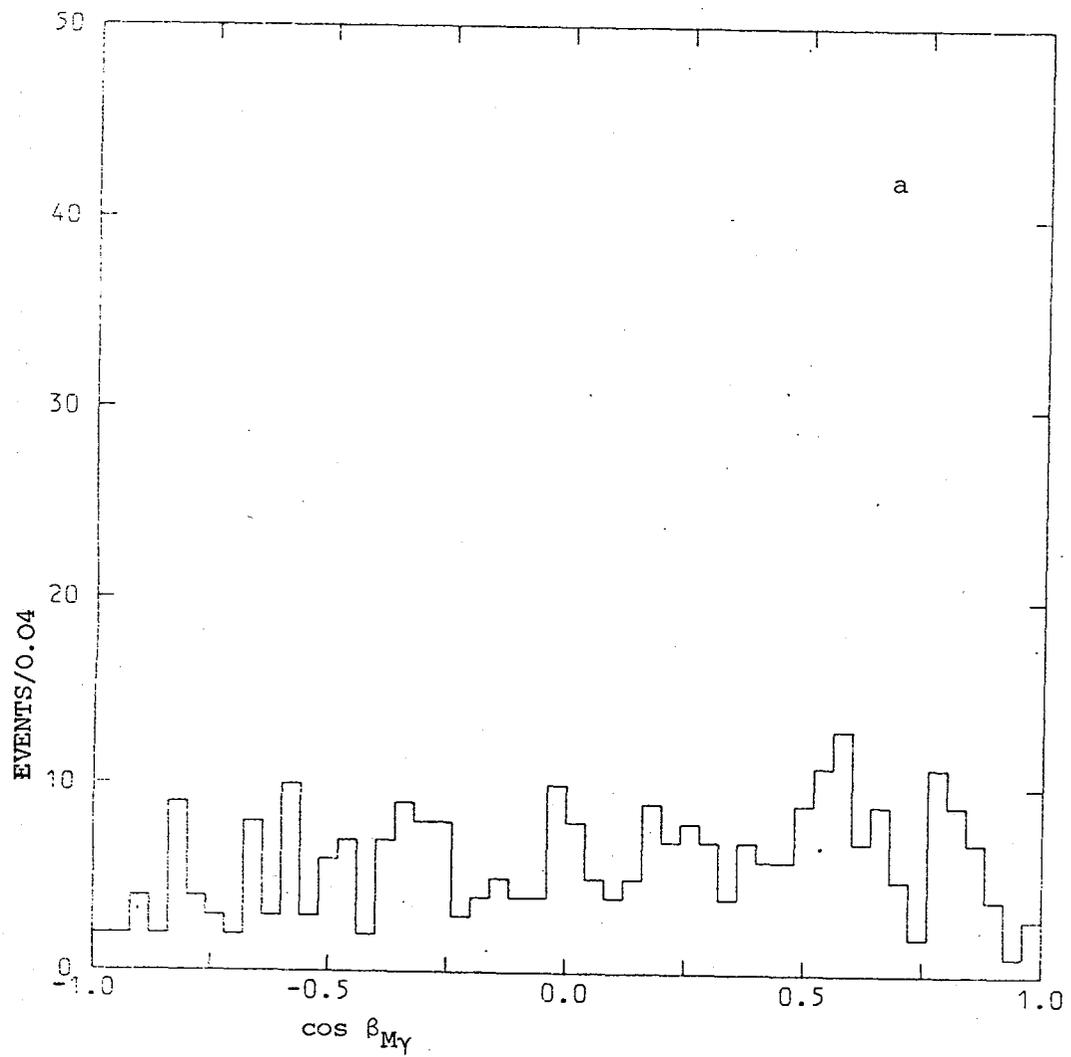
Fig. II.6   The γ-distributions for events finally assigned to the channels (a) $\pi^+ d \rightarrow K^+ \Sigma^0 p_s$
(b) $\pi^+ d \rightarrow K^0 \Sigma^0 \pi^+ p_s$
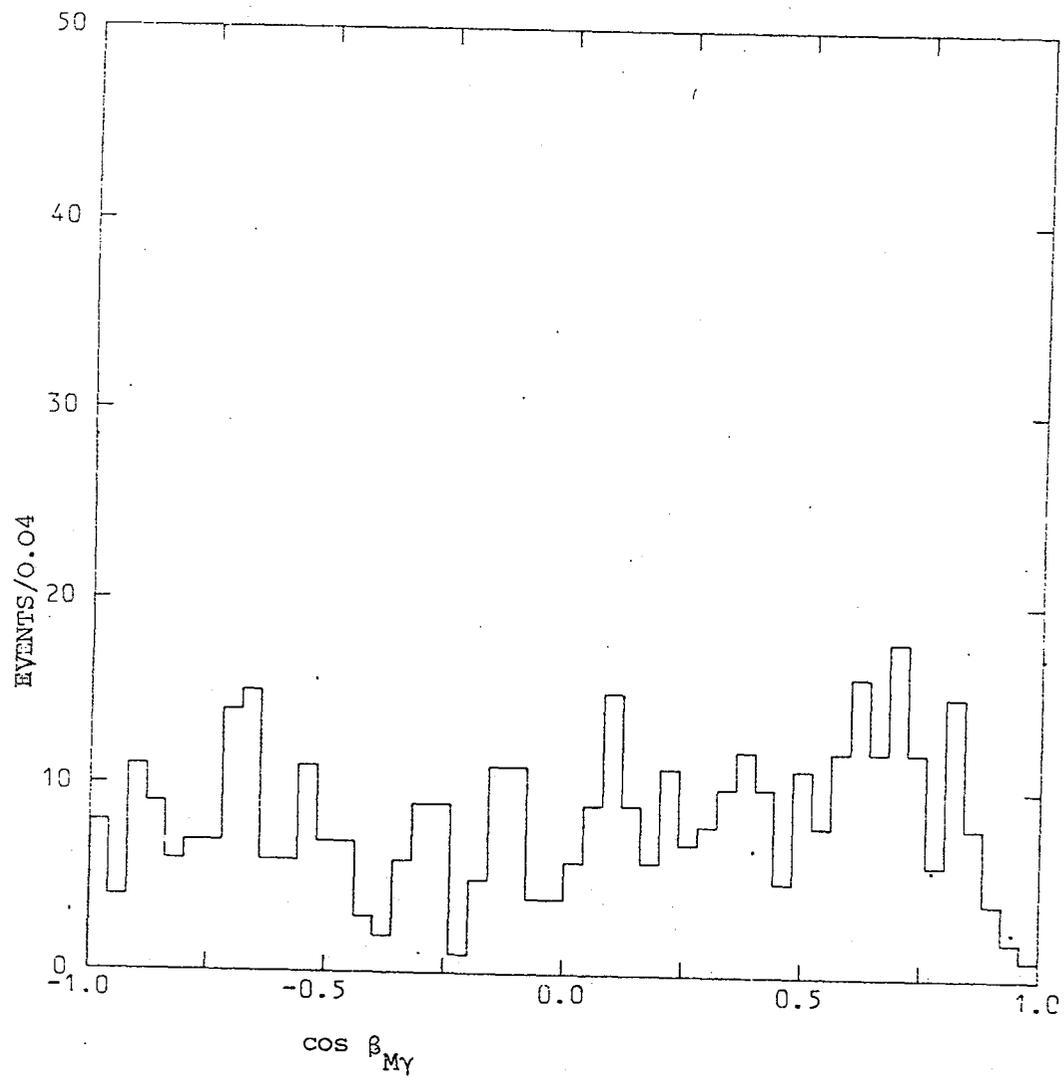
Fig. II.6(c) The γ-distribution for events finally assigned to the channel

$$\pi^+ d \rightarrow K^+ \Sigma^0 \pi^+ \pi^- p_s$$
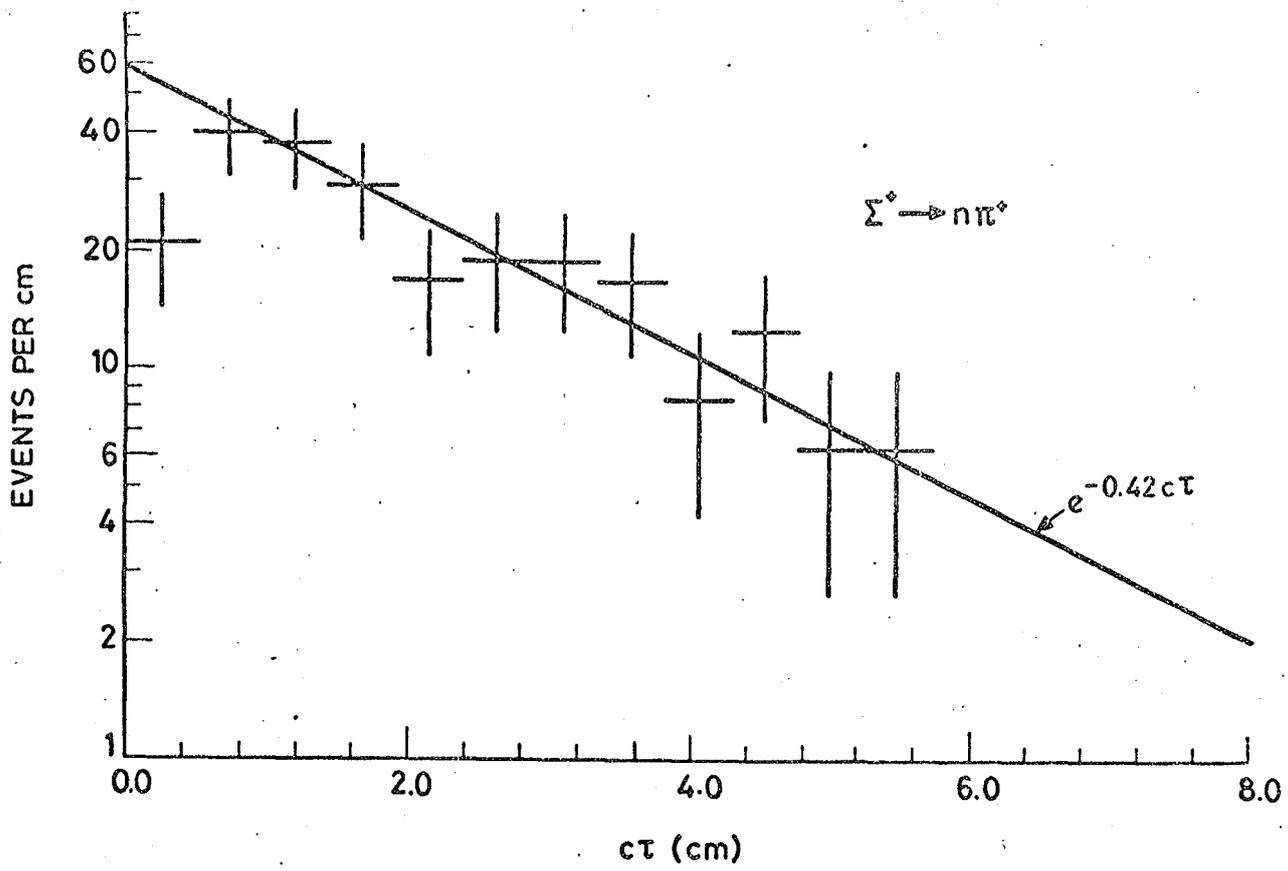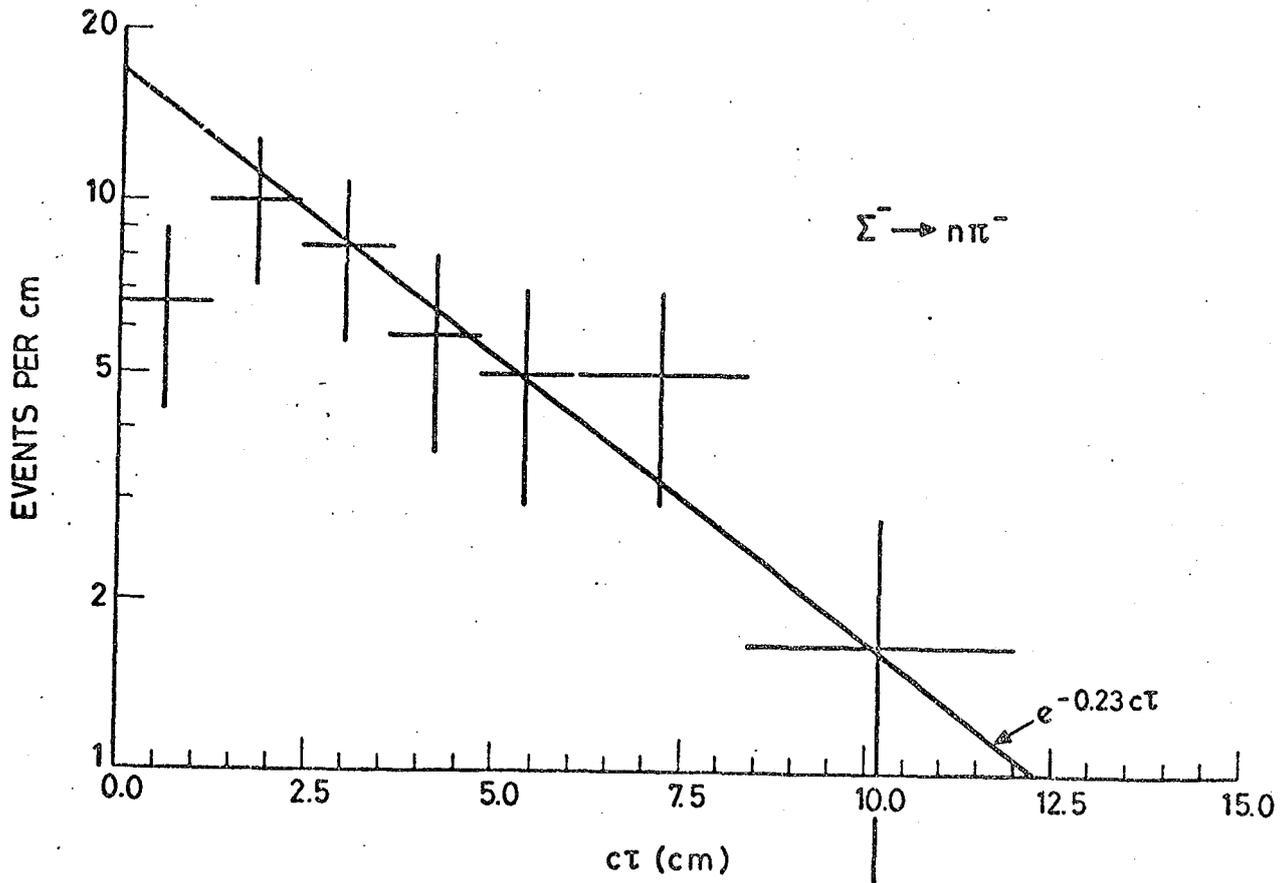
Fig. II.7 Proper time distributions for the Σ decays (exponentials give expected distributions).

$c\tau$ is plotted for convenience. The expected distribution is an exponential of slope $-1/c\tau_o$, where τ_o is the known mean lifetime of the decaying particle (ref. II.3). The agreement is good, except at low values of τ where there is a depletion due to short decay length losses (see section III.3.2), showing that contamination from inter-actions simulating the Σ decay is not significant.

Mean lifetimes for the K_s^o, Λ^o, Σ^+ and Σ^- have been determined by fitting the undistorted region of the proper lifetime distributions with exponentials of varying slope and intercept, and are compared in table II.4 with accepted values (ref. II.3).

TABLE II.4

A COMPARISON OF FITTED LIFETIMES (τ_o)
WITH ACCEPTED VALUES

Decay	Fitted $c\tau_o$ (cm)	Accepted $c\tau_o$ (cm)
$\Lambda^o \rightarrow p\,\pi^-$	$7.4 \pm .3$	7.73
$K^o \rightarrow \pi^+ \pi^-$	$2.57 \pm .07$	2.68
$\Sigma^+ \rightarrow \pi^+ n$	$2.3 \pm .3$	2.40
$\Sigma^- \rightarrow \pi^- n$	4.7 ± 1.8	4.44

CHAPTER III

ESTIMATION OF CHANNEL CROSS-SECTIONS

III.1 Introduction

In the previous chapter the resolution of ambiguities was discussed enabling each event to be uniquely assigned to a particular channel. The numbers of resolved events are now used to determine the cross-sections for the following channels, all of which have a seen V^0 (see section I.4),

$$
\pi^+ d \rightarrow
\left.
\begin{array}{l}
K^0\ \Lambda^0\ +\ 1\ \text{nucleon} \\[4pt]
K^0\ \Sigma^0\ +\ 1\ \text{nucleon} \\[4pt]
K^0\ \Sigma^+\ +\ 1\ \text{nucleon} \\[4pt]
K^0\ \Sigma^-\ +\ 1\ \text{nucleon} \\[4pt]
K^+\ \Lambda^0\ +\ 1\ \text{nucleon} \\[4pt]
K^+\ \Sigma^0\ +\ 1\ \text{nucleon} \\[4pt]
K^0\ K^-\ +\ 2\ \text{nucleons} \\[4pt]
K^0\ \bar{K}^0\ +\ 2\ \text{nucleons} \\[4pt]
K^+\ \bar{K}^0\ +\ 2\ \text{nucleons}
\end{array}
\right\}\quad +\ \text{pions}
$$
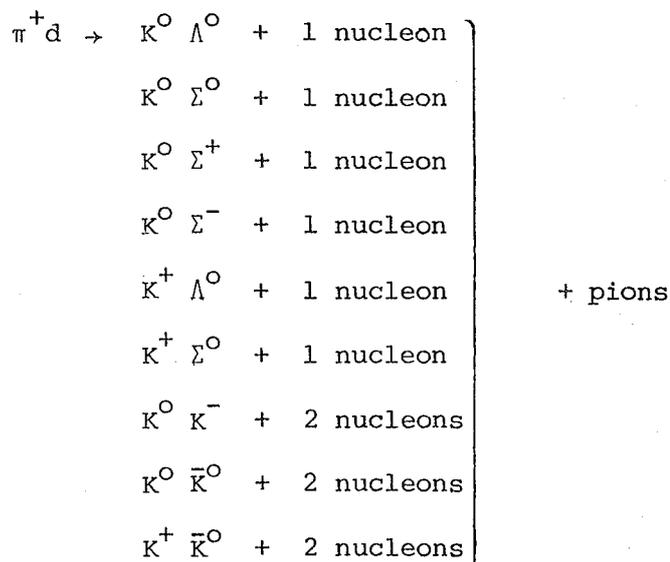
In view of the lack of data on the associated production of strange particles in π - nucleon collisions (see table I.1) cross-sections have been calculated for channels with as few as 15 or more events. However below this number there are insufficient statistics to allow a reliable determination of the cross-section. Even when numbers are substantial they are sometimes subject to large corrections, firstly because events are lost through poor geometry in the chamber, and secondly because V^0's are unseen when they decay by neutral modes.

The topological cross-sections are first calculated from a sub-sample of frames distributed evenly through the whole sample, for which the scanning efficiency and the number of beam tracks per frame is known. The corrections for losses are then considered enabling an overall

weighting factor to be obtained for each channel. Finally the channel cross-sections are evaluated in which neutral modes of decay and geometrical losses are properly taken into account.

III.2 Topological cross-sections

The cross-section for a particular topology, t, is given by

$$\sigma_t = N_t/\rho L$$

where the symbols have the following meanings:

(i) $N_t = N_t' \ c_s$,

where N_t' = the total number of interactions of topology, t, found within the scanning volume in the sub-sample of frames. An interaction was included even if an acceptable fit had not been reached, provided it was judged to be a good event on the scan table. In this way the cross-section is independent of measuring and fitting efficiency.

$$c_s = (\text{scanning efficiency})^{-1}$$

The scanning efficiency has already been discussed in section I.4.

(ii) ρ is the density of deuterium nuclei

$$\rho = N_o \ d/A$$

where N_o = Avogodro's number,

d = density of liquid deuterium,

A = deuterium atomic weight

(iii)   L is the total beam track length:

$$L \; = \; F \; n \; l \; c_a \; c_c$$

where F = number of frames in the sub-sample

n = average number of tracks per frame,

l = average length for non-interacting beam tracks. This

is calculated from the beam direction and the length of

the fiducial volume,

c_a = correction factor for the beam attenuation due to

interacting tracks:

$$C_a \; = \; l_c/l$$

where $$l_c \; = \; 1 \; - \; \rho \; \sigma_T \int_0^1 \exp \; (-\rho \; \sigma_T \; l') (1-l') \; dl'$$

and σ_T is the total cross-section from counter results (refs. III.1

and I.21)

c_c = correction for beam contamination (see section I.3)

The values of these for both exposures are given in table III.1

following.

TABLE III.1

Exposure	F	n	l (cm)	c_a	c_c	L (cm)
1	105,523	11.54+.07	76.0+.1	0.920+.001	0.95+.03	$(8.09+.26) \times 10^7$
2	94,910	11.73+.05	76.0+.1	0.920+.001	0.95+.03	$(7.40+.24) \times 10^7$

To obtain the microbarn equivalent (i.e. the number of microbarns an event contributes to the cross-section) the topological cross-section must be divided by the total number of events of that topology in the whole sample. The topological cross-sections together with their micro-barn equivalents are presented in table III.2. These are not corrected for geometrical losses and unseen decay modes which are dealt with separately for each individual channel. The differences in the micro-barn equivalents can be accounted for by the variation of scanning, measuring and fitting efficiency between topologies.

III.3 Correction factors

This section deals with the corrections applied to the observed number of events due to branching ratios into unseen (or unused) modes of decay (ref. II.3), and geometrical losses related to the visibility of events.

III.3.1 Corrections for unseen or unused decaymodes

In general only those decays which have a reasonable probability of occurring inside the chamber are fitted in KINEMATICS. This depends on the mean lifetime of the strange particle and also on the branching ratio into the decaymode considered. The decays together with their correction factors are given in table III.3. The table presents the factors $c_d =$ (branching ratio)$^{-1}$. In addition some details concerning the decaymodes are discussed below.

(a) $\Sigma^+ \rightarrow p\pi^o$
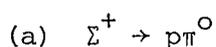
TABLE III.2 TOPOLOGICAL CROSS-SECTIONS

Topology	Cross-section (μb)	μb/event
2 prong + 1 neutral V	831 ± 39	$.064 \pm .003$
2 prong + 2 neutral V's	96 ± 8	$.055 \pm .005$
2 prong + 1 neutral V + 1 charged V	43.7 ± 3.4	$.076 \pm .006$
4 prong + 1 neutral V	365 ± 26	$.070 \pm .005$
4 prong + 2 neutral V's	10.6 ± 1.7	$.070 \pm .013$
4 prong + 1 neutral V + 1 charged V	33.6 ± 3.0	$.089 \pm .009$
6 prong + 1 neutral V	20.3 ± 2.0	not used*

* Since no channel contains more than 15 events.

TABLE III.3   CORRECTIONS FOR UNSEEN MODES OF DECAY

Decay	Correction Factor, c_d
$\Lambda \rightarrow p\pi^-$	$1.56 \pm .01$
$*K^0 \rightarrow \pi^+ \pi^-$	$2.92 \pm .01$
$\Sigma^+ \rightarrow \pi^+ n$	$2.07 \pm .03$
$\Sigma^+ \rightarrow p\pi^0$	not used
$\Sigma^- \rightarrow \pi^- n$	~ 1.00
$\Sigma^0 \rightarrow \Lambda\gamma$	~ 1.00

* including a correction for K^0_L

Events with a $\Sigma^+ \rightarrow p\pi^0$ decay are not used since the proton, because

of its large mass, continues generally in the same direction as the Σ^+

in the laboratory system. This makes the events difficult to detect, and

when they are it is difficult to distinguish them from small angle

scatterings with a very short target recoil. On the basis of comparison

with the $\Sigma^+ \rightarrow n\pi^+$ decaymode, which should be almost equally populated,

the loss is estimated to be ~50%. Rather than correct for this loss,

because of the reason above, it was decided to use only the $\Sigma^+ \rightarrow n\pi^+$

events and to correct for the unused decaymode from the well-known branch-

ing ratio into protons and into neutrons (ref. II.3).

(b) $K^{\pm}$ decays.

Although decays of $K^{\pm}$ mesons are seen and fitted, they occur too

infrequently to warrant them being used in cross-section calculations.

(c) K^0 decays.

The K^0 has an equal probability of being short-lived (K^0_S) or long-

lived (K^0_L). However, the K^0_L has a large mean lifetime ($\tau_0 = 5.2 \times 10^{-8}$ sec.)

so that it decays inside the chamber less than 3% of the time. Con-

sequently its decaymode, $K^0_L \rightarrow \pi^+ \pi^- \pi^0$ has not been fitted in KINEMATICS.

The K^0_V sample may therefore be taken to consist only of the K^0_S component.

The situation is apparently complicated when there is a resonant $K^0\bar{K}^0$

state, since charge-parity invariance requires the following strong decays:

$$\phi \ (1019) \rightarrow K^0_S \ K^0_L$$

$$f^0 \ (1260) \rightarrow K^0_S \ K^0_S \quad \text{or} \quad K^0_L \ K^0_L$$

$$A^0_2 \ (1310) \rightarrow K^0_S \ K^0_S \quad \text{or} \quad K^0_L \ K^0_L$$

so that procedures for calculating the correction factors must be modified from those where equal probabilities of K_S^O and K_L^O have been taken. One method of doing this is to estimate the amount of resonance production in the $K^O \bar{K}^O$ channels. However, statistics are generally low in these channels so that it is difficult to obtain a reliable estimate of the resonance signal. Instead the following method has been used where there is information on both the $K_v^O K_i^O$ and $K_v^O K_v^O$ final states:

As outlined above the $K_v^O K_v^O$ will contain only events with two short-lived K^O's. The $K_S^O K_S^O$ cross-section may therefore be calculated directly from the $K_v^O K_v^O$ sample using the branching ratio of the K_S^O into seen and unseen modes of decay (ref. II.3). This may then be used to calculate the $K_S^O K_S^O$ contribution to the $K_v^O K_i^O$ sample. The remaining $K_v^O K_i^O$ events are then assumed to be $K_S^O K_L^O$. Finally because of charge-parity invariance the $K_L^O K_L^O$ cross- section may be put equal to that of the $K_S^O K_S^O$ events. In summary, the cross-section for $K_S^O K_S^O$ may be expressed as

$$\sigma_{ss} = U_{vv} N_{vv}/R^2$$

where U_{vv} = the microbarn equivalent for the $K_v^O K_v^O$ events (see table III.2)

R = the branching ratio of the K_S^O into visible decay-modes (ref. II.3)

and N_{vv} = the number of $K_v^O K_v^O$ events after correction for geometrical losses (section III.3.2) and chi-squared probability selection (sec. II.2).

The cross-section for $K_S^O K_L^O$ is then

$$\sigma_{sL} = U_{vi} N_{vi} - \sigma_{ss} \; 2R(1-R)$$

where U_{vi} = the microbarn equivalent for the $K_v^o K_i^o$ events

(see table III.2)

N_{vi} = the number of $K_v^o K_i^o$ events after correction for

geometrical losses (section III.3.2) and chi-squared

probability selection (section II.2).

Putting σ_{LL} equal to σ_{ss}, the total $K^o \bar{K}^o$ cross-section is simply

$$\sigma_T = 2\sigma_{ss} + \sigma_{sL}$$

When the $K^o \bar{K}^o$ combination is produced in conjunction with a missing

neutral the $K_v^o K_i^o$ sample will fall into the zero constraint category.

Since such events are not used in cross-section calculations (the reasons

for this are given in section II.3) then the only available information

is from the $K_v^o K_v^o$ sample. Consequently the cross-section may only be

calculated for the $K_s^o K_s^o$ events.

(d) $K^o \Lambda^o / \Sigma^o$ combinations.

For a K^o produced in association with a Λ^o there are three

possibilities to calculate the cross-section depending on whether one or

both V^o's decay visibly:

1. $K_v^o \Lambda_v^o$ 2. $K_v^o \Lambda_i^o$ 3. $K_i^o \Lambda_v^o$

The probabilities for each combination are respectively

$$P_1 = r(K^o) r(\Lambda^o)$$

$$P_2 = r(K^o) (1 - r(\Lambda^o))$$

$$P_3 = (1 - r(K^o)) r(\Lambda^o)$$

where $r(K^o)$ = the branching ratio of the K^o into visible decaymodes

($r(K^o)$ = R/2 since it must allow for the unseen K_L^o component)

$r(\Lambda^o)$ = the branching ratio of the Λ^o into visible decaymodes.

If all three combinations together are used to calculate the cross-section the total probability is given by the sum,

$$P_T = P_1 + P_2 + P_3$$

The correction factor to account for the unseen combination, $K_i^O \Lambda_i^O$, is then $c_T = (P_T)^{-1}$. Similar considerations apply to the $K^O \Sigma^O$ final state. However in this case there are only two possibilities, $K_v^O \Sigma_v^O$ and $K_v^O \Sigma_i^O$, since the $K_i^O \Sigma_v^O$ combination falls into the unused zero constraint category because of the two missing neutrals, K^O and γ. The correction factors calculated in this way for $K^O \Lambda^O$ and $K^O \Sigma^O$ are (1.14 $\pm$ .01) and (2.92 $\pm$ .01) respectively.

III.3.2 Geometrical losses

In general a loss of events due to poor geometry will produce a depleted region in the observed distribution of a particular track length or angle. By using well known characteristics of the interactions concerned (for example the mean lifetime of a decaying particle) it is possible to predict the expected distribution which then enables the loss to be estimated by comparing the predicted number of events with the number found experimentally in the depleted region. An alternative method would be to reject all the events within the depleted region and then to predict the corrected number of events in this region by using the expected distribution. In practice there is no significant difference between the results of either method. However the first has been adopted since it avoids the unnecessary rejection of events. Details of the correction factors which have been estimated in this way are given below. Apart from the small opening angle loss discussed in (iv), the fraction of events lost through poor geometry in each case is less than ¨6%. Consequently the combined correction factor (see section III.4) consists

mainly of corrections for unused or neutral decaymodes which have been calculated from accurately known branching ratios in section III.3.1.

(i) Short length losses

When the projected distance between the primary and decay vertices is less than about 1 mm. it becomes extremely difficult to distinguish between the two vertices, so that the correct topology for the event may not be recognised. For example a two-prong event with two V^o's may be recorded as a four-prong with one V^o. However because the topological cross-sections for single V events are between ~3.5 - 9 times greater than those for two V events (see table III.2) such contamination is negligible. On the other hand losses of this type produce a marked depletion of charged and neutral V's at very small decay lengths. This is illustrated in figure III.1, where the projected decay lengths of the K^o_s, Λ^o, Σ^+ and Σ^- are shown. The loss may be estimated by comparing the observed and expected distributions of proper lifetime, τ, at low values of τ. This method has already been described in section II.4.v), where it was used to investigate the possible contamination of $\Sigma^{\pm}$ decays. The correction factors are listed in table III.4.

(ii) Long length losses

These are due to the decays, listed in table III.3, occurring outside the bubble chamber and may be estimated in a similar way to (i) above by comparing the observed and expected distributions at large proper lifetime. For a bubble chamber as large as the CERN 2m chamber such losses are expected to be small, and indeed no significant loss is detected for K^o_s, Λ^o, Σ^+ or Σ^-.

(iii) Steeply dipping tracks

These often have short projected lengths making them difficult to see on the scan table, so that as with the decay length losses the

FIG. III.1

PROJECTED DECAY LENGTH (cm)

$\Sigma^+ \rightarrow n \, \pi^+$

PROJECTED DECAY LENGTH (cm)

$\Sigma^- \rightarrow n \, \pi^-$
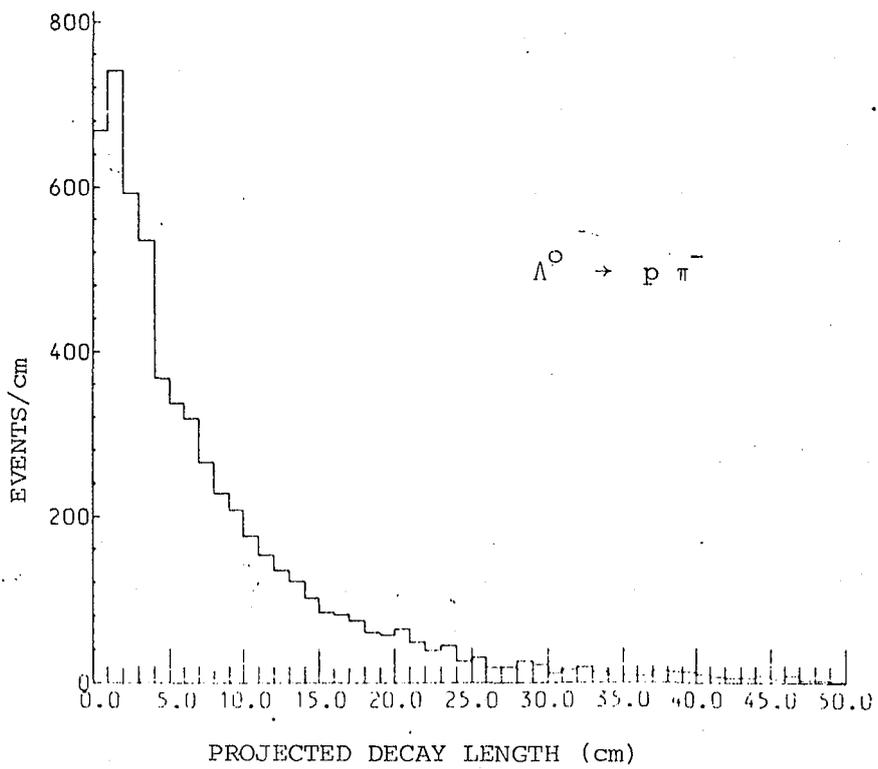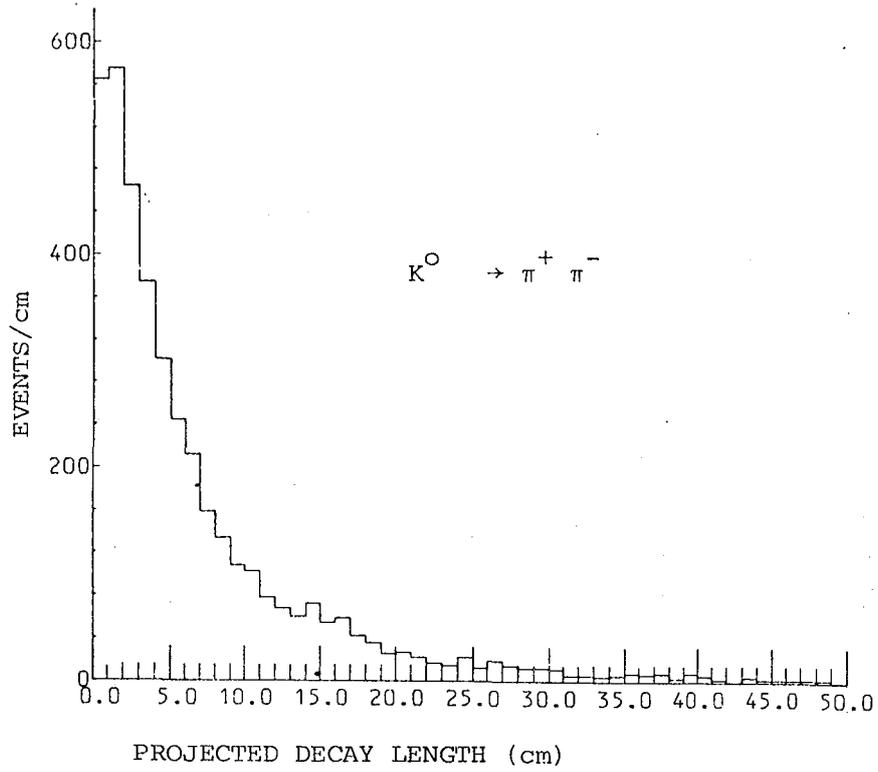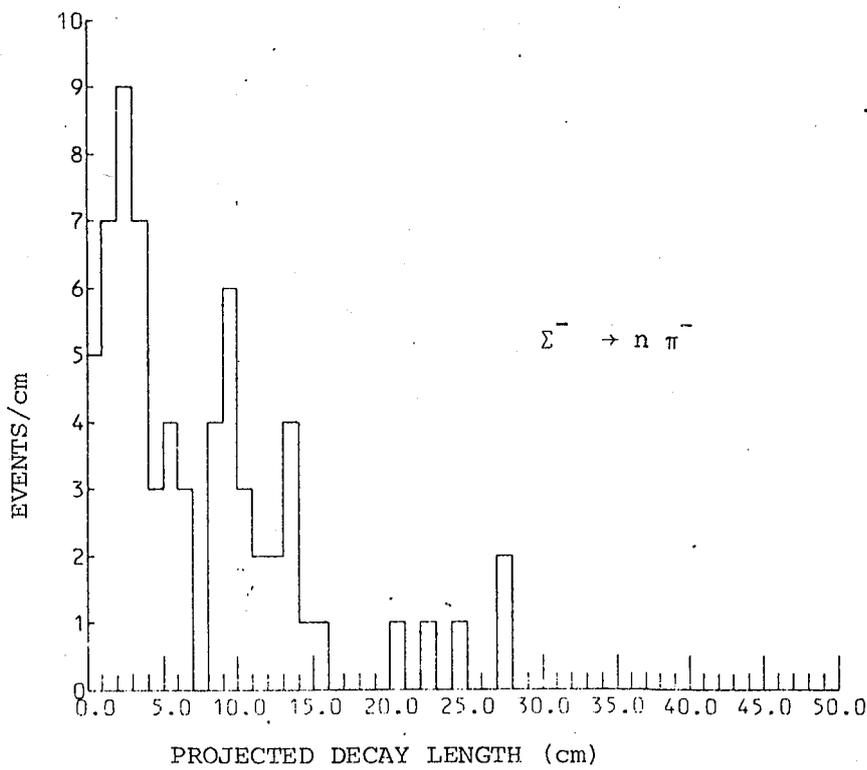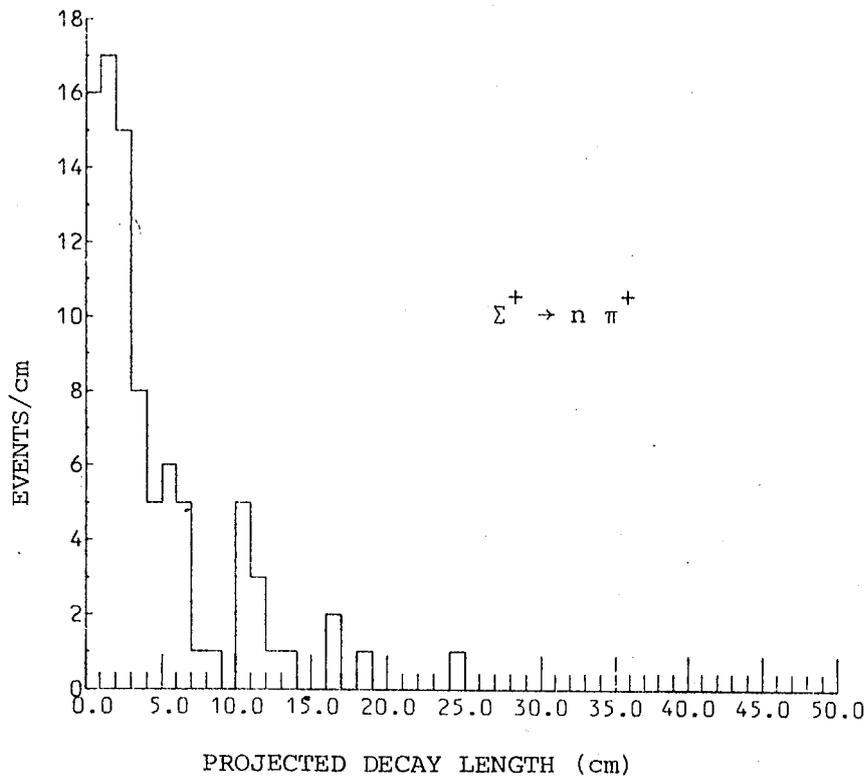
Fig. III.1 (Cont.)

TABLE III.4   CORRECTIONS FOR SHORT LENGTH CUT-OFF

Decay	Short length correction
$\Lambda \rightarrow p\pi^-$	$1.034 \pm .005$
$K^0_s \rightarrow \pi^+ \pi^-$	$1.056 \pm .006$
$\Sigma^+ \rightarrow \pi^+ n$	$1.14 \pm .02$
$\Sigma^- \rightarrow \pi^- n$	$1.19 \pm .06$

TABLE III.5   CORRECTIONS FOR SMALL ANGLE LOSSES

Decay	Small angle correction
$\Lambda \rightarrow p\pi^-$	~ 1.00
$K^0_s \rightarrow \pi^+ \pi^-$	~ 1.00
$\Sigma^+ \rightarrow \pi^+ n$	$1.25 \pm .08$
$\Sigma^- \rightarrow \pi^- n$	$1.16 \pm .08$

correct topology for the event may not be recognised. The loss is
significant for the proton track from the Λ^0 decay, since a V^0 with one
extremely short track is almost certain to be missed. In order to
correct for this loss, the rotational symmetry of the interactions
around the beam direction has been used. This requires that the pro-
jected angular distribution of the proton from the Λ^0 decay with respect
to the beam should be identical for all projection planes through the
beam direction. By choosing a horizontal plane with respect to the
chamber the projected angular distribution should be free from loss, so
that it may be compared with the vertically projected distribution after
normalising the undistorted part of the distributions to the same number
of events. The loss of Λ^0 events in this way is estimated to be
$(5.1 \pm 0.6)\%$. The loss is illustrated in figure III.2, which is a two-
dimensional plot of the horizontally and vertically projected distributions.
Losses of this type from the two V^0 sample will appear in the single V^0
topological class. However the final channel cross-sections have been
calculated from the combined topologies contributing to the channel, so
that the correction need only be applied to the single V^0 sample.

(iv) Small angle loss

When the projected angle of decay of a charged or neutral V decay
is small the event is often difficult to detect. The kink, which is the
usual signature for a charged V decay, will appear as a single track;
the V^0 decay may be misinterpreted as a Dalitz pair. The loss has been
estimated in a similar way to (iii) above. However, in this case the
vertically projected distribution is the one which is free from loss.
The only significant loss is for the $\Sigma^+ \rightarrow n\pi^+$ and $\Sigma^- \rightarrow n\pi^-$ decays,
which require substantial correction factors (see table III.5). In spite
of this the resulting contamination of the single V sample due to small
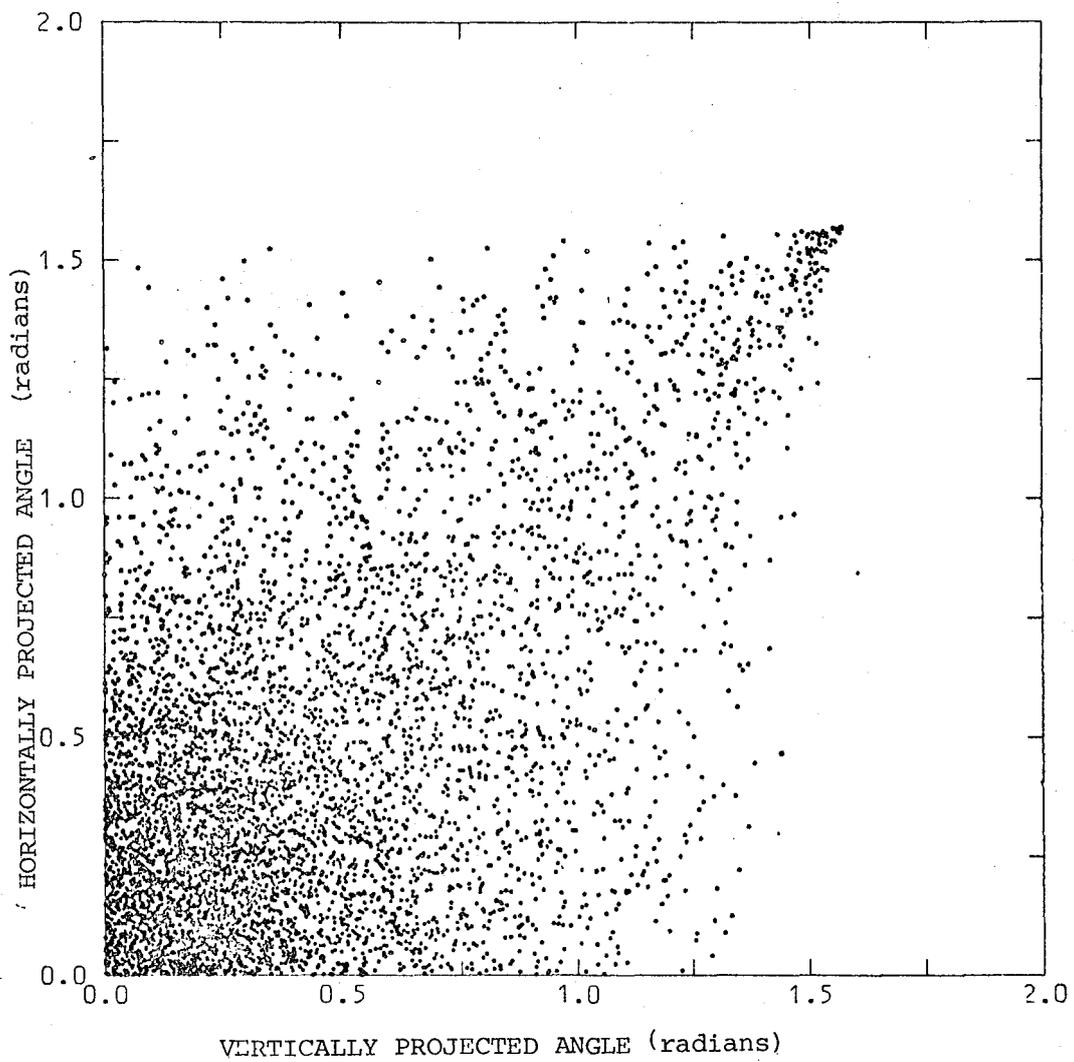
Fig. III.2 Horizontally projected angle versus vertically projected
angle for the proton from the Λ° decay.

angle losses of the two V events is estimated to be negligible (c.f.(i) above).

(v) Low four-momentum transfer

Losses which have a strong dependence on the four-momentum transfer, t, will produce dips in the differential cross-section distributions. These may then be wrongly interpreted as being due to a particular exchange mechanism (see chapter V). It is therefore important that such losses are detected and corrections applied to the appropriate t-region.

If an interaction produces a single charged track at the primary vertex accompanied by an unseen spectator proton, it will appear as a one-prong event on the scan-table. If in addition the charged secondary is produced at low four-momentum transfer, the event will appear as a single track and may not be recognised as an interaction. The loss may be estimated by comparing the t-distributions of seen and unseen spectator proton events. The channels which are affected are listed in table III.6 together with the correction factors to be applied to the indicated region of reduced four-momentum transfer, t' $(=|t|-|t|_{min})$. No appreciable correction need be applied to the total cross-sections for these channels.

The Λ^o/Σ^o ambiguities discussed in section II.3 B tend to occur at low values of t'. This is evident both from the real data and from the FAKE simulations. The t'-distributions for those events finally assigned to the channels

$$\pi^+ d \; \rightarrow \; K^+ \; \Lambda^o_v \; p_s$$

$$\text{and} \; . \; \pi^+ d \; \rightarrow \; K^+ \; \Sigma^o_v \; p_s$$
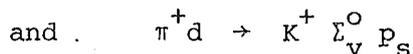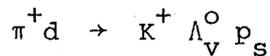
are shown in figure III.3. Assuming an exponential dependence the observed surplus of some 12 events in the region $t' < 0.05$ GeV/c^2 of the

TABLE III.6

CORRECTIONS FOR t'DEPENDENT LOSSES

Final State	t' region $(GeV/c)^2$	Correction factor
$K^+ \Lambda^o p_s$	0 - 0.05	$1.15 \pm .05$
$K^+ \Sigma^o p_s$	0 - 0.05	$1.18 \pm .11$
$K^+ \Sigma^o (1385) p_s$	0 - 0.05	$1.67 \pm .33$
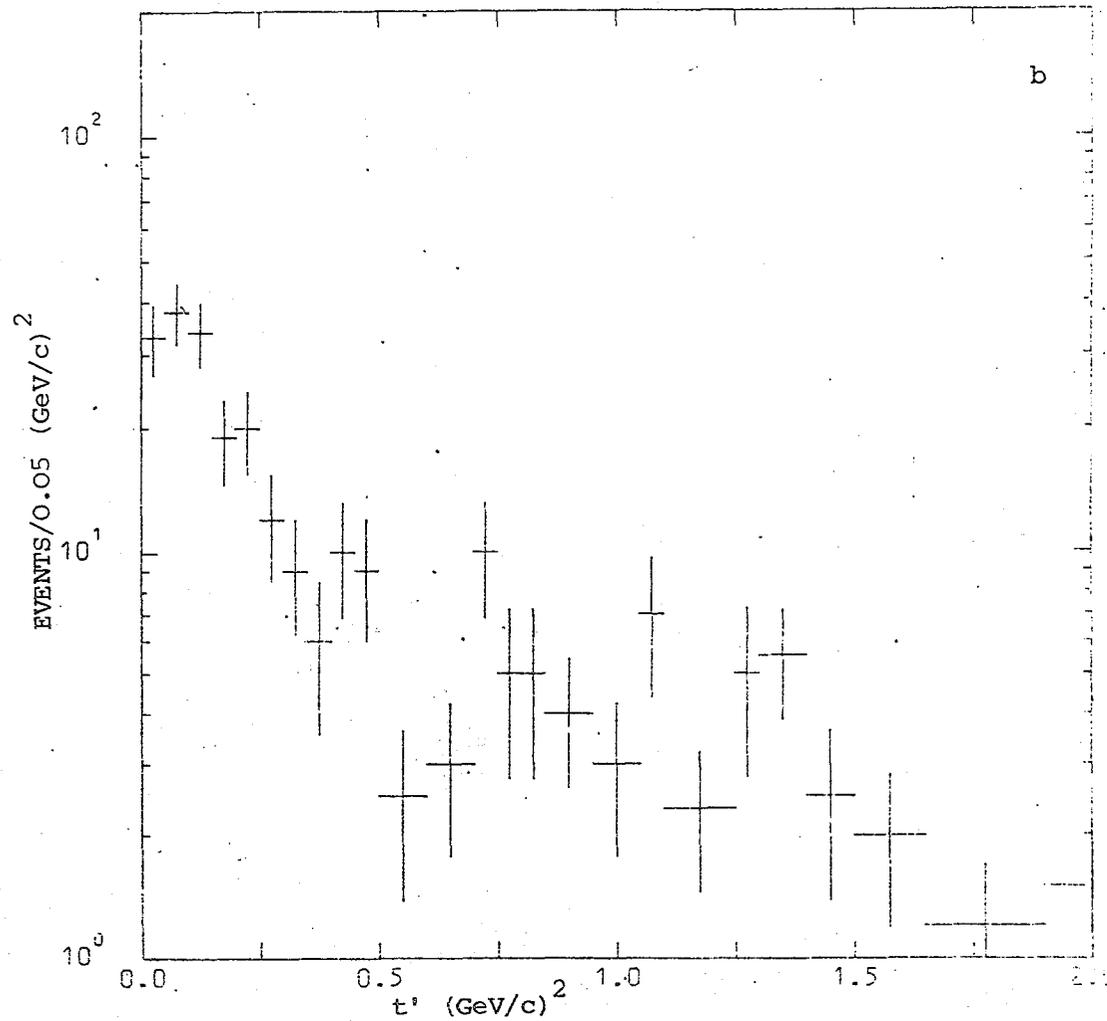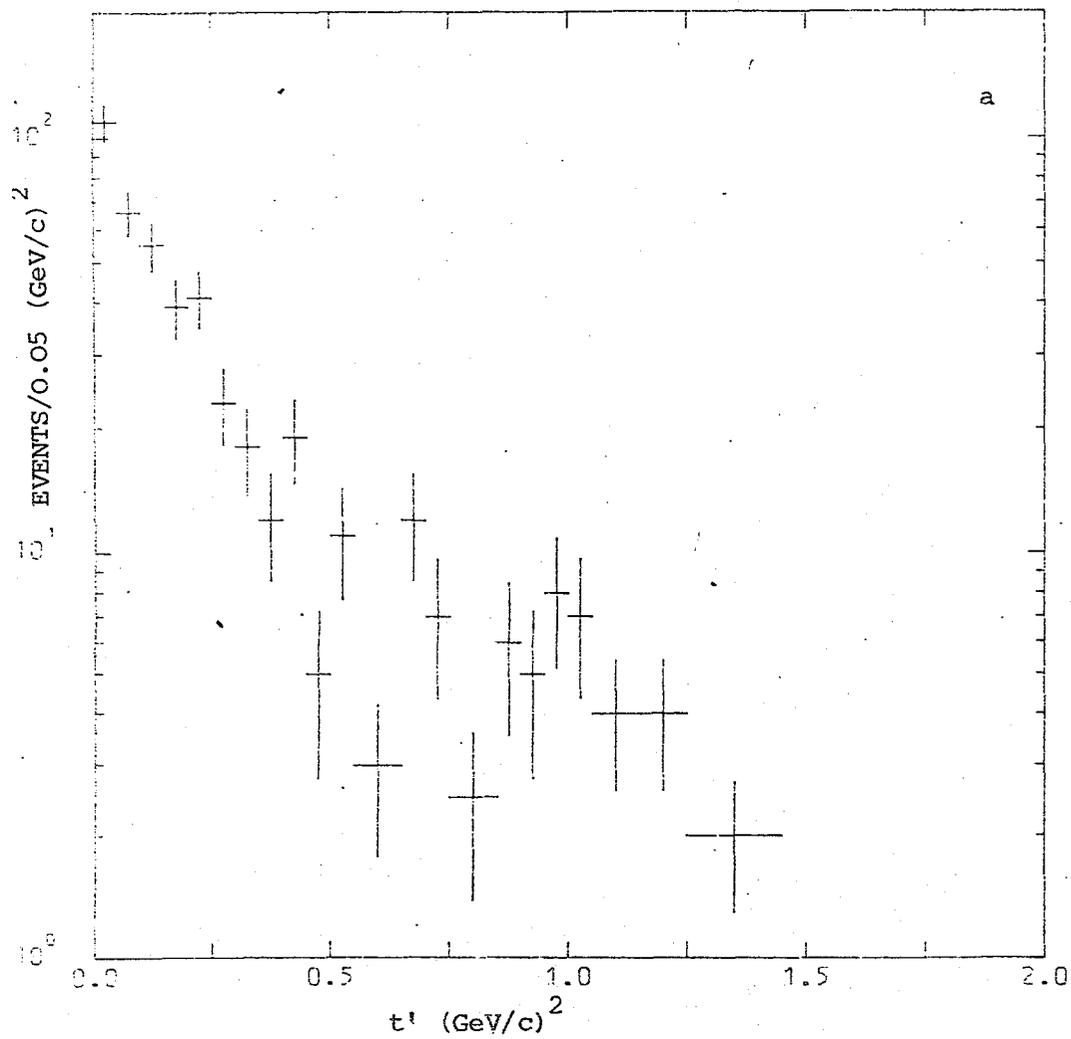
Fig. III.3. The t'-distributions for the channels (a) $K^+ \Lambda^0 p_s$ (b) $K^+ \Sigma^0 p_s$ corrected for unseen spectator proton losses.

Λ^O-channel corresponds to the depletion of events in the same region for the Σ^O-channel. FAKE simulations yield identical results. Consequently these events are re-assigned to the Σ^O-channel in calculating the differential cross-sections.

III.4 Final channel cross-sections

When the losses above are properly considered an overall weighting factor for each channel is evaluated. This must also include, where relevant, a correction for the chi-squared probability and the Σ^O decay angle selections imposed in sections II.2 and II.3 respectively to resolve ambiguous channels. It has been assumed that the overlap between correction factors is negligible. In other words there is no loss of events which has been accounted for in more than one correction factor. Such an overlap is most likely to occur between the corrections for geometrical losses (section III.3.2) and the correction for scanning efficiency (section I.4). However even in this case the assumption is reasonable since if an event is not detectable in one scan because of bad geometry, it will probably not be detectable in any subsequent scan.

The weighting factors are given in table III.7 together with the number of events finally assigned to each channel. Also shown are the channel cross-sections which have been calculated using the microbarn-equivalents listed in table III.2. Where a channel appears in several topological classes the sum of the events in each class has been used to calculated the cross-section, which explains why these channels have only a small weighting factor (see section III.3.1). When a channel contains two nucleons in the final state, the spectator is taken to be the one with the lower momentum. Monte Carlo simulations (section II.3) have shown that this is incorrect for less than ~3% of the cases.

TABLE III.7

$\pi^+ d \to$ strange particles: Channel cross-sections at 4 Gev/c with overall weight factors

Channel	Events	Weight Factor	Cross-section (μb)
$K^+ \Lambda$ + 1N + π's			
$K^+ \Lambda^0 \, p_s$	510	1.68	53 ± 3
$K^+ \Lambda^0 \, p_s \, \pi^0$	722	1.81	83 ± 5
$K^+ \Lambda^0 \, n_s \, \pi^+$	748	1.81	86 ± 5
$K^+ \Lambda^0 \, p_s \, \pi^+ \, \pi^-$	753	1.63	86 ± 6
$K^+ \Lambda^0 \, p_s \, \pi^+ \, \pi^- \, \pi^0$	624	1.81	79 ± 6
$K^+ \Lambda^0 \, n_s \, \pi^+ \, \pi^+ \, \pi^-$	165	1.81	21 ± 2
K^+ + 1N + π's			
$K^+ \Sigma^0 \, p_s$	296	1.80	34 ± 3
$K^+ \Sigma^0 \, p_s \, \pi^+ \, \pi^-$	414	1.8$_2$	5$_3$ ± 5
$K^0 \Lambda^0$ + 1N + π's			
$K^0 \Lambda^0 \, p_s \, \pi^+$	1174	1.45	106 ± 6
$K^0 \Lambda^0 \, p_s \, \pi^+ \, \pi^0$	255	5.59	79 ± 7
$K^0 \Lambda^0 \, n_s \, \pi^+ \, \pi^+$	160	5.59	49 ± 4
$K^0 \Lambda^0 \, p_s \, \pi^+ \, \pi^+ \, \pi^-$	416	1.49	43 ± 4
$K^0 \Sigma^0$ + 1N + π's			
$K^0 \Sigma^0 \, p_s \, \pi^+$	255	3.15	48 ± 6
$K^0 \Sigma^0 \, p_s \, \pi^+ \, \pi^+ \, \pi^-$	47	3.15	10 ± 2
$K^0 \Sigma^+$ + 1N + π's			
$K^0 \Sigma^+ \, n_s \, \pi^+$	108	9.58	79 ± 11
$K^0 \Sigma^+ \, p_s \, \pi^+ \, \pi^-$	46	9.13	37 ± 7
$K^0 \Sigma^-$ + 1N + π's			
$K^0 \Sigma^- \, p_s \, \pi^+ \, \pi^+$	68	4.28	25 ± 4
$K^0 \, K^-$ + 2N + π's			
$K^0 \, K^- \, pp_s \, \pi^+$	282	3.10	62 ± 6
$K^0 \, K^- \, pn_s \, \pi^+ \, \pi^+$	67	3.25	16 ± 3
$K^0 \, K^- \, np_s \, \pi^+ \, \pi^+$	94	3.25	22 ± 3
$K^0 \, K^- \, pp_s \, \pi^+ \, \pi^0$	73	3.25	17 ± 2

TABLE III.7 (Continued)

Channel	Events	Weight Factor	Cross-section (μb)
$K^O \bar{K}^O + 2N + \pi$'s			
$K^O_s K^O_s pp_s$	129($K^O_v K^O_v$)	2.36	17 ± 2
$K^O_s K^O_L pp_s$	174 ± 21	1.62	21 ± 2
$K^O_s K^O_s pp_s \pi^O$	55	2.45	7 ± 1
$K^O_s K^O_s pn_s \pi^+$	101	2.48	14 ± 2
$K^O_s K^O_s np_s \pi^+$	66	2.48	9 ± 1
$K^O_s K^O_s pp_s \pi^+ \pi^-$	16	2.36	3 ± 1
$K^O_s K^O_L pp_s \pi^+ \pi^+$	92 ± 11	1.62	10 ± 1
$K^O K^+ + 2N + \pi$'s			
$K^O K^+ pn_s$	204	3.25	42 ± 4
$K^O K^+ np_s$	323	3.25	66 ± 5
$K^O K^+ pp_s \pi^-$	240	3.10	52 ± 5
$K^O K^+ pn_s \pi^+ \pi^-$	67	3.25	16 ± 2
$K^O K^+ np_s \pi^+ \pi^-$	94	3.25	21 ± 2
$K^O K^+ pp_s \pi^- \pi^O$	88	3.25	20 ± 2

III.5 Comparison with other experiments

Where they can be checked with π^+d cross-sections at higher or lower

energies or with charge symmetric reactions, after a correction of about

3% for nucleon-nucleon shadowing (see section I.2.6), the cross-sections

agree well which gives confidence in the criteria used to resolve the

ambiguities. A compilation of cross-sections for the well-populated

channels is shown in figure III.4 for both hydrogen and deuterium over a

range of beam momentum. These are mainly taken from the CERN/HERA tables

(ref. I.21) and some other sources (ref. III.1).   Deuterium

cross-sections have been corrected for nucleon-nucleon shadowing. The

new deuterium data are particularly useful since they occupy the region

between ~ 2.5 and 5 GeV/c where no previous deuterium cross-section values

exist. The comparison with π^+p and the charge symmetric π^-p cross-sections

reveals that the new data are at least as accurate as any previous values

in the 4 GeV/c region. In all cases the cross-sections fit well into the

observed variation of existing cross-sections at higher and lower energies.

This has been illustrated for the two body channels in the region of

momentum, p, well above threshold, where the momentum dependance of the

cross-section, σ, may be fitted to the form σ ~ p^{-n}. The following values

for n were obtained:

$$
\left.
\begin{array}{l}
\pi^+ n \;\rightarrow\; K^+ \, \Lambda^o \\[2mm]
\pi^- p \;\rightarrow\; K^o \, \Lambda^o
\end{array}
\right\}
\qquad n \;=\; (1.8 \pm .2)
$$

$$
\left.
\begin{array}{l}
\pi^+ n \;\rightarrow\; K^+ \, \Sigma^o \\[2mm]
\pi^- p \;\rightarrow\; K^o \, \Sigma^o
\end{array}
\right\}
\qquad n \;=\; (1.9 \pm .2)
$$

These values are in agreement with those found for other reactions

involving strange meson exchange. (Exchange mechanisms will be discussed

in detail in chapter V.)
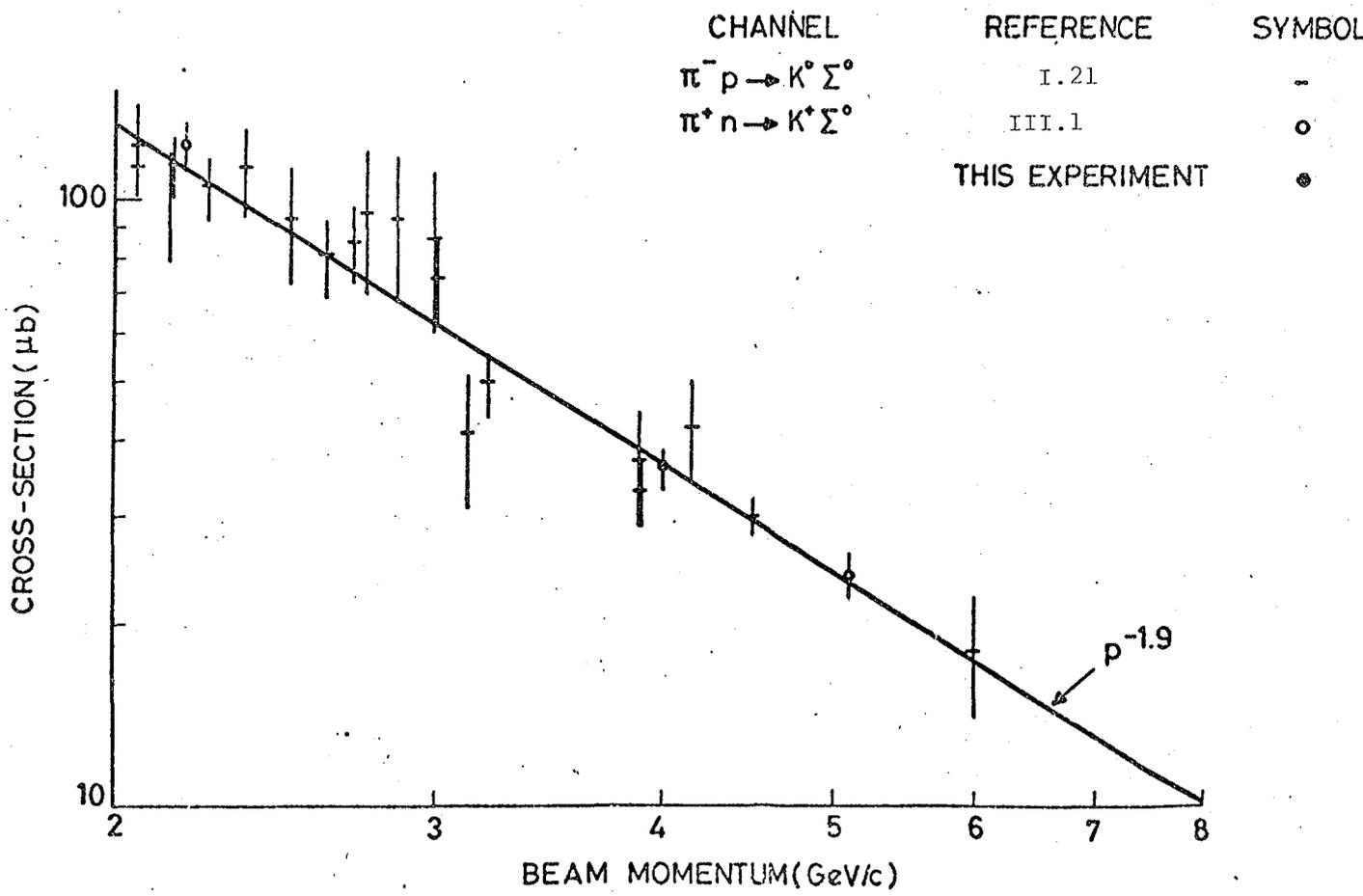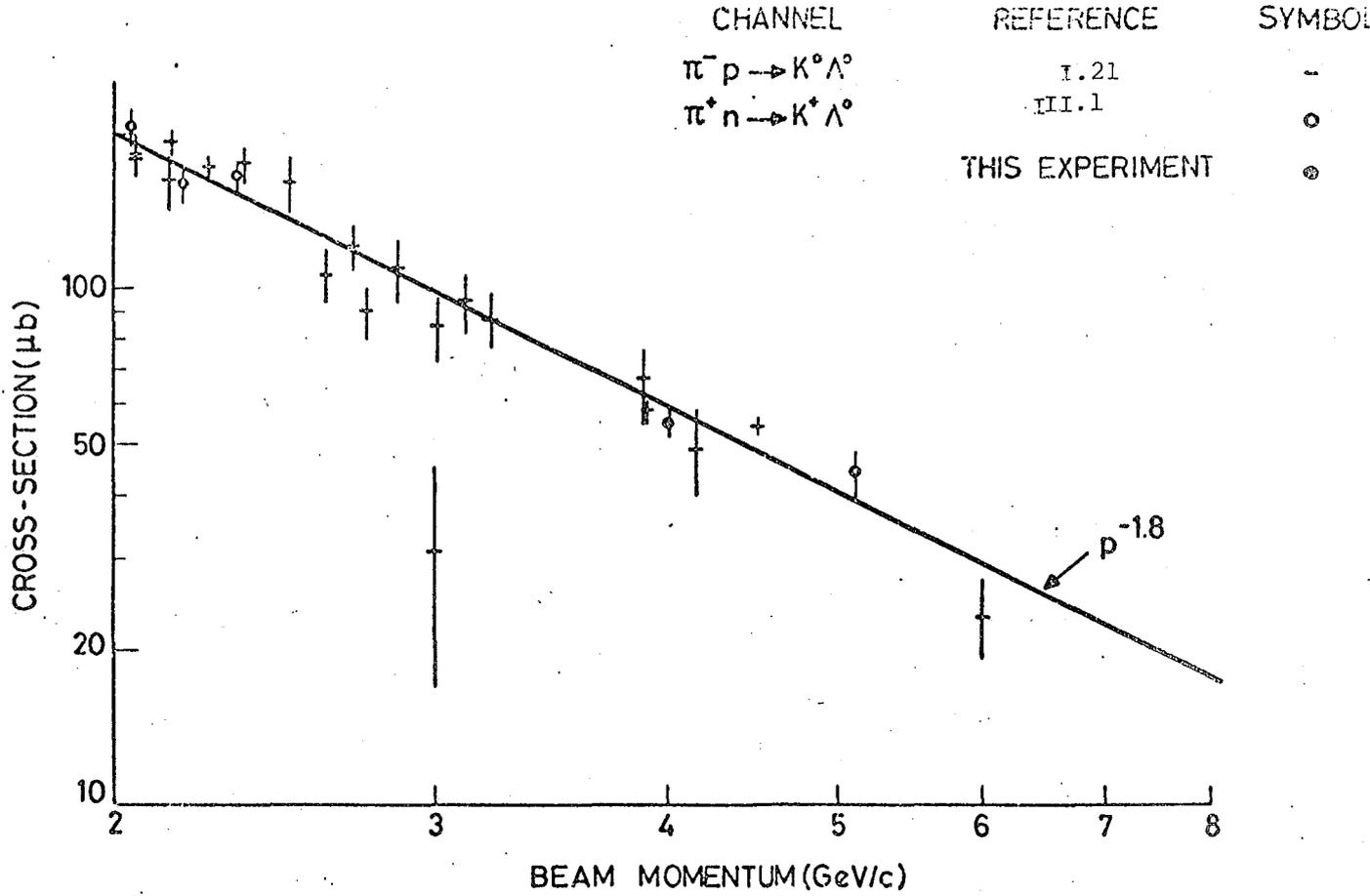
Fig. III.4
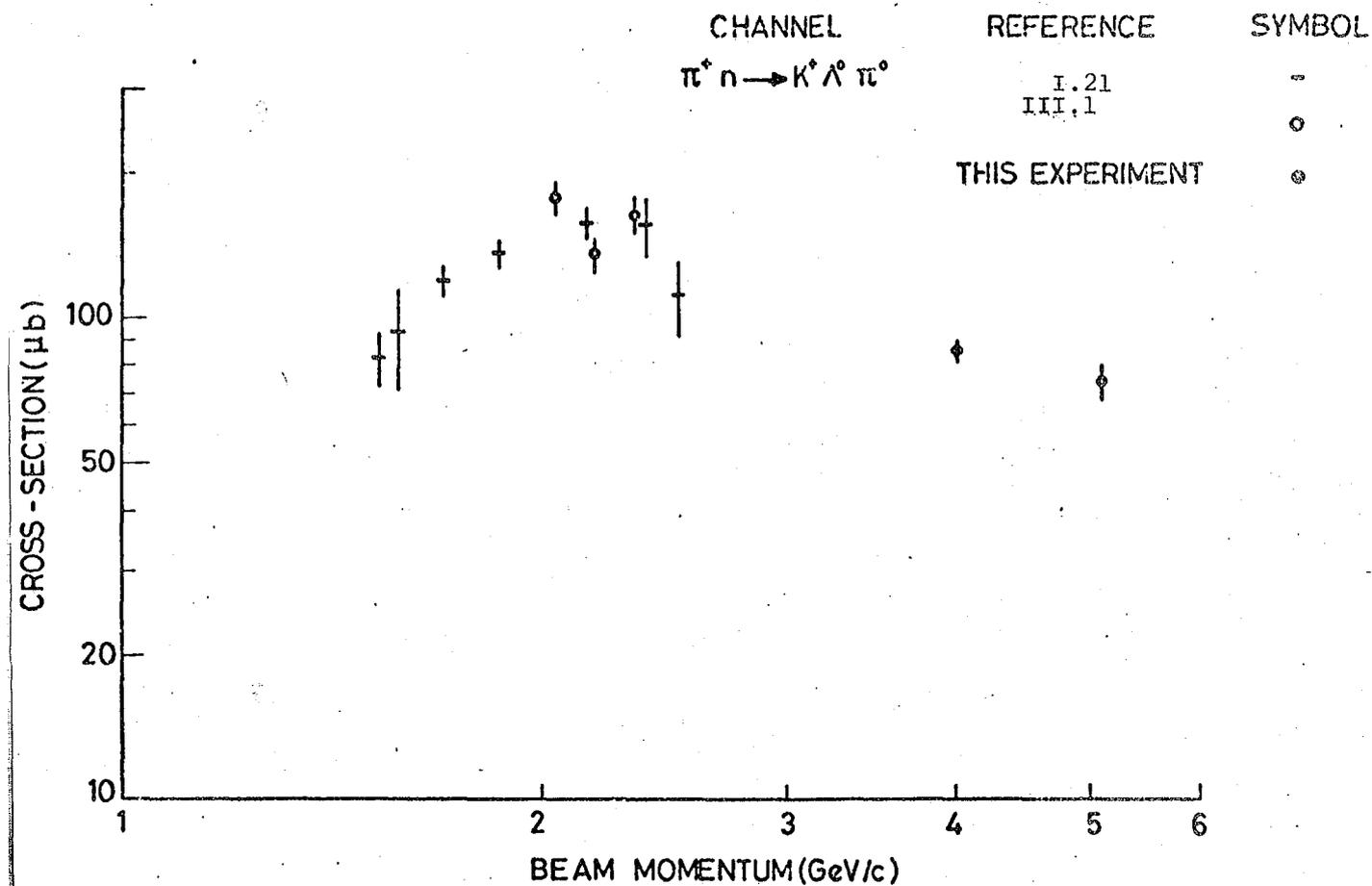
(c)
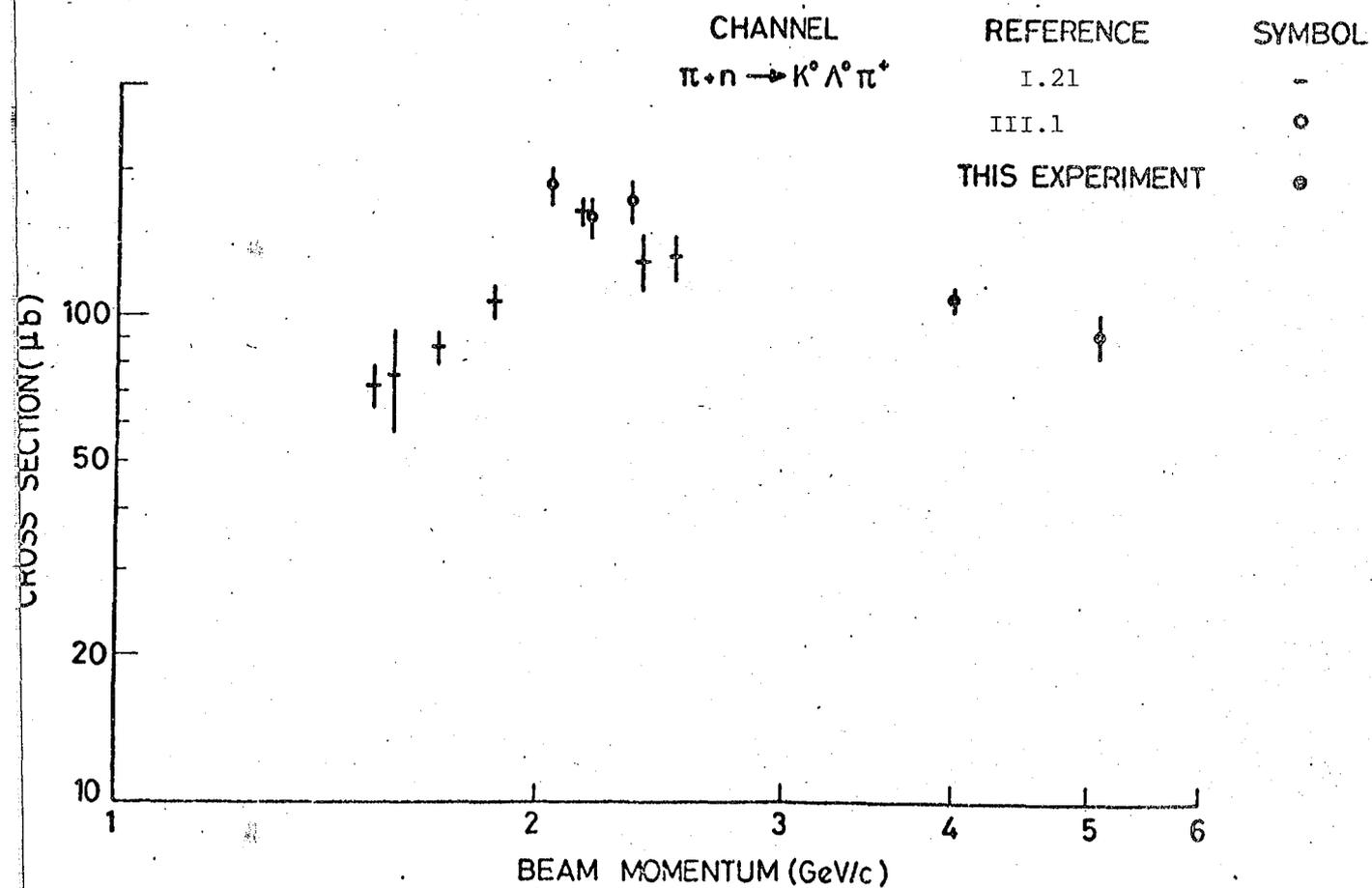
(d)

Fig. III.4 (Cont.)

CHAPTER IV

RESONANCE PRODUCTION AND REACTION CROSS-SECTIONS

IV.1 Introduction

This chapter is primarily concerned with the estimation of cross-sections for the production of well established resonances in those channels which contain more than 100 events (see table III.7). Channels with fewer than 100 events were considered to be insufficiently populated for a reliable determination of their reaction cross-sections. The reactions may be divided into two classes:

(i) those which produce particles with strangeness quantum number $S \neq 0$, but which involve the subsequent decay of one or more of the reaction products into strange particles. Such reactions are only partially represented in the strange particle sample, but their cross-sections may be checked with those calculated from non-strange channels using the branching ratios into strange and non-strange decaymodes

$$e.g. \quad \pi^+ d \rightarrow A_2^0 \ p \ p_s$$
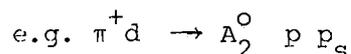
where the A_2^0 decays into $K\bar{K}$ ~5% of the time.

(ii) Reactions producing particles with $S = 0$, and which therefore involve strangeness-exchange mechanisms (these mechanisms will be dealt with in chapter V).

$$e.g. \quad \pi^+ d \rightarrow K^{*+} (890) \ \Lambda^0 \ p_s$$
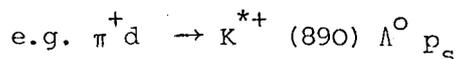
where the K^{*+} (890) has the following dominant decaymodes:

$$K^{*+} (890) \rightarrow K^0 \ \pi^+$$
$$\rightarrow K^+ \ \pi^0$$
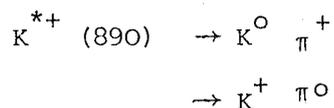
IV.2   Methods of estimation

Resonances found in this experiment manifest themselves by enchance-
ments in effective mass distributions. The effective mass of a system of
n particles is given by

$$M^2_{eff} (m_1, m_2 \ldots m_n) = (\sum_{i=1}^{n} E_i)^2 - (\sum_{i=1}^{n} p_i)^2$$

where m_1, m_2 .... m_n denote the masses of the n particles, E_i denotes the
energy and p_i the momentum of the i-th particle. If a resonance is
formed from the n particles, then the effective mass distribution will
display a peak at the resonance mass value, with a characteristic
width, Γ - the "full width at half height". The width is related to the
lifetime of the resonance by $\tau \sim 1/\Gamma$. If on the other hand the system
of n particles is produced without an intermediate resonance, the dis-
tribution of M_{eff} $(m_1, m_2 \ldots m_n)$ will correspond to that where all
kinematical configurations satisfying energy and momentum conservation
are equally probable. Such distributions are called "phase space" dis-
tributions. (They are dealt with in detail in, for example, the High
Energy and Nuclear Physics Data Handbook - ref. IV.1).

IV.2.1   Estimation of background

In general an effective mass distribution will be a mixture of both
resonance production and phase space contributions. Consequently the
resonance will be manifest as an enhancement of mass points on a back-
ground from phase space. It is not possible to separate these back-
ground events from the true resonant signal on a purely event-by-event
basis. However, the separation may be made in an overall way by using
the phase space prediction as a first approximation to the background.

The method may be further refined by including the influence ("reflection") of enhancements in the effective mass distributions of other particle combinations, although it is found that this does not appreciably affect the estimated amount resonant signal. Other methods of background estimation have been employed in earlier parts of this experiment. Essentially they correspond to a phenomenological parameterisation of the background. For example J. D. Thomas (ref. IV.2) in fitting the three-pion effective mass distribution for the channel,

$\pi^+ d \longrightarrow \pi^+ \pi^+ \pi^- n\ p_s$, used the following prescription to describe the background. The non-resonant contribution to the effective mass distribution was parameterised using the Derenzo-Hildebrand function,

$$F(\nu) \quad = \quad K\ \nu^\alpha\ (1 - \nu)^\beta$$

where $\qquad \nu \quad = \quad \dfrac{M_{eff} - M_L}{M_u - M_L}$,

$\qquad\qquad M_L \quad =$ the lower limit of the effective mass distribution,

$\qquad\qquad M_u \quad =$ the upper limit of the effective mass distribution,

$\qquad\qquad \alpha,\ \beta \qquad$ are parameters to be varied,

and K is a normalisation constant,

This is purely a parameterisation of the background and has no physical basis. However, by varying α and β a large family of background shapes can be accommodated.

The two methods of background estimation (phase space and background parameterisation) are compared in section IV.3.1 for the channel $K^+ \Lambda^0 \pi^0\ p_s$. The phase space method is usually adopted.

IV.2.2 Estimation of resonance production

Two methods are used depending on the amount of signal within the resonance mass band:

A: Event counting above background

If statistics are low then the effective mass distribution well away from the resonance mass band (where the resonant signal is negligible) is fitted with a phase space curve of the type described in section IV.2.1. The curve is then extrapolated into the resonance region enabling the number of events above background and within the resonance mass band to be counted. Where statistics are too low even to allow a fitted background curve, a handdrawn curve joining the background on either side of the assumed resonance will usually suffice. A tail correction (see below) is made afterwards to account for resonance production outside the selected mass band.

B: Fitting of phase space + resonance curves to the experimental effective mass distribution

With sufficient statistics it is possible to fit the experimental effective mass distribution with a phase space contribution, $B(M)$, and a contribution from each resonance, $R_i(M)$, where M denotes the effective mass. Neglecting interference effects between resonances as well as between resonances and phase space ([*]) (ref. IV.3), the fitted curve may be written as,

$$F(M) = b\, B(M) + \sum_{i=1}^{N_R} r_i\, R_i(M) \qquad\qquad (IV.1)$$

where N_R is the number of resonances and b and r_i are the fractions of the total number of events attributed to phase space and the i-th

---

([*]) An example of how to deal with resonance-resonance interference is given in section IV.3. However in general statistics do not justify the use of such elaborate methods.

resonance respectively.

$$(b + \sum_{i=1}^{N_R} r_i = 1)$$

The fitted curve is normalised to the experimental distribution, $E(M)$, using the relations

$$\int_K B(M) \, dM = \int_K R_i(M) \, dM = \int_K E(M) \, dM \qquad (IV.2)$$

where K indicates that the integral is over the whole of the kinematically accessible region.

The effective mass distributions of resonances with two body decays is parameterised using the well-known Breit-Wigner form (ref. IV.4):

$$R_i(M) = A_i \, B(M) \, M^2 \, Q^{-1}(M) \, \Gamma_i(M) \, / \, ((M^2 - M_i^2)^2 + M_i^2 \, \Gamma_i^2(M)) \qquad (IV.3)$$

$$\text{with} \quad Q(M) = \left[((m_1^2 - m_2^2 - M^2)^2 / 4M^2) - m_2^2 \right]^{\frac{1}{2}} \qquad (IV.4)$$

$$\text{and} \quad \Gamma_i(M) = \Gamma_i^0 \, (M_i/M) \, (Q(M)/Q(M_i))^{2L+1} \qquad (IV.5)$$

where A_i = a normalisation constant (see expression (IV.2)

M_i = the central mass value for the i-th resonance

(i.e. the "resonance mass" - ref. II.3)

$\Gamma_i^0 = \Gamma_i(M_i)$ - the characteristic width of the i-th resonance
(ref. II.3)

L = the relative orbital angular momentum of the decay

products

m_1 = the larger mass of the two decay products

m_2 = the smaller mass of the two decay products.

If $m_1 = m_2$ the expression (IV.4) for $Q(M)$ becomes

$$Q(M) = (M^2/4 - m_1^2)^{\frac{1}{2}}$$

$Q(M)$ is by definition the momentum of one of the decay products in the rest system of the resonance. It will therefore have a range of values for a resonance decaying into three particles. For particles of identical mass, m_1, the value of $Q(M)$ when the momenta of the three decay products are equal in the resonance rest system is given by

$$Q(M) = \frac{1}{3} (M^2 - 9 m_1^2)^{\frac{1}{2}}$$

This corresponds to the most probable kinematical configuration and is therefore the best approximation for $Q(M)$. It has proved to be adequate during earlier work in the experiment in fitting the $\omega^o(783)$ signal in the three pion effective mass distribution of the channel

$$\pi^+ d \longrightarrow \pi^+ \pi^- \pi^o \; p \; p_s \qquad \qquad \text{(ref. I.19)}.$$

It has therefore been used in the present work for the reaction

$$\pi^+ d \longrightarrow K^+ \Lambda^o \, \omega(783) \; p_s \; ; \qquad \omega^o(783) \longrightarrow \pi^+ \pi^- \pi^o .$$
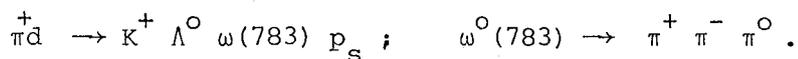
The centrifugal barrier factors (ref. IV.5) in the expression (IV.5) for the energy dependent width, $\Gamma_i(M)$, have been omitted since the narrow width of the resonances considered renders the effects of such refinements to be minimal.

In the absence of measurement and fitting errors, the resonance signal could be displayed in discrete intervals of effective mass and parameterised by the Breit-Wigner function alone (IV.3). However, the presence of errors redistributes the events in each mass interval in accordance with the shape of the resolution function. In effect events

initially assigned to a given mass interval will be redistributed into neighbouring regions to produce the observed effective mass distribution, E(M). Consequently expression (IV.3) must be convoluted with the resolution function. Since the background has little structure, folding in errors affects the background distribution in only a small way.

It is expected that the distribution of errors on the effective mass squared will be Gaussian for events in the same region of the chamber and with identical effective mass squared. For events distributed throughout the chamber and with a range of values for effective mass squared, the expected error distribution (the resolution function) will therefore be a superposition of many Gausian distributions. M. Dale (ref. I.19) has found that the resolution function approximates to a Breit-Wigner shape in mass squared. The width, γ, of the resolution function may be determined from the observed distribution of errors on the effective mass squared, using the errors calculated in KINEMATICS on the measured quantities. The width is also allowed to be a free parameter in the fitting process in order to provide a check on the validity of the final fit.

The best values for the parameters r_i, M_i, Γ_i^o and γ are found by minimising the total chi-squared,

$$\chi^2 = \sum_{j=1}^{N} \frac{F(M_j) - E(M_j)}{F(M_j)}$$

where M_j is the central mass value of the j-th mass interval and N is the total number of intervals. Normally the width of the mass intervals is taken to be 25 MeV/c^2. The minimisation was achieved using a programme called MINUIT (ref. IV.6). In some cases it was necessary to restrict the range of one or more of the masses or widths to that given in ref. II.3.

Using expression (IV.3) it is possible to estimate the amount of resonance signal outside a particular mass band. This enables the "tail correction" to be estimated in method A, taking nominal values for the width and mass of the resonance (ref. II.3).

IV.2.3 Significance of enhancements

Having estimated the possible contribution of a resonance signal to the effective mass distribution, it is necessary to ascertain whether the signal is a real effect or merely a fluctuation in the background. The significance of an enhancement, sig, is taken to be a measure of the "strength" of the resonance contribution:

$$\text{sig} = N_r / \sigma_r$$

where $N_r = N_t - N_b$

and $\sigma_r = (N_t + (\Delta N_b)^2)^{\frac{1}{2}}$

with N_r = the number of resonance events,

N_b = the number of background events,

N_t = the total number of events,

and ΔN_b = the estimated error in N_b events.

All the above quantities are determined within the chosen mass band of the resonance. In general signals with sig. < 2 are discarded.

IV.3 Resonance production

Resonance production has been estimated in the more populated channels ($\gtrsim$ 100 events) shown in table III.7. These may be divided

into channels with three, four or five outgoing particles (not including the spectator nucleon):

Three body channels

(a) $K \Lambda^0$ (+ pions) N_s

$K^+ \Lambda^0 \pi^0 p_s$

$K^0 \Lambda^0 \pi^+ p_s$

$K^+ \Lambda^0 \pi^+ n_s$

(b) $K \Sigma$ (+ pions) N_s

$K^0 \Sigma^0 \pi^+ p_s$

$K^0 \Sigma^+ \pi^+ n_s$

(c) $K \bar{K} NN_s$

$K^+ K^- pp_s$

$K^0 \bar{K}^0 pp_s$

$K^+ \bar{K}^0 pn_s$

$K^+ \bar{K}^0 np_s$

Four body channels

(a) $K \Lambda^0$ (+ pions) N_s

$K^+ \Lambda^0 \pi^+ \pi^- p_s$

$K^0 \Lambda^0 \pi^+ \pi^0 p_s$

$K^0 \Lambda^0 \pi^+ \pi^+ n_s$

(b) $K \Sigma$ (+ pions) N_s

$K^+ \Sigma^0 \pi^+ \pi^- p_s$

(c) $K \bar{K}$ (+ pions) NN_s

$K^0 K^- \pi^+ pp_s$

$K^+ \bar{K}^0 \pi^- pp_s$

Five body channels

$K \Lambda^0$ (+ pions) N_s

$K^+ \Lambda^0 \pi^+ \pi^- \pi^0 p_s$

In view of the limited statistics not all enhancements found in the strange particle sample are explained as resonances. The primary aim of the analysis is to study the production reactions of known particles and resonances. In general enhancements are only considered when at or near the position of well established resonances. However some discussion on the possible existence of exotic resonances is given in section IV.3.8, and in sections IV.39 and IV.3.10 the significance of enhancements in the $(K\bar{K}\pi)$ and $(K\pi\pi)$ effective mass distributions is considered. The dominant (sig. > 2) resonances found in the above channels may be classified as follows:

Mesons $S \neq 0$: K^* (890) and K^* (1420).

Mesons $S = 0$: ω^0 (783), A_2 and f^0 (1270)

Baryons $S \neq 0$: Λ^0 (1520), Σ (1385) and Σ (1670)

Table IV.1 gives a summary of resonance production. For each reaction the cross-section, method of estimation and the relevant figure number are shown. The significance for low strength enhancements is also given. The notation

$$K^{*+} (890) \ \Lambda^0 \ \pi^0 \ p_s$$

includes all final states of the channel in which the K^{*+} (890) is produced

i.e. $\qquad K^{*+}$ (890) $\Lambda^0 \ \pi^0 \ p_s$

$\qquad\qquad K^{*+}$ (890) Σ^0 (1385) p_s

$\qquad\qquad$ etc.

One further remark on notation is that (AB ....) is used to indicate the effective mass distribution of the particle combination AB ... A notation such as $(AB \ ...)^{+, \ 0, \ -}$, indicates the effective mass distribution

TABLE IV.1

A SUMMARY OF RESONANCE PRODUCTION

Channel	Reaction	%	Sig	Cross-section (μb)	Method	Figure
$K^+\Lambda^\circ\pi^\circ p_s$	$K^{*+}(890)\Lambda^\circ\, p_s$	26 ± 2		22 ± 2	A	IV.1 (b)
	$K^{*+}(1420)\Lambda^\circ\, p_s$	4.7 ± 1.0	2.1	3.9 ± 0.8	B	IV.1 (b)
	$K^+\Sigma^\circ(1385)\, p_s$	23 ± 2		19 ± 2	A	IV.2
$K^\circ\Lambda^\circ\pi^+ p_s$	$K^{*+}(890)\Lambda^\circ\, p_s$	39 ± 2		41 ± 3	A	IV.3
	$K^{*+}(1420)\Lambda^\circ\, p_s$	6.1 ± 0.9	2.8	6.5 ± 0.9	B	IV.3
$K^+\Lambda^\circ\pi^+ n_s$	$K^+\Sigma^+(1385)\, n_s$	22 ± 2		20 ± 2	A	IV.8
$K^\circ\Sigma^\circ\pi^+ p_s$	$K^{*+}(890)\Sigma^\circ\, p_s$	44 ± 4		21 ± 3	A	IV.12
$K^\circ\Sigma^+\pi^+ n_s$	$K^{*+}(890)\Sigma^+\, n_s$	78 ± 8		61 ± 9	A	IV.14
$(K\bar{K})^\circ p\, p_s$	$f^\circ p\, p_s$			25 ± 3	A	IV.20
	$A_2^\circ p\, p_s$			28 ± 3	A	IV.20
$K^+ K^- p\, p_s$	$K^+\Lambda^\circ(1520)\, p_s$	17 ± 1		16 ± 2	A	IV.22
$K^+\bar{K}^\circ p\, n_s$	$A_2^+ p\, n_s$	55 ± 5		23 ± 3	A	IV.23
$K^+\bar{K}^\circ n\, p_s$	$A_2^+ n\, p_s$	38 ± 3		25 ± 3	A	IV.24
	$K^+\Lambda^\circ(1520)\, p_s$	15 ± 2	5.9	10 ± 2	B	IV.25
$K^+\Lambda^\circ\pi^+\pi^- p_s$	$K^{*\circ}(890)\Lambda^\circ\pi^+\, p_s$	30 ± 2		26 ± 2	A	IV.29
	$K^+\pi^+\Sigma^-(1385)p_s$	21 ± 2		18 ± 2	A	IV.30
	$K^+\pi^-\Sigma^+(1385)p_s$	15 ± 1		13 ± 1	A	IV.31
$K^\circ\Lambda^\circ\pi^+\pi^\circ p_s$	$K^{*+}(890)\Lambda^\circ\pi^\circ\, p_s$	40 ± 4		31 ± 4	A	IV.33
	$K^\circ\pi^+\Sigma^\circ(1385)p_s$	24 ± 3		19 ± 2	A	IV.34
	$K^{*+}(890)\Sigma^\circ(1385)p_s$	21 ± 5		17 ± 5		
	$K^{*\circ}(890)\Lambda^\circ\pi^+\, p_s$	9 ± 2	2.3	7 ± 2	B	IV.35
$(K\pi\pi)^+\Lambda^\circ\, p_s$	$K^{*+}(1420)\,\Lambda^\circ\, p_s$	13 ± 1	4.9	22 ± 2	B	IV.58(a)
$K^\circ\Lambda^\circ\pi^+\pi^+ n_s$	$K^{*+}(890)\,\Lambda^\circ\,\pi^+ n_s$	69 ± 7		34 ± 3	A	IV.39
	$K^\circ\pi^+\Sigma^+(1385)\, n_s$	42 ± 5		23 ± 3	A	IV.40
	$K^{*+}(890)\Sigma^+(1385)n_s$	13 ± 8		6 ± 4		
$K^+\Sigma^\circ\pi^+\pi^- p_s$	$K^{*\circ}(890)\Sigma^\circ\,\pi^+\, p_s$	28 ± 3		16 ± 2	A	IV.41

Table IV.1   (Continued)

Channel	Reaction	%	Sig	Cross-section (μb)	Method	Figure
$K^O K^- \pi^+ p\, p_s$	$K^{*+}(890)\ K^-\ p\ p_s$	55 ± 4		34 ± 4	A	IV.48
	$K^O\ \pi^+\ \Lambda^O(1520)\ p_s$	14 ± 2	3.9	9 ± 2	B	IV.49
	$\bar{K}^{*O}(890)K^O\ p\ p_s$	17 ± 3	3.8	10 ± 2	B	IV.50
$K^+K^O\ \pi^-\ p\, p_s$	$K^{*O}(890)\ \bar{K}^O\ p\ p_s$	44 ± 4		23 ± 3	A	IV.52
	$K^{*-}(890)\ K^+\ p\ p_s$	41 ± 4		21 ± 3	A	IV.53
	$K^+\pi^-\Sigma^+(1670)\ p_s$	12 ± 3	2.2	6 ± 2	B	IV.54
$K^+\Lambda^O\pi^+\pi^-\pi^O\, p_s$	$K^+\ \Lambda^O\ \omega^O(783)\ p_s$	27 ± 2		21 ± 2	A	IV.56

of a subset of this particle combination whose combined charge is given by the index.

In the following sections the details of the individual reactions are discussed.

IV.3.1   The channels $K^+ \Lambda^\circ \pi^\circ p_s$, $K^\circ \Lambda^\circ \pi^+ p_s$ and $K^+ \Lambda^\circ \pi^+ n_s$

The first of these channels shows strong K^{*+} (890) and Σ°(1385) signals in $(K^+ \pi^\circ)$ and $(\Lambda^\circ \pi^\circ)$ respectively (see table IV.1). It is therefore a useful channel in which to study the effects of reflections on the phase space distributions and on the resulting estimation of the resonance contribution. Figures IV.1 (a), (b) and (c) show $(K^+ \pi^\circ)$ fitted with a Breit-Wigner and three different background curves (see section IV.2.1):

(a)   phase space alone,

(b)   phase space plus reflection from Σ° (1385)

and   (c)   the Derenzo-Hildebrand function with $\alpha = 0.642$ and $\beta = 0.896$.

Fits (a) and (b) show some discrepancy at the upper limit of the effective mass distribution since the target nucleon has been taken to be at rest for the phase space prediction. However, for deuterium interactions the spectator nucleon has a momentum distribution which has been predicted by Hulthen and Sugaware (section I.2). This will produce a small variation in the centre of mass energy, E_{cM}. The effect of this variation on the phase space distribution may be illustrated by considering the Dalitz plot of $M^2(\Lambda^\circ \pi^\circ)$ versus $M^2(K^+ \pi^\circ)$ in figure IV.5. Here three boundaries are shown corresponding to $E_{cM} = 2.73$, 2.90 and 3.06 (the second value is for the target nucleon at rest). For E_{cM} constant the area within the boundary should be uniformly populated provided there are no resonance contributions. Therefore by projecting a uniform
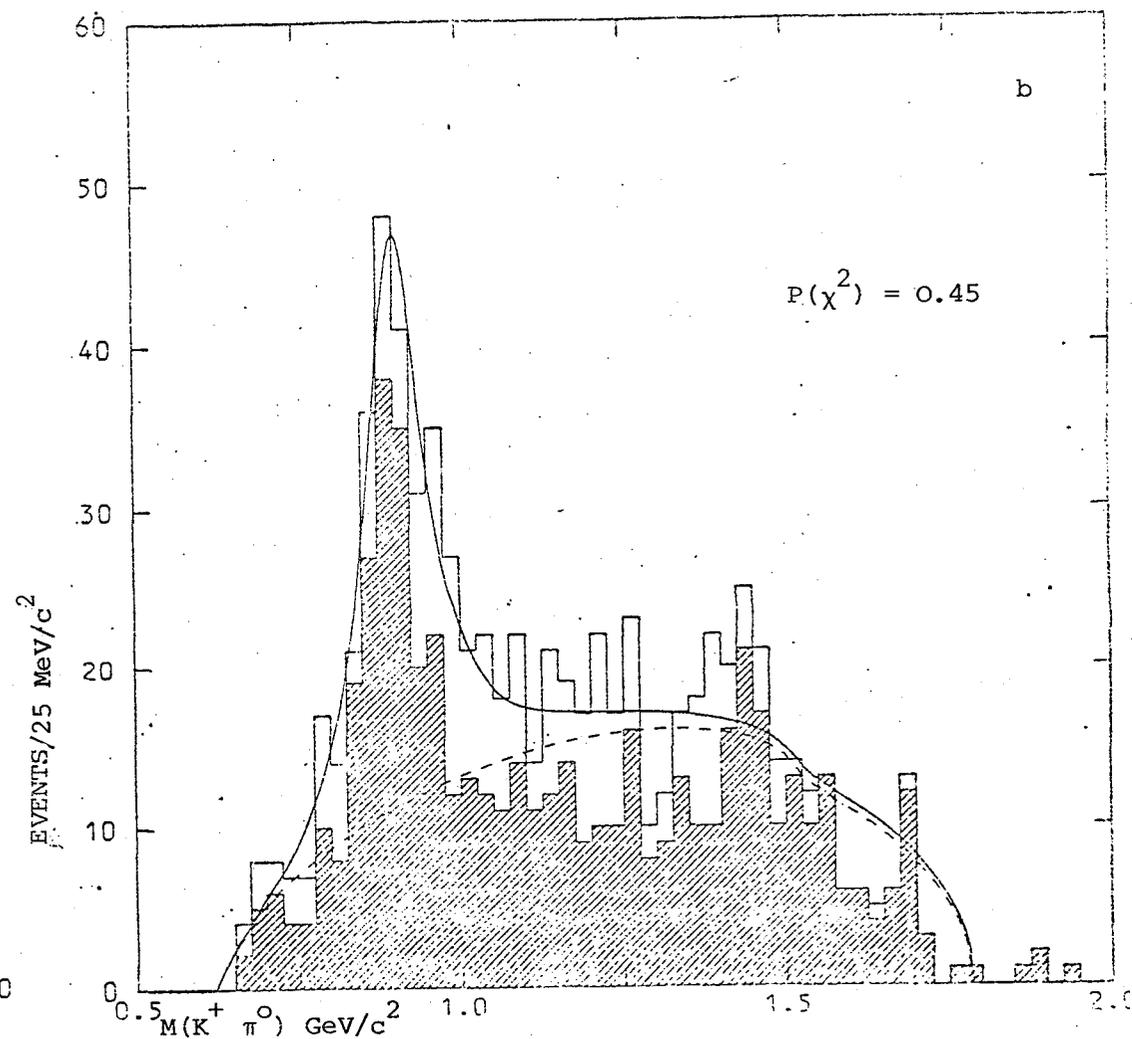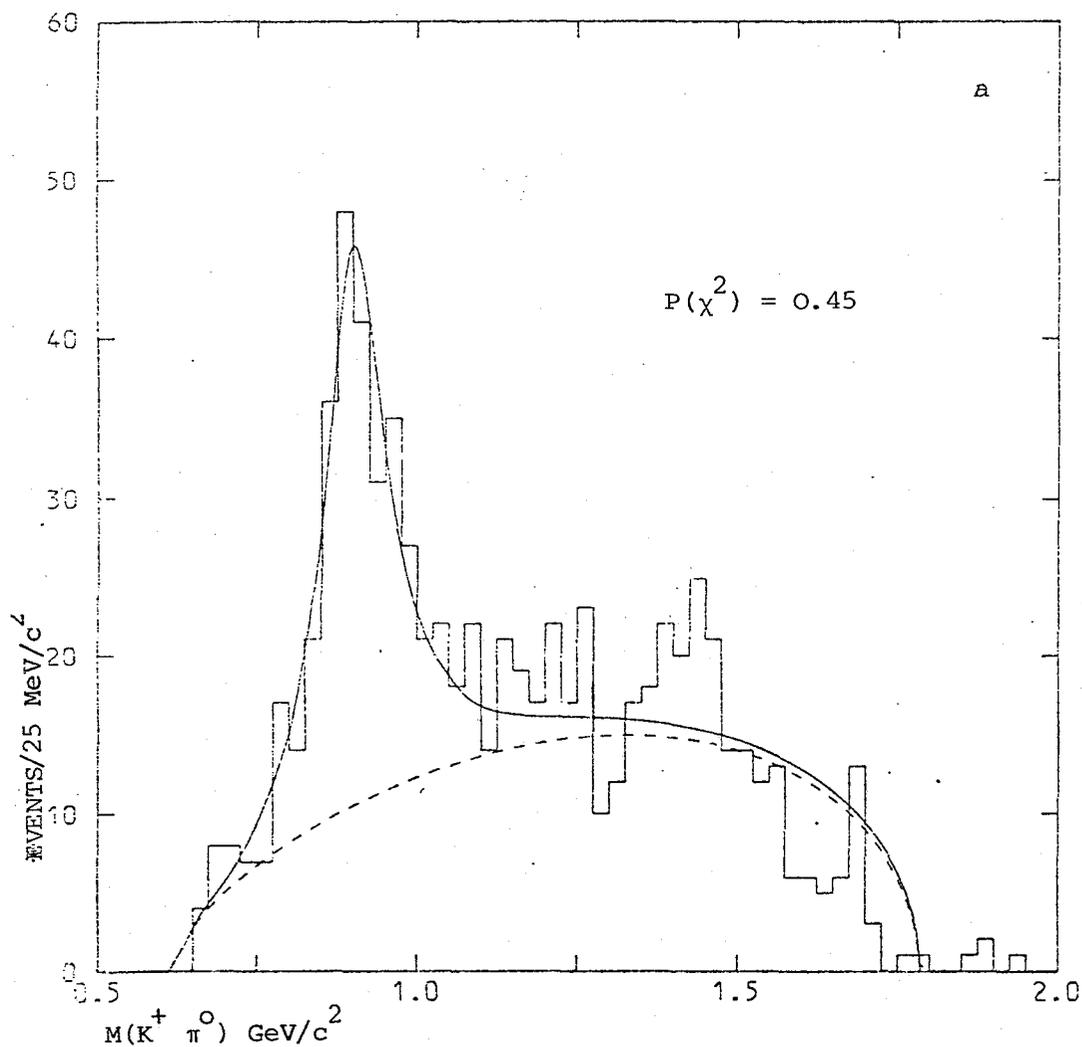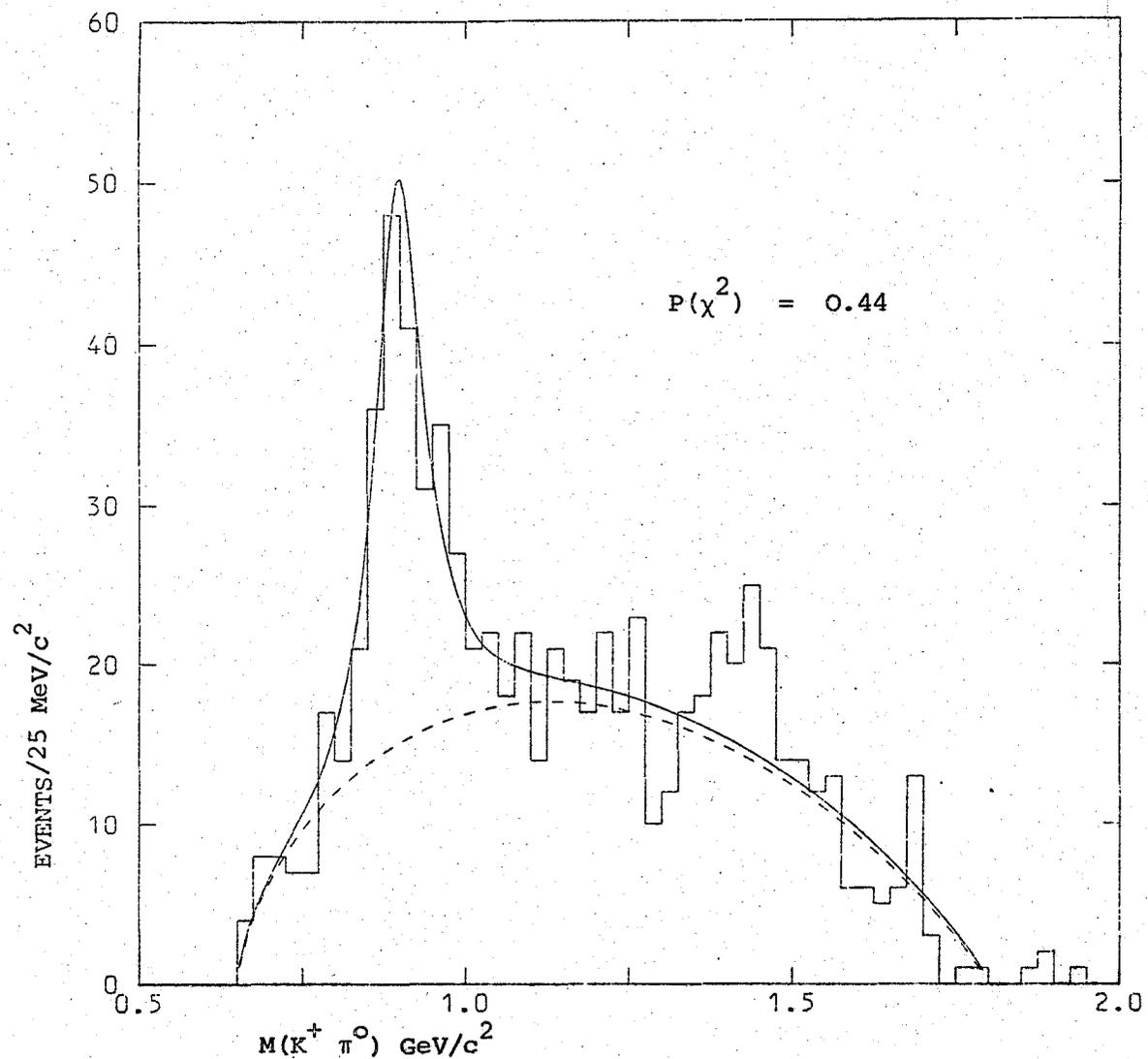
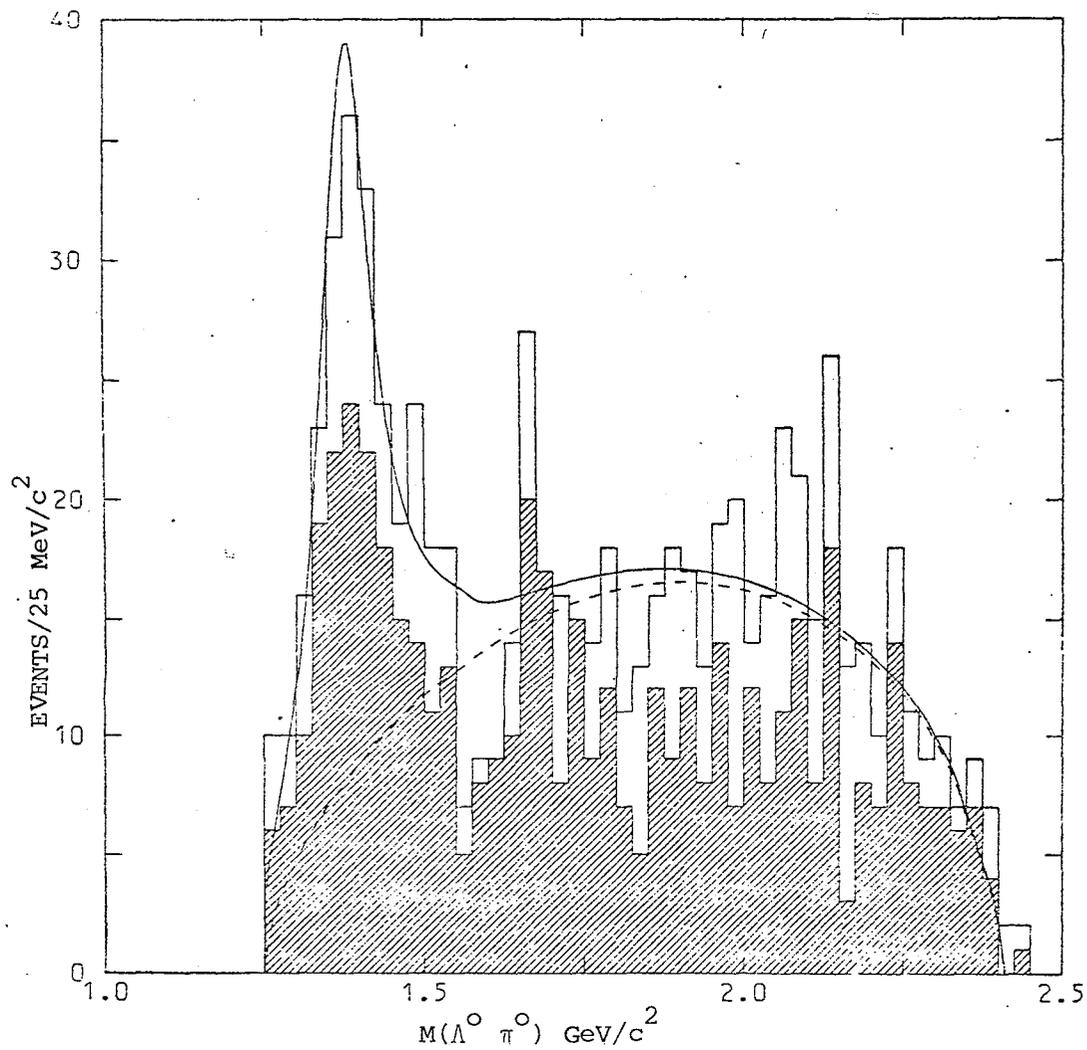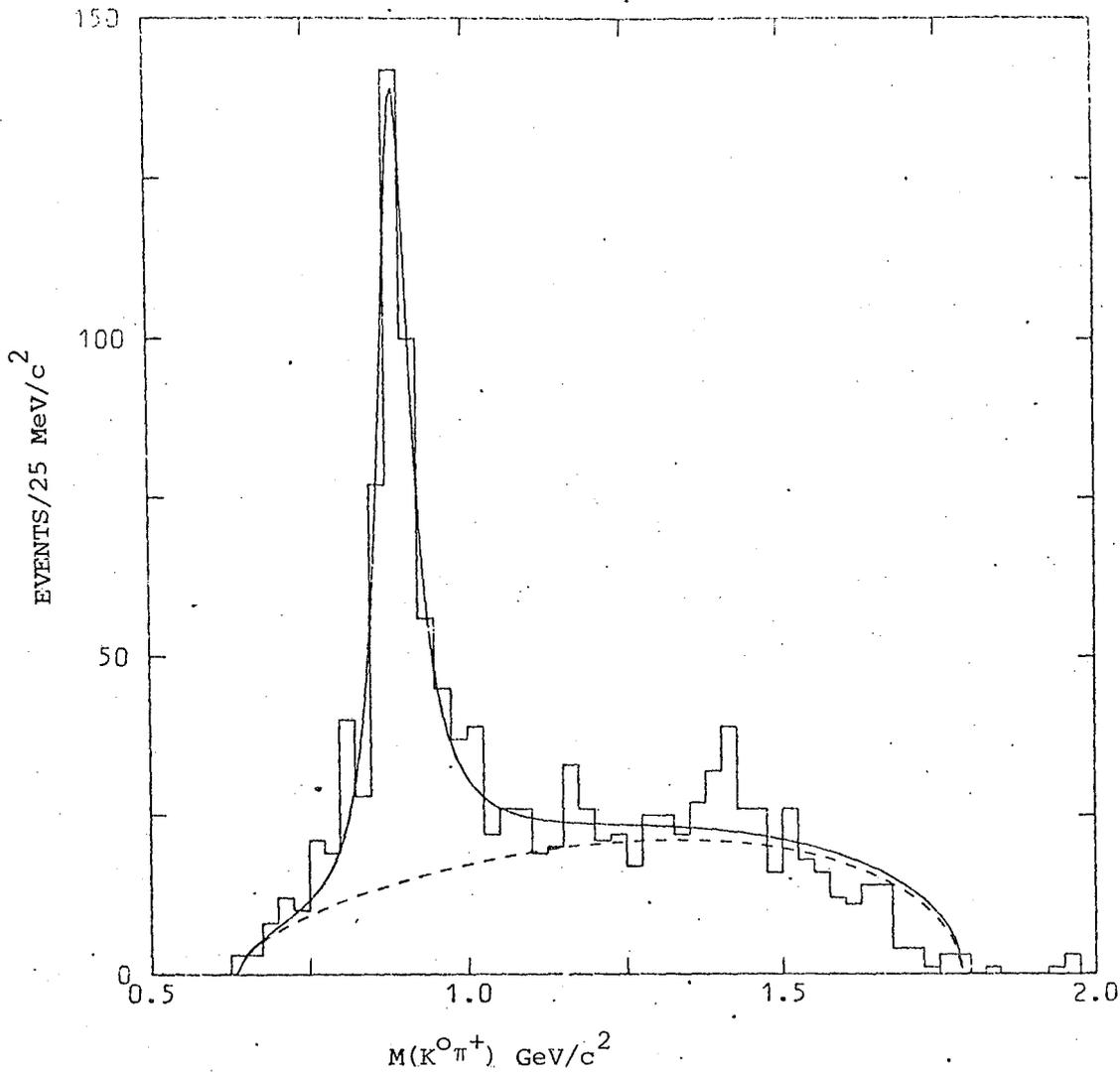Fig. IV.1 The $K^+ \pi^o$ effective mass distribution for the channel $K^+ \Lambda^o \pi^o{}_{ps}$ fitted with a $K^{*+}(890)$ Breit-Wigner expression and (a) phase space (b) phase space plus reflection from $\Sigma^o(1385)$. The $K^{*+}(1420)$ mass band (1.375 GeV/c$^2 <$ $M(K^+ \pi^o) < 1.475$ GeV/c^2) has not been fitted and the curve extrapolated into this region. The hatched area corresponds to events with $M(\Lambda^o \pi^o) > 1.5$ GeV/c^2.

$P(\chi^2) = 0.44$

(c) The $K^+\pi^o$ effective mass distribution for the channel $K^+ \Lambda^o \pi^o p_s$ fitted with a $K^{*+}(890)$ Breit-Wigner expression and the Derenzo-Hildebrand function.
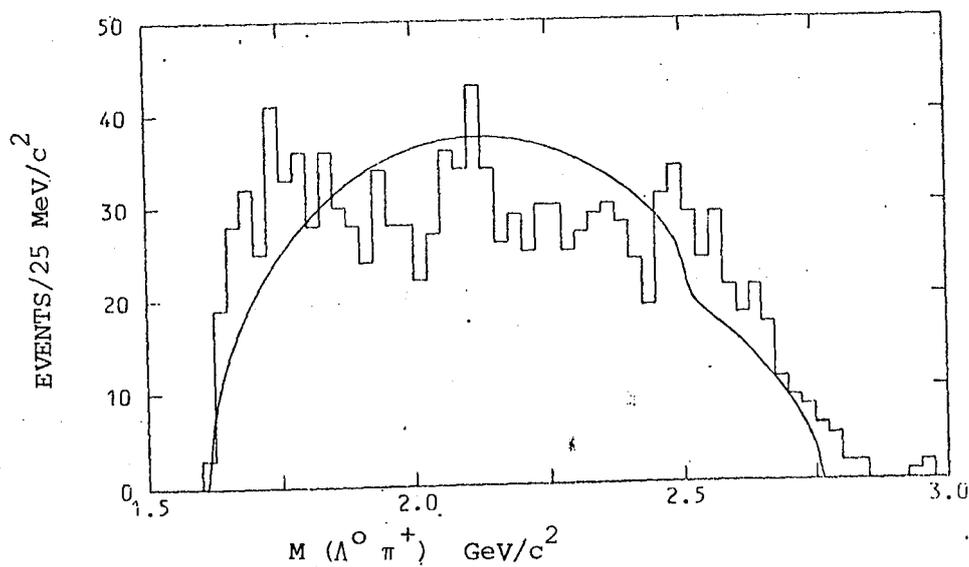
Fig. IV.2   The Λ^O π^O effective mass distribution for the channel $K^+ \Lambda^O \pi^O p_s$ fitted with a Σ^O(1385) Breit-Wigner expression and phase space plus reflection from $\bar{K}^{*+}$ (890). The hatched area corresponds to those events with $M(K^+ \pi^O) < 0.79$ GeV/c^2 and $M (K^+ \pi^O) > 0.99$ GeV/c^2.

IV.3 The $K^O\pi^+$ effective mass distribution for the element $K^O \Lambda^O \pi^+ p_s$ fitted with a K^{*+} (890) Breit-Wigner expression and phase space. The K^{*+}(1420) mass band has not been fitted and the curve extrapolated into this region.

IV.4 The $\Lambda^O \pi^+$ effective distribution for the channel $K^O \Lambda^O \pi^+ p_s$. The curve represents phase space plus reflection from K^{*+} (890) normalised to the total number of events.
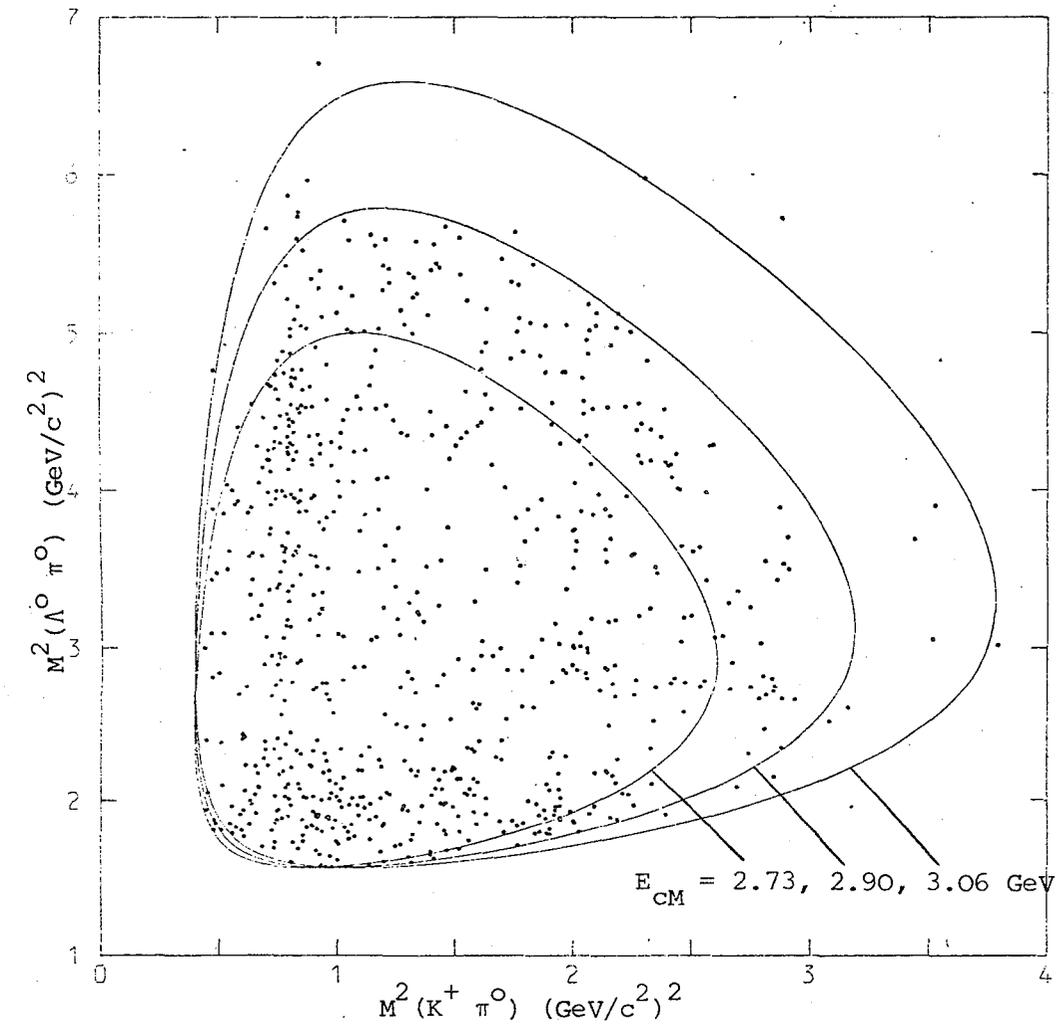
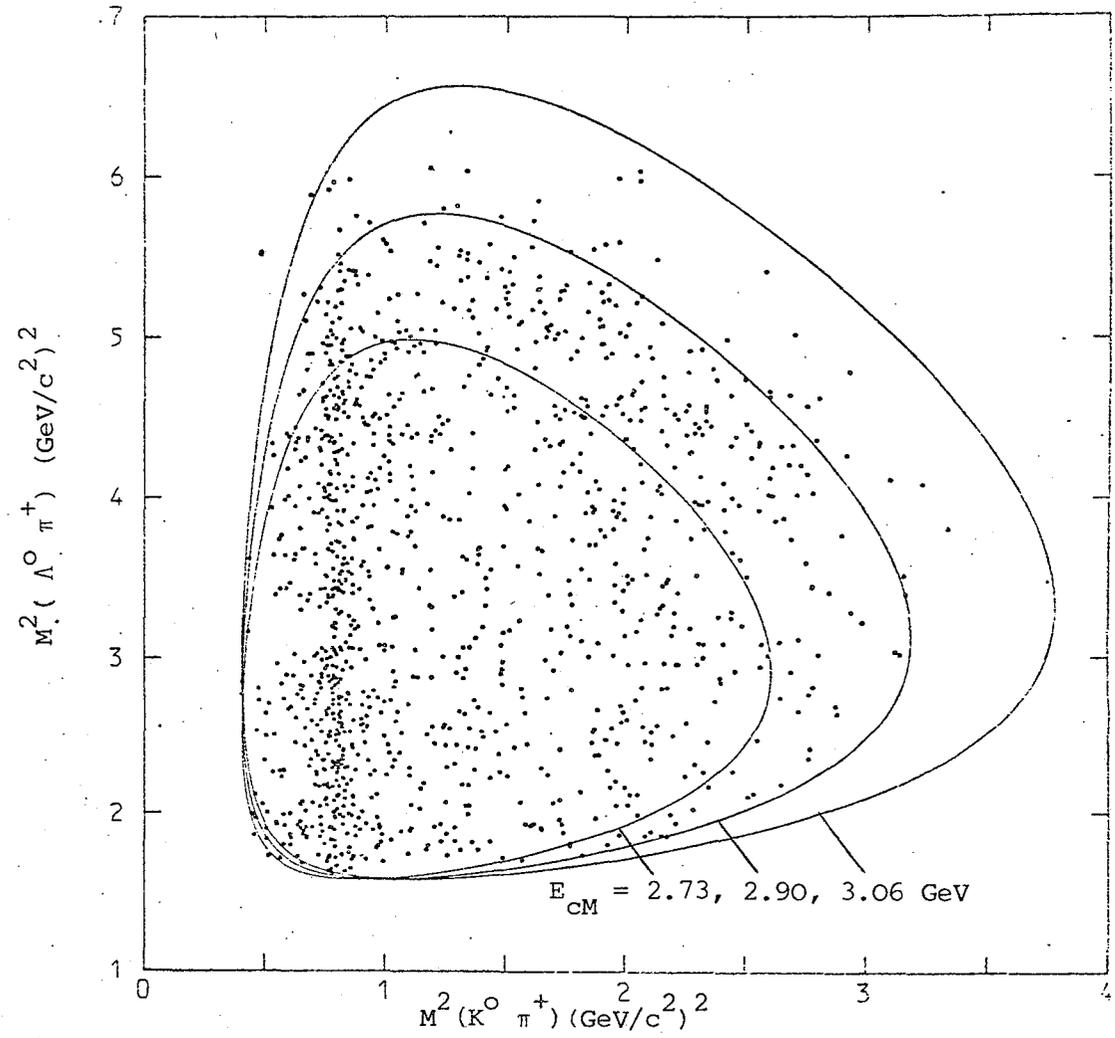Fig. IV.5 Dalitz plot for the channel $K^+ \Lambda^0 \pi^0 p_s$

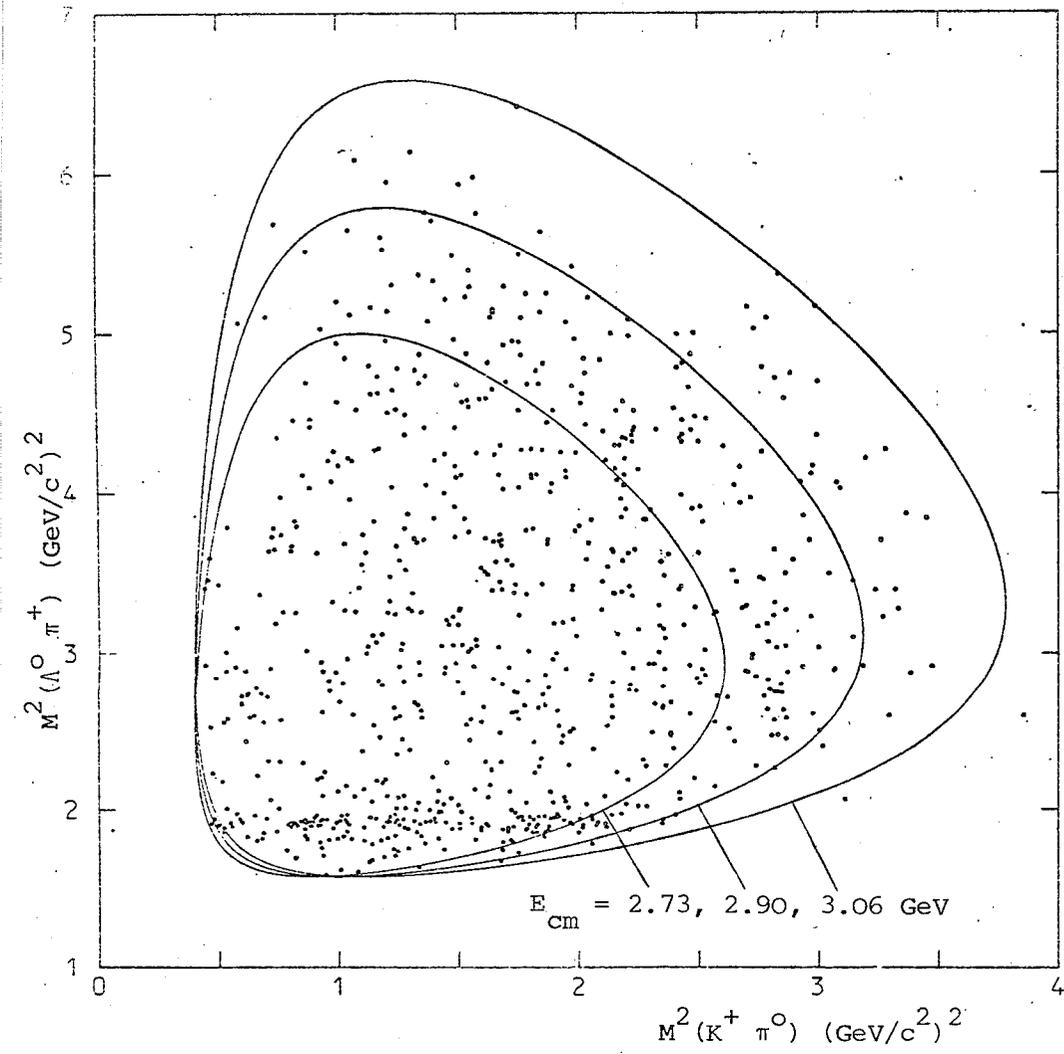Fig. IV.6 Dalitz plot for the channel $K^0 \Lambda^0 \pi^+ p_s$

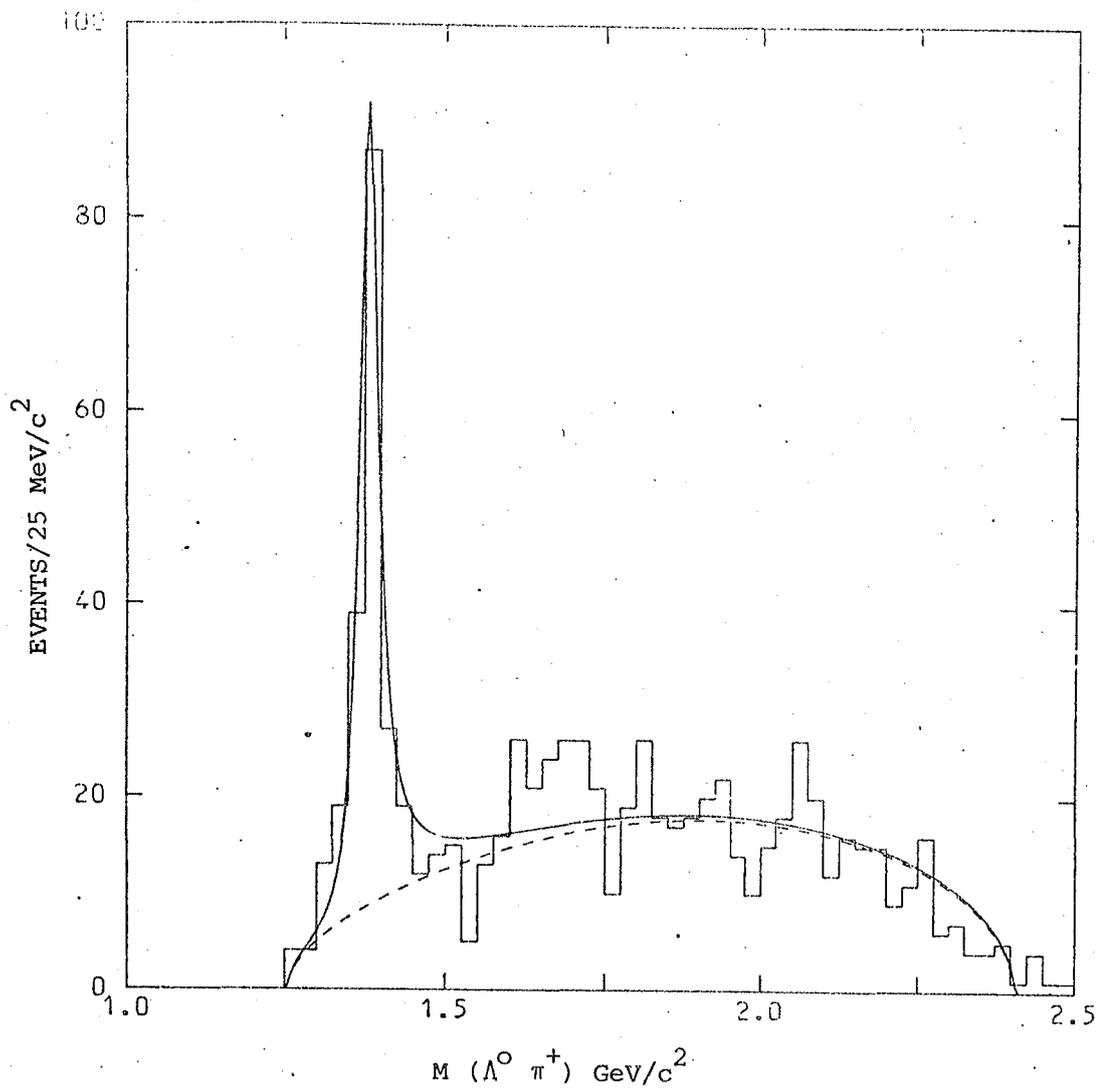Fig. IV.7 Dalitz plot for the channel $K^+ \Lambda^0 \pi^+ n_s$

Fig. IV.8. The $\Lambda^o \pi^+$ effective mass distribution for the channel $K^+ \Lambda^o \pi^+ n_s$ fitted with a $\Sigma^+(1385)$ Breit-Wigner expression and phase space.
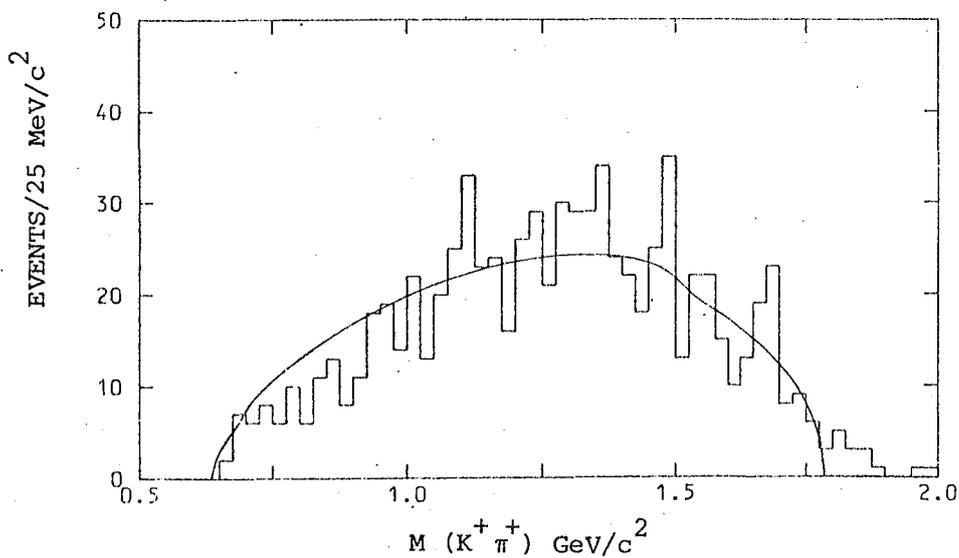

Fig. IV.9 The $K^+ \pi^+$ effective mass distribution for the channel $K^+ \Lambda^o \pi^+ n_s$. The curve represents phase plus reflection from $\Sigma^+(1385)$ normalised to the total number of events.

distribution onto the $(\Lambda^o \pi^o)$ or the $(K^+ \pi^o)$ axis the phase space pre-diction may be obtained. However the variation of E_{cM} will distort this uniformity as can be seen in figure IV.2. Clearly the main dis-tortion of the resulting phase space curves will be for the higher values of effective mass. In principle it is possible to accommodate the variation of E_{cM} in the phase space prediction. However the dis-crepancy is not serious and therefore the value of E_{cM} corresponding to the target nucleon at rest has been taken as a reasonable approximation. For fit (c) the overall agreement with the experimental distribution is better, although this is to be expected since there are two more free parameters in the Derenzo-Hildebrand function than in the phase space prediction. Even so there is no appreciable difference in the estimates of resonance contribution from the three separate background curves as can be seen from table IV.2. In general the phase space prediction has been used for background estimation since it has a physical basis, whereas the Derenzo-Hildebrand function is merely a parameterisation of the background. Reflection effects have been included for three body final states where they require a reasonably simple modification to the phase space curve.

The Dalitz plots for the remaining two channels, $K^o \Lambda^o \pi^+ p_s$ and $K^+ \Lambda^o \pi^+ n_s$, are shown in figures IV.6 and IV.7 respectively. For the first of these channels the production of $\Sigma^+(1385)$ in $(\Lambda^o \pi^+)$ is sup-pressed (see figure IV.4) since this would involve the exchange of an "exotic" meson or a baryon with charge +1 and strangeness -1. (A detailed analysis of exchange mechanisms is given in chapter V). From the cross-sections given in table IV.1 for $K^{*+}(890)$ and $K^{*+}(1420)$ production, the following ratios may be evaluated:

Table IV.2

COMPARISON OF BACKGROUND ESTIMATION METHODS
FOR THE CHANNEL $K^+ \Lambda^o \pi^o p_s$

Reaction	%	Cross-section (µb)	Method
K^{*+} (890) $\Lambda^o p_s$	26 ± 2	22 ± 2	Phase space alone
	26 ± 2	22 ± 2	Phase space plus reflections
	24 ± 2	20 ± 2	Derenzo-Hildebrand function
K^{*+} (1420) $\Lambda^o p_s$	5.5 ± 1.0	4.6 ± 0.9	Phase space alone
	4.7 ± 1.0	3.9 ± 0.8	Phase space plus reflections
	6.1 ± 1.1	5.0 ± 0.9	Derenzo-Hildebrand function

$$\frac{\sigma \ (K^{*+} \ (890) \ \Lambda^{o} \ \rightarrow \ K^{o} \ \pi^{+} \ \Lambda^{o})}{\sigma \ (K^{*+} \ (890) \ \Lambda^{o} \ \rightarrow \ K^{+} \ \pi^{o} \ \Lambda^{o})} \ = \ 1.9 \ \overset{+}{-} \ 0.2$$

$$\frac{\sigma \ (K^{*+} \ (1420) \ \Lambda^{o} \ \rightarrow \ K^{o} \ \pi^{+} \ \Lambda^{o})}{\sigma \ (K^{*+} \ (1420) \ \Lambda^{o} \ \rightarrow \ K^{+} \ \pi^{o} \ \Lambda^{o})} \ = \ 1.7 \ \overset{+}{-} \ 0.4$$

From the Clebsch-Gordan coefficients for K^{*+}(890) and K^{*+}(1420) decay both ratios should equal 2. The first shows good agreement, whereas the second agrees within errors. By combining the $K^{o} \pi^{+}$ and $K^{+} \pi^{o}$ spectra a more accurate value for K^{*+}(1420) production may be obtained:

$$\sigma \ (\pi^{+}d \ \rightarrow \ K^{*+} \ (1420) \ \Lambda^{o} \ p_{s}) \ = \ 12.3 \ \overset{+}{-} \ 1.3 \ \mu b$$

For the channel $K^{+} \ \Lambda^{o} \ \pi^{+} \ n_{s}$ there is no evidence for a doubly charged meson resonance in $(K^{+} \ \pi^{+})$ (see figure IV.9) and indeed the effective mass distribution is fitted reasonably well by a phase space curve plus reflection from the strong Σ^{+} (1385) signal in $(\Lambda^{o} \ \pi^{+})$ (figure IV.8).

IV.3.2. The channels $K^{o} \ \Sigma^{o} \ \pi^{+} \ p_{s}$ and $K^{o} \ \Sigma^{+} \ \pi^{+} \ n_{s}$

The Dalitz plots for these channels are shown in figures IV.10 and IV.11 respectively. Both channels show strong K^{*+} (890) production (see table IV.1) although statistics are too low to allow a reliable determination of any K^{*+} (1420) signal should it be present. Figure IV.13 shows that Σ^{+} (1385) production is suppressed in $K^{o} \ \Sigma^{o} \ \pi^{+} \ p_{s}$ (c.f $K^{o} \ \Lambda^{o} \ \pi^{+} \ p_{s}$, fig IV.4)
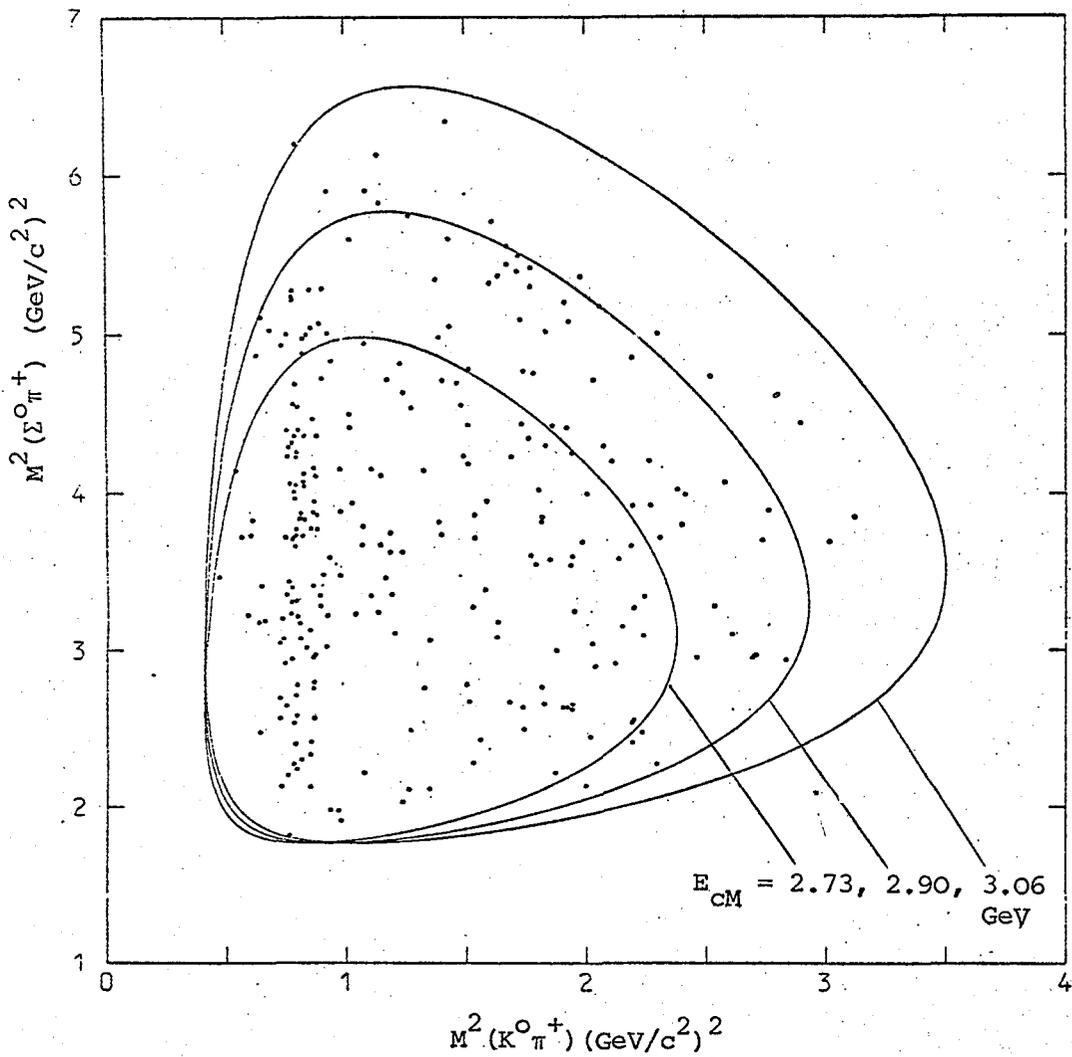
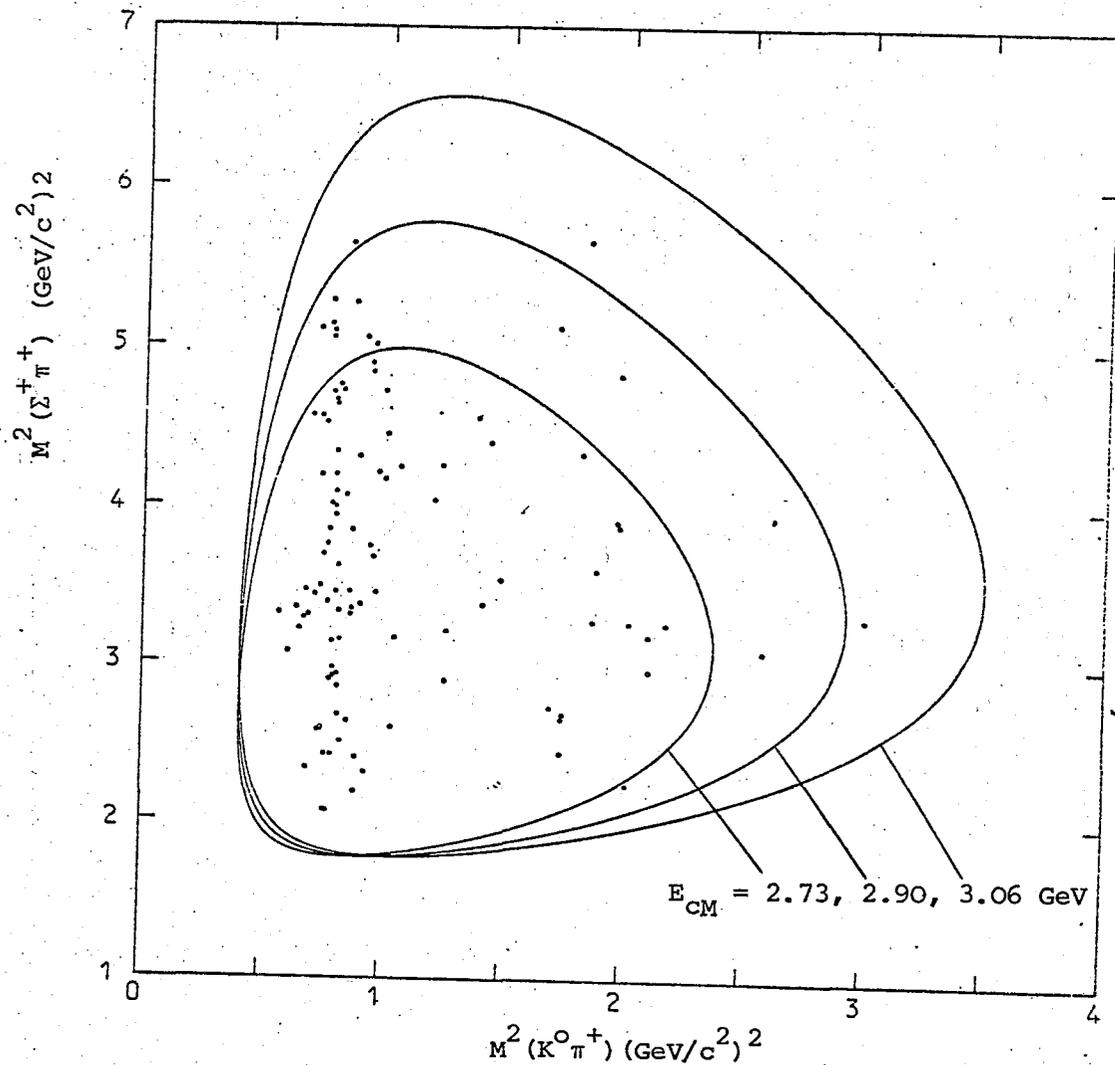Fig. IV.10 Dalitz plot for the channel $K^O \Sigma^O \pi^+ p_s$

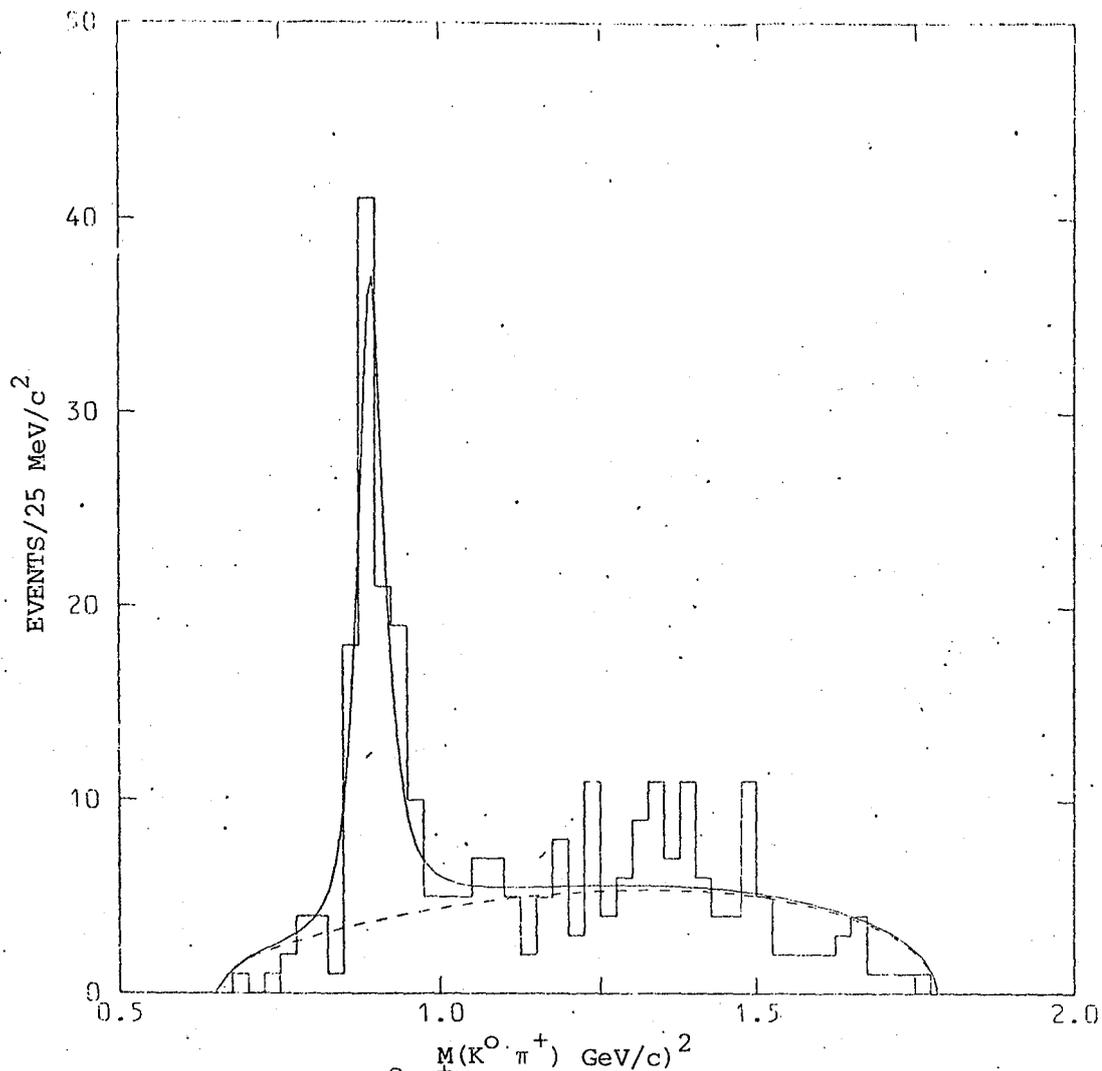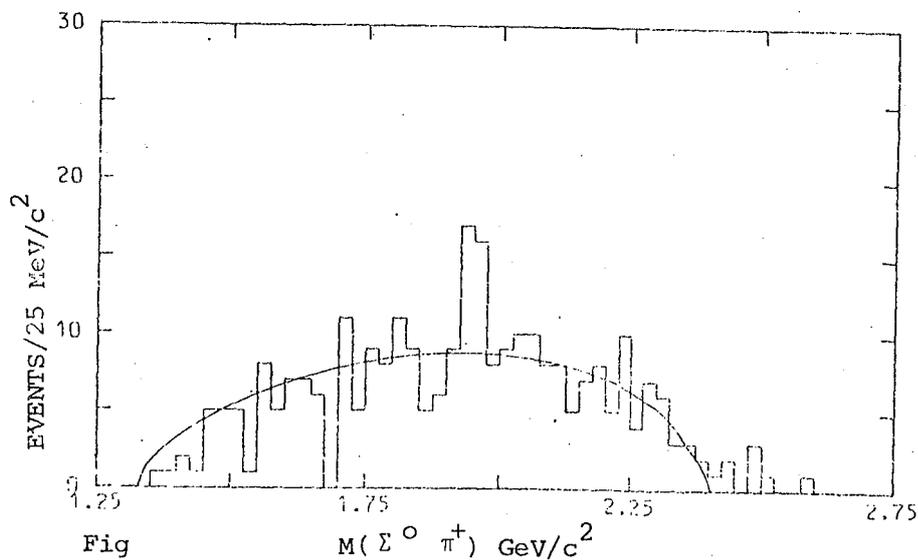Fig. IV.11 Dalitz plot for the channel $K^O \Sigma^+ \pi^+ n_s$

Fig. IV.12 The $K^O \pi^+$ effective mass distribution for the
channel $K^O \Sigma^O \pi^+ p_s$ fitted with a K*+(890) Breit-Wigner
expression and phase space.

Fig

M($\Sigma^O \pi^+$) GeV/c^2

Fig. IV.13 The $\Sigma^O \pi^+$ effective mass distribution for the channel $K^O \Sigma^O \pi^+$
The curve represents phase space plus reflection from K^{*+}(890)
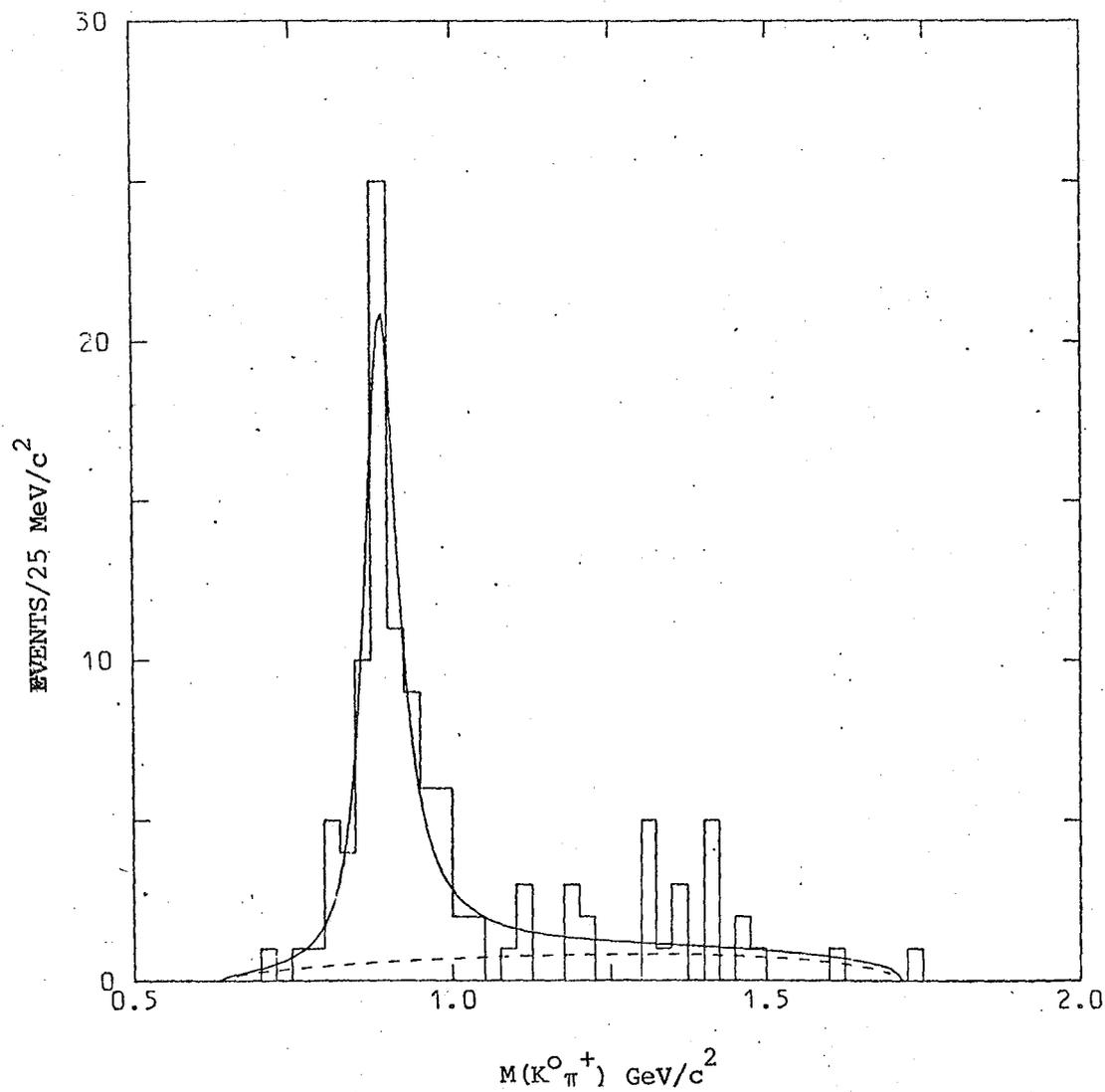normalised to the total number of events.

Fig. IV.14 The $K^O \pi^+$ effective mass distribution for the channel
$K^O \Sigma^+ \pi^+ n_s$ fitted with a K^{*+} (890) Breit-Wigner expression
and phase space.

IV.3.3.   The channels $K^+ K^-$ pp$_s$, $K^0 \bar{K}^0$ p p$_s$, $K^+ \bar{K}^0$ pn$_s$ and $K^+ \bar{K}^0$np$_s$

The Dalitz plots of $M^2(\bar{K}N)$ versus $M^2(K\bar{K})$ are shown for each channel

in figures IV.15, IV.16, IV.17 and IV.18 respectively. For the $K^0 \bar{K}^0$

final state there is no means of distinguishing between K^0 and $\bar{K}^0$.

However figure IV.21 shows that there is no evidence for resonance pro-

duction in K^0p or $\bar{K}^0$p (both combinations have been plotted), so that the

effective mass distributions of either V^0 combined with the proton

should be essentially the same (i.e. phase space plus reflections). The

channel $K^+ K^-$ pp$_s$ has already been studied in an earlier paper on f^0

branching ratios (ref. IV.7). However it is included in the present

work to deal with interference effects between f^0 and A_2^0 in $(K^0 \bar{K}^0)$. The

ambiguities had been resolved in a similar way to that given in

chapter II by rejecting those events which have a chi-squared probability

less than 0.001%or which are ambiguous with the $\pi^+ \pi^-$ pp$_s$ channel. The

method which has been adopted to deal with the interference is similar

to that of Biswas et al. (ref. IV.8). The resonant signal in $(K^+ K^-)$ is

parameterised in the form

$$\frac{dN}{dM} \sim |f|^2 + |A_2|^2 + 2\, \alpha\, |f| (A_2) \cos\, (\Theta_f - \Theta_A - \phi)$$

where f is the f^0 amplitude,

A_2 is the A_2^0 amplitude,

Θ_f is the f^0 phase,

Θ_A is the A_2^0 phase,

ϕ is the relative $f^0 - A_2^0$ phase,

and α is a coherence factor.

/

$E_{CM} = 2.73, 2.90, 3.06$ GeV

Fig. IV.15 Dalitz plot for the channel $K^+ K^- pp_s$.
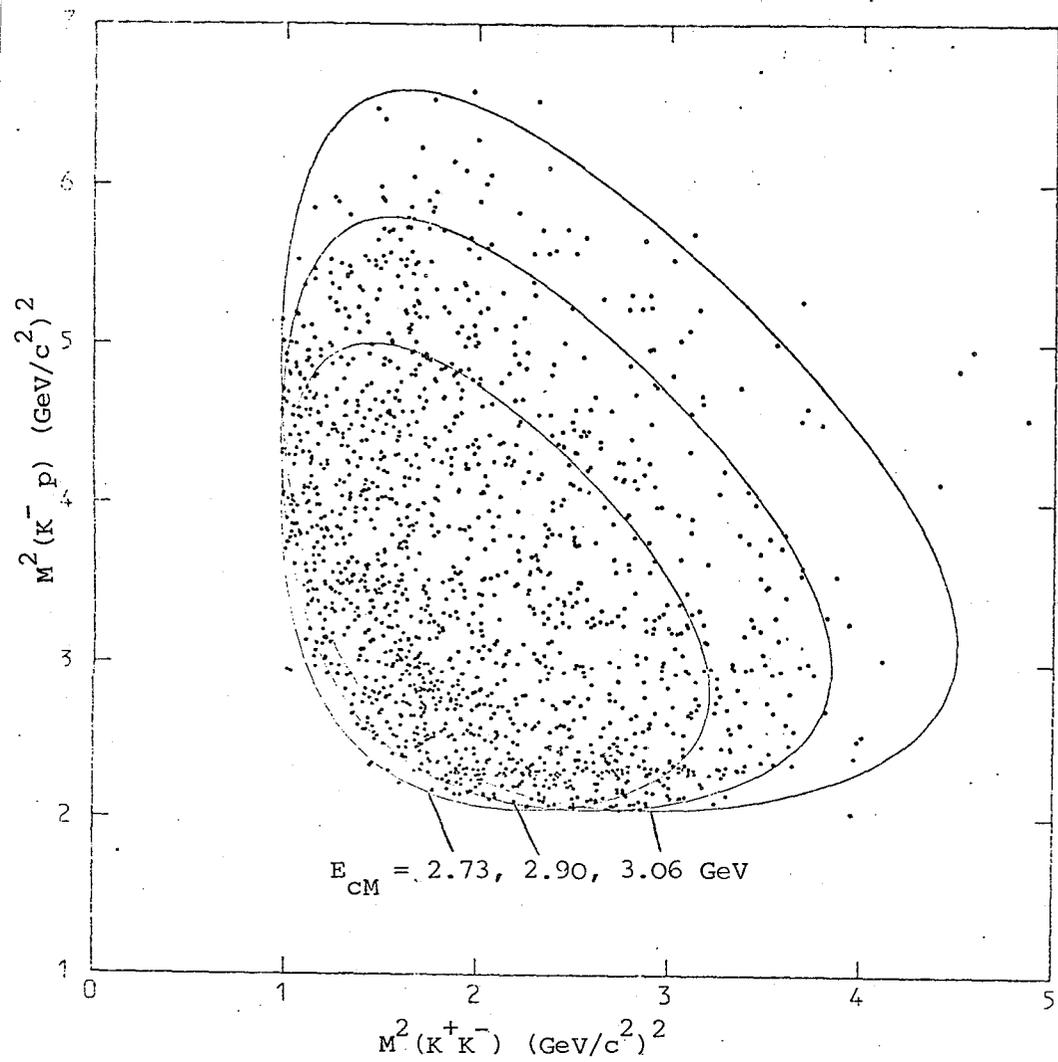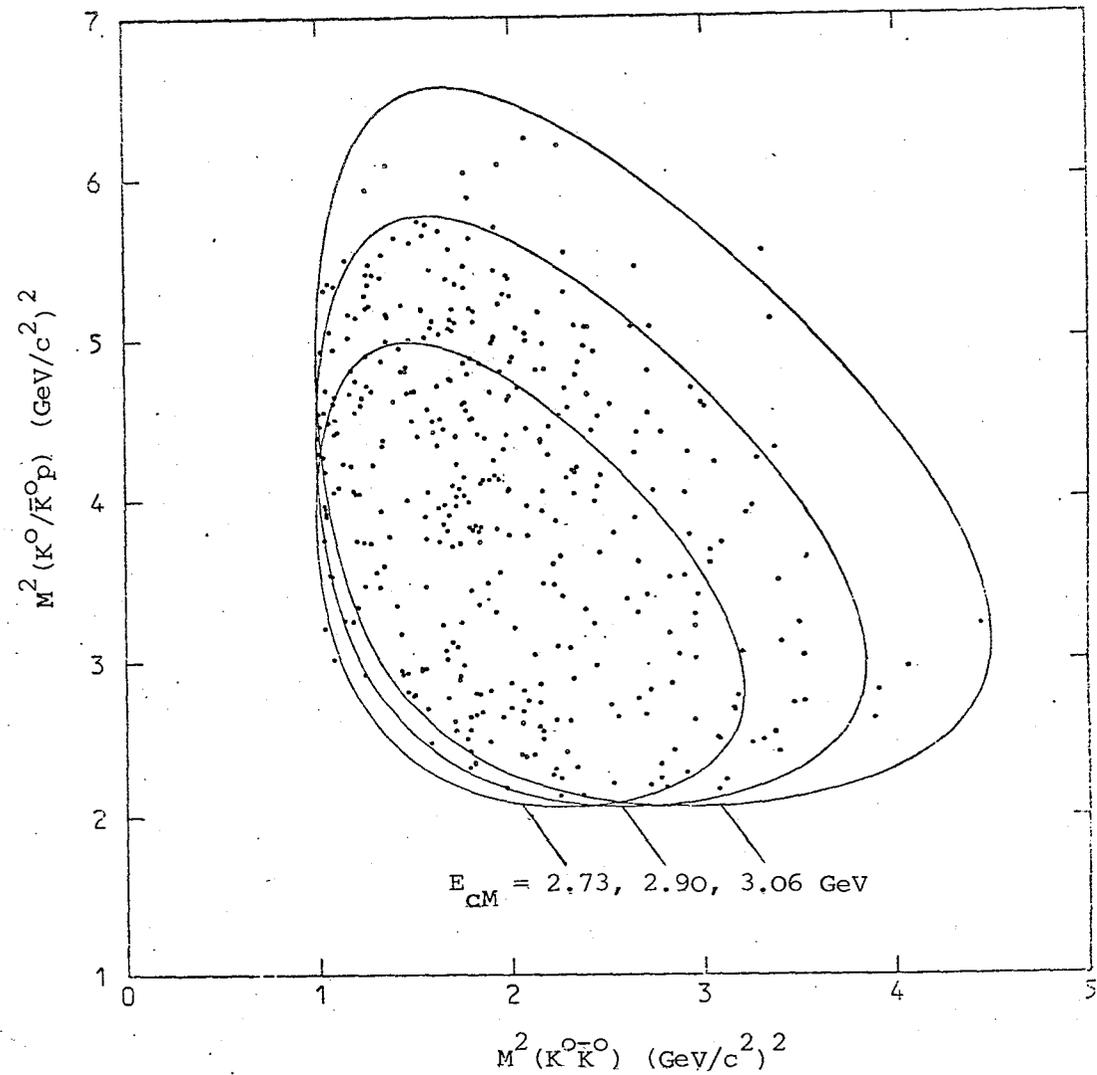

$E_{CM} = 2.73, 2.90, 3.06$ GeV

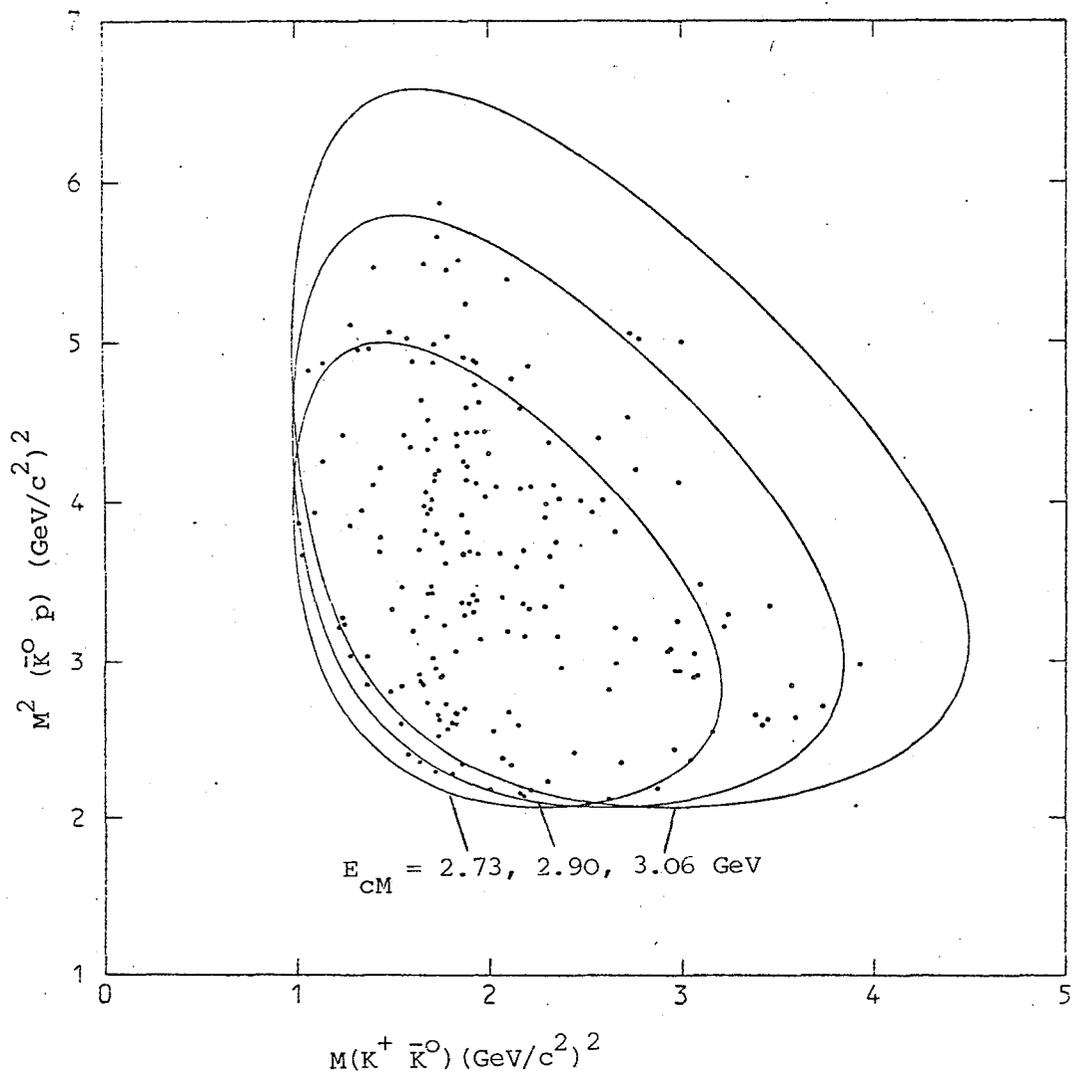Fig. IV.16 Dalitz plot for the channel $K^o \bar{K}^o pp_s$

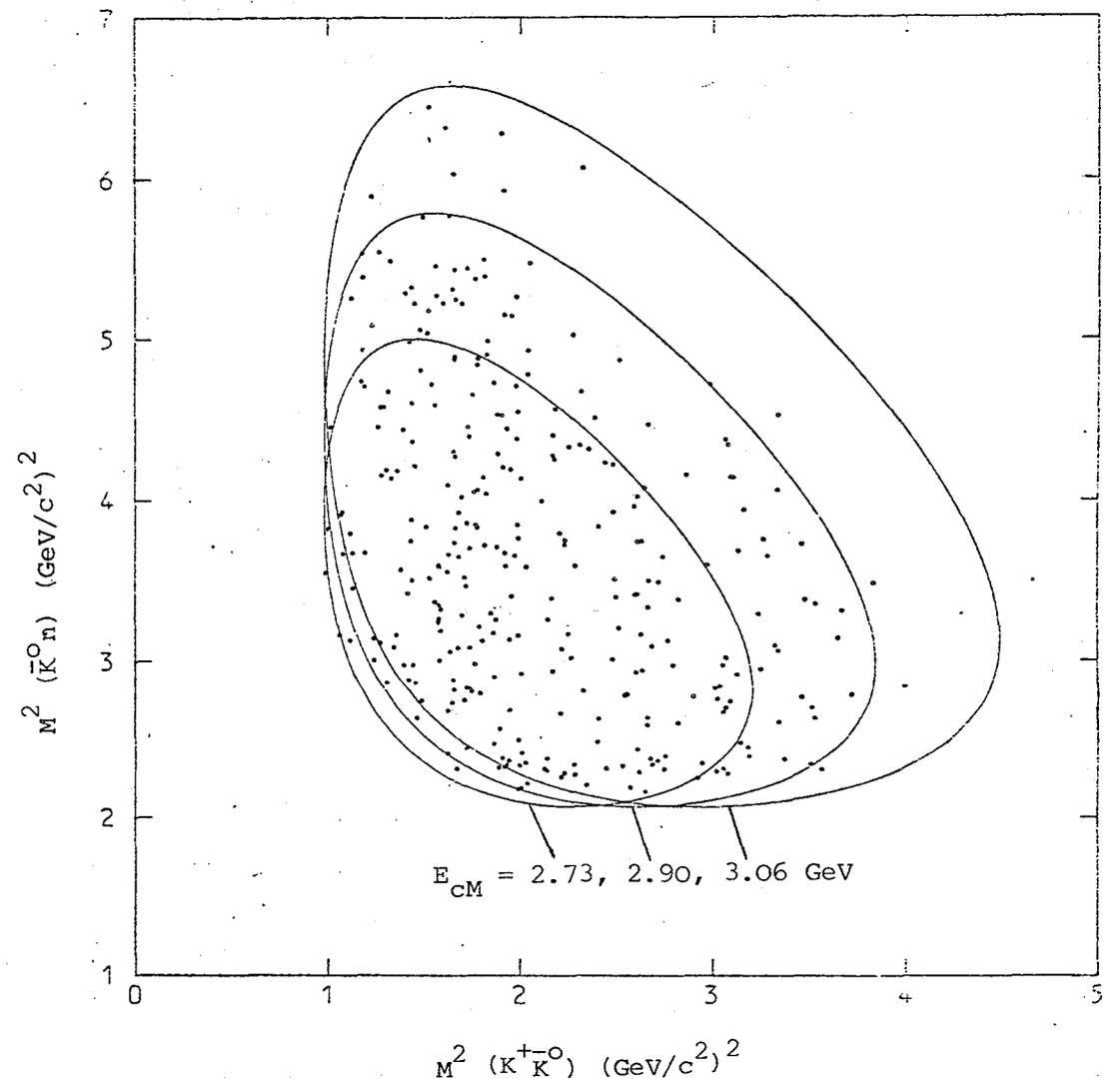Fig. IV.17 Dalitz plot for the channel $K^+\bar{K}^0 pn_s$

Fig. IV.18 Dalitz plot for the channel $K^+\bar{K}^0 np_s$
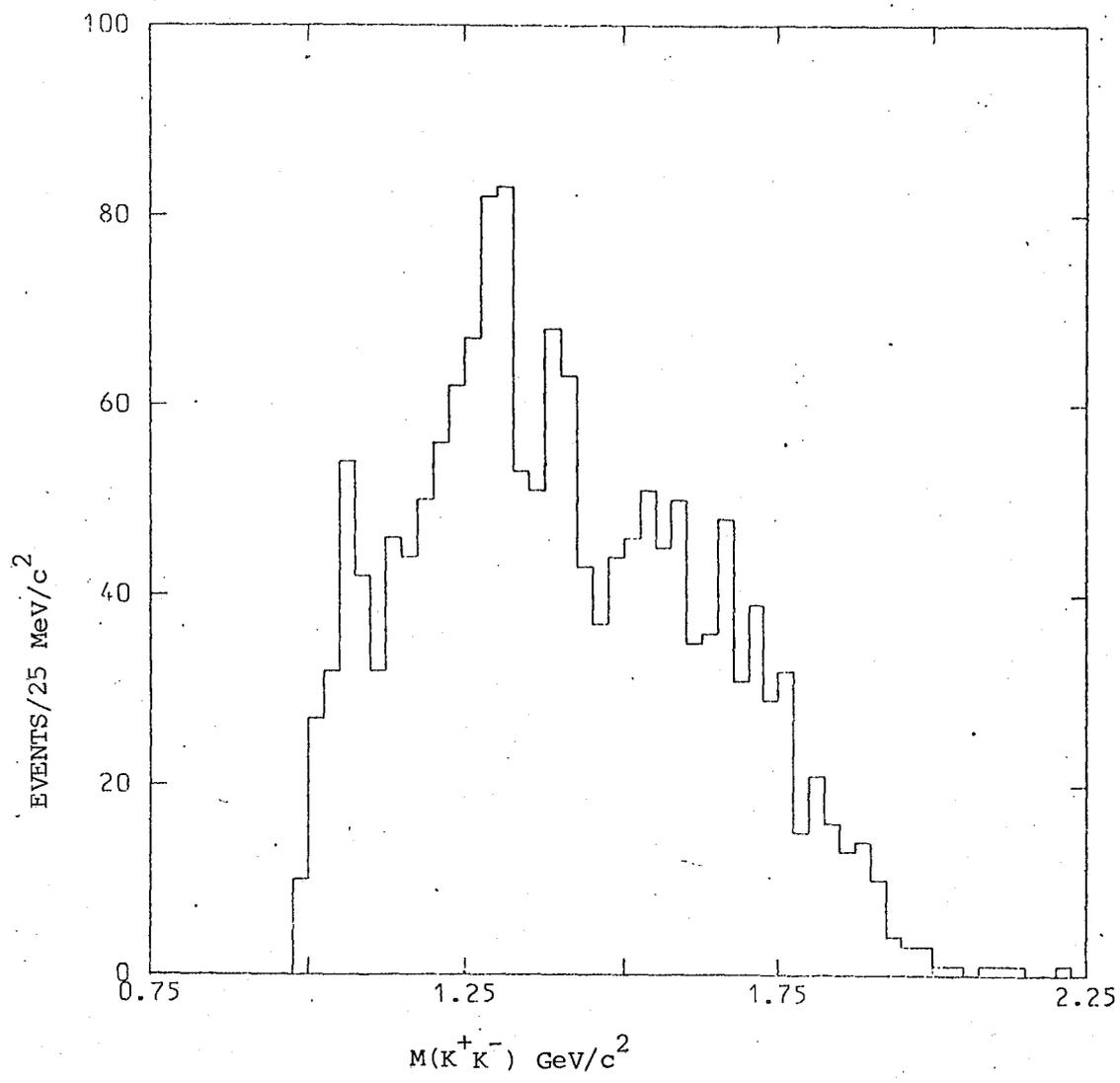
Fig. IV.19 (a) The $K^+ K^-$ effective mass distribution
for the channel $K^+ K^- p p_s$
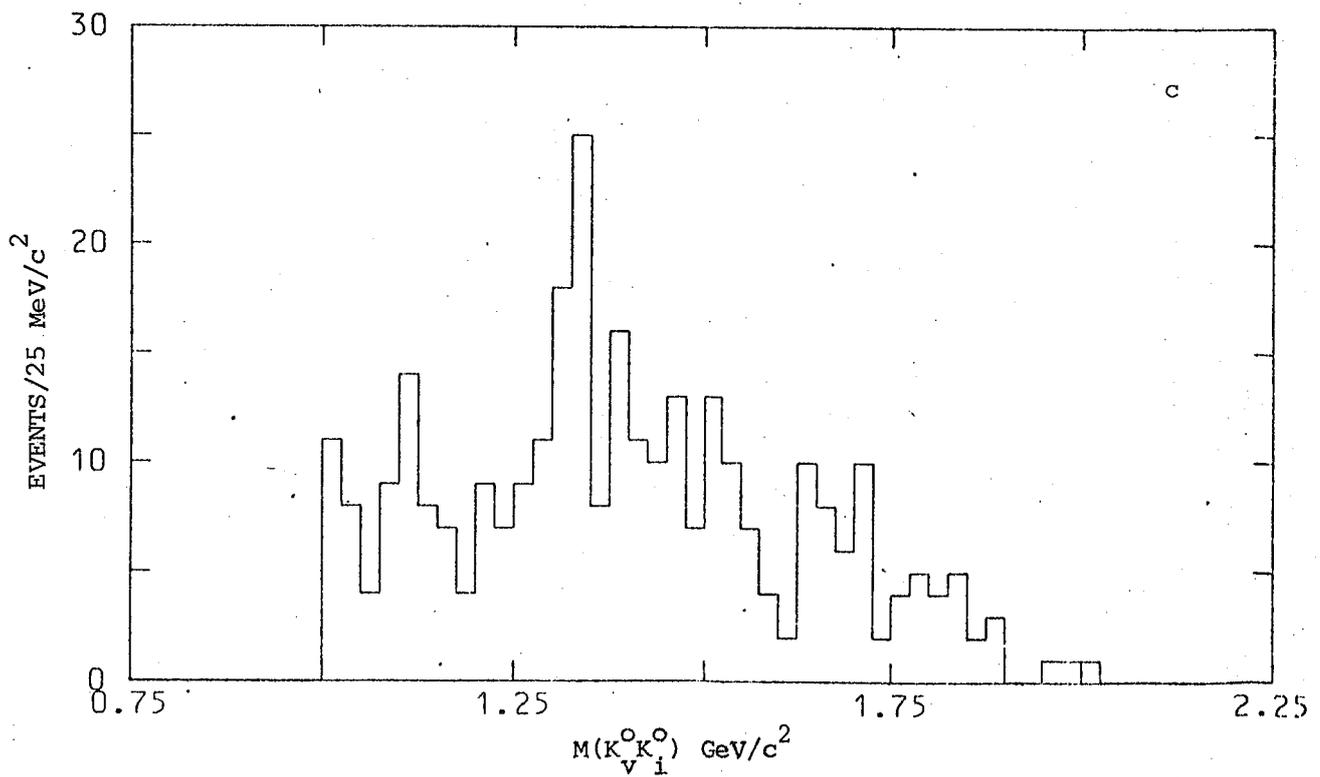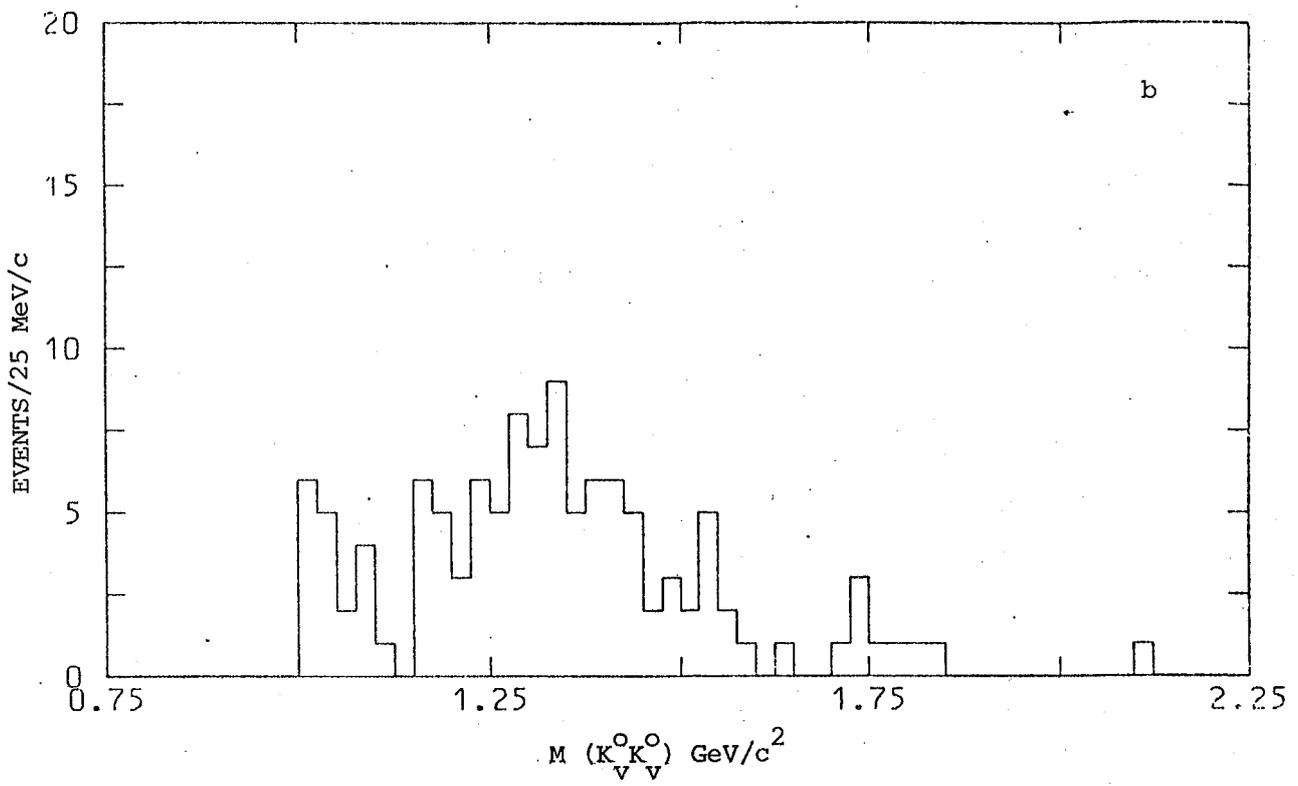
Fig. IV.19 (b) The $K_v^0 K_v^0$ and (c) the $K_v^0 K_i^0$ effective mass distributions for the channel $K^0 \bar{K}^0 pp_s$.
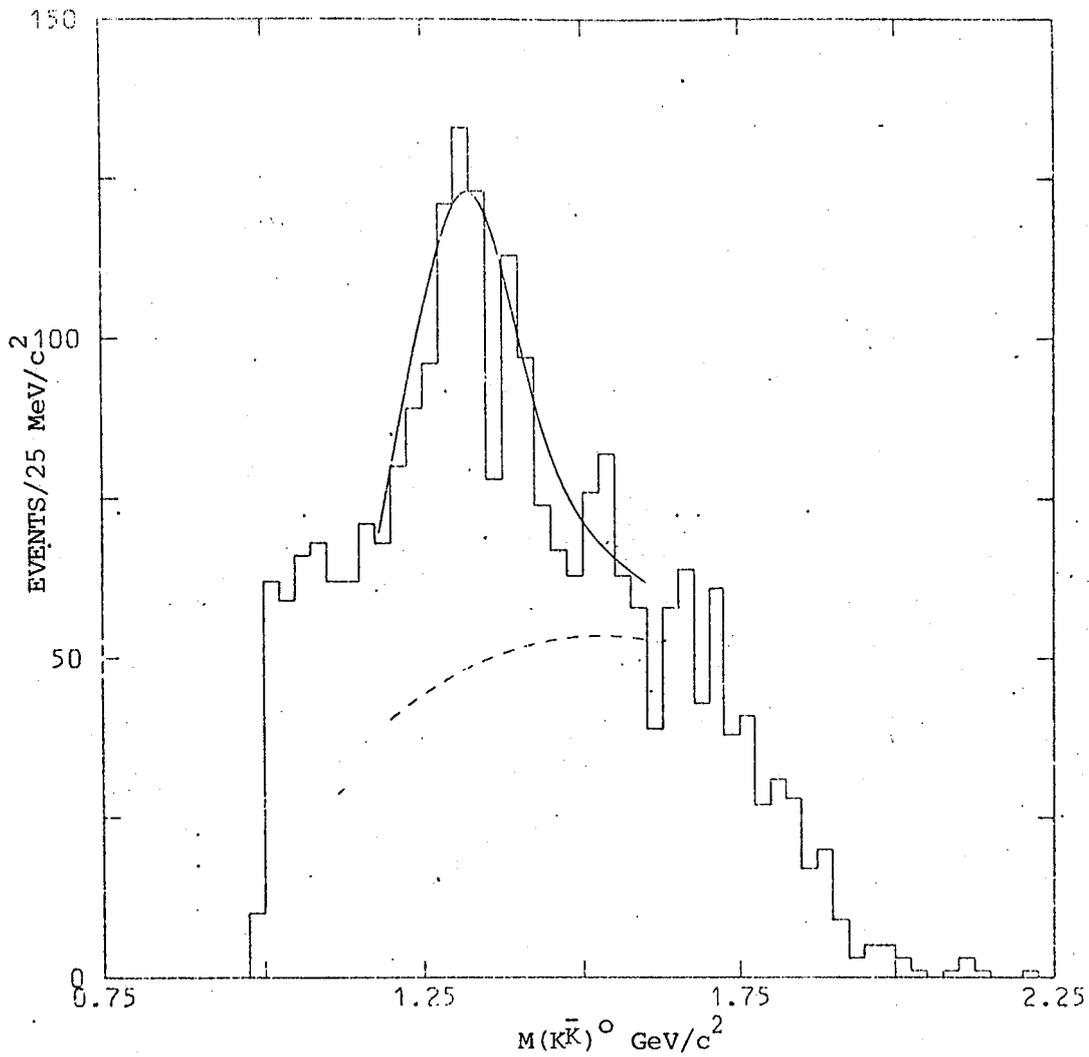
Fig. IV.20 The combined $(K\bar{K})^{0}$ effective mass distribution for the $(K\bar{K})^{0} pp_{s}$ find states fitted with f^{0} and A_{2}^{0} Breit-Wigner expressions and phase space.

Fig. IV.21 The $\bar{K}/K^{0}p$ effective mass distribution for the channel $K^{0}\bar{K}^{0} pp_{s}$ The curve represents phase space normalised to the total number of events.
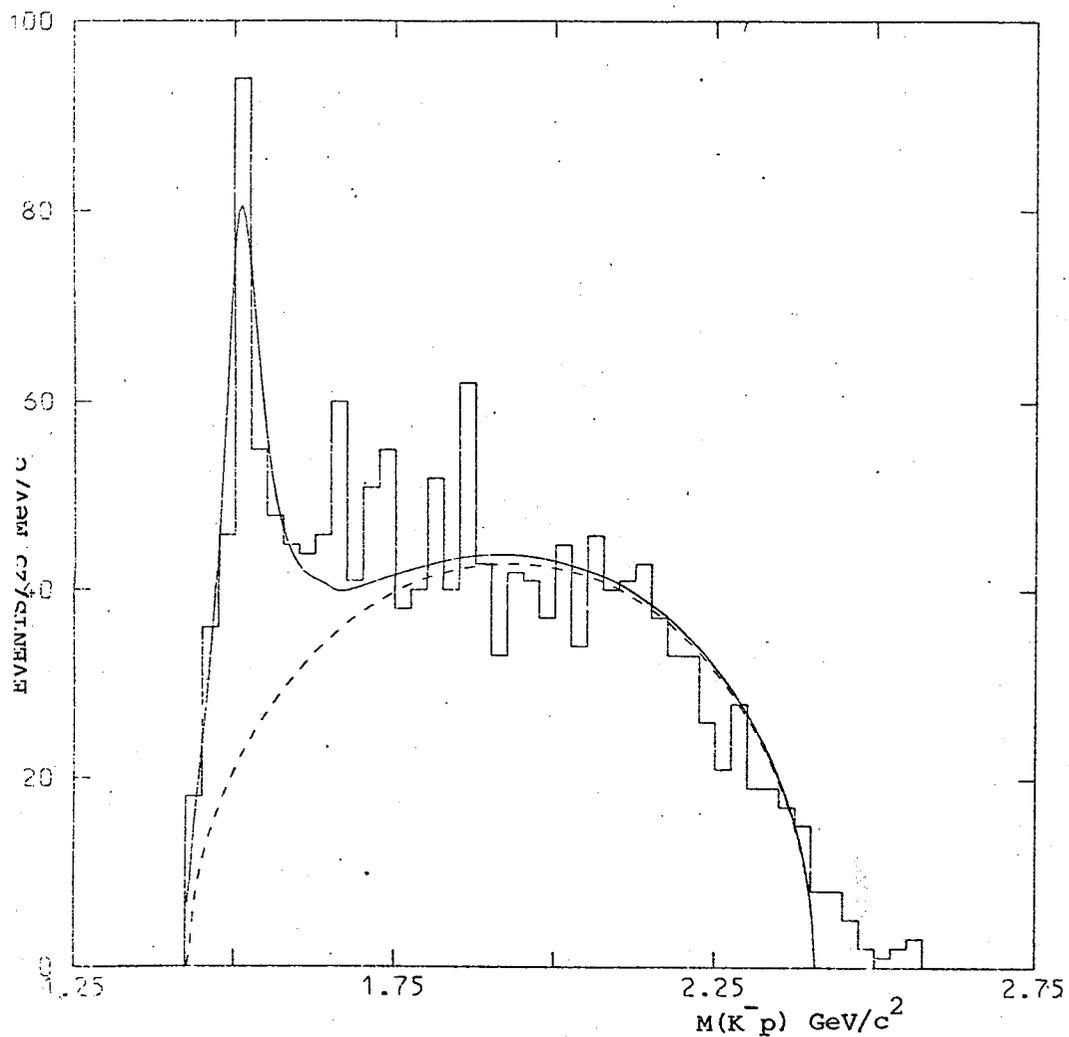
Fig. IV.22 The K^-p effective mass distribution for the channel $K^+K^-pp_s$ fitted with a $\Lambda^0(1520)$ Breit-Wigner expression and phase space.
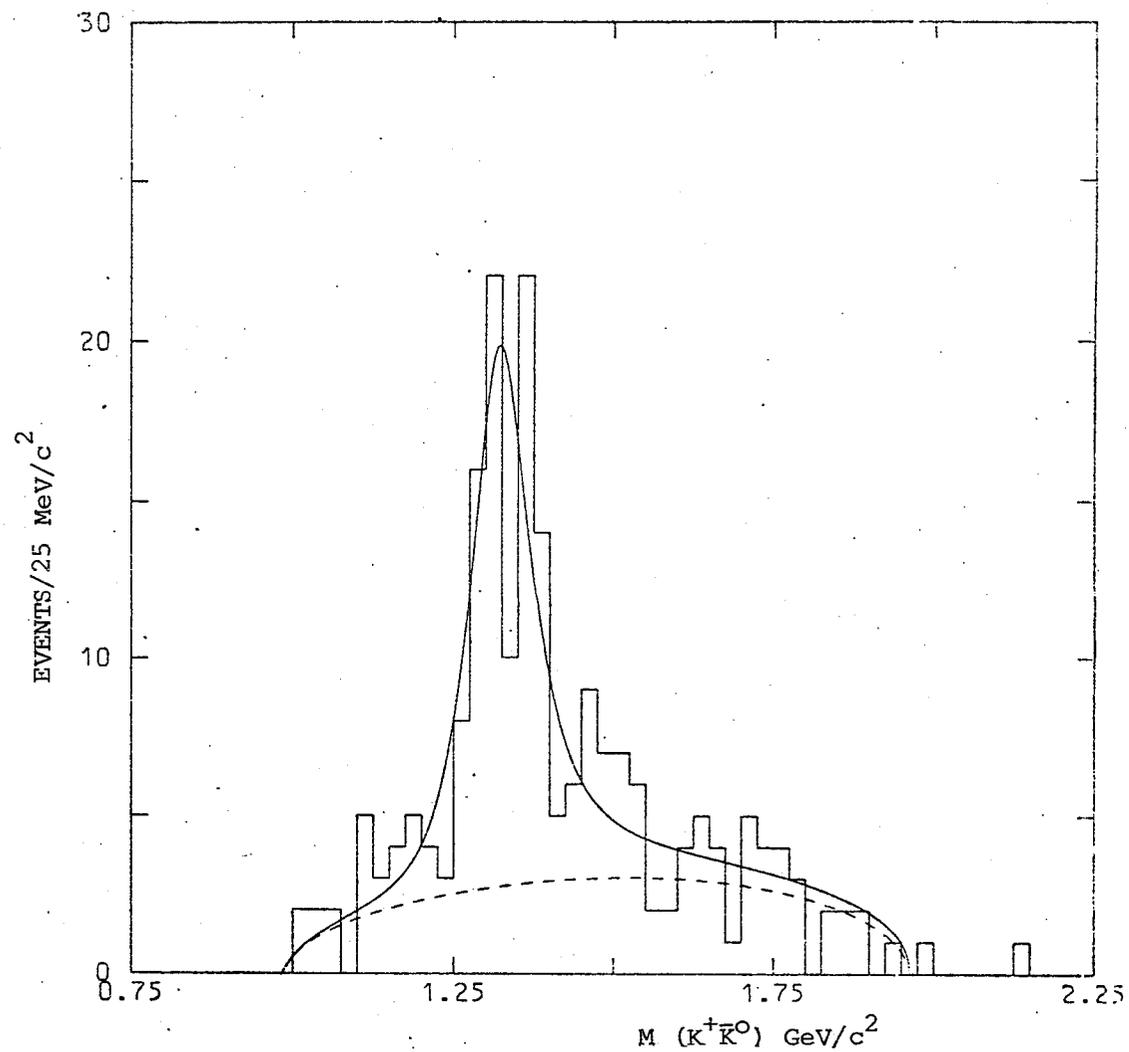
Fig. IV.23 The $K^+\bar{K}^0$ effective mass distribution for the channel $K^+\bar{K}^0 p n_s$ fitted with an A_2^+ Briet-Wigner expression and phase space.

Fig. IV.24 The $K^+\bar{K}^O$ effective mass distribution
for the channel $K^+\bar{K}^O$ n p_s, fitted
with an A_2^+ Breit-Wigner expression and
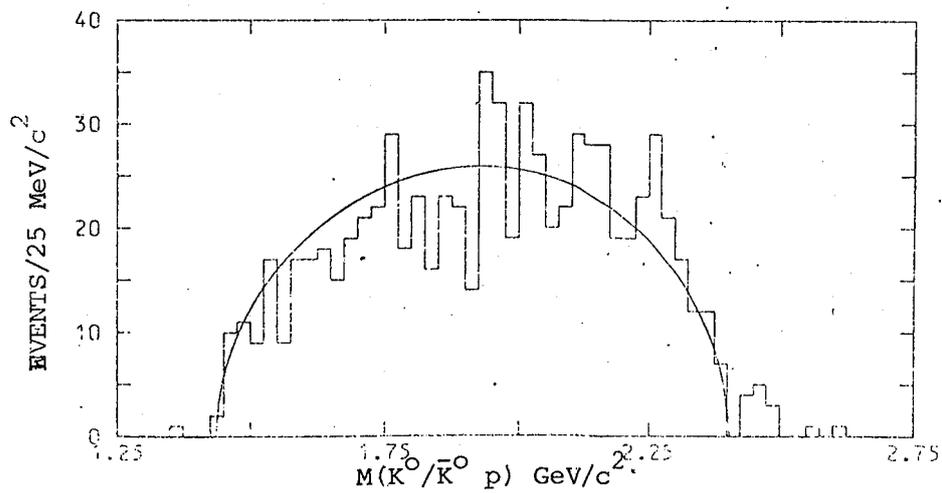and phase space plus reflection from $\Lambda^O(1520)$
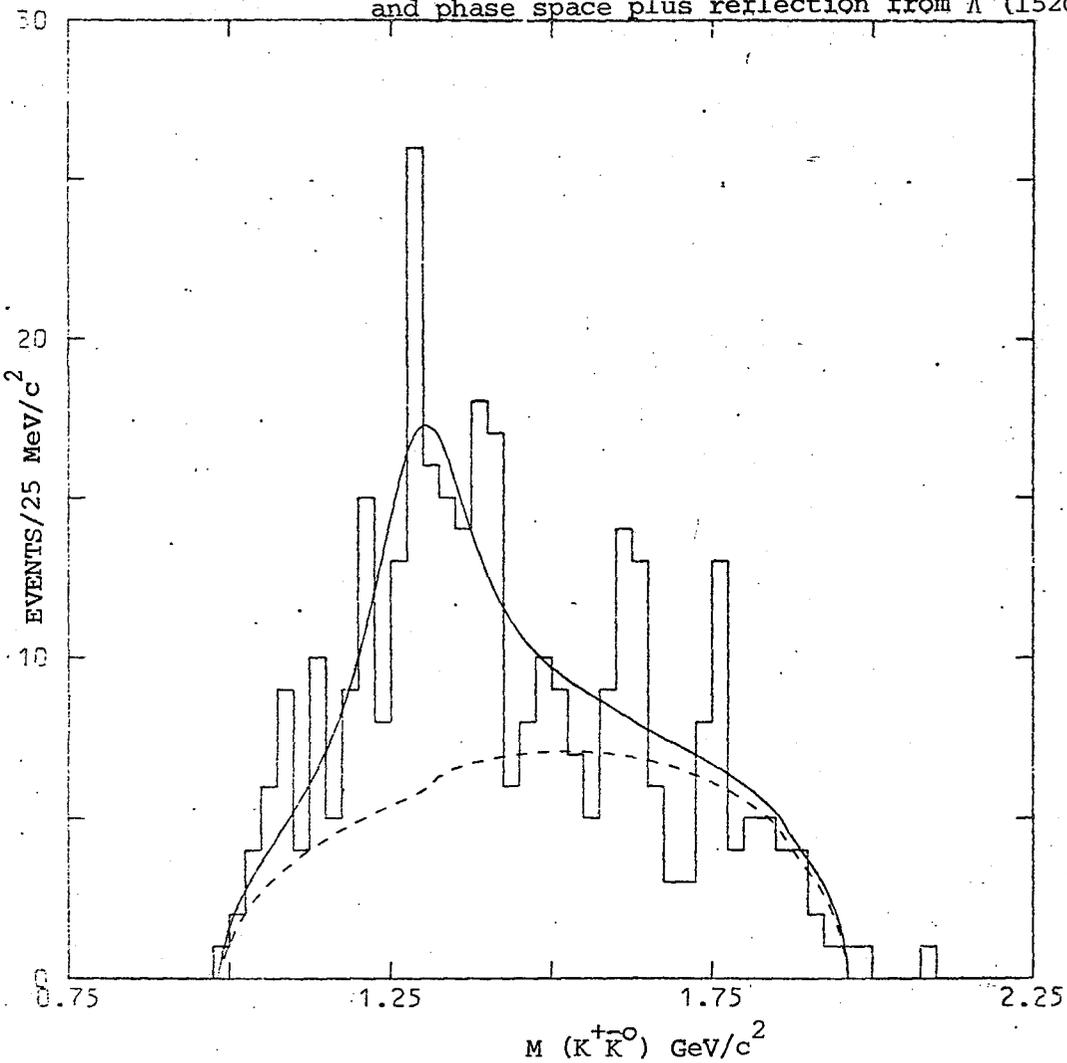
Fig. IV.25 The $\bar{K}^O$ n effective mass distribution for the
channel $K^+\bar{K}^O$ n p_s. The curve represents phase
space plus reflection from A_2^+ normalised to the
events above 1.575 GeV/c^2.

The hatched area corresponds to events with
$M(K^+\bar{K}^O) > 1.41$ GeV/c^2.
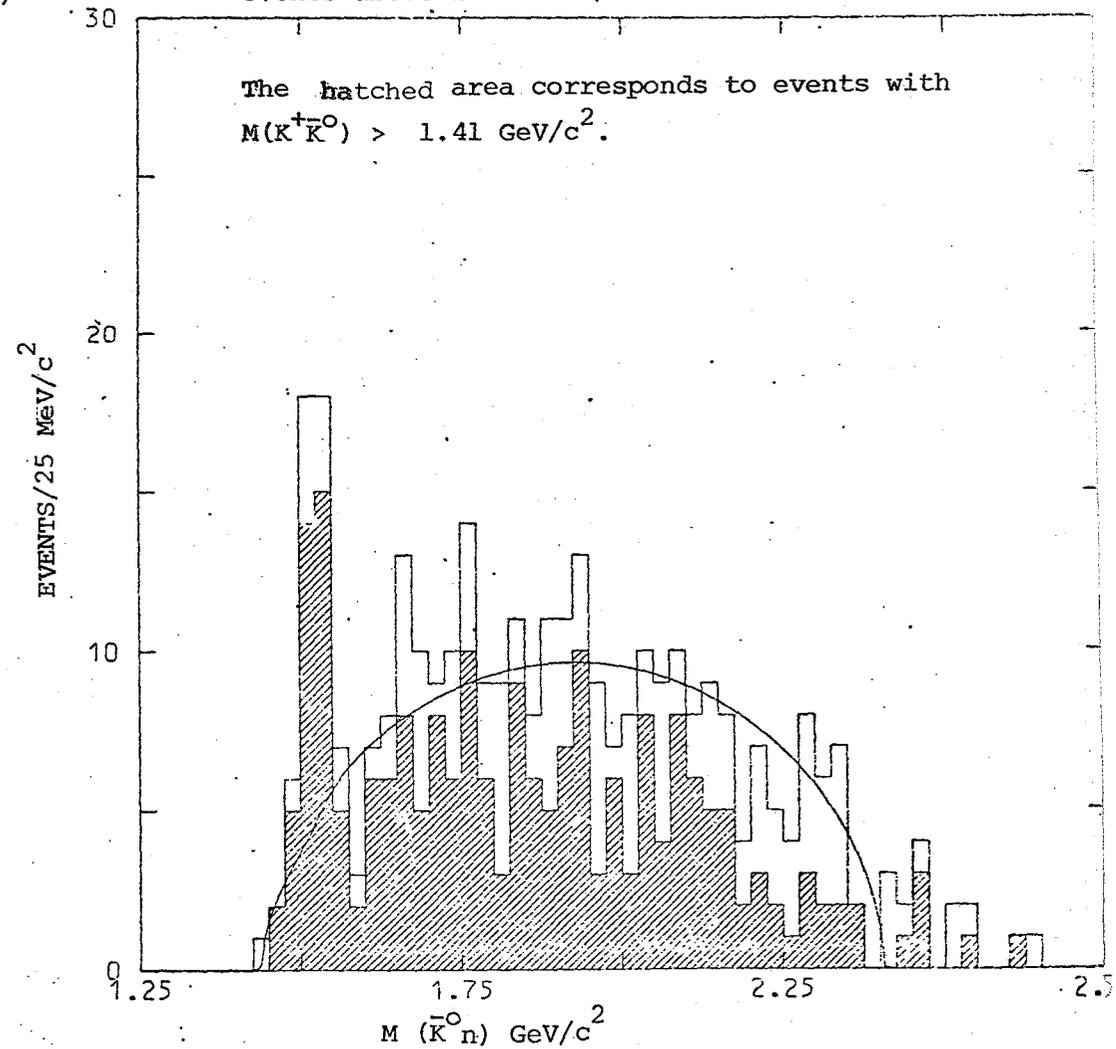
The interference term for the $K^O \bar{K}^O$ signal has opposite sign, so by simply adding the two spectra the interference may be cancelled. Before doing this however, the $K^O_V K^O_V$ and $K^O_V K^O_i$ must be scaled by factors A and B respectively to ensure that the $K^O \bar{K}^O$ spectrum corresponds to the same number of events per microbarn as the $K^+ K^-$ spectrum:

$$A \; \Delta N(K^O_V K^O_V) + B \; \Delta N \; (K^O_V K^O_i) = U \; (\Delta\sigma(K^O_S K^O_S) + \Delta\sigma(K^O_S K^O_L) + \Delta\sigma(K^O_L K^O_L)) \qquad (IV.6)$$

where U is the number of observed events per microbarn for $K^+ K^-$,

 ΔN, $\Delta\sigma$ are the number of observed events and the cross-section

        respectively for the mass interval, ΔM.

      Charge-parity invariance requires

$$\Delta\sigma(K^O_S K^O_S) = \Delta\sigma(K^O_L K^O_L).$$

In addition the cross-sections are related to the number of observed events by the following expressions:

$$\Delta\sigma(K^O_S K^O_S) = C_1 \; \Delta N \; (K^O_V K^O_V) + C_2 \; \Delta N \; (K^O_V K^O_i)$$

$$\Delta\sigma(K^O_S K^O_L) = C_3 \; \Delta N \; (K^O_V K^O_i)$$

where C_1, C_2, C_3 are the microbarn equivalents corrected for the losses discussed in chapter III. Here it has been assumed that the correction factors are independent of the effective mass, M (*). Combining these expressions with equation (IV.6) enables A and B to be obtained:

$$A = 2U \; C_1$$

$$B = 2U \; C_2 + UC_3$$

It is found that A = 2.16 and B = 2.04

(*) A study of the variation of M with respect to the angular distributions and decay lengths of charged and neutral V's has shown that this is a reasonable assumption.

The separate effective mass distributions for K^+K^-, $K^0_v K^0_v$ and $K^0_v K^0_i$ are shown in figures IV.19 (a), (b) and (c) respectively. After weighting the $K^0_v K^0_v$ and $K^0_v K^0_i$ spectra, it is found that $(K^0 \bar{K}^0)$ contains about $\frac{1}{3}$ of the resonant signal found in $(K^+ K^-)$. This implies strong f^0-A_2^0 interference, since for a pure resonance signal the ratio should be equal to unity. The combined spectrum is shown in figure IV.20 and has been fitted with two Breit-Wigner functions plus phase space. In the fitting process the widths and masses of the f^0 and A_2^0 have been constrained to the range of values given in ref. II.3. The resulting cross-sections are given in table IV.1. The cross-section for f^0 production determined from non-strange channels is

$$\sigma(f^0\, p \longrightarrow (\pi\pi)^0\, p) = (720 \overset{+}{-} 75)\ \mu b \qquad\qquad \text{(ref. I.18)}$$

which enables the branching ratio to be calculated:

$$\frac{f^0 \longrightarrow (K\bar{K})^0}{f^0 \longrightarrow (\pi\pi)^0} = 0.035 \overset{+}{-} 0.006$$

This agrees within errors with the accepted value of $(0.033 \overset{+}{-} 0.007)$ (ref. II.3).

The remaining resonances found in the $K\bar{K}$ NN_s channels are given in table IV.1. The cross-section for A_2^+ production in $K^+\bar{K}^0 n\, p_s$ may be compared with that found by J. D. Thomas (ref. IV.2) from non-strange channels:

$$\sigma(A^+ n \longrightarrow (\rho\pi)^+ n) = (400 \overset{+}{-} 60)\ \mu b$$

enabling the A_2^+ branching ratio to be calculated:

$$\frac{A_2^+ \longrightarrow K^+\bar{K}^0}{A_2^+ \longrightarrow (\rho\pi)^+} = 0.063 \overset{+}{-} 0.012$$

This is in agreement with the accepted value of $(0.066 \overset{+}{-} 0.007)$ (ref. II.3)

IV.3.4   The channels $K^+ \Lambda^0 \pi^+ \pi^- p_s$, $K^0 \Lambda^0 \pi^+ \pi^0 p_s$ and $K^0 \Lambda^0 \pi^+ \pi^+ n_s$
_____

All three channels exhibit strong K^* (890) and Σ (1385) production

in various ($K\pi$) and ($\Lambda\pi$) combinations. (see table IV.1). Figures IV.26,

IV.27 and IV.28 respectively show the Goldhaber plots of $M(\Lambda\pi)$ versus

$M(K\pi)$. In each case there is a clear overlap in the K^* (890) Σ (1385)

region. By using the "slice" technique (ref. IV.9) it is possible to

estimate the number of events which include the production of both

resonances together (associated production). Obviously this can only be

done in an overall way rather than on an event-by-event basis (c.f.

section IV.2.1). The $M(\Lambda\pi)$ axis of the Goldhaber plot is divided into

intervals of width 100 MeV/c^2. For each interval the amount of K^* (890)

production is estimated by method B (see section IV.2.2). The Σ (1385)

signal in each interval may be estimated by using the fitted Breit-Wigner

function plus phase space which has already been used to determine the

total Σ (1385) production. Hence the amount of associated production may

be calculated. A similar procedure may be performed for intervals along

the $M(K\pi)$ axis. The amount of associated production in both cases is

found to be the same within errors. The results are given in table IV.1.

For the channel $K^+ \Lambda^0 \pi^+ \pi^- p_s$ the associated production of K^{*0} (890) and

Σ^+ (1385) is found to be negligible as expected, since this would involve

the exchange of an "exotic" meson or a baryon with charge +1 and strange-

ness -1 (c.f. $K^0 \Lambda^0 \pi^+ p_s$ - section IV.3.1). If events are selected within

the K^{*0} (890) mass band the Σ^+ (1385) signal is greatly reduced. (This corres-

ponds to the hatched histogram in figure IV.31). Figure IV.32(a) shows

a weak (sig $\simeq$ 2.5) enhancement in ($\pi^+ \pi^-$) near to the ρ^0 (773 MeV/c^2).

However this disappears on selecting events outside the K^{*0} (890) and

Σ^- (1385) mass bands (see hatched area), indicating that the enhancement

is possibly due to reflection effects from these resonances. Similarly
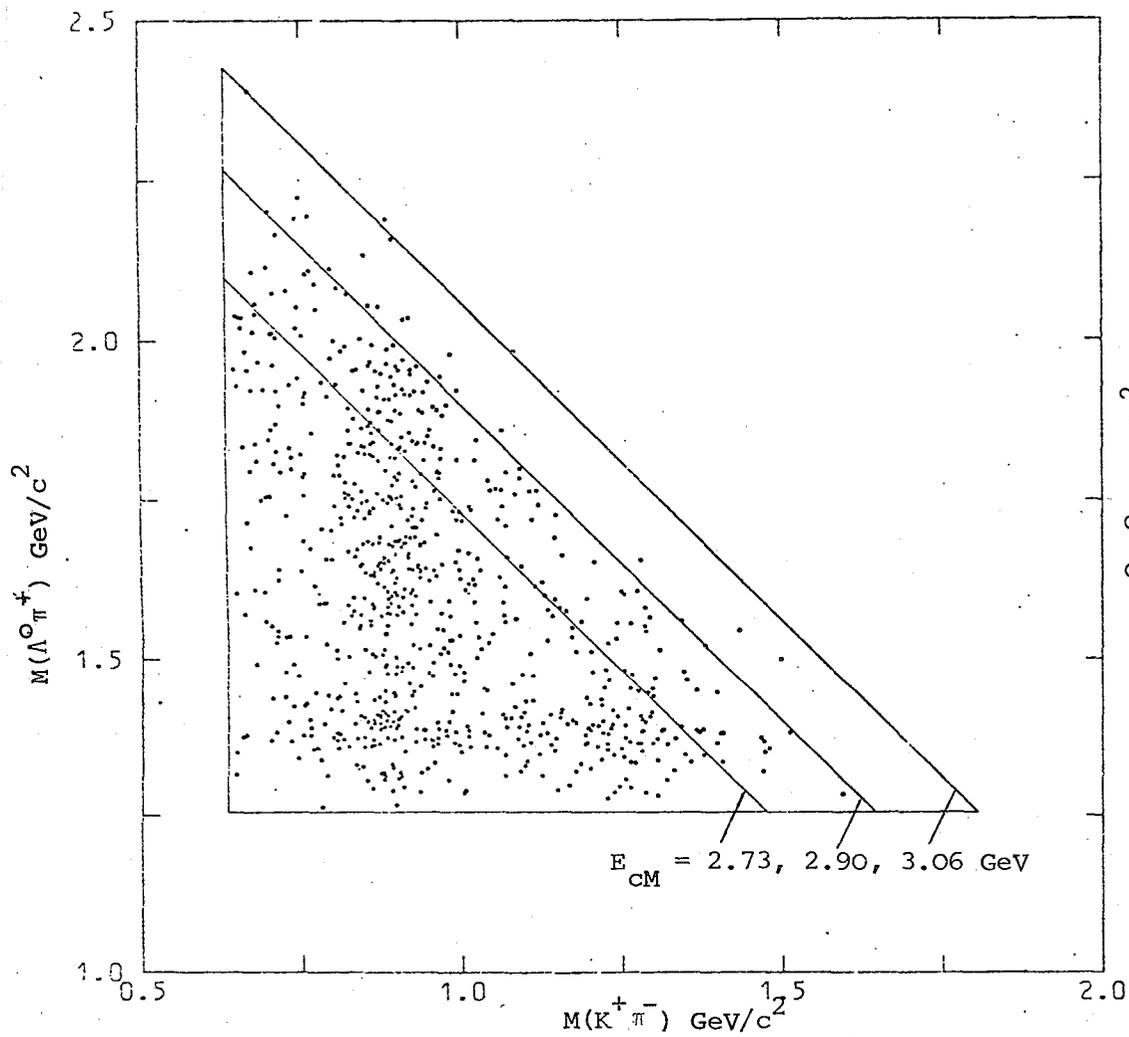
Fig. IV.26 Goldhaber plot for the channel $K^+\Lambda^0\pi^+\pi^-$ p_s.

Fig. 27. Goldhaber plot for the channel $K^0\Lambda^0\pi^+\pi^0$ p_s

In Fig. IV.26, the axes are $M(K^+\pi^-)$ GeV/c^2 (horizontal) and $M(\Lambda^0\pi^+)$ GeV/c^2 (vertical), with $E_{cM} = 2.73,\ 2.90,\ 3.06$ GeV.

In Fig. 27, the axes are $M(K^0\pi^+)$ GeV/c^2 (horizontal) and $M(\Lambda^0\pi^0)$ GeV/c^2 (vertical), with $E_{cM} = 2.73,\ 2.90,\ 3.06$ GeV.
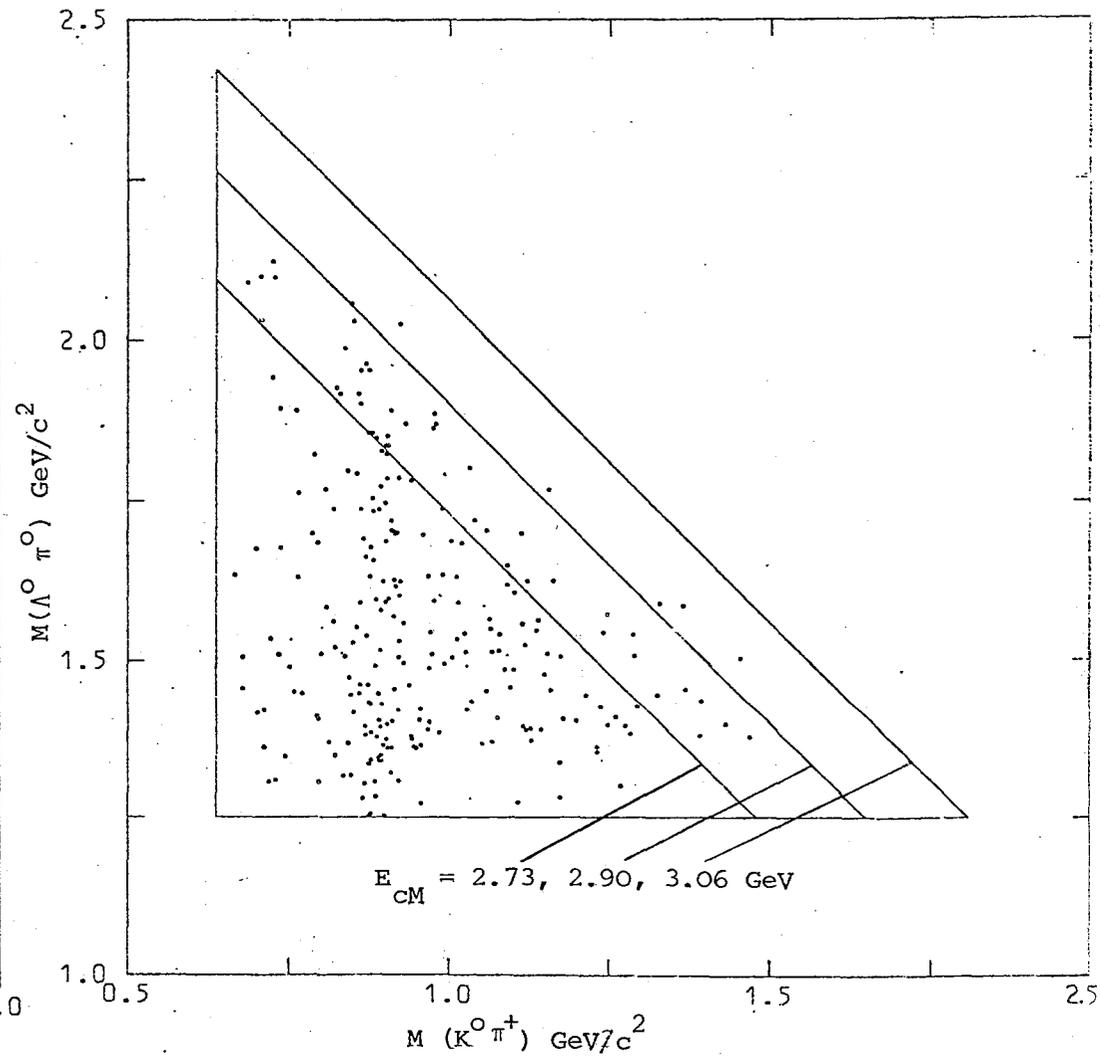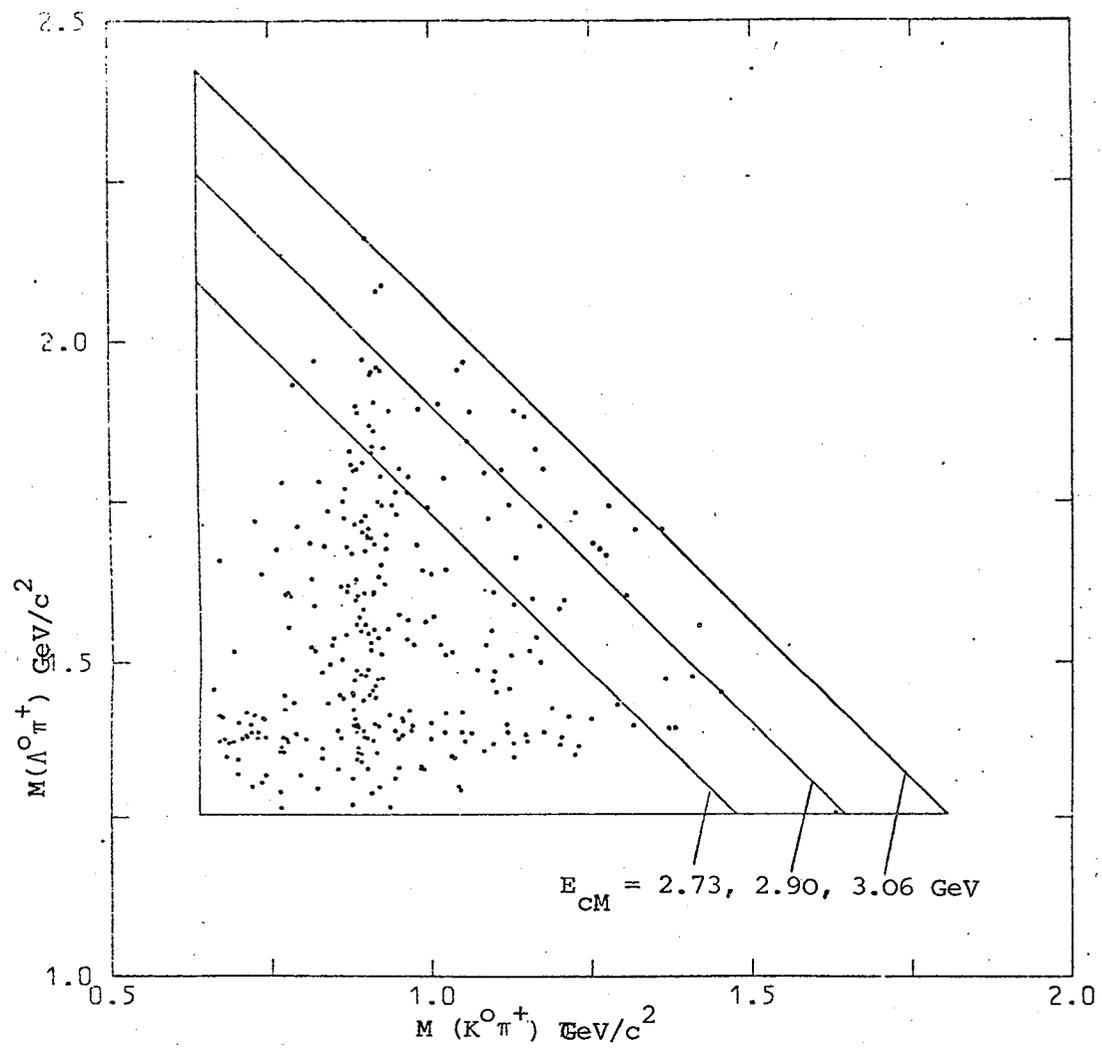
Fig. IV.28 Goldhaber plot for the channel
$K^0 \Lambda^0 \pi^+ \pi^+ n_s$

E_{cM} = 2.73, 2.90, 3.06 GeV
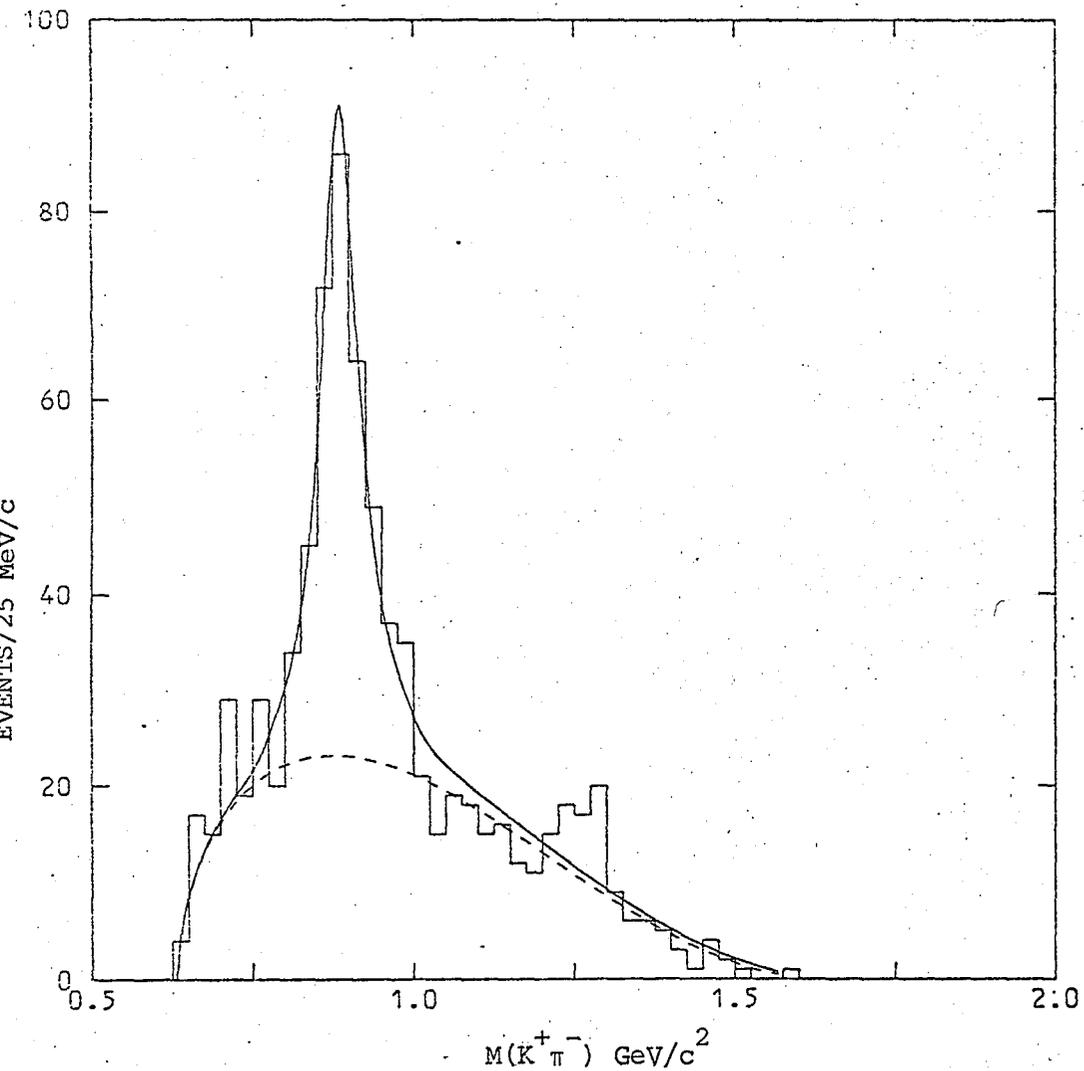
Fig. IV. 29 The $K^+\pi^-$ effective mass distribution for the
channel $K^+\Lambda^0\pi^+\pi^-$ p, fitted with a $K^{*0}(890)$

Fig. IV.30 The $\Lambda^0\pi^-$ effective mass distribution for the

Fig. IV.31 The $\Lambda^0 \pi^+$ effective mass distribution for the channel $K^+ \Lambda^0 \pi^+ \pi^- p_s$ fitted with a $\Sigma^+(1385)$ Breit-Wigner expression and phase space. The hatched area corresponds to those events within the $K^{*0}(890)$ mass band.

Fig. IV.32 (a) The $\pi^+\pi^-$ effective mass distribution for the channel $K^+\Lambda^0\pi^+\pi^-$ p_s. The curve represents phase space normalised to the total number of events. The hatched area corresponds to events outside the K^{*0} (890) and Σ^- (1385) mass bands.

Fig. IV.32 (b) The $\pi^+\pi^0$ effective mass distribution for the channel $K^0\Lambda^0\pi^+\pi^0$ p_s. The curve represents phase space normalised to the total number of events. The hatched area corresponds to events outside the K^{*+} (890) and Σ^0 (1385) mass bands.
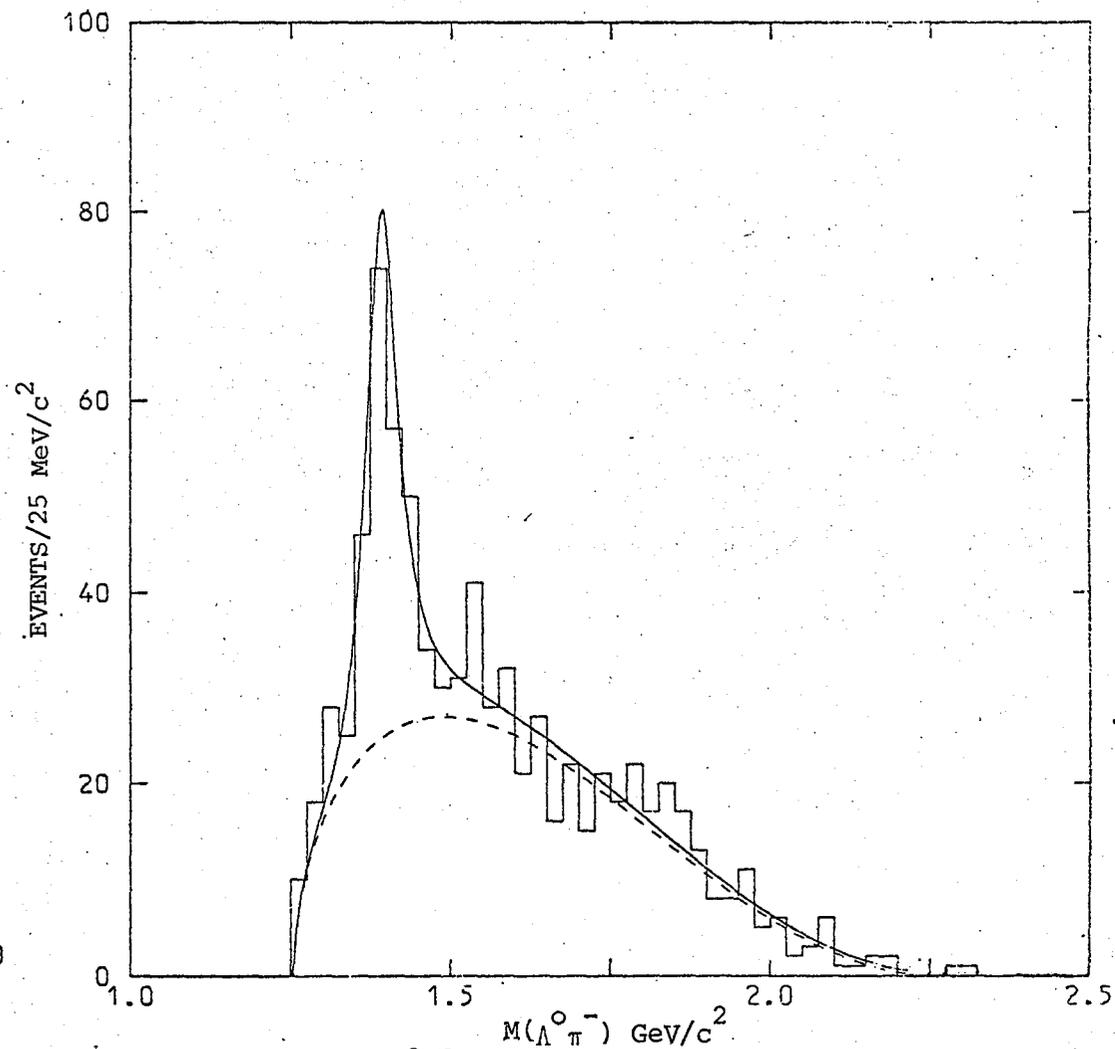
Fig. IV.33 The $K^O\pi^+$ effective mass distribution for the channel $K^O\Lambda^O\pi^+\pi^O$ p_s fitted with a $K^{*+}(890)$ Breit-Wigner expression and phase space.
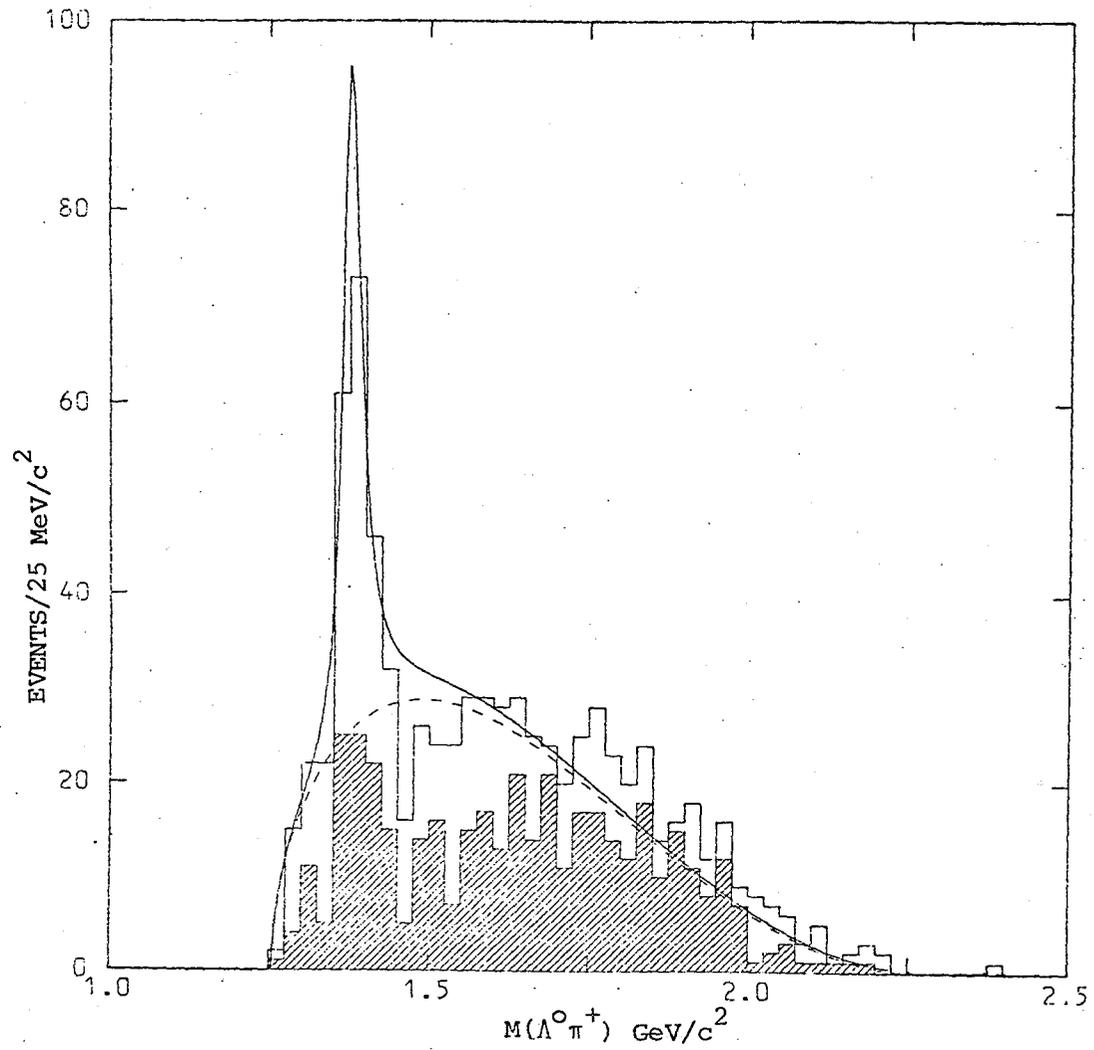
Fig. IV.34 The $\Lambda^O\pi^O$ effective mass distribution for the channel $K^O\Lambda^O\pi^+\pi^O$ p_s fitted with a $\Sigma^O(1385)$ Breit-Wigner expression and phase space. The $\Lambda^O(1520)$ mass band $(1.50$ GeV/c^2 < M$(\Lambda^O\pi^O)$ < 1.55 GeV/c$^2)$ has not been fitted and the curve extrapolated into this region.
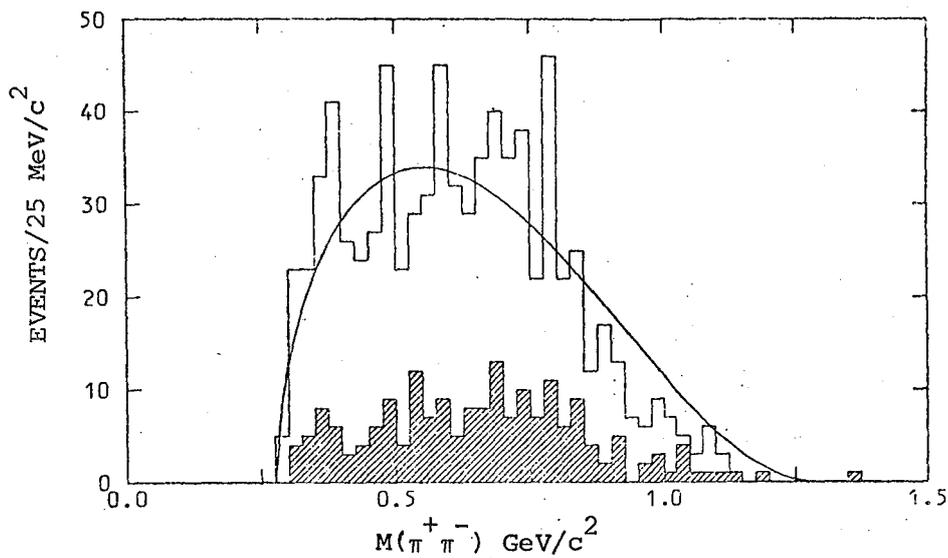
Fig. IV.35 The $K^O\pi^-$ effective mass distribution for the channel
$K^O\Lambda^O\pi^+\pi^O.p_s$ The curve represents phase .space
normalised to the total number of events outside the
K^{*O} (890) mass band.

Fig. IV.36 The $\Lambda^O\pi^+$ effective mass distribution for the channel
$K^O\Lambda^O\pi^+\pi^O p_s$. The curve represents phase space
normalised to the total number of events.

Fig. IV.37 The $K^+\pi^+\pi^-$ effective mass distribution for the channel
$K^+\Lambda^o\pi^+\pi^-$ p_s. The curve represents phase space normalised
to the total number of events. The hatched area corresponds
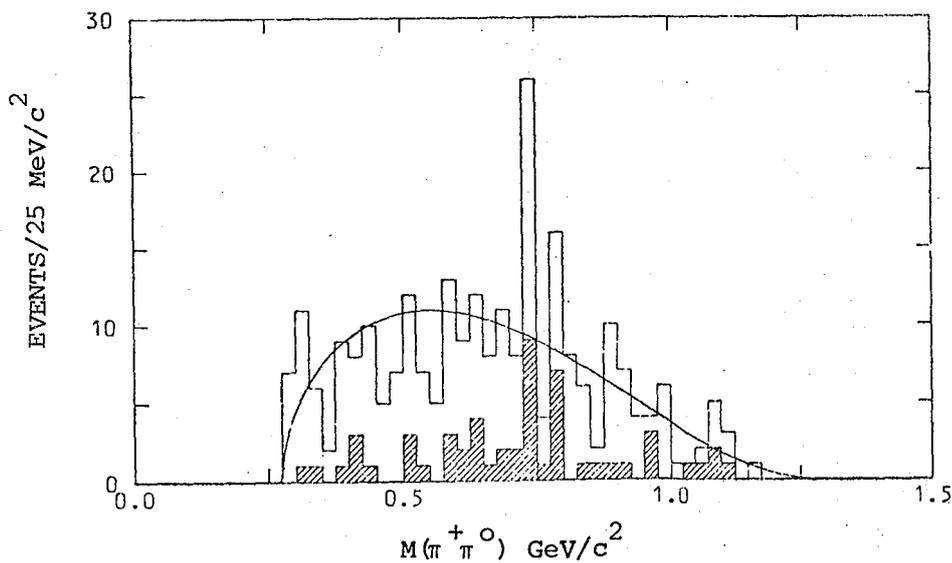to events outside the Σ^- (1385) mass band.

- $M(K^+\pi^+\pi^-)$ GeV/c^2

Fig. IV.38 The $K^o\pi^+\pi^o$ effective mass distribution for the channel
$K^+\Lambda^o\pi^+\pi^o$ p_s. The curve represents phase space normalised
to the total number of events. The hatched area corresponds
to events outside the Σ^o(1385) mass band.

$M(K^o\pi^+\pi^o)$ GeV/c^2

Fig. IV.39 The $K^0\pi^+$ effective mass distribution for the
channel $K^0\Lambda^0\pi^+\pi^+ n_s$ fitted with a $K^{*+}(890)$
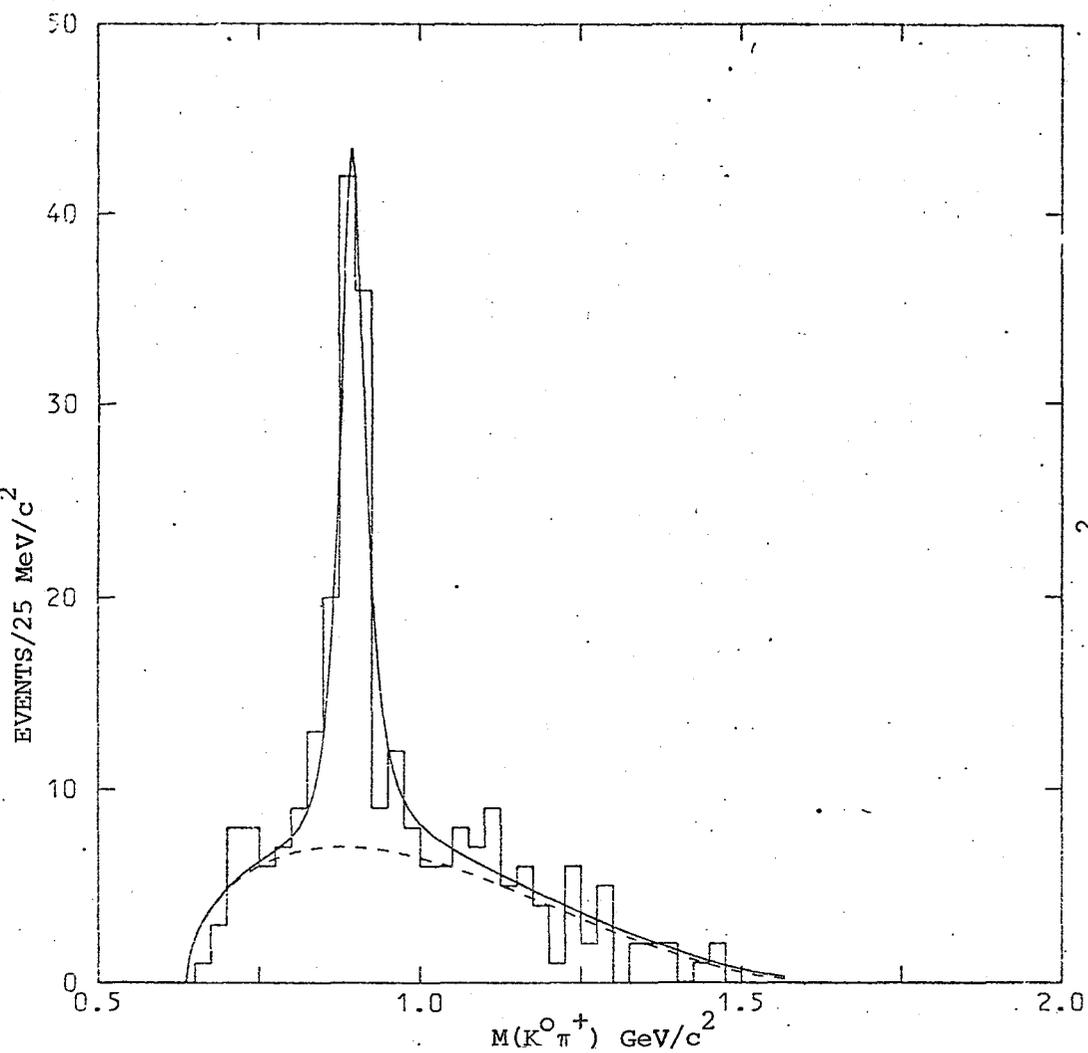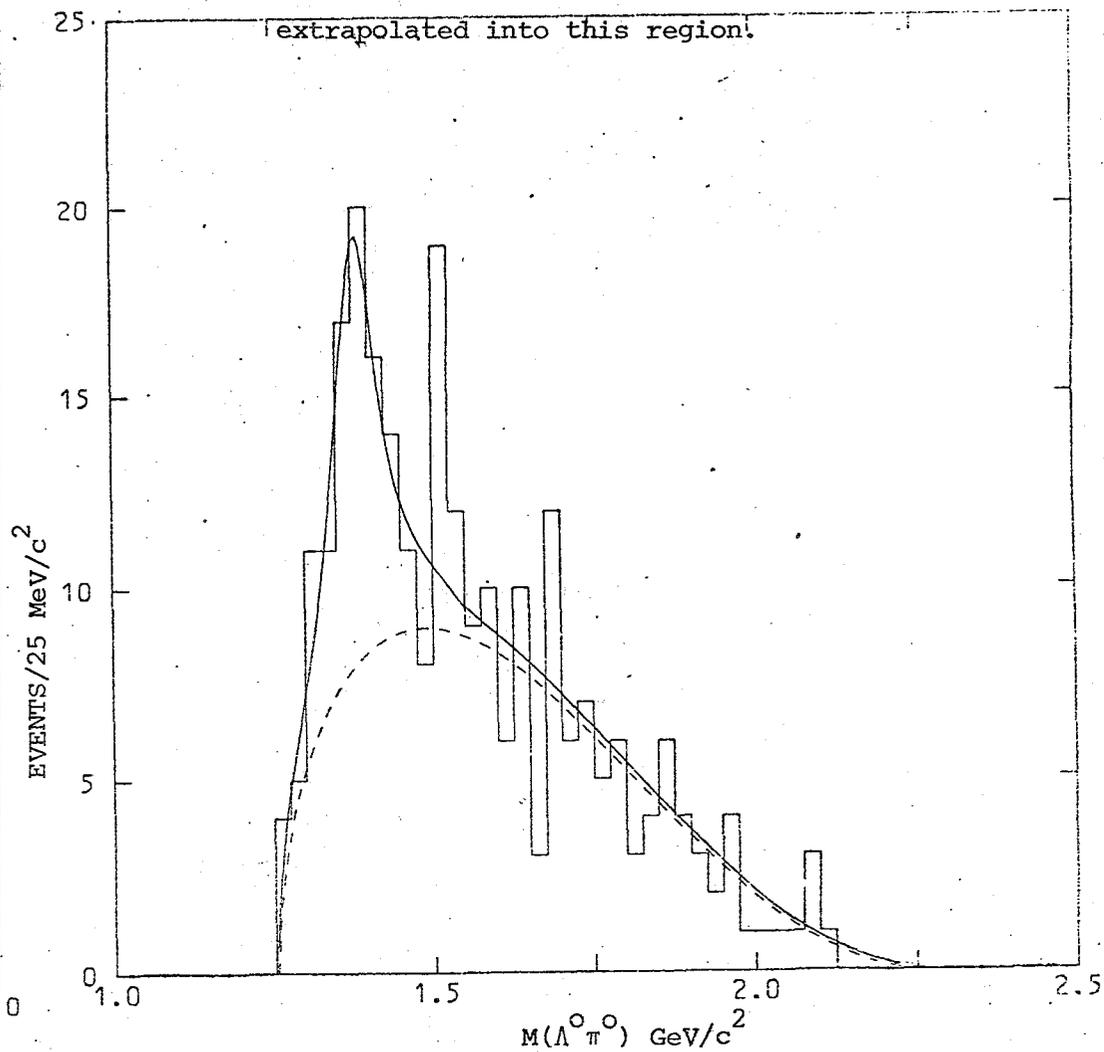Breit-Wigner expression and phase space.
Both $K^0\pi^+$ combinations have been plotted.
The hatched histogram is obtained by choosing
the π^+ which does not give a $\Lambda^0\pi^+$ effective
mass within the $\Sigma^0(1385)$ mass band

Fig. IV.40 The $\Lambda^0\pi^+$ effective mass distribution for the
channel $K^0\Lambda^0\pi^+\pi^+ n_s$ fitted with a $\Sigma^+(1385)$
Breit-Wigner expression and phase space.
Both $\Lambda^0\pi^+$ combinations have been plotted. The
hatched histogram is obtained by choosing the π
which does not give a $K^0\pi^+$ effective mass within
the $K^{*+}(890)$ mass band.
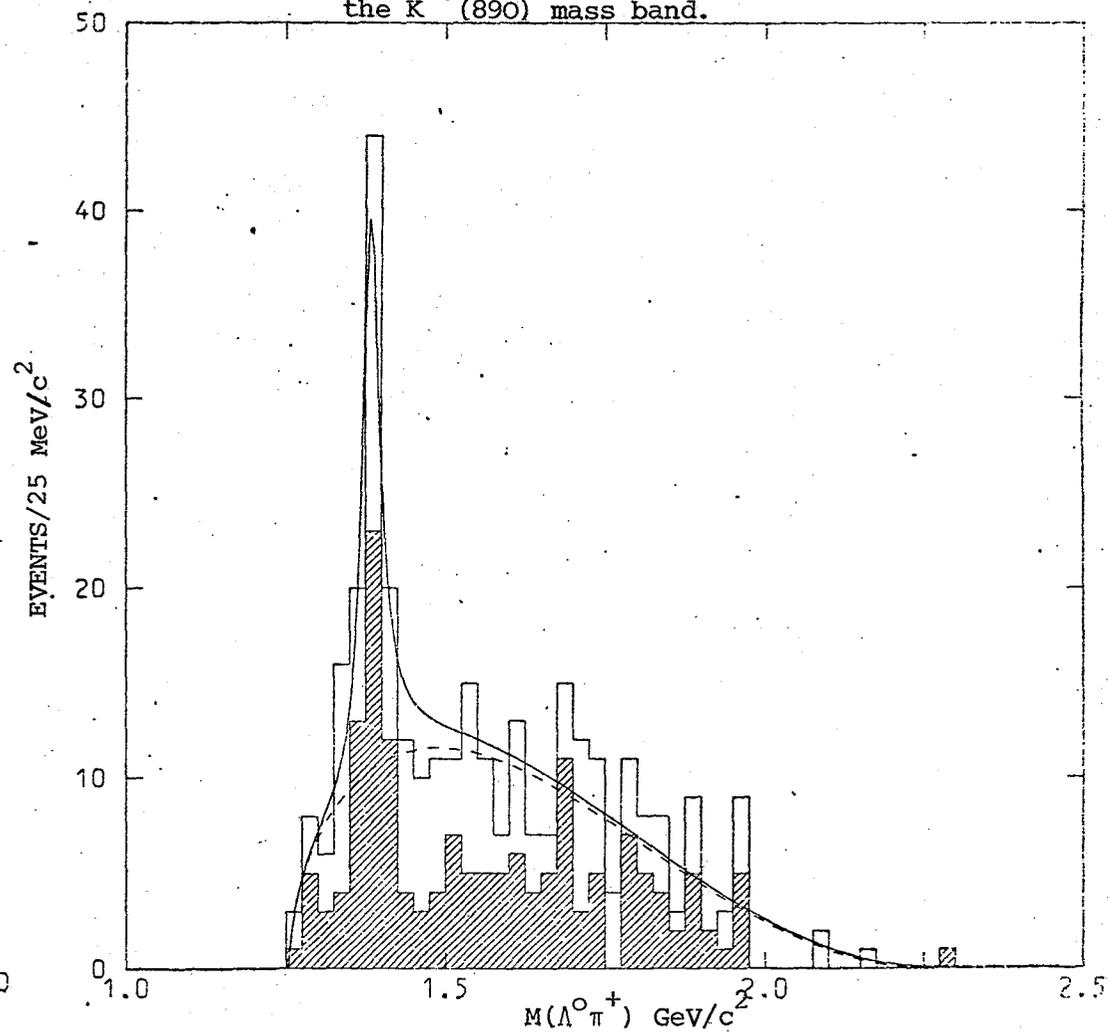
there is little evidence for ρ^+ production in $(\pi^+ \pi^0)$ from the channel $K^0 \Lambda^0 \pi^+ \pi^0 p_s$ (figure IV.32 (b)). Figure IV.36 shows that the production of Σ^+ (1385) in this channel is suppressed (c.f. the associated production of K^{*0} (890) and Σ^+ (1385) above).

The $(K\pi\pi)^+$ spectra from the channels $K^+ \Lambda^0 \pi^+ \pi^- p_s$ and $K^0 \Lambda^0 \pi^+ \pi^0 p_s$ are shown in figures IV.37 and IV.38 respectively. There is some evidence for the K^{*+} (1420) and for an enhancement in the region 1200 - 1325 MeV/c^2. This enhancement persists even after selection of events outside the Σ^- (1385) or the Σ^0 (1385) mass bands, so that it is difficult to dismiss in terms of reflection effects. The possible existence of resonances in the so-called "Q-region" of $(K\pi\pi)$ is discussed in section IV.3.10.

IV.3.5. The channel $K^+ \Sigma^0 \pi^+ \pi^- p_s$

The prominent feature of this channel is the strong K^{*0} (890) signal in $(K^+ \pi^-)$ (see table IV.1, figure IV.41). There is also a small amount of Σ^+ (1385) and Σ^- (1385) production in $(\Sigma^0 \pi^+)$ and $(\Sigma^0 \pi^-)$ respectively (figures IV.42 and IV.43.). However both signals are weak (sig $\sim$ 2) so that no cross-section calculations have been attempted.

The $(K\pi\pi)^+$ spectrum (figure IV.44) shows evidence for a sig = 3.2 signal between 1200 and 1325 MeV/c^2 (see section IV.3.10).

The Goldhaber plot of $M(\Sigma^0 \pi^+)$ versus $M(K^+ \pi^-)$ is shown in figure IV.45.

Fig. IV.41 The $K^+\pi^-$ effective mass distribution for the channel $K^+\Sigma^0\pi^+\pi^-$ p_s fitted with a K^{*+} (890) Breit-Wigner expression and phase space.
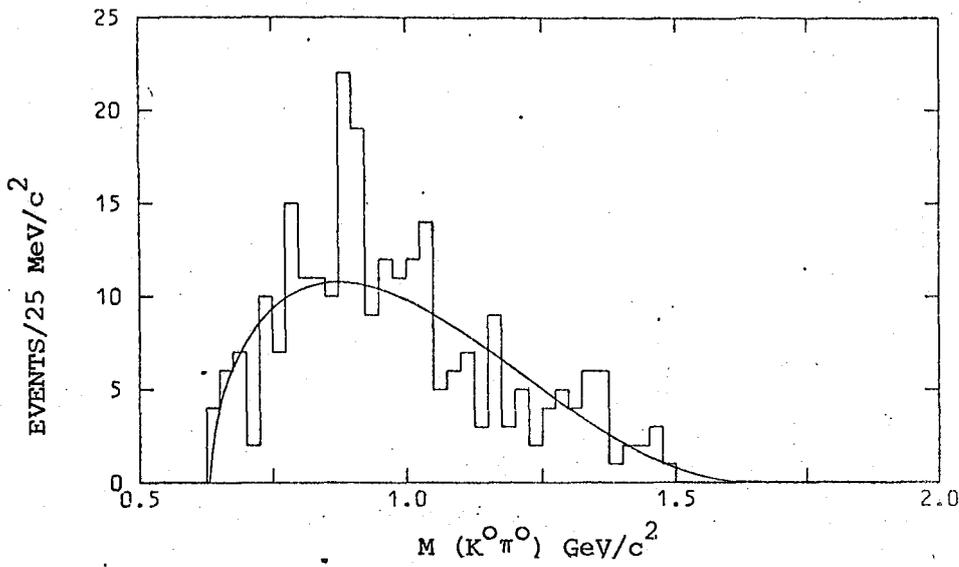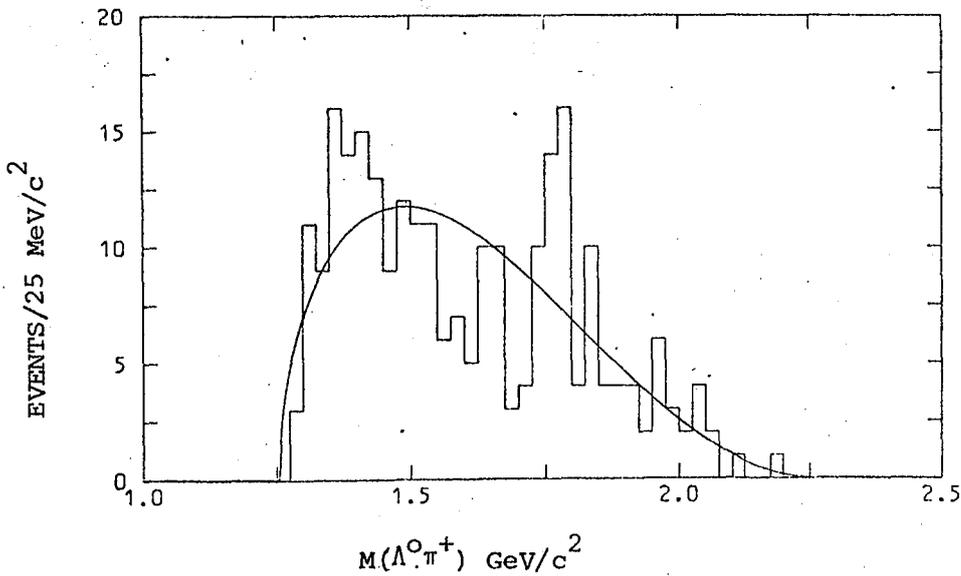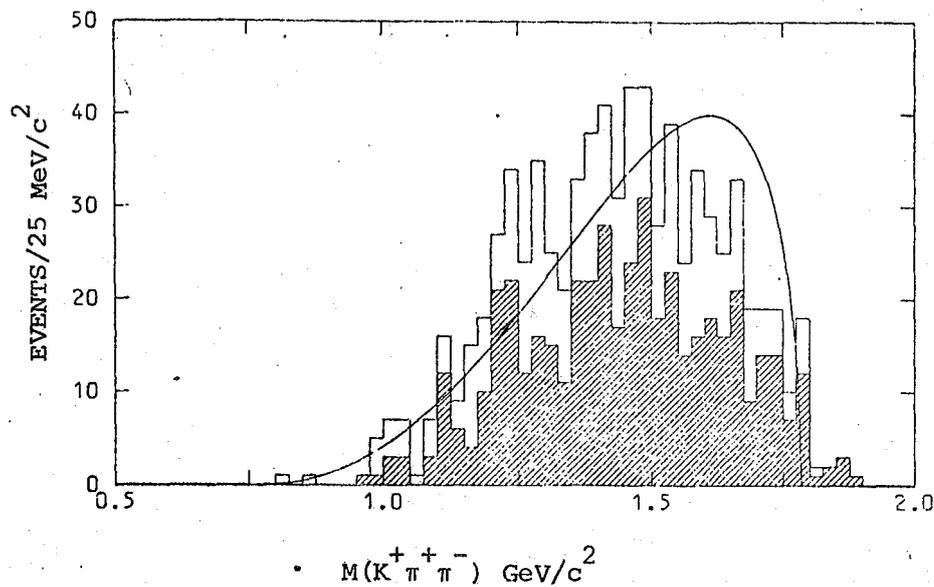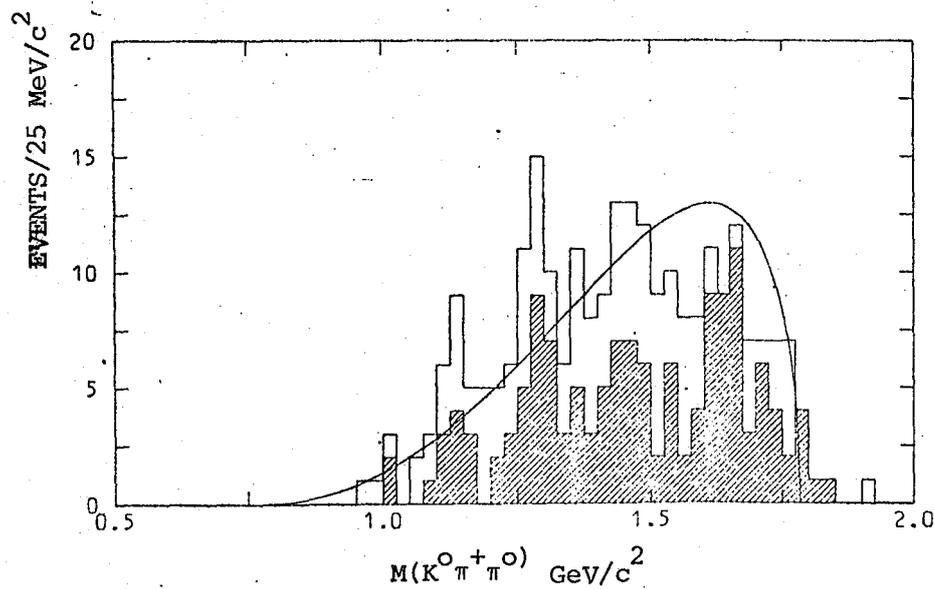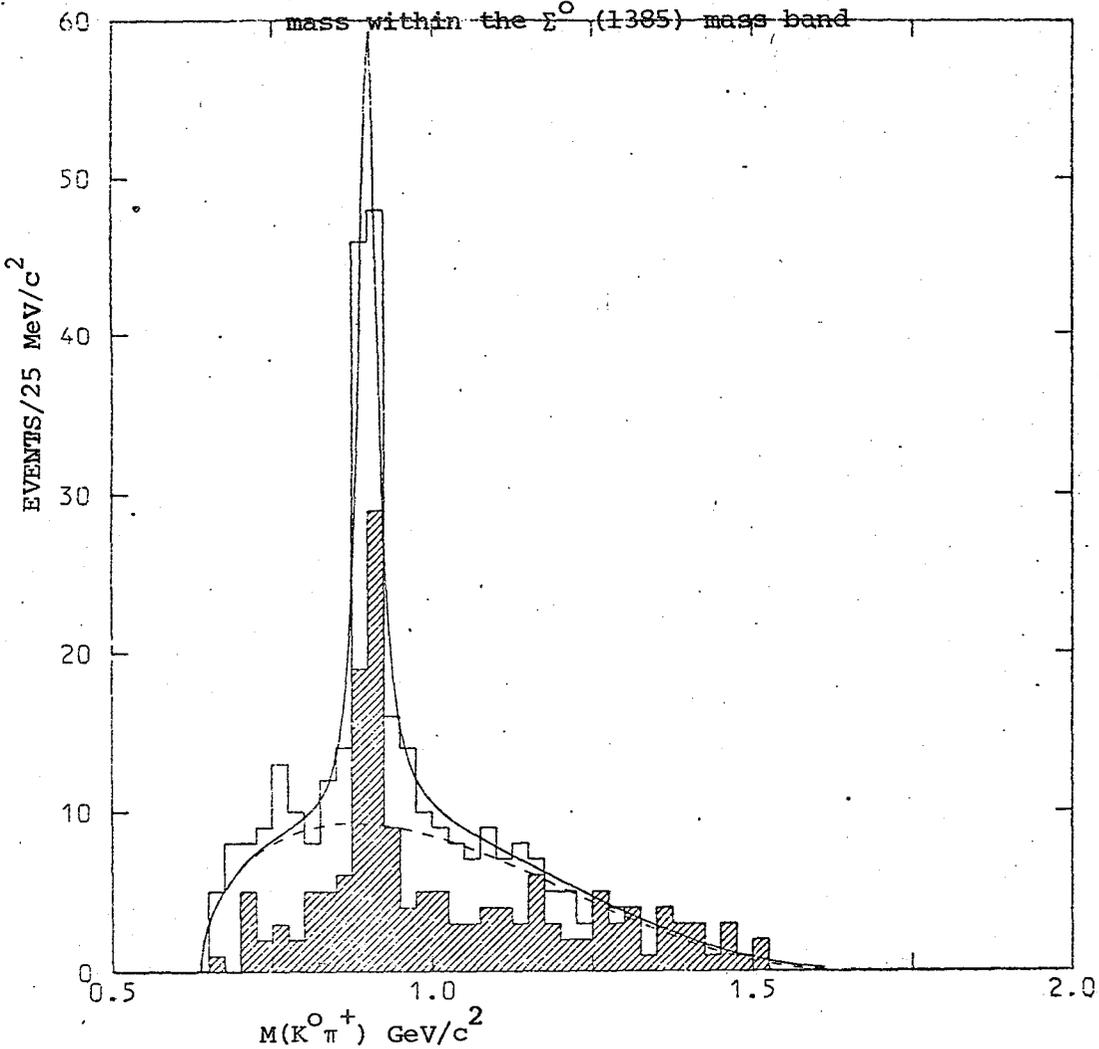
Fig. IV.42 The $\Sigma^0\pi^+$ effective mass distribution for the channel $K^+\Sigma^0\pi^+\pi^-$ p_s. The curve represents phase space normalised to the events outside the Σ^+(1385) mass band.

Fig. IV.43 The $\Sigma^0\pi^-$ effective mass distribution for the channel $K^+\Sigma^0\pi^+\pi^-$ p_s. The curve represents phase space normalised to the total number of events.

M($\Sigma^0\pi^-$) GeV/c^2

Fig. IV.44 The $K^+\pi^+\pi^-$ effective mass distribution for the channel $K^+\Sigma^0\pi^+\pi^-$. The curve represents phase space normalised to the total number of events. The hatched area corresponds to events outside the $\Sigma^-(1385)$ mass band.

M ($K^+\pi^+\pi^-$) GeV/c2
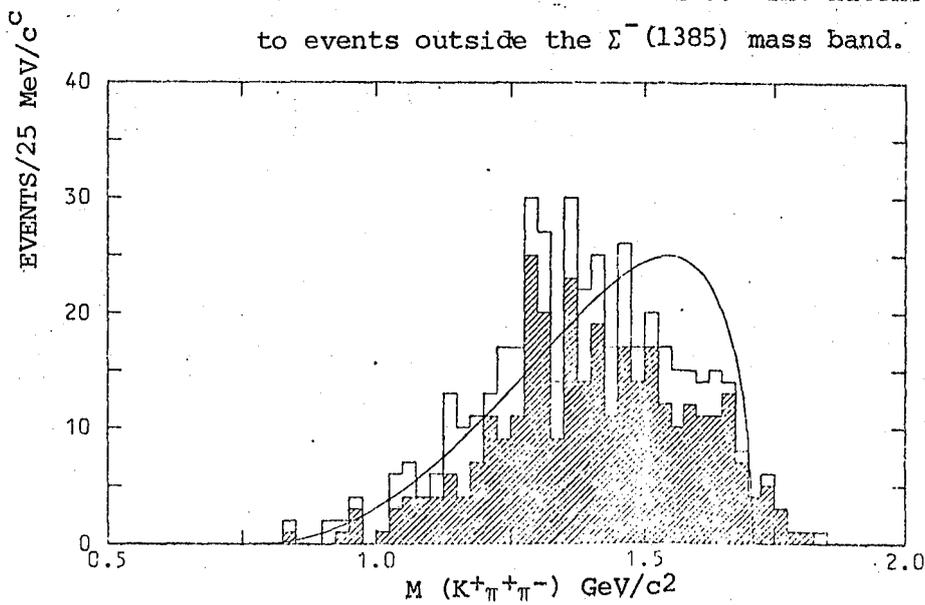
Fig. IV.45 Goldhaber plot for the channel $K^+\Sigma^0\pi^+\pi^-p_s$

$E_{cM} = 2.73, 2.90, 3.06$ GeV

$M(\Sigma^0\pi^+)$ GeV/c^2

$M(K^+\pi^-)$ GeV/c^2
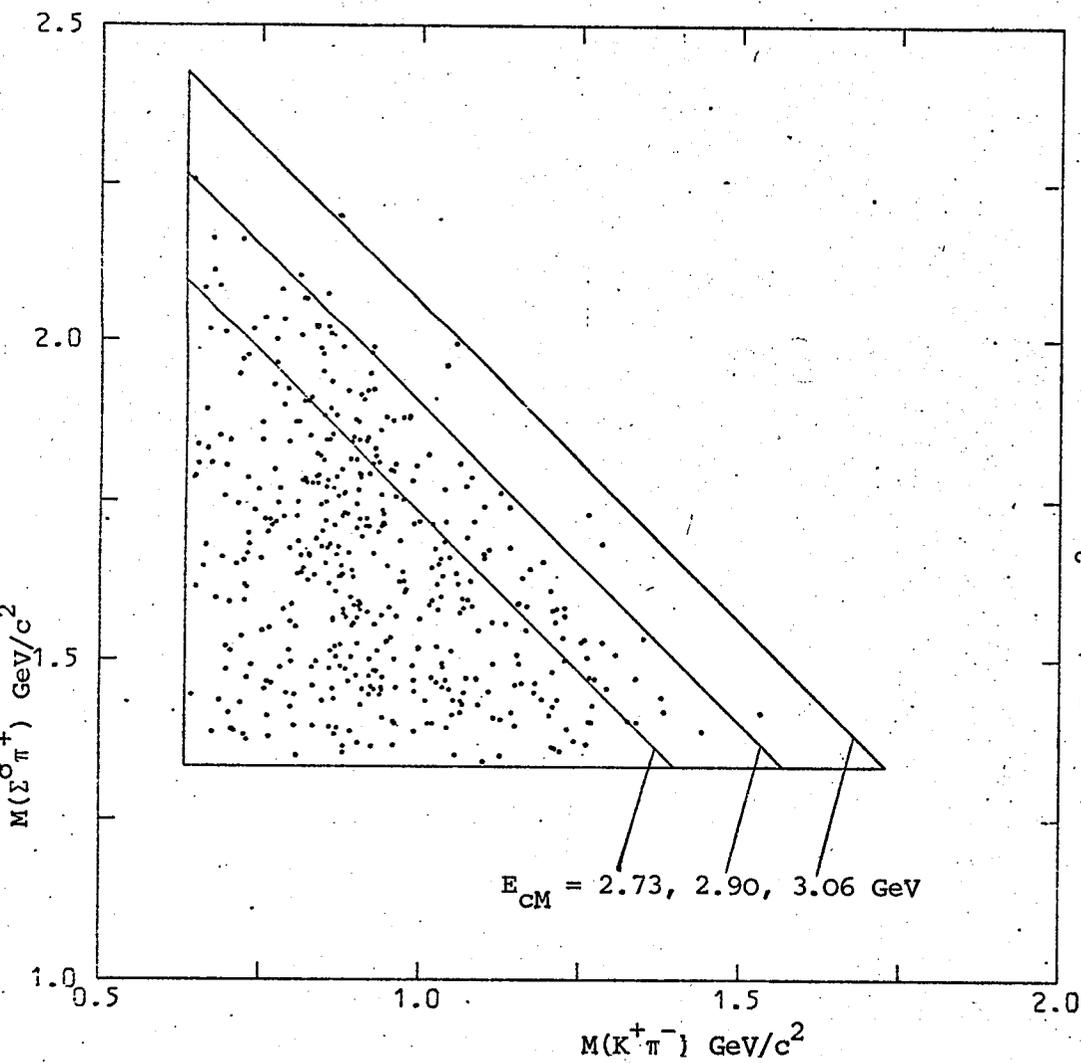
Fig. IV.46 Goldhaber plot for the channel $K^0K^-\pi^+pp_s$.

$E_{cM} = 2.73, 2.90, 3.06$ GeV

$M(K^-p)$ GeV/c^2

$M(K^0\pi^+)$ GeV/c^2
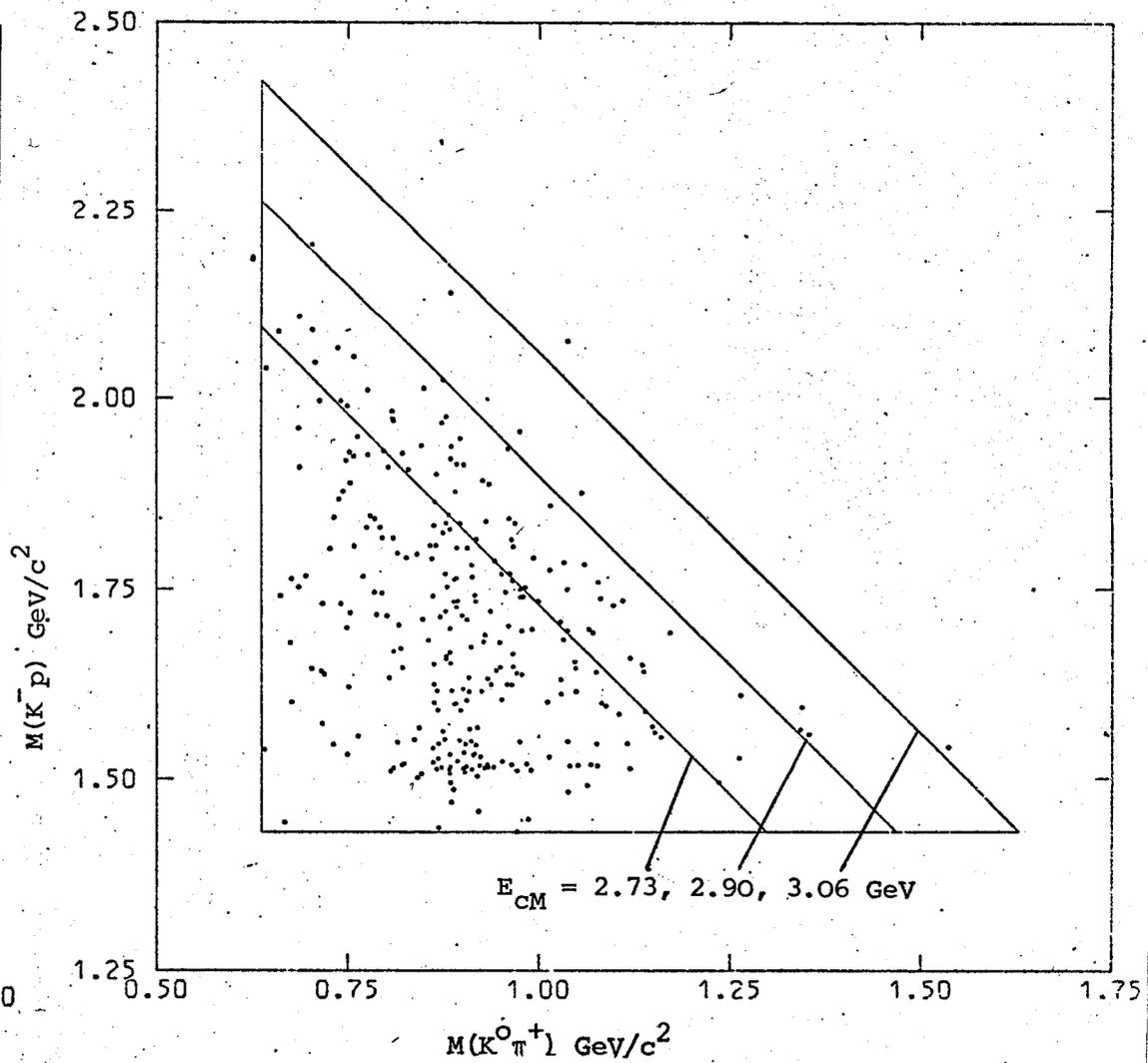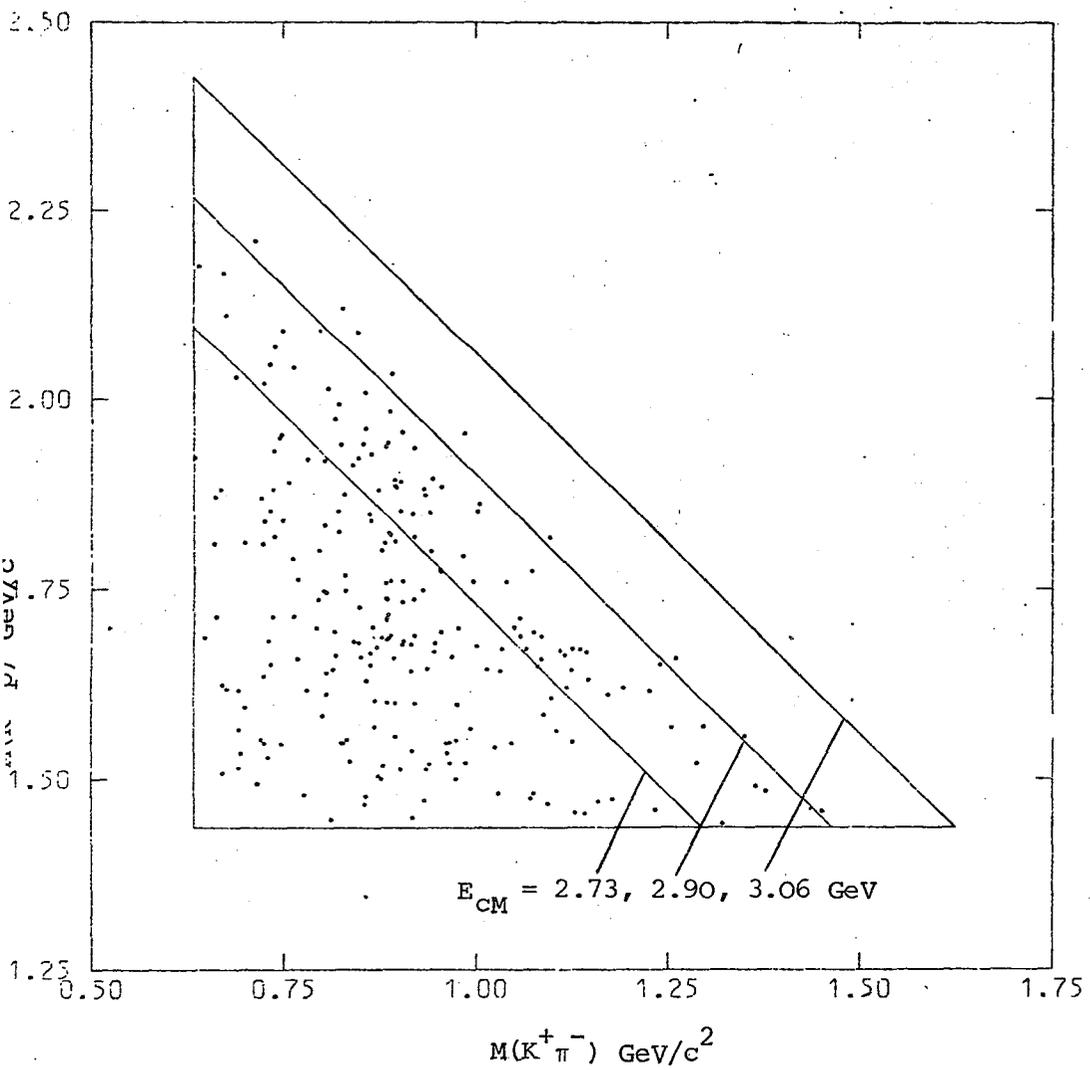
Fig. IV.47 Goldhaber plot for the channel $K^+\bar{K}^0\pi^-$ pp_s.

IV.3.6   The channels $K^O K^- \pi^+ pp_s$ and $K^+ K^{-O} \pi^- pp_s$

The Goldhaber plots of $M(\bar{K} p)$ versus $M(K\pi)$ for these channels are shown in figures IV.46 and IV.47 respectively. The dominant resonances are listed in table IV.1. In addition the $(K^O p)$ spectrum (figure IV.51) for the first channel shows an enhancement (sig = 3.5) between 1850 and 1950 MeV/c^2. This is in the region of the Z_O (1865) which, if it exists, would be an exotic baryon resonance with charge and strangeness both equal to +1 (see section IV.3.8). The combined $(K\bar{K}\pi)^O$ spectrum is discussed in detail in section IV.3.9.

IV.3.7   The channel $K^+ \Lambda^O \pi^+ \pi^- \pi^O p_s$

The Goldhaber plot of $M(K^+ \Lambda^O)$ versus $M(\pi^+ \pi^- \pi^O)$ for this channel is shown in figure IV.55. The only prominent feature is the strong $\omega^O(783)$ signal in $(\pi^+ \pi^- \pi^O)$ (see table IV.1, figure IV.56). Here the Derenzo-Hildebrand function has been used to parameterise the background since reflections in a five body final state are difficult to accommodate in the phase space prediction.

IV.3.8.   The search for exotic baryon resonances

The existence of baryons with strangeness +1 (exotic) is still not definitely established. The available evidence for these so-called "Z-type" resonances is summarised in ref. IV.10, where enhancements at mass values of 1780 and 1865 MeV/c^2 (isospin = 0) and 1900, 2150 and 2500 MeV/c^2 (isospin = 1) are reported.

The sig = 3.5 enhancement in figure IV.51 could possibly be associated with the Z_O (1865). On selection of events outside the $K^{*+}(890)$

Fig. IV.48 The $K^O\pi^+$ effective mass distribution for the channel $K^O K^- \pi^+ pp_s$ fitted with a $K^{*+}(890)$. Breit-Wigner expression and phase space.
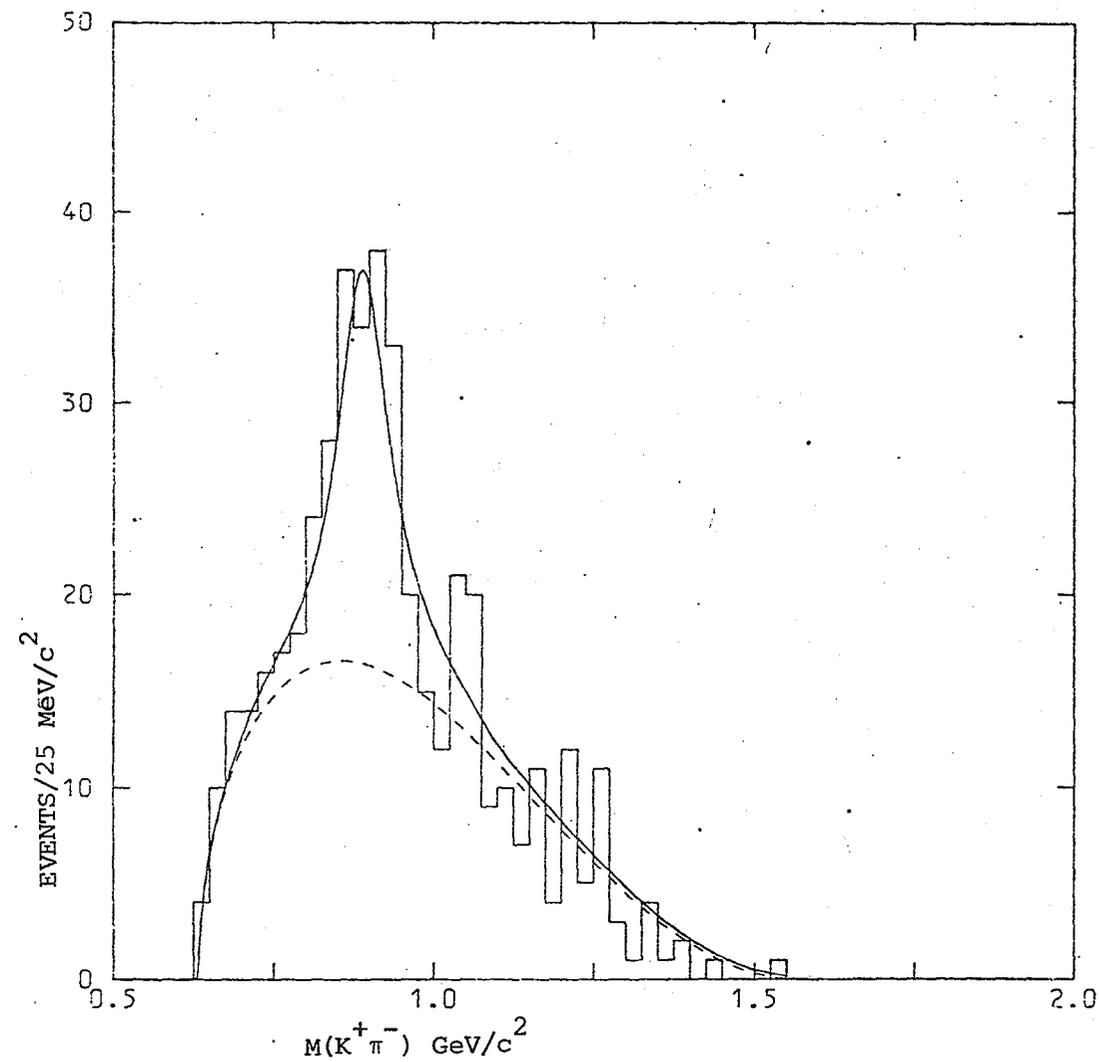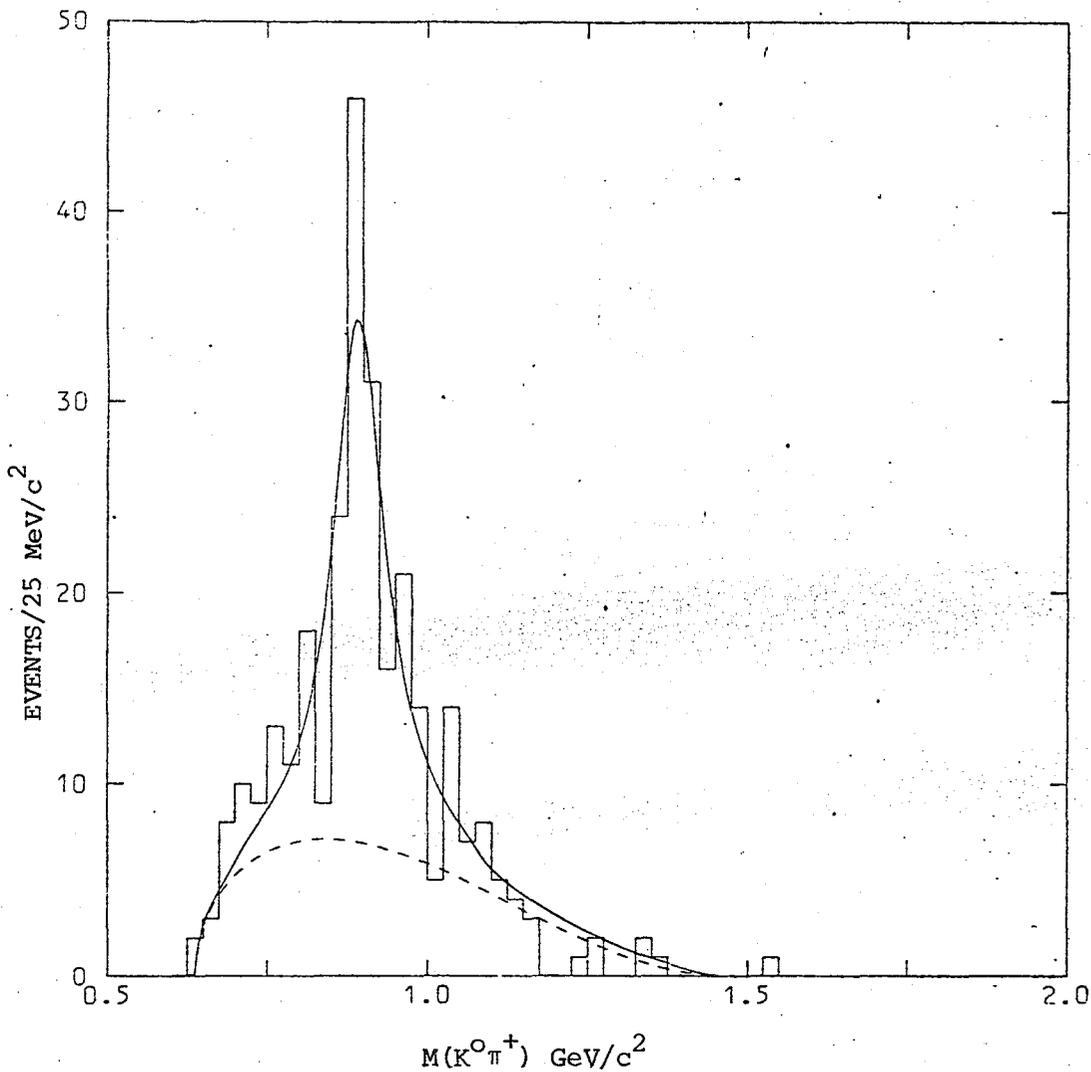
Fig. IV.49 The $\bar{K}p$ effective mass distribution for the channel $K^O K^- \pi^+ pp_s$. The curve represents phase space normalised to the events outside the $\Lambda^O(1520)$ mass band.

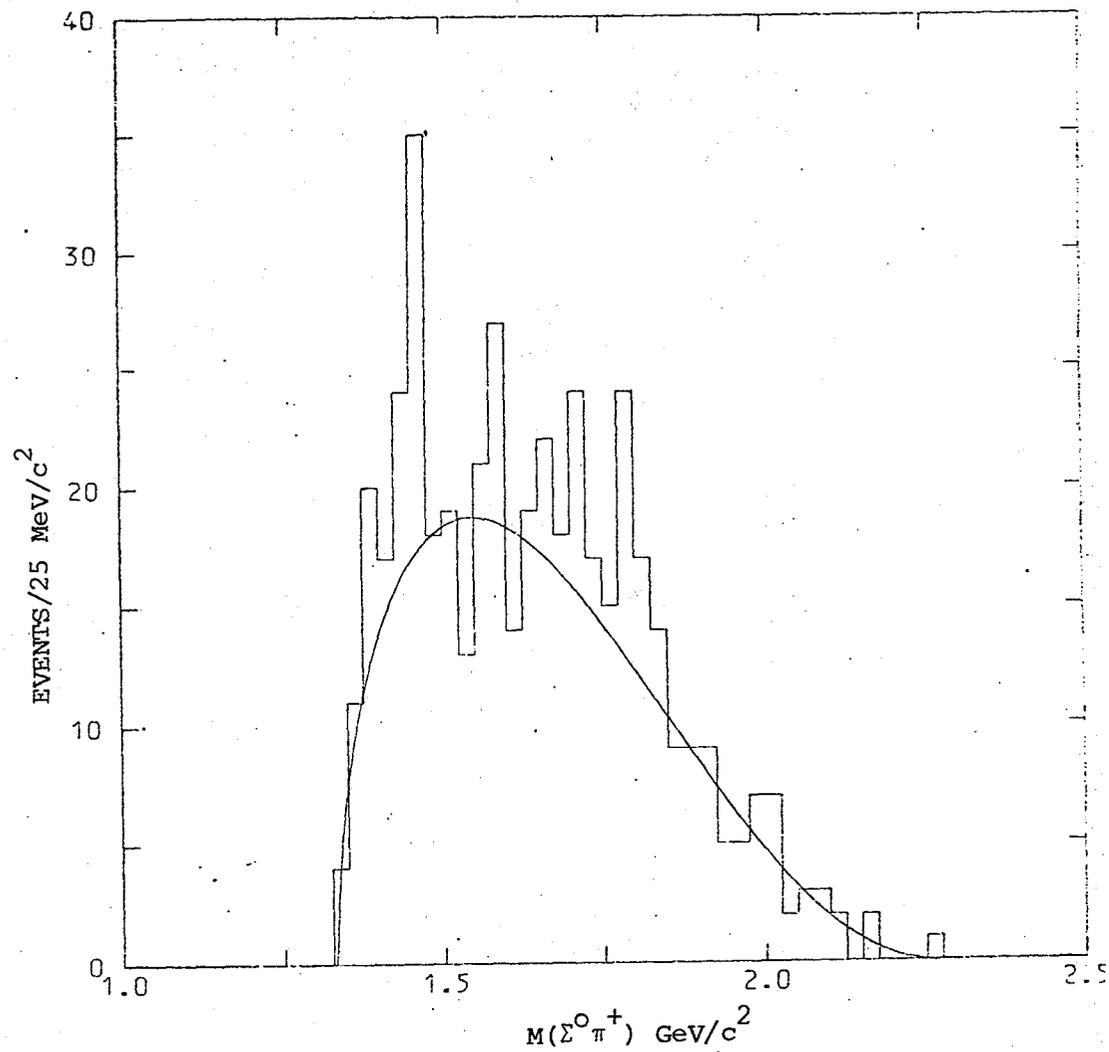EVENTS/25 MeV/c^2

$M(K^O\pi^+)$ GeV/c^2

EVENTS/25 MeV/c^2

$M(\bar{K}p)$ GeV/c^2
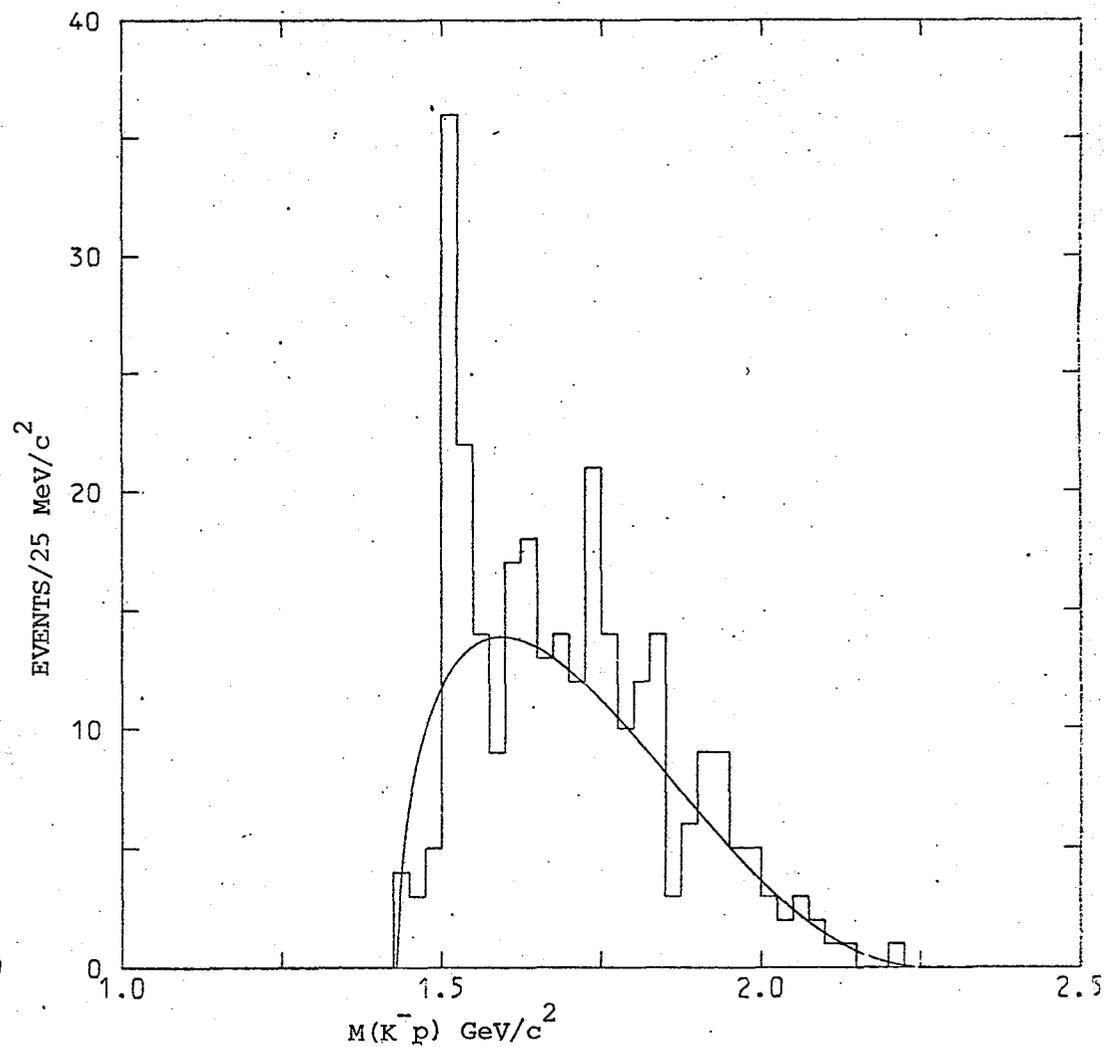
Fig. IV.50 The $K^-\pi^+$ effective mass distribution for the channel $K^0K^-\pi^+$ pp_s. The curve represents space normalised to the events outside the $\bar{K}^{*0}(890)$ mass band.

M($K^-\pi^+$) GeV/c^2

EVENTS/25 MeV/c
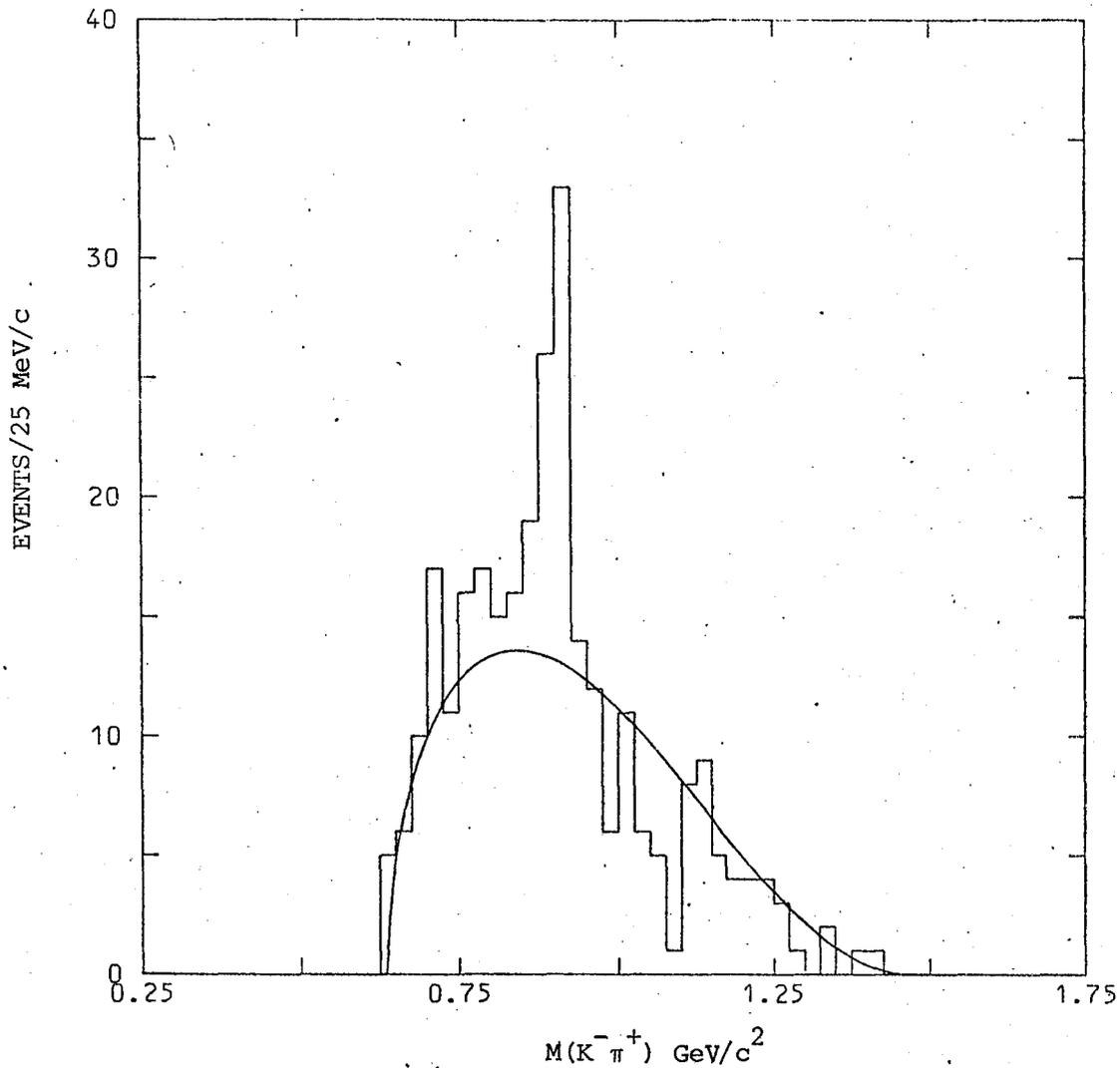
Fig. IV.51 The K^0p effective mass distribution for the channel $K^0K^-\pi^+$ pp_s. The curve represents phase space normalised to the total number of events.
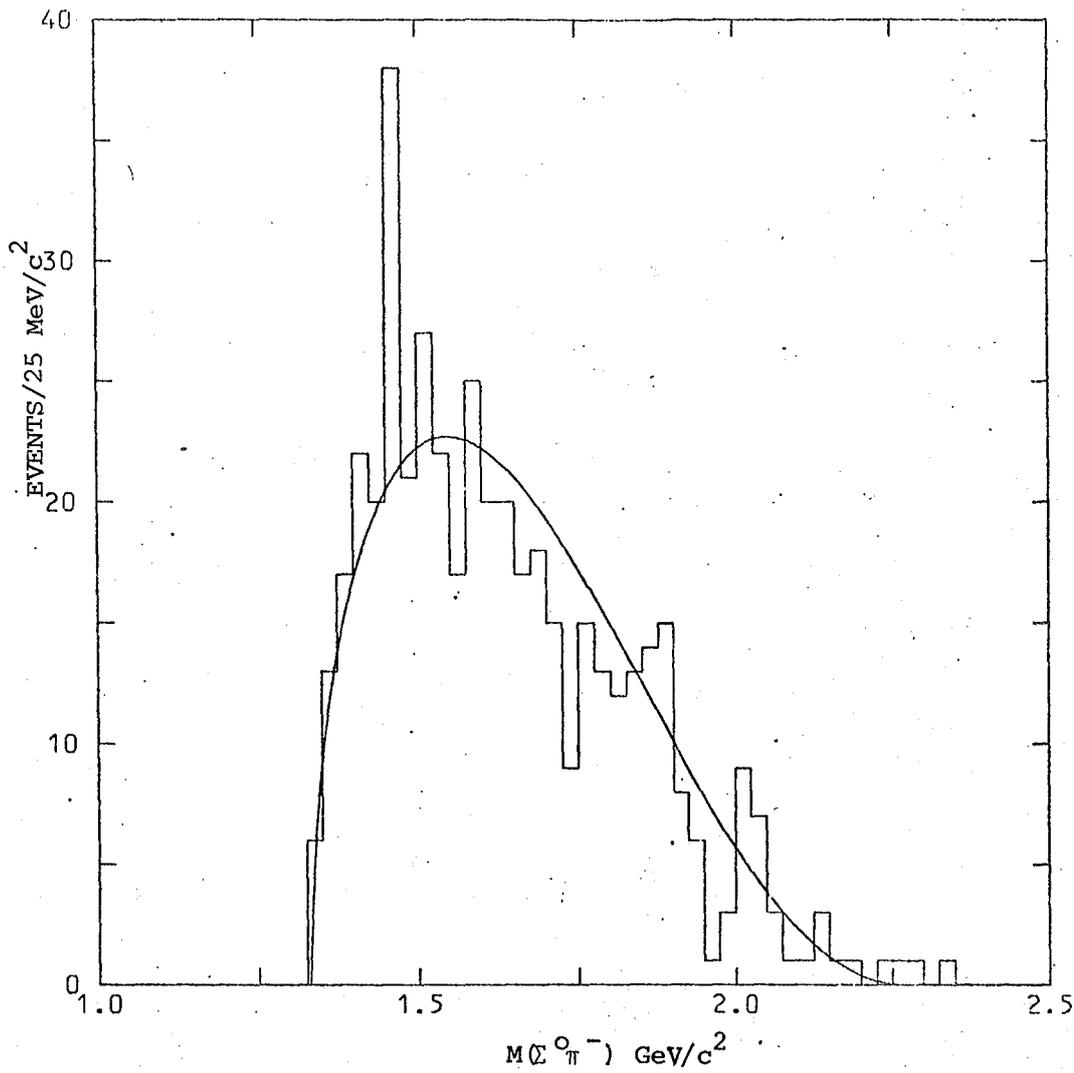
The hatched area corresponds to events outside the $K^{*+}(890)$ mass band.

M(K^0p) GeV/c^2

EVENTS/25 MeV/c^2
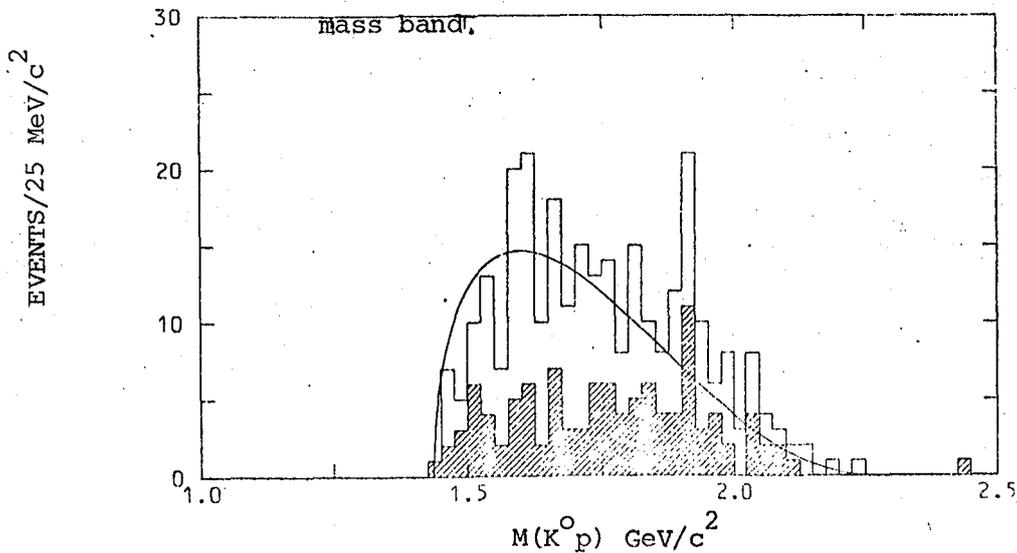
Fig. IV.52 The $K^+\pi^-$ effective mass distribution for the
channel $K^+\bar{K}^0\pi^-$ pp_s fitted with a $K^{*0}(890)$
Breit-Wigner expression and phase space.
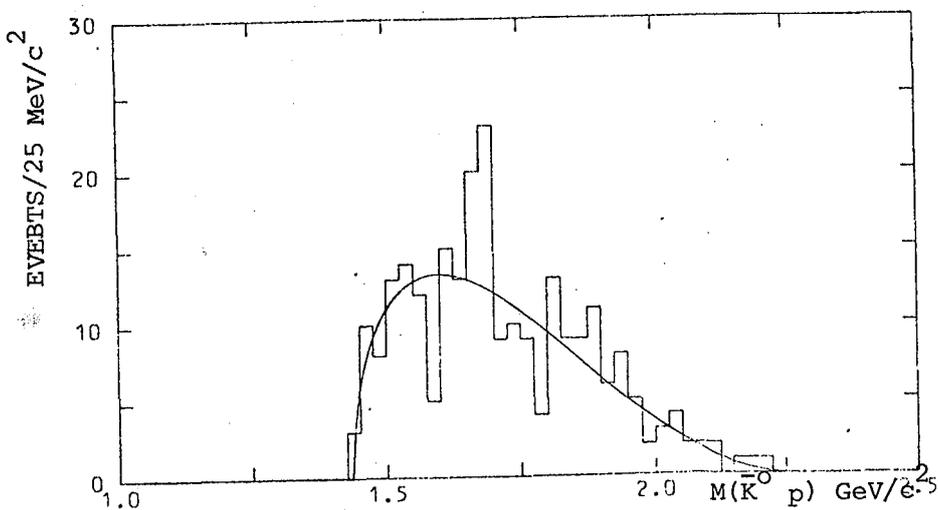
EVENTS/25 MeV/c^2

$M(K^+\pi^-)$ GeV/c^2

Fig. IV.53 The $\bar{K}^O \pi^-$ effective mass distribution for the
channel $K^+ \bar{K}^O \pi^- pp_s$ fitted with a $K^{*-}(890)$
Breit-Wigner expression and phase space.

V. 54 The $\bar{K}^O p$ effective mass distribution for the channel $K^+ \bar{K}^O \pi^- pp_s$. The curve
represents phase space normalised to the events outside the $\Sigma^+(1670)$ mass band.
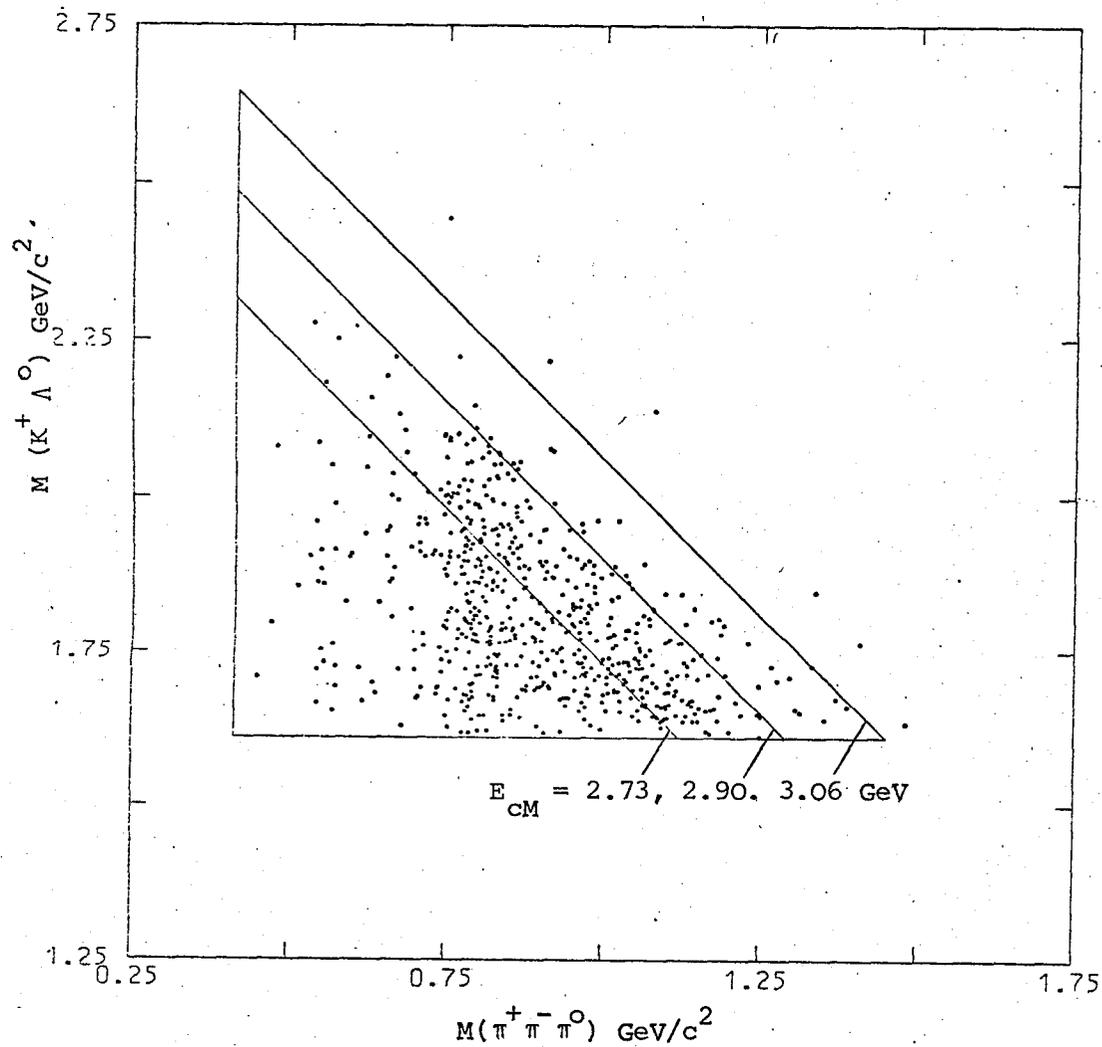
Fig. IV.55 Goldhaber plot for the channel $K^+ \Lambda^0 \pi^+ \pi^- \pi^0 p_s$
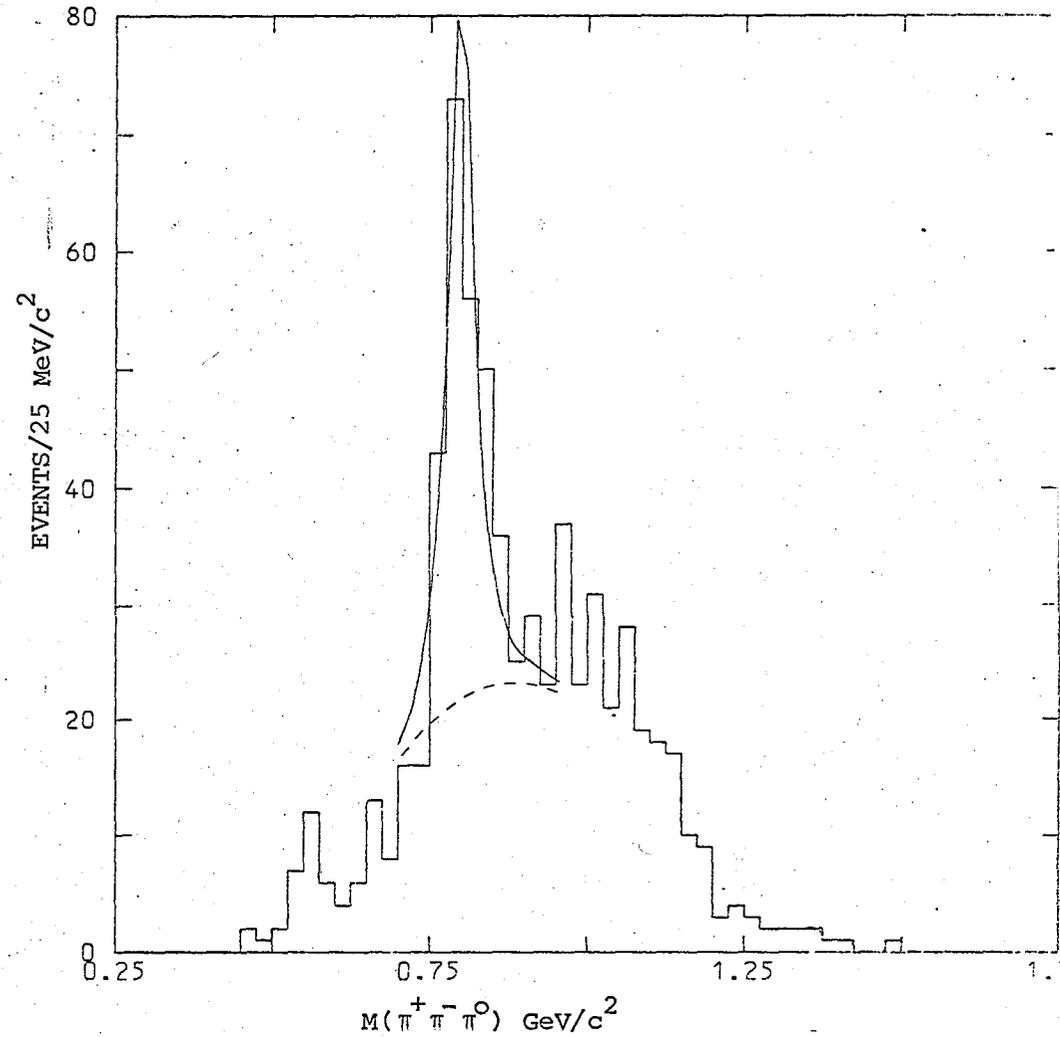
Fig. IV.56 The $\pi^+ \pi^- \pi^0$ effective mass distribution for the channel $K^+ \Lambda^0 \pi^+ \pi^- \pi^0 p_s$ fitted with an ω^0 (783) Breit-Wigner expression and the Derenzo-Hildebran function.

mass band (see hatched area) the signal maintains a significance of 2.2, so that the enhancement is difficult to dismiss in terms of reflections.

IV.3.9 The ($K\bar{K}\pi$) spectra

Figure IV.57 shows the combined $(K\bar{K}\pi)^0$ spectra from the channels $K^0 K^- \pi^+ pp_s$ and $K^+\bar{K}^0 \pi^- pp_s$. There is some evidence for the D(1285) (sig = 2.6) and E (1420) (sig = 3.4), although the E(1420) is not a well established resonance (but see ref. IV.11). There is no evidence for the g (1680). If at least one $K\pi$ combination is required to have an effective mass within the K^* (890) mass band (see hatched area), then the D(1285) signal disappears whereas the E(1420) maintains a significance of 2.8, indicating the possible decaymode:

$$E(1420) \rightarrow K^* \bar{K} \quad \text{or} \quad \bar{K}^* K$$

IV.3.10 The ($K\pi\pi$) spectra

Evidence may be found in the literature for the existence of resonances in the so-called Q-region of ($K\pi\pi$) spectra between 1200 and 1400 MeV/c^2 (for a review of the current data see ref. II.3). In particular Conforto and Conforto (ref. IV.12) report an enhancement at a mass value of 1279 ± 4 MeV/c^2 with a width of 52^{+13}_{-11} MeV/c^2. The dominant decay mode is found to be $K\rho$. If the Q exists then it should also be present in the $(K\pi\pi)^+$ spectra from this experiment. The channels $K^+ \Lambda^0 \pi^+ \pi^- p_s$, $K^0 \Lambda^0 \pi^+ \pi^0 p_s$ and $K^+ \Sigma^0 \pi^+ \pi^- p_s$ have been examined for structure in $(K\pi\pi)^+$ (see sections IV.3.4 and IV.3.5). The combined spectrum from the first two channels (figure IV.58 (a)) shows an enhancement (sig = 4.8) between 1200 and 1350 MeV/c^2 in addition to the
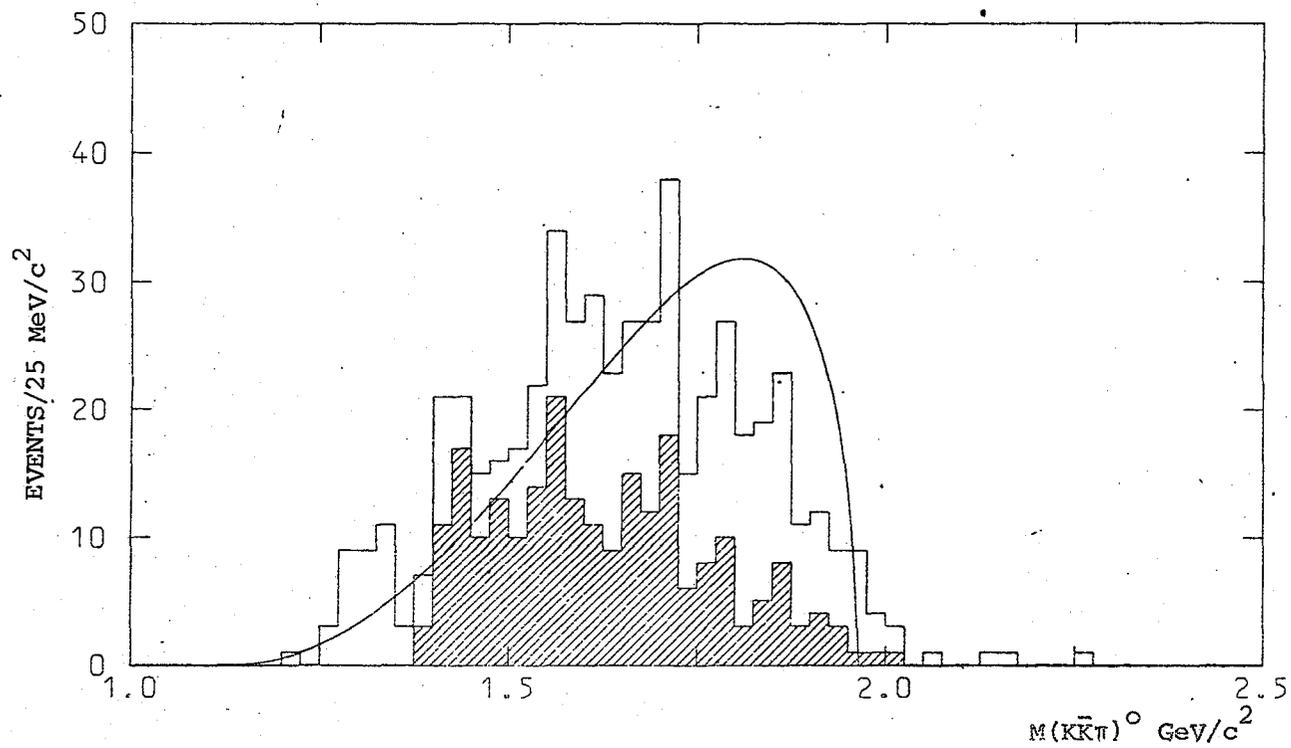
Fig. IV.57 The combined $(K\bar{K}\pi)^{0}$ effective mass distributions from the channels $K^{0}K^{-}\pi^{+}$ pp_{s} and $K^{+}\bar{K}^{0}\pi^{-}$ pp_{s}. The curve represents phase space normalised to the total number of events. The hatched area corresponds to events with at least one $K\pi$ effective mass within the $K^{*}(890)$ mass band.
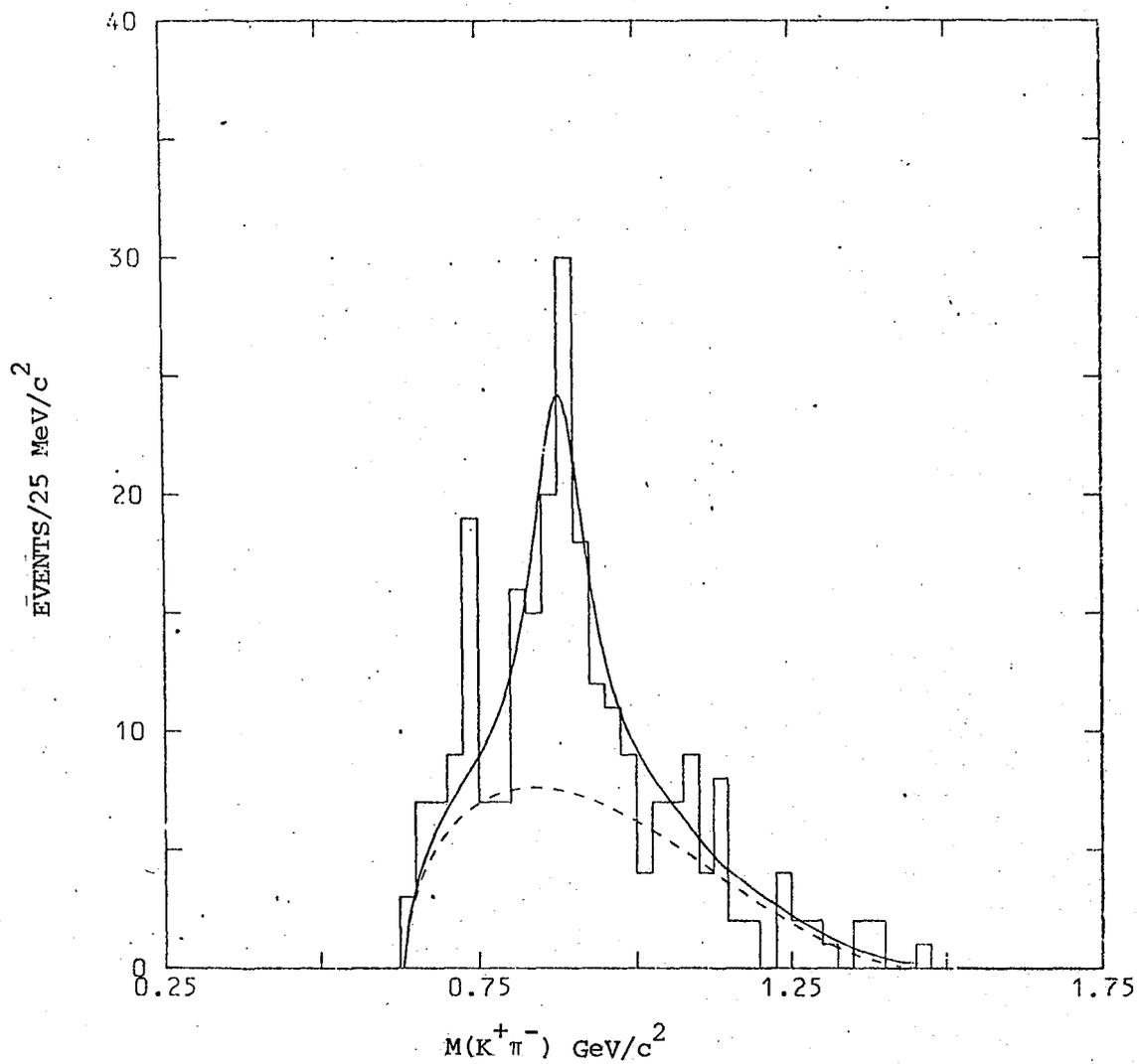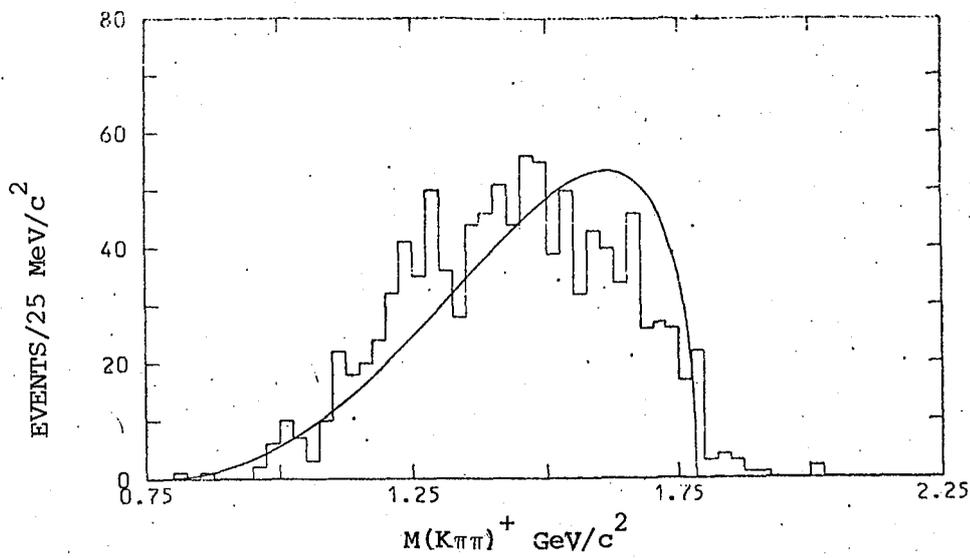
Fig. IV.58 (a) The combined $(K_{\pi\pi})^+$ effective mass
distributions for the channels
$K^+ \Lambda^O \pi^+ \pi^- p_s$ and $K^O \Lambda^O \pi^+ \pi^O p_s$
The curve represents phase space normalised
to the total number of events.
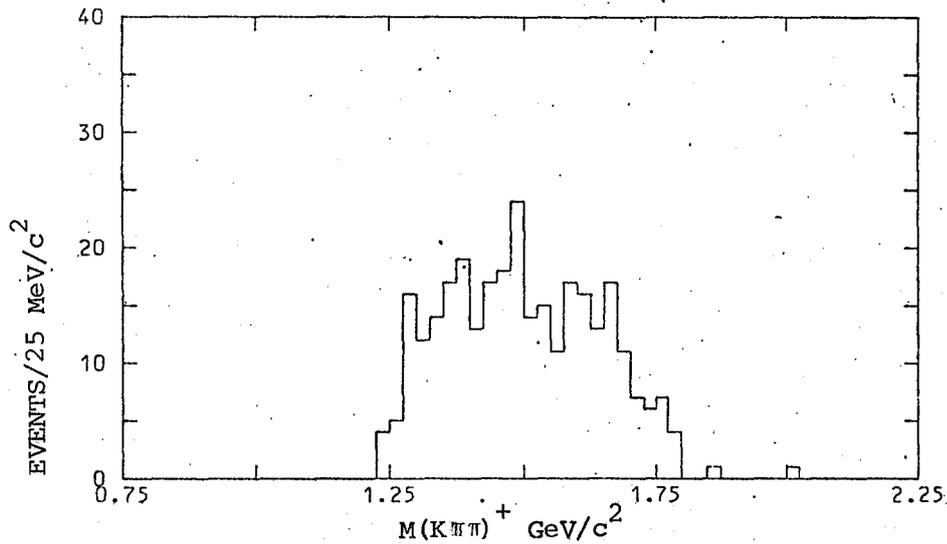
(b) Events within the ρ mass band
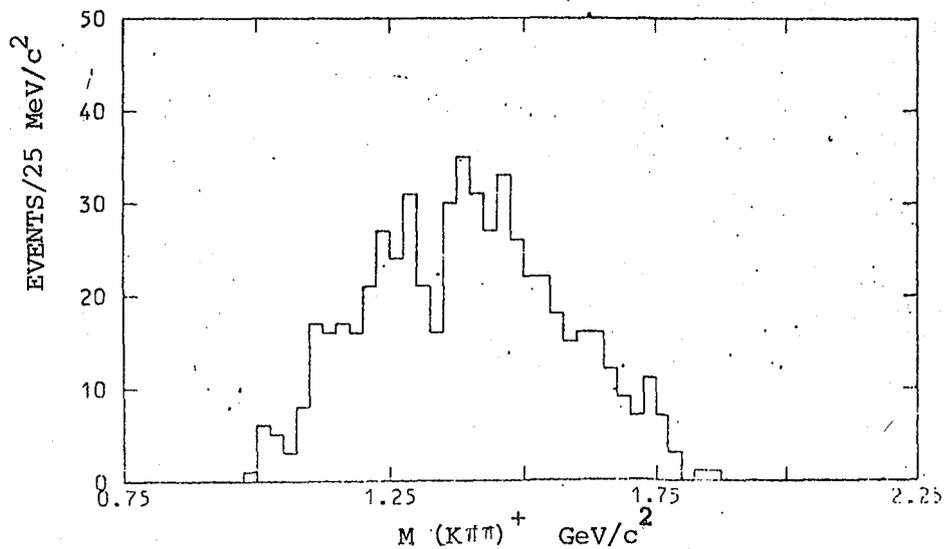
(b) Events within the $K^*(890)$ mass-band

well established $K^*(1420)$ signal (see table IV.1). However the significance

of the enhancement largely depends on the position of the background curve,

which is difficult to estimate accurately with such low statistics. In

both these channels there is little evidence for ρ in $(\pi\pi)$ (see figures

IV.32 (a) and (b)). Moreover when the combined $(K\pi\pi)^+$ spectrum is

plotted for those events whose di-pion effective mass is within the ρ mass

band (i.e. 750 MeV/c^2 < M $(\pi\pi)$ < 850 MeV/c^2) then the enhancement com-

pletely disappears (figure IV.58 (b)). If on the other hand the $(K\pi\pi)^+$

spectrum is plotted for those events with at least one $K\pi$ effective mass

within the $K^*(890)$ mass band, then the enhancement maintains a significance

of 4.1 (figure IV.58 (c)). If this is taken to be evidence for a dominant

$K^*\pi$ decay mode, it is difficult to explain the apparent contradiction with

the data from ref. IV.12, unless the Q has isospin $\frac{1}{2}$ in which case the

branching ratio,

$$\frac{Q^+ \rightarrow K^o \rho^+}{Q^+ \rightarrow K^+ \rho^o} = 2$$

would mean that the $K\rho$ decay mode occurred predominently in the $K^o \Lambda^o \pi^+ \pi^o p_s$

final state for which the detection probability is low in this experiment.

IV.4 Summary

The cross-sections have been calculated for the production of well

established resonances in final states consisting of three, four and five

particles (not including the spectator nucleon). Where they can be

checked, the branching ratios agree with previous estimates or those pre-

dicted by Clebsch-Gordan coefficients. Evidence for the existence of the

$Z_o(1865)$, E (1420) and Q (1280) is not conclusive. Of the well established

resonances, $K^*(890)$ production occurs in some 25% of the strange particle

sample considered, and $\Sigma(1385)$ in approximately 8%. This forms the basis of the following chapter in which the quasi-two body processes involving the production of one or both of these resonances are studied in detail.

CHAPTER V

QUASI-TWO BODY REACTIONS

V.1 Introduction

In the previous chapter strong signals of $K^*(890)$ and $\Sigma(1385)$ were

found in the data. Consequently there are sufficient statistics to allow

a detailed analysis of the quasi-two body reactions which involve the

production of these resonances. In particular information about their

production mechanisms may be extracted from the decay distributions of

the resonances by using the spin density matrix formalism (section V.3).

In this chapter the following two body and quasi-two body reactions are

discussed (*):

1. $\pi^+ n \rightarrow K^+ \Lambda^0$

2. $\pi^+ n \rightarrow K^+ \Sigma^0$

3. $\pi^+ n \rightarrow K^{*+}(890) \Lambda^0$

4. $\pi^+ n \rightarrow K^{*+}(890) \Sigma^0$

5. $\pi^+ p \rightarrow K^{*+}(890) \Sigma^+$

6. $\pi^+ n \rightarrow K^+ \Sigma^0(1385)$

7. $\pi^+ p \rightarrow K^+ \Sigma^+(1385)$

8. $\pi^+ n \rightarrow K^{*+}(890) \Sigma^0(1385)$

For each of these reactions the differential cross-section is studied

as a function of four-momentum transfer. The Λ^0/Σ^0 polarisation is calcu-

lated for reactions 1-4 and a spin density matrix analysis is carried out

for reactions 3-8. Reaction 3 is of particular interest since there are

sufficient statistics to allow a study of the correlated decay distributions

(*) The spectator nucleon has been omitted throughout this chapter and
all cross-sections have been corrected for nucleon-nucleon shadowing
(Section I.2)

of the $K^{*+}(890)$ and the Λ°. This enables ten out of twelve independent

quantities which describe the reaction to be determined (see chapter VI).

The $K^{*}(890)$ and $\Sigma(1385)$ signals have been extracted by demanding

790 MeV/c^2 < M (Kπ) < 990 MeV/c^2 and 1250 MeV/c^2 < M($\Lambda^{\circ}\pi$) < 1500

MeV/c^2 respectively. No attempt has been made to correct for the small

fraction of background events in these mass bands (usually less than about

20%). The statistics rarely justify the use of elaborate methods to

account for background contamination. One such method is given in

section V.4.2 for reaction 3. However, the results are indistinguishable

from those obtained by using all the events in the K*(890) mass band.

Before presenting the experimental data, an outline of the production

mechanisms is discussed.

V.2 Regge-pole models

The basic ideas behind the Regge-pole theory stem from the relation-

ship between high and low energy scattering using the analyticity of the

reaction amplitude A(s, t, u) and crossing symmetry. These concepts,

together with the definitions of the Mandelstam variables s, t and u, are

discussed in appendix B.

Two body and quasi-two body processes occurring at high energies

(s > 8 (GeV)^2) are characterised by small momentum transfer. This means

that the outgoing particles will be predominantly in the same direction as

the beam or target in the centre of mass system. The interaction is said

to be peripheral; in other words it is dominated by long range forces. This

forward-backward preference of the interaction is consistent with the

physical idea of particle exchange (Yukawa forces). Figure V.1 represents

an interaction between particles a and b via the exchange of one or more
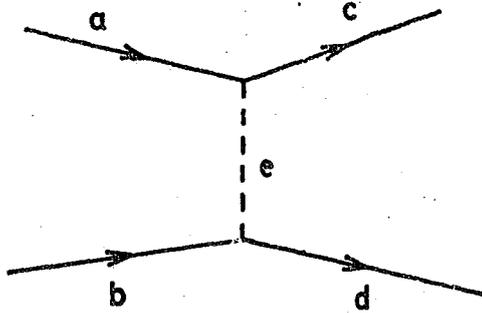
Fig. V.1   A two body reaction mediated by
an exchange process
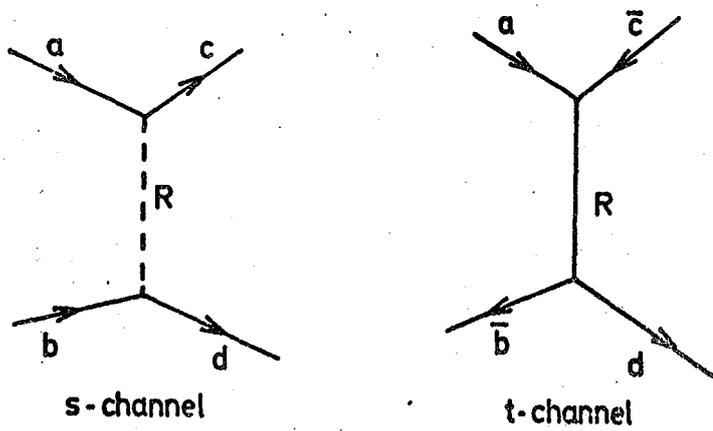
s-channel   t-channel

Fig. V.2   An s- and t-channel reaction
mediated by the same Regge
trajectory R.

physical region | physical region

s - channel | t - channel

(exchange) | (resonances)
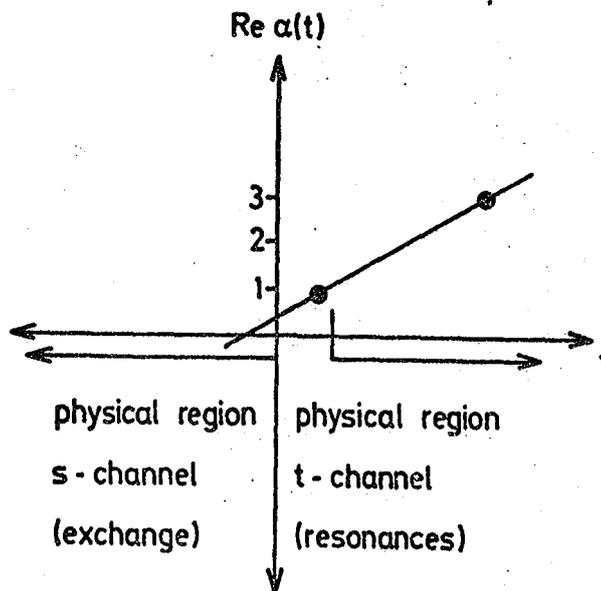
Fig. V.3   Chew-Frautschi plot for an odd
signature Regge trajectory.

intermediate objects denoted by e. The interaction produces the particles

or resonances c and d. The strong interaction conserves the total

isospin (I), G-parity (G), angular momentum (1), parity (P), baryon number

(B) and strangeness (S) at each of the vertices (aec) and (bed). This

puts a restriction on the allowed quantum numbers of e. The "mass" of

the exchanged quantity is given by

$$m_e^2 = (E_a - E_c)^2 - (q_a - q_c)^2$$

$$= (P_a - P_c)^2 = t \qquad \text{(cf equation (B.2), appendix B)}$$

Since t is negative, e is said to be "off the mass shell".

The basis of the Regge-pole theory is that exchange particles in the

s-channel correspond to intermediate resonances produced in the crossed

t-channel according to the scheme $a + \bar{c} \longrightarrow R \longrightarrow \bar{b} + d$ (see figure V.2.)

The t-channel reaction corresponds to low energy scattering (t small and

positive), and may therefore be described in terms of partial wave

amplitudes, A (1, E), where 1 and E are the angular momentum and

energy of the combination $(a\bar{c})$. By considering the angular momentum as

a complex function of energy, $\alpha(E)$, Regge has shown that the partial

wave amplitudes will have poles for values of E where $\alpha(E)$ is a positive

integer. The poles are associated with bound states (E < 0) or

resonances (E > 0). The function, $\alpha(E)$, is known as the "Regge trajectory"

and is usually expressed in terms of t, the square of the c.m. energy for

the t-channel reaction. By using the principle of crossing symmetry the

trajectory may also be used to obtain the t-dependence for the high-

energy s-channel reaction. This is illustrated in figure V.3 which shows

a Chew-Frautschi diagram of Re $\alpha(t)$ versus t for a hypothetical case.

The real part of the trajectory is assumed to depend linearly on t, an

assumption which is borne out by the experimentally observed spin versus

mass squared dependence for $t > 0$. Hence by extrapolating the trajectory into the s-channel region, the t-dependence of the high-energy collision may be predicted and the following amplitude obtained:

$$A_{cd;\ ab}\ (s,\ t,\ u)\ \xrightarrow{\quad s\ \to\ \infty\quad}\ \sum \beta_{cd;\ ab}(t)\ \left[\frac{\tau + e^{-i\pi\alpha(t)}}{\sin\ \pi\alpha(t)}\right]\ \left(\frac{\upsilon}{\upsilon_o}\right)^{\alpha(t)} \qquad (V.1)$$

where $\upsilon = \frac{1}{2}\ (s-u)$ and υ_o is a scale factor

The summation runs over all possible Regge trajectories, each characterised by a different set of allowed internal quantum numbers. The indices a, b, c and d denote the helicities of the respective particles. The quantity $\beta_{cd;\ ab}(t)$ is known as the "residue function" which must factorise into the particle couplings, γ_{ac} and γ_{bd}, at the incoming and outgoing vertices of the t-channel reaction.

$$\beta_{cd;\ ab}(t)\ =\ \gamma_{ac}(t)\ \gamma_{bd}(t)$$

Both the trajectory and the residue function are generally real in the high energy region of the s-channel reaction. The SU(3) relations for the particle couplings enable different high energy processes to be compared (see for example section V.4.1). Kinematical factors to account for conservation of total angular momentum may be included in the residue function. The quantity τ gives the signature of the trajectory so that poles with even spin ($\tau = + 1$), or odd spin ($\tau = - 1$), are linked together (Figure V.3 for example links together poles with odd signature). For zero interference between amplitudes of differing signature both their trajectories and residue functions must be identical. This is known as "strong exchange degeneracy". Weak exchange degeneracy requires only the trajectories to be identical.

Non-zero polarisation of the final state particles requires the exchange of two interfering trajectories. Consequently the hyperon polarisation measurements in strange particle production will provide a useful test of exchange degeneracy. In addition the assumption of weak exchange degeneracy enables certain predictions to be made about the polarisation and differential cross-section relations between line-reversed reactions (see for example section V.4.1).

For poles in the u-channel reaction, t must be replaced by u in expression (V.1), and for baryon exchange, α is replaced by $\alpha-\tfrac{1}{2}$ in the square bracket. At high energies the amplitude is dominated by the highest lying trajectories (α large). For this reason baryon exchange is small compared with meson exchange (see for example section IV.3.1). One often approximates the amplitude by considering only the trajectory with the largest $\alpha(t)$ (i.e. the leading trajectory).

The exchange of trajectories with exotic quantum numbers is expected to be suppressed. In strange meson exchange for example this would mean the $I = \tfrac{1}{2}$ amplitude, $A_{\frac{1}{2}}$, is dominant. For the reactions $\pi^+ n \longrightarrow K^+ \Sigma^0$ and $\pi^+ p \longrightarrow K^+ \Sigma^+$ (section V.4.1), the exotic $I = \tfrac{3}{2}$ amplitude, $A_{\frac{3}{2}}$, may be determined from the cross-section ratio

$$\frac{\sigma \ (\pi^+ p \longrightarrow K^+ \Sigma^+)}{\sigma \ (\pi^+ n \longrightarrow K^+ \Sigma^0)} = \frac{|A_{\frac{3}{2}}|^2 + 4|A_{\frac{1}{2}}|^2 + 4 \ \mathrm{Re} \ (A_{\frac{3}{2}}^* A_{\frac{1}{2}})}{2|A_{\frac{3}{2}}|^2 + 2|A_{\frac{1}{2}}|^2 - 4 \ \mathrm{Re} \ (A_{\frac{3}{2}}^* A_{\frac{1}{2}})} \qquad (V.2)$$

A value of 2 for this ratio indicates the absence of any $I = \tfrac{3}{2}$ exchange. Similar considerations apply to the $K^*(890) \ \Sigma$ and $K \ \Sigma(1385)$ final states (sections V.4.2 and V.4.3).

The overall helicity flip for the reaction is given by $n = |a-b-c+d|$. Conservation of angular momentem requires amplitudes with $n \geqslant 1$ to vanish

at zero scattering angle. This will produce a dip in $d\sigma/dt'$ at $t' \sim 0$, where t' is the reduced momentum transfer, $|t| - |t|_{min}$ (see appendix B, equation (B.7)).

To eliminate poles at unphysical values of angular momentum, the residue function must vanish at negative right-signature values of α ($\alpha - \frac{1}{2}$ for baryons).

i.e. $\quad \alpha = 0, -2, -4, -6 \ldots\ldots$ $\qquad\qquad (\tau = + 1)$

$\qquad \alpha = -1, -3, -5 \ldots\ldots\ldots$ $\qquad\qquad (\tau = - 1)$

Simple exchange degeneracy of the residues for opposite-signature poles predicts that the residue function must also vanish at the wrong-signature negative values (which are right-signature values for the partner pole). This effect is known as a nonsense wrong-signature zero (NWSZ) and may produce a dip or break in $d\sigma/dt$ (see for example section V.4.1). It should be noted however that statistics are generally poor for large values of t', so that some caution must be exercised in the interpretation of dips in this region.

The forward differential cross-section can in general be approximated to an exponential since

$$s^{\alpha(t)} \sim s^{\alpha_0} \exp(t\, \alpha' \ln s) \qquad\qquad\qquad (V.3)$$

where a linear trajectory has been assumed:

$$\alpha(t) = \alpha_0 + \alpha' t \qquad\qquad\qquad\qquad (V.4)$$

The exponential slope of the forward peak should therefore increase logarithmically with s, and the rate of shrinkage measures α'.

Integration of equation (V.1) over t does not give a simple expression for the s-dependence of the total cross-section. Nevertheless, provided the differential cross-section is steep enough, and the explored s range is not too big, an approximate formula for the total cross-section is

$$\sigma \sim \text{constant} \times s^{-n} \qquad (V.5)$$

where n is the average value of $2-2\alpha(t)$ over the t range considered.

A more detailed description of the above together with further aspects of the Regge pole model may be found in the literature (ref. V.1).

V.3 The spin density matrix

In an exchange process the mixture of spin substates of the reaction products will depend on the spin (J) and parity (P) of the exchanged objects. A study of the production mechanisms of quasi-two body processes will therefore involve the computation of the spin density matrix elements, ρ_{mn}, from the decay distributions of the resonances produced in the reaction. In some cases this enables the amount of natural ($(-1)^J = P$) and unnatural ($(-1)^J = -P$) parity exchange to be estimated. In this chapter the spin density matrix elements are calculated in both the s- and t-channel helicity frames. The co-ordinate axes used in this analysis are defined as follows:

(i)   In the s-channel (Helicity frame), $\hat{z}$ is the direction of the resonance in the C.M. system transformed into the resonance rest frame.

(ii)   In the t-channel (Gottfried-Jackson frame), $\hat{z}$ is the direction of the beam particle in the resonance rest frame.

(iii) In both frames the y-axis is the normal to the production plane, $\hat{y} = (q_a \times q_c) / |q_a \times q_c|$ where a is the incoming pion and c is the outgoing meson.

(iv) To obtain a right-handed co-ordinate system the x-axis is then $\hat{x} = \hat{y} \times \hat{z}$

If p denotes the direction of one of the decay products in the resonance rest frame, the decay angles are defined by:

$$\cos \Theta = \hat{z} \cdot \hat{p}$$

$$\tan \phi = (\hat{y} \cdot \hat{p}) / (\hat{x} \cdot \hat{p})$$

Any pure spin state $|\psi_k>$ may be expanded in terms of some fixed complete orthonormal set of states $|n>$:

$$|\psi_k> = \sum_n <n|\psi_k> |n> \qquad (V.6)$$

If each state $|\psi_k>$ occurs with probability p_k such that

$$\sum p_k = 1 \qquad (V.7)$$

then the expectation value of any operator, O, in a mixed spin state is given by

$$<O> = \sum_k p_k <\psi_k|O|\psi_k>$$

$$= \sum_{k,n} p_k <\psi_k|n> <n|O|\psi_k>$$

$$= \sum_n <n| O\rho |n> \qquad (V.8)$$

In terms of trace this becomes

$$<O> = Tr (O \rho) \qquad (V.9)$$

where $\rho = \sum_k |\psi_k> p_k <\psi_k|$

is the density matrix, with elements

$$\rho_{mn} = \sum_k <m|\psi_k> p_k <\psi_k|n> \qquad \text{(V.10)}$$

The main properties of the density matrix are:

(i)   it is Hermitian (i.e. $\rho_{mn} = \rho_{nm}^*$)

(ii)   it is Unitary (i.e. $\text{Tr}(\rho) = 1$)

(iii)   diagonal elements satisfy $0 \leqslant \rho_{nm} \leqslant 1$

An additional property for helicity-type quantisation (i.e. the z - axis lies in the production plane) is

(iv) $\rho_{-m -n} = (-1)^{m-n} \rho_{mn}$

Using the above properties the spin density matrix for a spin 1 particle (e.g. the $K^*(890)$) may be written as:

$$\rho(J = 1) = \begin{bmatrix} \tfrac{1}{2}(1 - \rho_{00}) & \rho_{10} & \rho_{1-1} \\[2ex] \rho_{10}^* & \rho_{00} & \rho_{10}^* \\[2ex] \rho_{1-1} & -\rho_{10} & \tfrac{1}{2}(1-\rho_{00}) \end{bmatrix} \qquad \text{(V.11)}$$

The matrix is therefore described by 4 independent parameters since ρ_{00} and ρ_{1-1} are real (see (i) and (iv) above).

For a spin $\tfrac{3}{2}$ particle (e.g. the $\Sigma(1385)$) the density matrix is:

$$\rho(J = \tfrac{3}{2}) = \begin{bmatrix} \rho_{33} & \rho_{31} & \rho_{3-1} & \rho_{3-3} \\[2ex] \rho_{31}^* & \tfrac{1}{2}-\rho_{33} & \rho_{1-1} & \rho_{3-1}^* \\[2ex] \rho_{3-1}^* & -\rho_{1-1} & \tfrac{1}{2}-\rho_{33} & -\rho_{31}^* \\[2ex] -\rho_{3-3} & \rho_{3-1} & -\rho_{31} & \rho_{33} \end{bmatrix} \qquad \text{(V.12)}$$

where $\rho_{n/2\ m/2}$ had been written as ρ_{nm} for convenience. In this case the matrix is described by 7 independent parameters, since two elements are complex (ρ_{31} and ρ_{3-1}) and three are real (ρ_{33}, ρ_{3-3} and ρ_{1-1}).

One method of determining experimentally the values of the density matrix is the method of moments. The angular distribution for the decay A $\rightarrow$ B + C must first be expanded in terms of orthogonal functions. This is achieved by thinking of the decay process as transforming a spin state $|$ m $>$ of A into a spin state of the system B + C:

$$M \ |m> \ = \ \sum_k M_{km} \ (\Theta, \phi) \ | \ k >$$ (V.13)

where $< k \ |M| \ m> = M_{km} \ (\Theta, \phi)$, the transition matrix. The decay angular distribution, W (Θ, ϕ), is then given by the expectation value of the operator M^+M in the state $|$ m $>$. Using equation (V.9) this becomes:

$$W \ (\Theta, \phi) \ = \ Tr \ (M \ \rho \ M^+)$$

$$= \ \sum_{k,m,n} M_{kn} \ (\Theta, \phi) \ \rho_{nm} \ M^*_{km} \ (\Theta, \phi)$$ (V.14)

For a spin 1 particle decaying into two spin 0 particles (e.g. K^* (890) $\longrightarrow$ Kπ) the distribution takes the form:

$$W(\Theta, \phi) \ = \ \frac{3}{4\pi} \left[\tfrac{1}{2}(1-\rho_{00}) + \tfrac{1}{2} (3\rho_{00}-1) \ cos^2\Theta \right.$$

$$\left. -\rho_{1-1} \ sin^2 \ \Theta \ cos2\phi - \sqrt{2} \ Re \ \rho_{10} \ sin \ 2 \ \Theta \ cos \ \phi \right]$$ (V.15)

The average value, $\bar{f}$, of any function f (cos Θ, ϕ) is given by:

$$\bar{f} \ = \ \int_0^{2\pi} d\phi \int_{-1}^{+1} d(cos \ \Theta) \ f(cos \ \Theta, \ \phi) \ W(cos \ \Theta, \ \phi)$$ (V.16)

since $W(\cos \Theta, \phi)$ is normalised such that

$$\int_0^{2\pi} d\phi \int_{-1}^{+1} d(\cos \Theta) \, W(\cos \Theta, \phi) = 1 \qquad (V.17)$$

By inserting the expression for $W(\cos \Theta, \phi)$ (equation V.15) into equation (V.16) and choosing suitable orthogonal functions for f, the individual matrix elements are projected out:

$$\overline{\cos^2 \Theta} = \frac{1}{5}(1 + 2\,\rho_{00})$$

$$\overline{\sin^2 \Theta \cos 2\phi} = -\frac{4}{5}\,\rho_{1-1} \qquad (V.18)$$

$$\overline{\sin 2\Theta \cos \phi} = \frac{4\sqrt{2}}{5}\,\mathrm{Re}\,\rho_{10}$$

These average values may be determined from the experimental angular distribution:

$$\text{e.g.} \quad \overline{\cos^2 \Theta} = \frac{1}{N} \sum_{i=1}^{N} \cos^2 \Theta_i$$

where Θ_i is the value of Θ for the i-th event and N is the total number of events.

In this way three out of the four parameters which characterise ρ may be determined (see equation (V.11)).

For a spin $\frac{3}{2}$ particle decaying into one spin $\frac{1}{2}$ and one spin 0 particle (e.g. $\Sigma(1385) \rightarrow \Lambda^0 \pi$) the expression for $W(\Theta, \phi)$ becomes:

$$W(\Theta, \phi) = \frac{3}{4\pi} \left[\frac{1}{6} (1 + 4 \rho_{33}) + \frac{1}{2} (1 - 4 \rho_{33}) \cos^2 \Theta \right.$$

$$\left. - \frac{2}{\sqrt{3}} \operatorname{Re} \rho_{3-1} \sin^2 \Theta \cos 2\phi - \frac{2}{\sqrt{3}} \operatorname{Re} \rho_{31} \sin 2\Theta \cos \phi \right] \qquad (V.19)$$

In this case three out of the seven parameters in equation (V.12) may be determined from the averages

$$\overline{\cos^2 \Theta} = \frac{1}{15} (7 - 8 \rho_{33})$$

$$\overline{\sin^2 \Theta \cos 2\phi} = \frac{-8}{5\sqrt{3}} \operatorname{Re} \rho_{3-1} \qquad (V.20)$$

$$\overline{\sin 2\Theta \cos \phi} = \frac{-8}{5\sqrt{3}} \operatorname{Re} \rho_{31}$$

Minnaert has shown (refs. V.10, V.11) that because the spin density matrix has positive eigenvalues, the matrix elements must satisfy certain conditions. For frames with the quantisation axis in the production plane the following positivity conditions hold:

spin 1:

$$|\rho_{1-1}| \leqslant \frac{1}{2} (1 - \rho_{00}) \qquad (V.21)$$

$$|\operatorname{Re} \rho_{10}| < \frac{1}{2} \left[\rho_{00} (1 - \rho_{00} - 2 \rho_{1-1}) \right]^{\frac{1}{2}} \qquad (V.22)$$

spin $\frac{3}{2}$:

$$(\rho_{33} - \frac{1}{4})^2 + (\operatorname{Re} \rho_{31})^2 + (\operatorname{Re} \rho_{3-1})^2 \leqslant \frac{1}{16} \qquad (V.23)$$

Further details of the spin density matrix formalism may be found in ref. V.2.

V.4 Experimental results

V.4.1 The reactions $\pi^+ n \rightarrow K^+ \Lambda^0$ and $\pi^+ n \rightarrow K^+ \Sigma^0$

The differential cross-sections for these two processes are given in table V.1 and are presented graphically in figure V.4. The distributions have been corrected for the t'-dependent losses described in section III.3.2 (v). Both distributions show departure from monotonic behaviour in the region $0.4-0.7(GeV/c)^2$ which could possibly be associated with the nonsense wrong-signature zero for $\alpha(t) = 0$.

Below $t' = 0.4 \ (GeV/c)^2$ the differential cross-sections have been fitted as shown in the figures with the form:

$$\frac{d\sigma}{dt'} = A \ e^{-bt'} \qquad (V.24)$$

In view of the above corrections to those events with $0(GeV/c)^2 < t' < 0.05 \ (GeV/c)^2$, this region has not been included in the fit. The values obtained for the slope, b, and intercept, A, are as follows:

	A $\mu b/(Gev/c)^2$	b $(GeV/c)^{-2}$	t' range $(GeV/c)^2$
$\pi^+ n \rightarrow K^+ \Lambda^0$	270 $\pm$ 24	6.6 $\pm$ 0.5	0.05 - 0.4
$\pi^+ n \rightarrow K^+ \Sigma^0$	190 $\pm$ 28	6.7 $\pm$ 0.9	0.05 - 0.4

TABLE V.1

DIFFERENTIAL CROSS-SECTIONS

(a) $\pi^+ n \to K^+ \Lambda^o$

(b) $\pi^+ n \to K^+ \Sigma^o$

| t' range $(GeV/c)^2$	Events	$d\sigma/dt'$ $\mu b/(GeV/c)^2$	t' range $(GeV/c)^2$	Events	$d\sigma/dt'$ $\mu b/(GeV/c)^2$
0 - 0.05	95	203 ± 24	0 - 0.05	28	114 ± 24
0.05 - 0.1	66	141 ± 17	0.05 - 0.1	38	90 ± 15
0.1 - 0.15	55	118 ± 16	0.1 - 0.15	34	81 ± 14
0.15 - 0.2	39	83 ± 13	0.15 - 0.2	19	45 ± 10
0.2 - 0.25	41	89 ± 14	0.2 - 0.25	20	47 ± 11
0.25 - 0.3	23	49 ± 10	0.25 - 0.3	12	28 ± 8
0.3 - 0.35	18	39 ± 9	0.3 - 0.35	9	21 ± 7
0.35 - 0.4	12	26 ± 7	0.35 - 0.4	6	14 ± 6
0.4 - 0.45	19	41 ± 9	0.4 - 0.45	10	24 ± 7
0.45 - 0.5	5	11 ± 5	0.45 - 0.5	9	21 ± 7
0.5 - 0.55	11	24 ± 7	0.5 - 0.6	5	5.9 ± 2.6
0.55 - 0.65	6	6.4 ± 2.6	0.6 - 0.7	6	7.1 ± 2.9
0.65 - 0.7	12	$.27 \pm 7$	0.7 - 0.75	10	24 ± 7
0.7 - 0.75	7	15 ± 6	0.75 - 0.8	5	12 ± 5
0.75 - 0.85	5	5.4 ± 2.4	0.8 - 0.85	5	12 ± 5
0.85 - 0.9	6	13 ± 5	0.85 - 0.95	8	9.5 ± 3.4
0.9 - 0.95	5	11 ± 5	0.95 - 1.05	6	7.1 ± 2.9
0.95 - 1.0	8	17 ± 6	1.05 - 1.1	7	17 ± 6
1.0 - 1.05	7	15 ± 6	1.1 - 1.25	7	5.5 ± 2.1
1.05 - 1.15	8	8.6 ± 3.0	1.25 - 1.3	5	12 ± 5
1.15 - 1.25	8	8.6 ± 3.0	1.3 - 1.4	11	13 ± 4
1.25 - 1.45	8	4.3 ± 1.5	1.4 - 1.5	5	5.9 ± 2.6
1.45 - 1.75	5	1.8 ± 0.8	1.5 - 1.65	6	4.7 ± 1.9
1.75 - 2.1	5	1.5 ± 0.7	1.65 - 1.9	6	2.8 ± 1.2
			1.9 - 2.1	6	3.6 ± 1.5
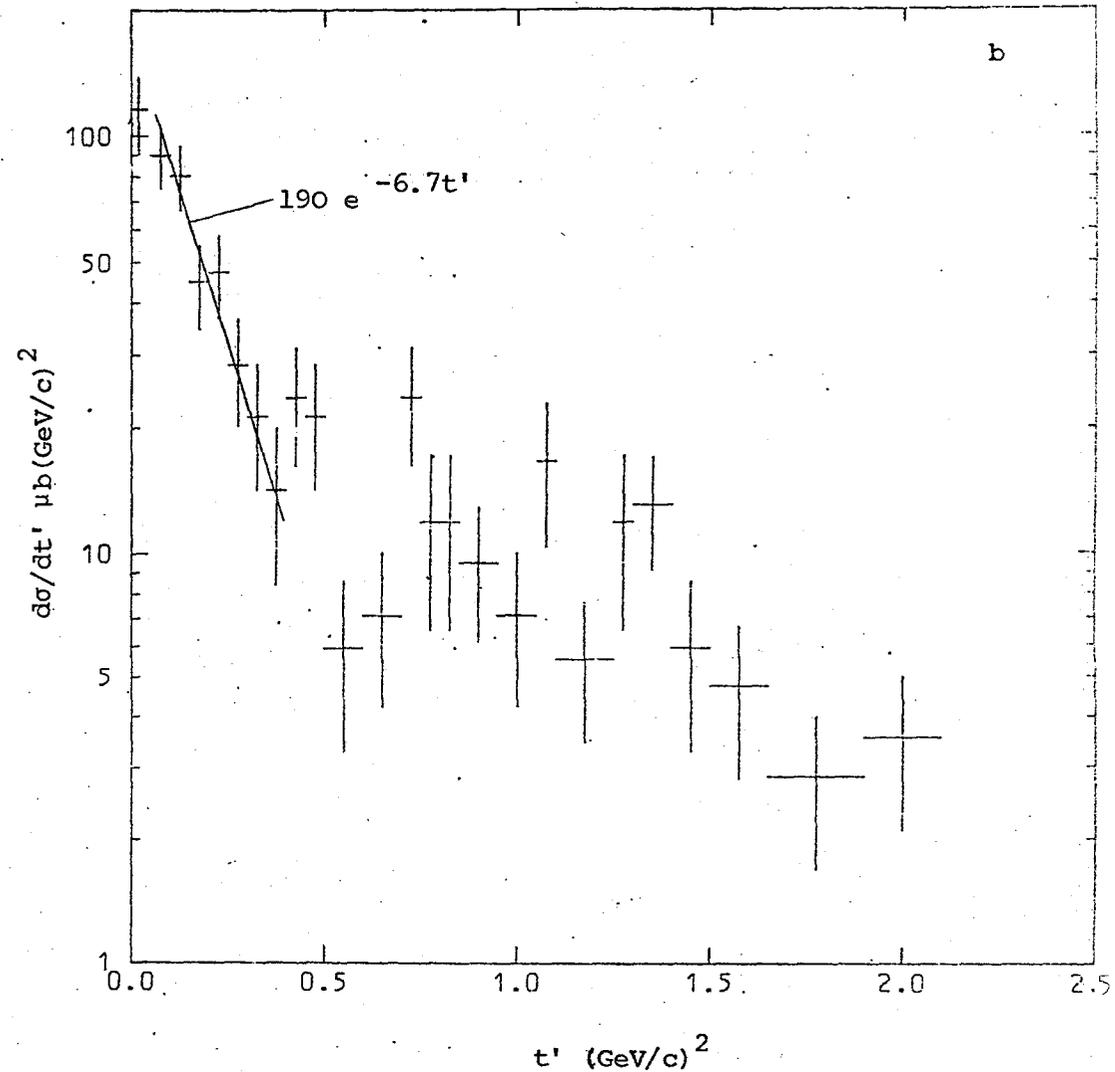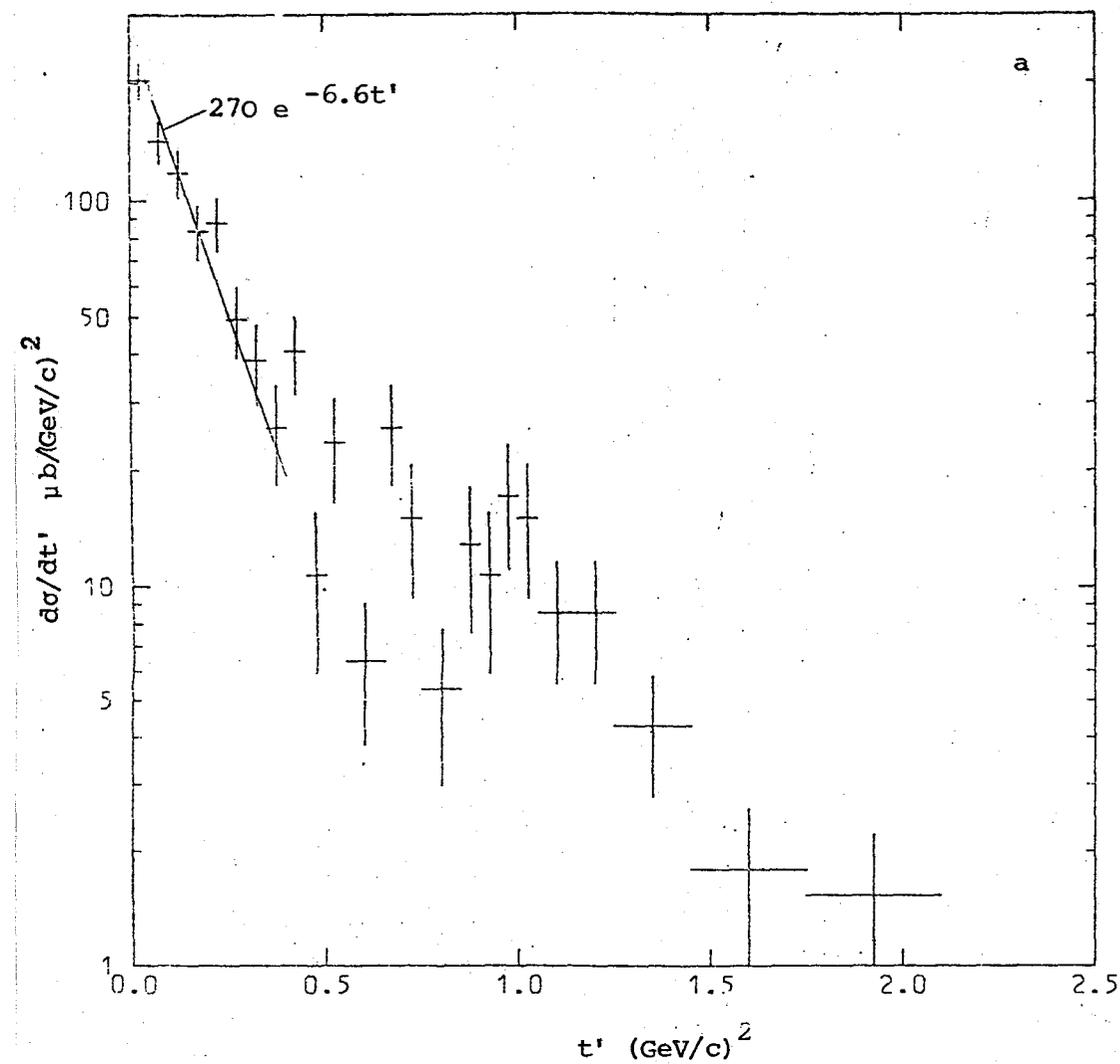
Fig.V.4 Differential cross-section distributions for the reactions (a) $\pi^+ n \to K^+ \Lambda^0$ (b) $\pi^+ n \to K^+ \Sigma^0$

The values for the slope parameter, b, are compared in figure V.5 with those obtained from similar fits to the above processes and their charge-symmetric reactions for a variety of beam momenta. However, no firm conclusions about the s-dependence of b may be made from the data. If on the other hand one ignores the points of Dahl (ref. V.3) and Abramovich (ref. I.5) in figure V.5(a) which are ~ 3 standard deviations above the value from this experiment, there is some evidence for shrinkage (see equation (V.3)).

The momentum dependence of the total cross-sections has already been fitted in section III.5 with the expression, $\sigma = $ constant $x \, p^{-n}$. At high energy the s-dependence has approximately the same form where n is the average value of $2-2\alpha(t)$ over the observed t range (see equation (V.5)). For strangeness exchange processes the average value of $\alpha(t)$ is ~ 0.2. This gives a value for n of 1.6 which is in reasonable agreement with those found from the data:

$$n = 1.8 \pm 0.2 \quad (\pi^+ n \rightarrow K^+ \Lambda^0 \text{ and } \pi^- p \rightarrow K^0 \Lambda^0)$$

$$n = 1.9 \pm 0.2 \quad (\pi^+ n \rightarrow K^+ \Sigma^0 \text{ and } \pi^- p \rightarrow K^0 \Sigma^0)$$

The Λ^0 polarisation has been computed as a function of t' from its decay angular distribution:

$$P_\Lambda : \frac{3}{\alpha N} \sum_{i=1}^{N} (\hat{q}_i \cdot \hat{n}_i) \qquad (V.25)$$

where N = the number of events in the t' interval considered

α = the asymmetry parameter for the decay

$$(\alpha_\Lambda = 0.647 \pm 0.013 - \text{Ref. II.3})$$
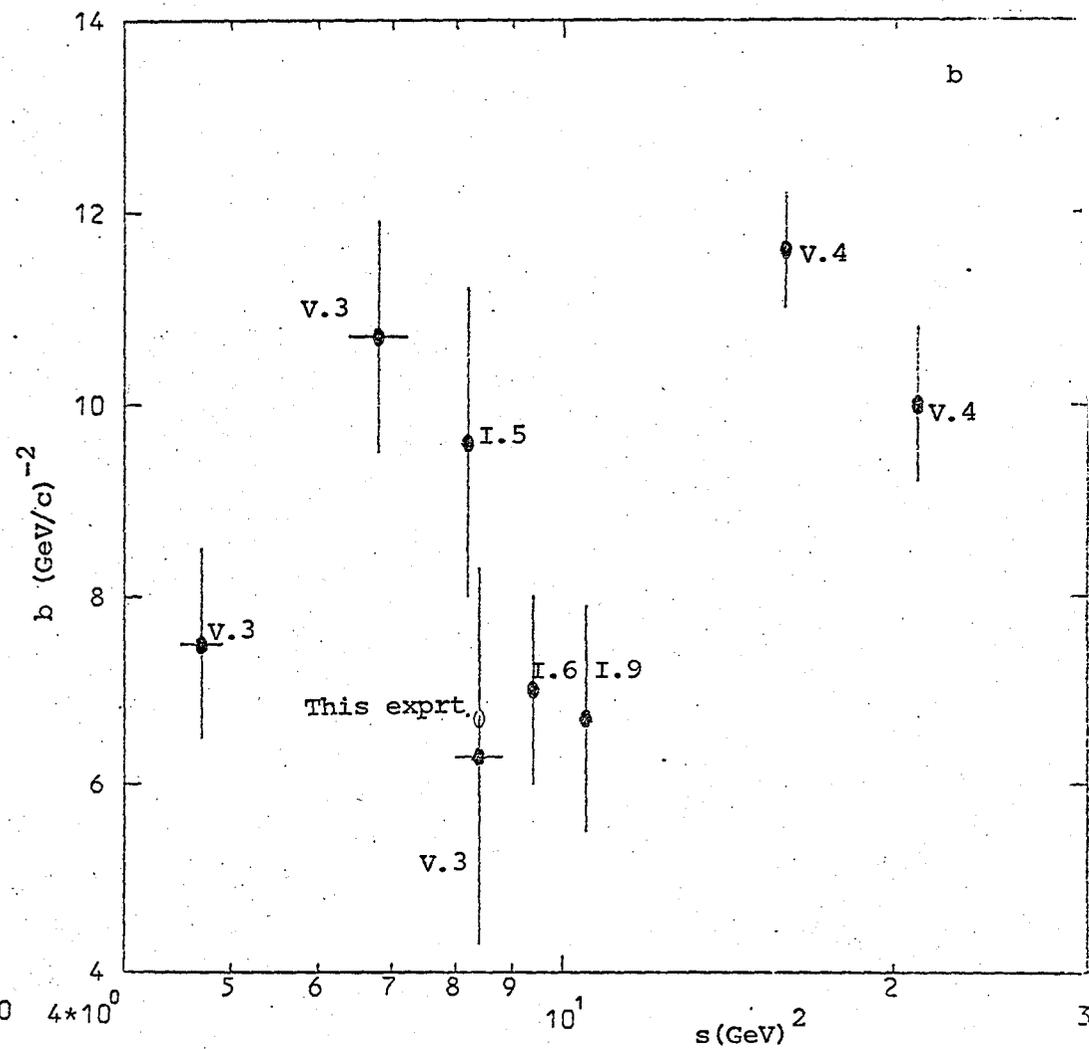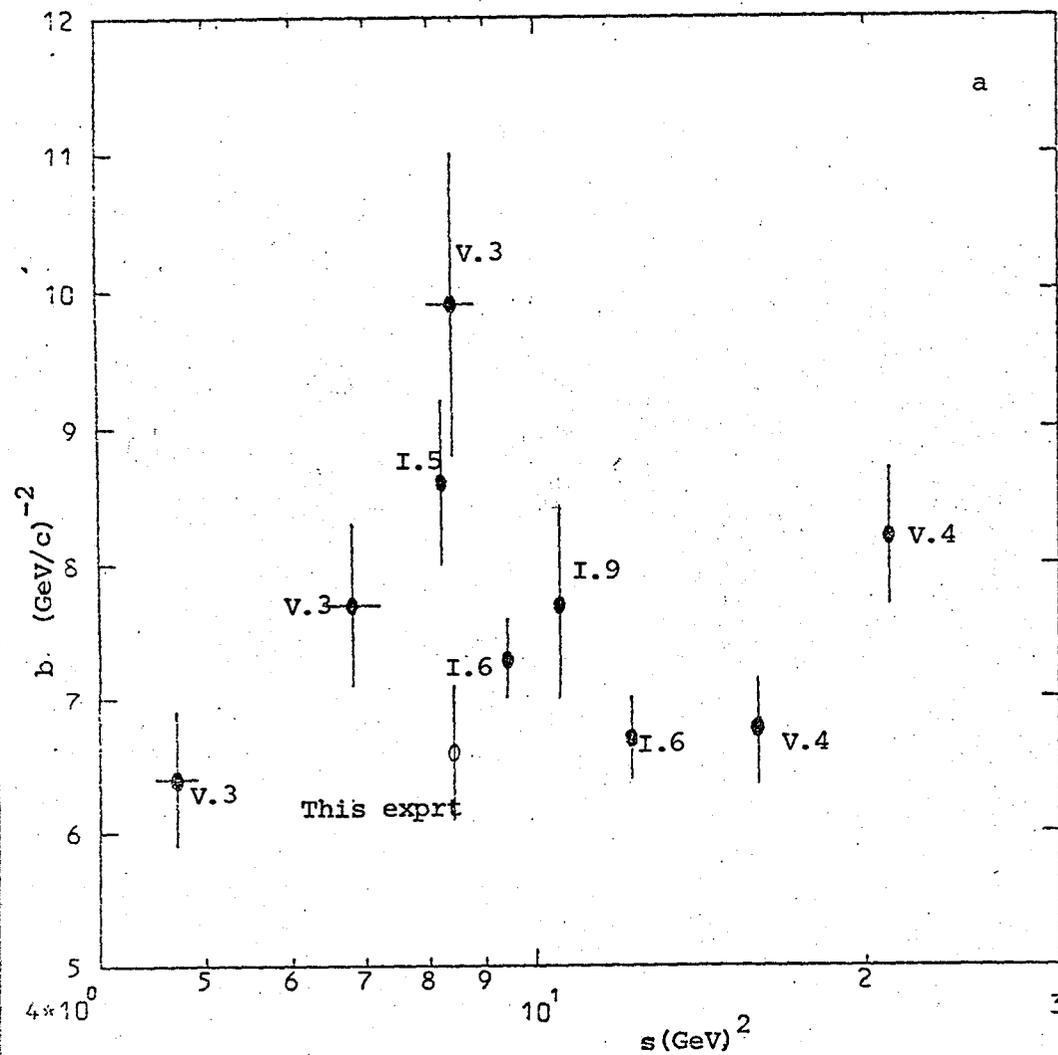
Fig.V.5 The slope parameter, b, as a function of s for the reactions (a) $\pi^+ n \to K^+ \Lambda^0$ and $\pi^- p \to K^0 \Lambda^0$ (b) $\pi^+ n \to K^+ \Sigma^0$ and $\pi^- p \to K^0 \Sigma^0$. The relevant references are given beside the data points.

$\hat{q}_i$ =   a unit vector along the decay proton direction in the Λ^o

            rest frame

$\hat{n}_i$ =   a unit vector along the production plane normal, $\hat{n}$ =

            $(q_\pi \times q_K)/|q_\pi \times q_K|$ where q_π and q_K are the three-

            momenta of the beam and K^+ respectively.

The results are shown in table V.2 (a) and figure V.6(a). Although the errors are large the polarisation appears to be positive for $t' \lesssim 0.35$ $(GeV/c)^2$ and negative for $t' \gtrsim 0.35$ $(GeV/c)^2$. It should be noted that the cross-over point occurs at approximately the same position as the discontinuity in the differential cross-section, a feature which is also present in the data for the charge-symmetric reaction at similar beam momentum (refs. I.5 and I.6).

The Σ^o polarisation has been calculated using

$$P_{\Sigma^o} = \frac{-9}{\alpha_\Lambda N} \sum_{i-1}^{N} (\hat{q}_i \cdot \hat{r}_i)(\hat{r}_i \cdot \hat{n}_i) \qquad \text{(V.26)}$$

where $\hat{r}_i$ is a unit vector along the direction of the Λ^o in the Σ^o rest frame. The results are given in table V.2 (b) and figure V. 6 (b).

At low values of t the two processes are expected to be dominated by K^* (890) and K^* (1420) exchange, the only allowed exchanges which are well established. Using the assumption of weak exchange degeneracy ($\alpha_{K^*(890)}(t) = \alpha_{K^*(1420)}(t)$), one can relate $\pi^+ n \rightarrow K^+ \Lambda^o$ to the line-reversed reaction, $K^- n \rightarrow \pi^- \Lambda^o$, at the same C.M. energy since both are mediated by the same exchange processes. Similarly $\pi^+ n \rightarrow K^+ \Sigma^o$ may be related to $K^- n \rightarrow \pi^- \Sigma^o$. The relationships which are obtained in this way are as follows:

TABLE V.2

HYPERON POLARISATION

(a) $\pi^+ n \rightarrow K^+ \Lambda^0$

(b) $\pi^+ n \rightarrow K^+ \Sigma^0$

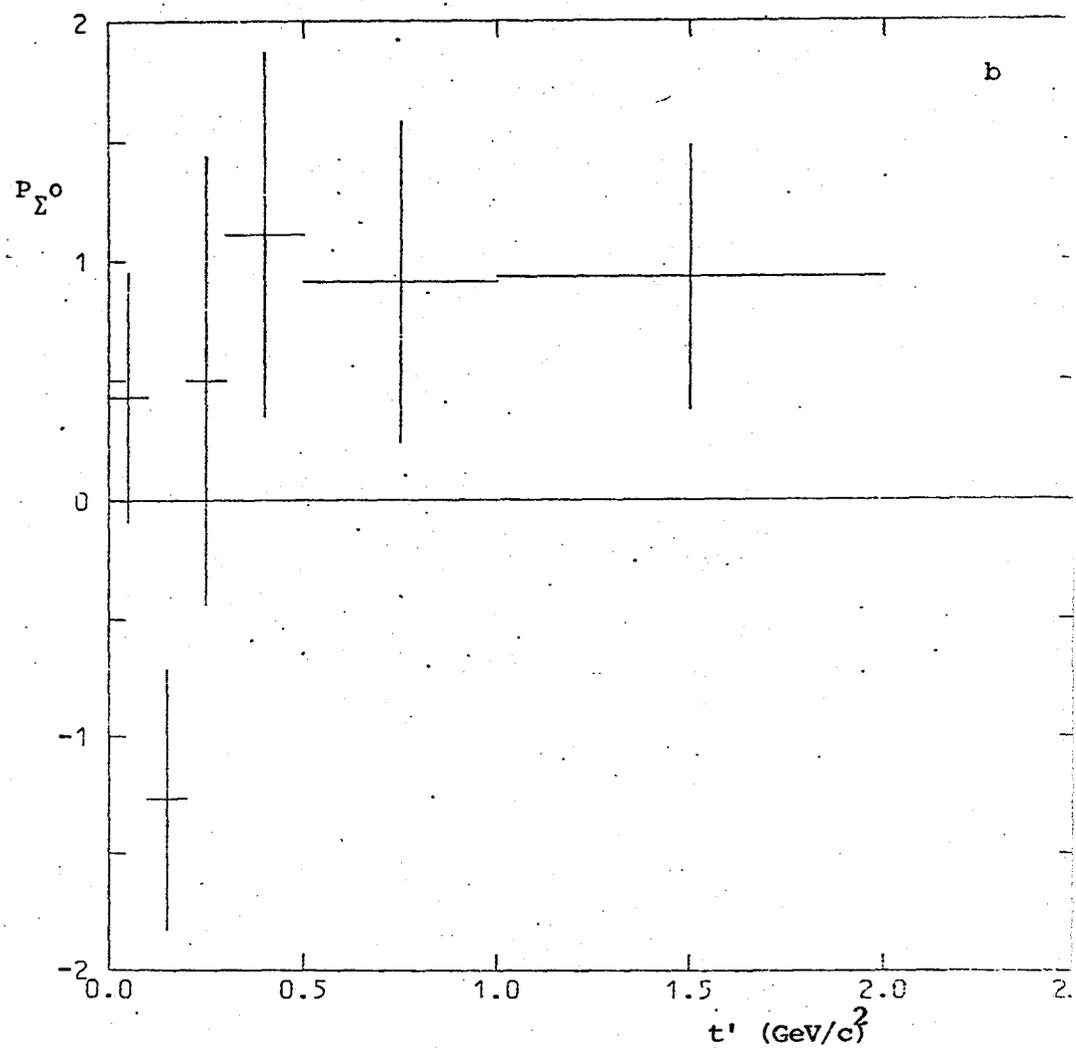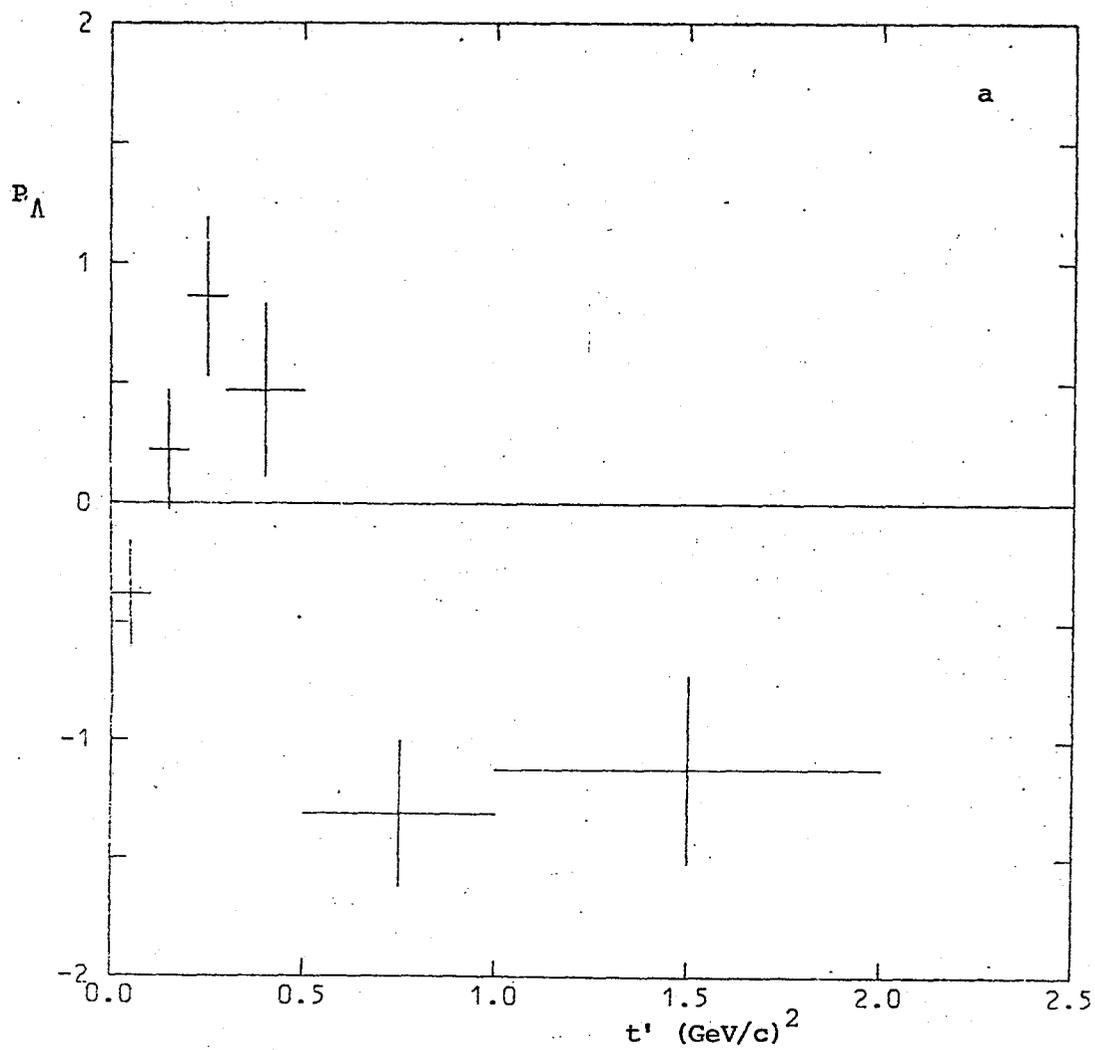| t' range $(GeV/c)^2$	P_Λ	t' range $(GeV/c)^2$	P_{Σ^0}
0 - 0.1	-0.38 ± 0.22	0 - 0.1	0.43 ± 0.52
0.1 - 0.2	0.22 ± 0.25	0.1 - 0.2	-1.27 ± 0.56
0.2 - 0.3	0.86 ± 0.33	0.2 - 0.3	0.50 ± 0.94
0.3 - 0.5	0.47 ± 0.36	0.3 - 0.5	1.11 ± 0.76
0.5 - 1.0	-1.31 ± 0.31	0.5 - 1.0	0.91 ± 0.67
1.0 - 2.0	-1.12 ± 0.40	1.0 - 2.0	0.93 ± 0.55

Fig.V.6 Hyperon polarisation for the reactions (a) $\pi^+ n \rightarrow K^+ \Lambda^0$ (b) $\pi^+ n \rightarrow K^+ \Sigma^0$
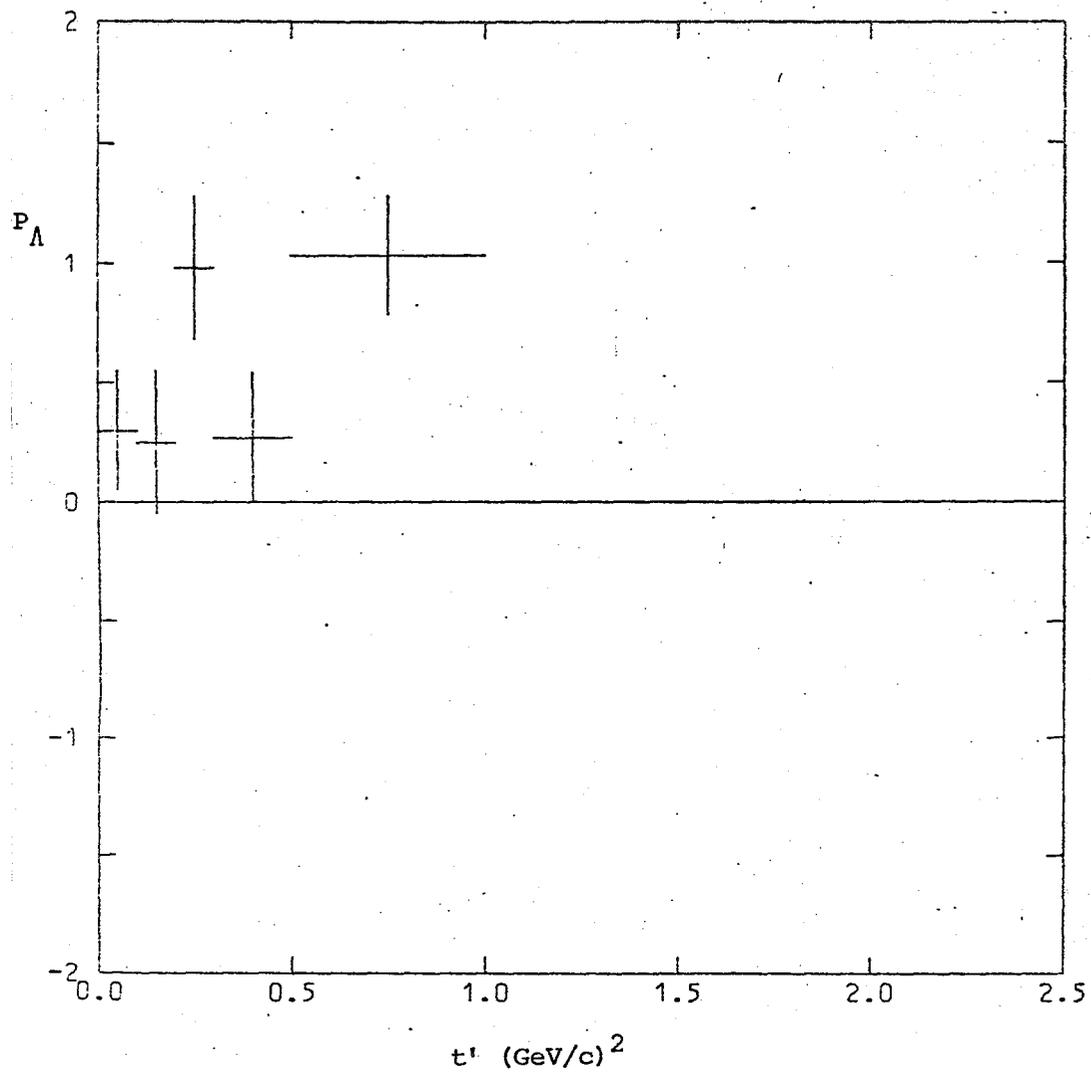
Fig.V.6 (c) Hyperon Polarisation for the reaction $K^- n \rightarrow \pi^- \Lambda^0$ at 3.9 GeV/c (ref. V.5)

$$\frac{d\sigma}{dt} \quad (\pi^+ n \rightarrow K^+ \Lambda^0) = \frac{d\sigma}{dt} \quad (K^- n \rightarrow \pi^- \Lambda^0) \tag{V.27}$$

$$P_\Lambda \quad (\pi^+ n \rightarrow K^+ \Lambda^0) = -P_\Lambda \quad (K^- n \rightarrow \pi^- \Lambda^0) \tag{V.28}$$

$$\frac{d\sigma}{dt} \quad (\pi^+ n \rightarrow K^+ \Sigma^0) = \frac{d\sigma}{dt} \quad (K^- n \rightarrow \pi^- \Sigma^0) \tag{V.29}$$

$$P_{\Sigma^0} \quad (\pi^+ n \rightarrow K^+ \Sigma^0) = -P_{\Sigma^0} \quad (K^- n \rightarrow \pi^- \Sigma^0) \tag{V.30}$$

If in addition the pole residues are assumed equal (strong exchange degeneracy), the hyperon polarisation must be identically zero. This prediction on polarisation is clearly not satisfied by the data.

The forward differential cross-section for the line-reversed reaction, $K^- n \rightarrow \pi^- \Lambda^0$, has been fitted at a beam momentum of 3.9 GeV/c by Crennell et al (ref. V.5) using the empirical formula of equation (V.24). The fitted value for the slope parameter was (4.2 ± 0.5) $(GeV/c)^{-2}$, which is significantly lower than the value of (6.6 ± 0.5) $(GeV/c)^{-2}$ obtained for $\pi^+ n \rightarrow K^+ \Lambda^0$ from this experiment, and therefore in direct contradiction with the prediction of weak exchange degeneracy (equation (V.27)). The Λ^0 polarisation was also determined for $K^- n \rightarrow \pi^- \Lambda^0$ and is presented in figure V.6 (c) for comparison with the polarisation from $\pi^+ n \rightarrow K^+ \Lambda^0$. Equation (V.28) is clearly not satisfied by the data.

Yen et al. (ref. V.6) have obtained a value of (5.1 ± 2.0) $(GeV/c)^{-2}$ for the $K^- n \rightarrow \pi^- \Sigma^0$ slope parameter at a beam momentum of 4.48 GeV/c. This agrees with the value of (6.7 ± 0.9) $(GeV/c)^2$ obtained for $\pi^+ n \rightarrow K^+ \Sigma^0$ from this experiment within the large errors quoted. However a systematic investigation by Crennell et al. (ref. I.6) for beam momenta ranging from 1.9 - 4.5 GeV/c has revealed that the slope parameter for $\pi^- p \rightarrow K^0 \Sigma^0$ (the charge-symmetric reaction) is on

average $\sim$ 1.6 times that for $K^- n \rightarrow \pi^- \Sigma^0$. No polarisation data exist

for $K^- n \rightarrow \pi^- \Sigma^0$, so that it is not possible to check relation (V.30).

An earlier experimental review of exchange degeneracy is given in

ref. V.7.

Assuming the absence of any exotic-meson $(I = \frac{3}{2}, S = 1)$ exchange

the differential cross-section for the reaction $\pi^+ p \rightarrow K^+ \Sigma^+$ should be

twice that for $\pi^+ n \rightarrow K^+ \Sigma^0$. Using the data of Pruss et al. (ref. I.2)

for a beam momentum of 4.0 GeV/c the weighted average for the ratio is

2.1 ± 0.2 for $t' < 0.4$ $(GeV/c)^2$. This is consistent with no $I = \frac{3}{2}$,

$S = 1$ exchange in either reaction.

From SU(3) considerations and octet dominance (ref. V.8), the

hyperon polarisation is expected to change sign under $\Lambda \rightarrow \Sigma$ interchange.

This is supported by the data for the reactions $\pi^+ n \rightarrow K^+ \Lambda^0$ and

$\pi^+ n \rightarrow K^+ \Sigma^0$ (Figures V. (a) and (b)) although the cross-over point for

the Σ^0 reaction occurs at a slightly lower value of t'.

At $t' \sim 0$ the ratio of $\sigma(\pi^+ n \rightarrow K^+ \Sigma^0)/\sigma (\pi^+ n \rightarrow K^+ \Lambda^0) = 0.70 \pm 0.12$.

Since the overall helicity flip contribution is negligible at $t' \sim 0$,

this ratio may be related to the helicity non-flip amplitudes A_{++}^{Σ} and
A_{++}^{Λ}:

$$\left[\sigma(\pi^+ n \rightarrow K^+ \Sigma^0) \; / \; \sigma(\pi^+ n \rightarrow K^+ \Lambda^0) \right]_{t' \sim 0} \sim \left[\frac{A_{++}^{\Sigma}}{A_{++}^{\Lambda}} \right]^2$$

$$= \frac{\gamma_{\Sigma}^2}{\gamma_{\Lambda}^2} \qquad \text{(V.31)}$$

where γ_{Σ} and γ_{Λ} are the particle couplings at the baryon vertex for

helicity non-flip, assuming the $K^*(890)$ and $K^*(1420)$ couplings are

identical. The particle couplings are in turn related to the D/F ratio

for helicity non-flip (i.e. the ratio of symmetric to antisymmetric octet exchange):

$$\frac{\gamma_\Sigma^2}{\gamma_\Lambda^2} = 3 \left[\frac{1 - D/F}{3 + D/F} \right]^2 \qquad (V.32)$$

Taking the positive root yields a value for D/F of - 0.30 $\pm$ 0.08, which is compatible with the value of -0.26 $\pm$ 0.12 given by Michael and Odorico (ref V.8) for the photo production processes $\gamma p \rightarrow K^+ \Lambda^0$ and $\gamma p \rightarrow K^+ \Sigma^0$.

V.4.2 The reactions $\pi^+ n \rightarrow K^{*+}(890) \Lambda^0$, $\pi^+ n \rightarrow K^{*+}(890) \Sigma^0$ and $\pi^+ p \rightarrow K^{*+}(890) \Sigma^+$

The differential cross-sections for these reactions are given in table V.3 and figure V.7. Contamination from the strong $\Sigma^0(1385)$ signal which is present in the $\pi^+ n \rightarrow K^+ \Lambda^0 \pi^0$ channel has been reduced by rejecting those events with 1.25 GeV/c^2 $\lesssim$ M ($\Lambda^0 \pi^0$) < 1.50 GeV/c^2. Apart from this all events in the K^{*+} (890) mass band have been used. An alternative method of calculating the differential cross-section which takes into account the small amount of remaining background contamination is to estimate the resonance production in each separate t' bin. The results are shown in brackets in table V.3 for the Λ^0 reaction. Since both methods yield almost identical values for the differential cross-section, the background contamination may be assumed to be negligible. The forward differential cross-sections have been fitted with the empirical form of expression (V.24). The results are compared with those of Yaffe (ref. I.12), Crennell (ref. I.6) and Toet (ref. I.8) in table V.4. Crennell reports a flattening of the differential cross-sections at small t' for the Λ^0 and Σ^0 reactions, and Yaffe finds

TABLE V.3

DIFFERENTIAL CROSS-SECTIONS

(a) $\pi^+ n \to K^{*+}(890) \Lambda^0$ (b) $\pi^+ n \to K^{*+}(890) \Sigma^0 (*)$

t' range $(GeV/c)^2$	Events	$d\sigma/dt'$ $\mu b/(GeV/c)^2$		t' range $(GeV/c)^2$	Events	$d\sigma/dt'$ $\mu b/(GeV/c)^2$
0 – 0.1	108	100 ± 10	(90 ± 10)	0 – 0.1	16	31 ± 8
0.1 – 0.2	84	78 ± 9	(77 ± 9)	0.1 – 0.2	13	25 ± 7
0.2 – 0.3	76	71 ± 9	(71 ± 9)	0.2 – 0.3	12	23 ± 7
0.3 – 0.4	65	60 ± 8	(48 ± 5)	0.3 – 0.4	11	21 ± 6
0.4 – 0.5	47	44 ± 7		0.4 – 0.5	10	19 ± 6
0.5 – 0.6	35	33 ± 6		0.5 – 0.6	6	12 ± 5
0.6 – 0.7	34	32 ± 6		0.6 – 0.7	8	16 ± 5
0.7 – 0.8	26	24 ± 5	(25 ± 2)	0.7 – 0.8	8	16 ± 5
0.8 – 0.9	14	13 ± 4		0.8 – 1.1	6	3.9 ± 1.6
0.9 – 1.0	16	15 ± 4		1.1 – 1.8	6	1.6 ± 0.6
1.0 – 1.1	17	16 ± 4				
1.1 – 1.3	5	2.4 ± 1.2				
1.3 – 1.5	9	4.1 ± 1.4				
1.5 – 1.6	8	7.2 ± 2.8	(4.1 ± 0.7)			
1.6 – 1.9	7	2.3 ± 0.9				
1.9 – 2.1	5	2.4 ± 1.2				

(c) $\pi^+ p \to K^{*+}(890) \Sigma^+ (*)$

t' range $(GeV/c)^2$	Events	$d\sigma/dt'$ $\mu b/GeV/c)^2$
0 – 0.1	4	30 ± 15
0.1 – 0.2	9	68 ± 23
0.2 – 0.4	11	42 ± 12
0.4 – 0.6	9	34 ± 11
0.6 – 1.0	14	26 ± 7

(*) not corrected for the $K^{*+}(890) \to K^0 \pi^+$ decay mode.
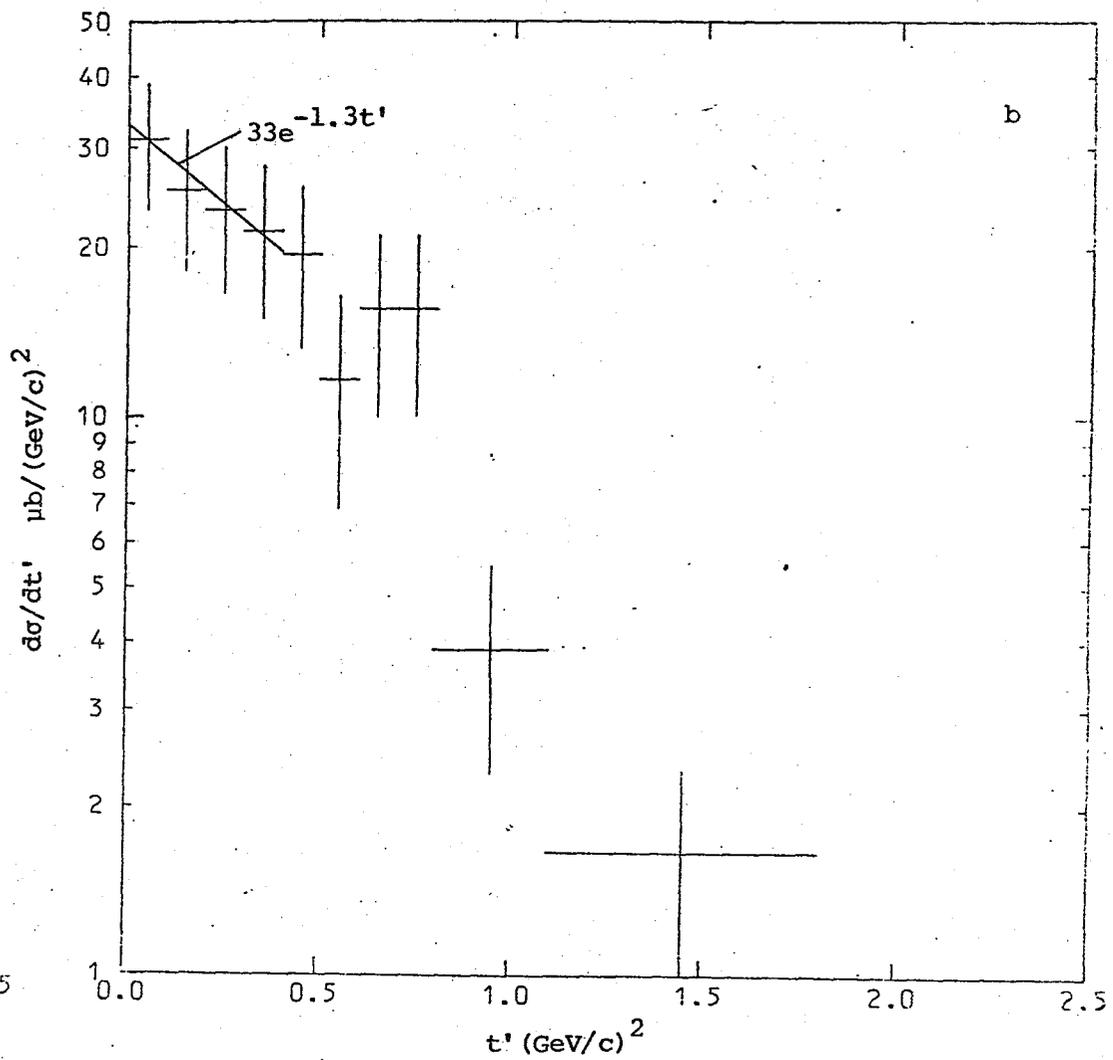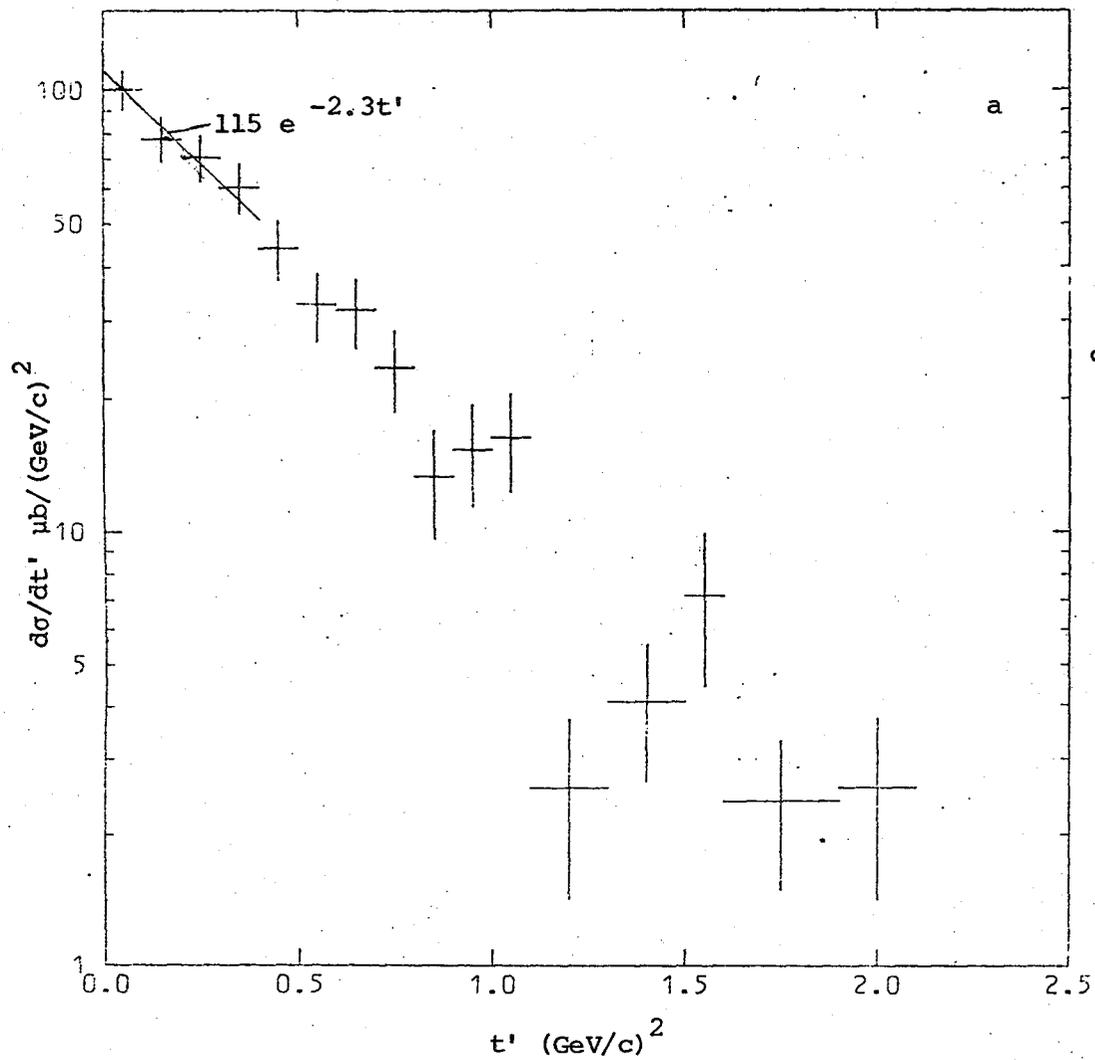
Fig V.7 Differential cross-section distributions for the reactions (a)$\pi^+ n \to K^{*+}(890) \Lambda^0$
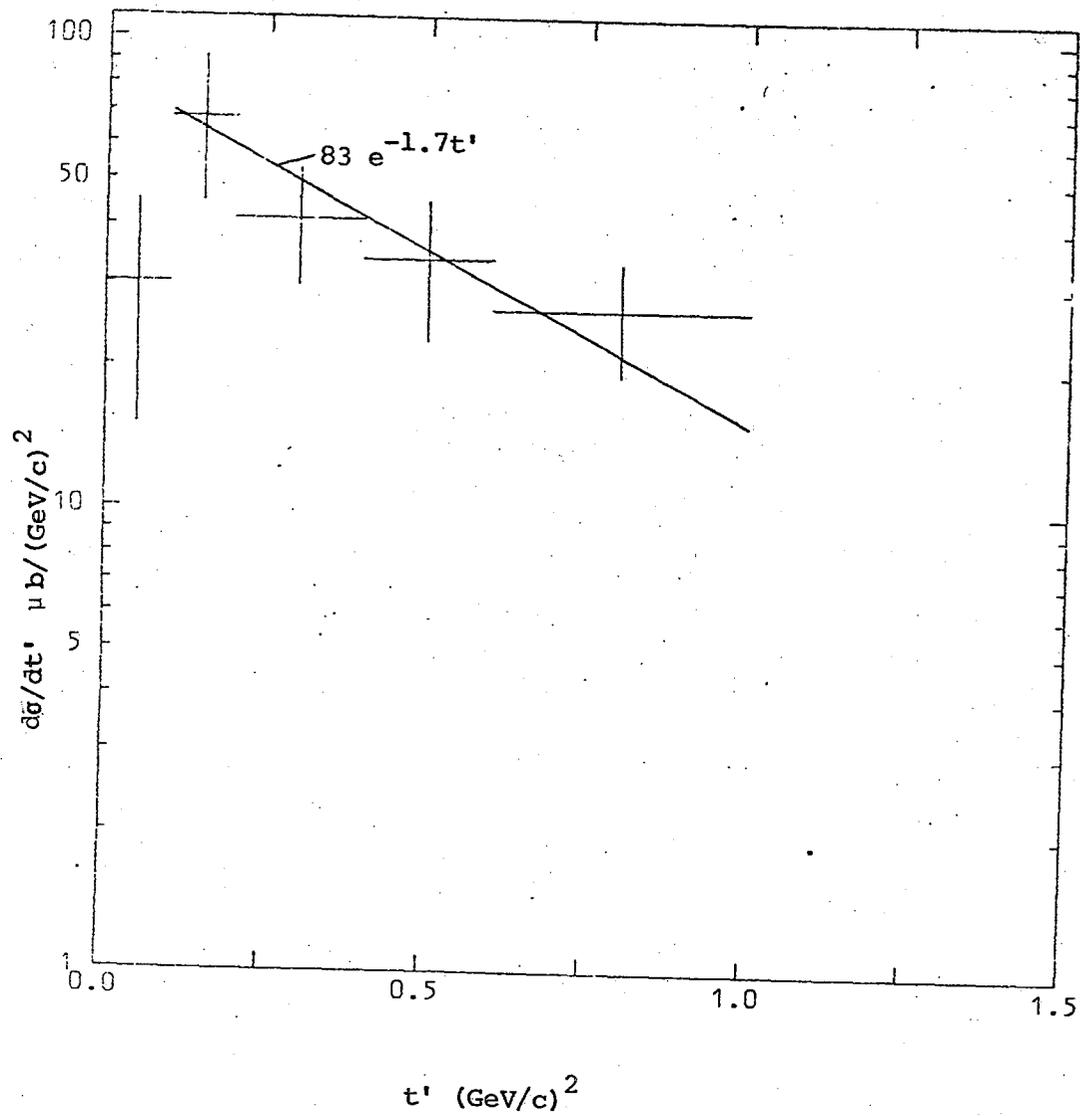
(b)$\pi^+ n \to K^{*+}(890) \Sigma^0$

Fig.V.7(c) Differential cross-section distribution for the reaction $\pi^+ p \rightarrow K^{*+}(890)\ \Sigma^+$

TABLE V.4

FITTED PARAMETERS IN $d\sigma/dt' = A \exp(-bt')$

Reaction	Beam momentum (GeV/c)	t' region (GeV/c)^2	A μb/(GeV/c)^2	b (GeV/c)$^{-2}$	Ref.
$\pi^- p \to K^{*0}(890) \Lambda^0$	3.93	0.0 - 1.2	-	2.20 ± 0.15	I.12
$\pi^+ n \to K^{*+}(890) \Lambda^0$	4.0	0.0 - 0.4	115 ± 14	2.3 ± 0.8	This expt.
$\pi^- p \to K^{*0}(890) \Lambda^0$	4.5	0.1 - 1.6	130 ± 11	2.5 ± 0.2	I.6
$\pi^- p \to K^{*0}(890) \Sigma^0$	3.93	0.1 - 1.2	-	2.50 ± 0.22	I.12
$\pi^+ n \to K^{*+}(890) \Sigma^0$	4.0	0.0 - 0.4	50 ± 6 (*)	1.3 ± 0.4	This expt.
$\pi^- p \to K^{*0}(890) \Sigma^0$	4.5	0.2 - 2.0	52 ± 8 (**)	2.1 ± 0.2	I.6
$\pi^+ p \to K^{*+}(890) \Sigma^+$	4.0	0.1 - 1.0	124 ± 12 (*)	1.7 ± 0.5	This expt.
$\pi^+ p \to K^{*+}(890) \Sigma^+$	5.0	0.1 - 1.0	-	3.3 ± 1.0	I.8

(*) corrected for the $K^{*+}(890) \to K^+ \pi^0$ decay mode.

(**) corrected for the $K^{*0}(890) \to K^0 \pi^0$ decay mode.

a marked dip at t' $\sim$0 for the Σ^o reaction. These features are not reproduced in the data from this experiment. Toet reports a dip at t' $\sim$ 0 in the Σ^+ reaction which is also present in the data from this experiment, indicating a strong overall helicity flip contribution.

The hyperon polarisation for the Λ^o reaction is given in table V.5 and figure V.8 (a) as a function of t'. The polarisation is negative for t' > 0.1 $(GeV/c)^2$ in agreement with the results of Yaffe (figure V.8 (b)). The average Σ^o polarisation for t' < 0.5 $(GeV/c)^2$ is 1.31 $\overset{+}{-}$ 0.79 to be compared with Yaffe's value of 1.04 $\overset{+}{-}$ 0.40.

The spin density matrix elements have been calculated as functions of t' for the K^{*+} (890) decay and are presented in table V.6 for the s- and t-channel helicity frames. The results are presented graphically in figures V.9, V.10 and V.11 for the Λ^o, Σ^o and Σ^+ reactions respectively. In the asymptotic limit of s/t the spin density matrix elements may be related to the natural (N) and unnatural (U) parity exchange contributions:

$$\rho_{11} + \rho_{1-1} = N^1$$

$$\rho_{11} - \rho_{1-1} = U^1 \qquad\qquad (V.33)$$

$$\rho_{00} = U^0$$

where the indices denote the helicity state of the K^{*+} (890). In all three reactions natural parity exchange appears to dominate for t' < 1.0 $(GeV/c)^2$. For the Λ^o and Σ^o reactions the dip in $(\rho_{11} + \rho_{1-1})$ at t' $\sim$ 0 is also present in Crennel's data, and indicates a strong over- all helicity flip contribution to the natural parity exchange. For strange meson exchange processes the unnatural parity contribution comes mainly from K exchange, and the natural parity contributions from K^* (890) and K^* (1420) exchange. The values of ρ_{00} for the Σ^o and Σ^+

TABLE V.5

HYPERON POLARISATION FOR $\pi^+ n \rightarrow K^{*+}(890) \Lambda^o$

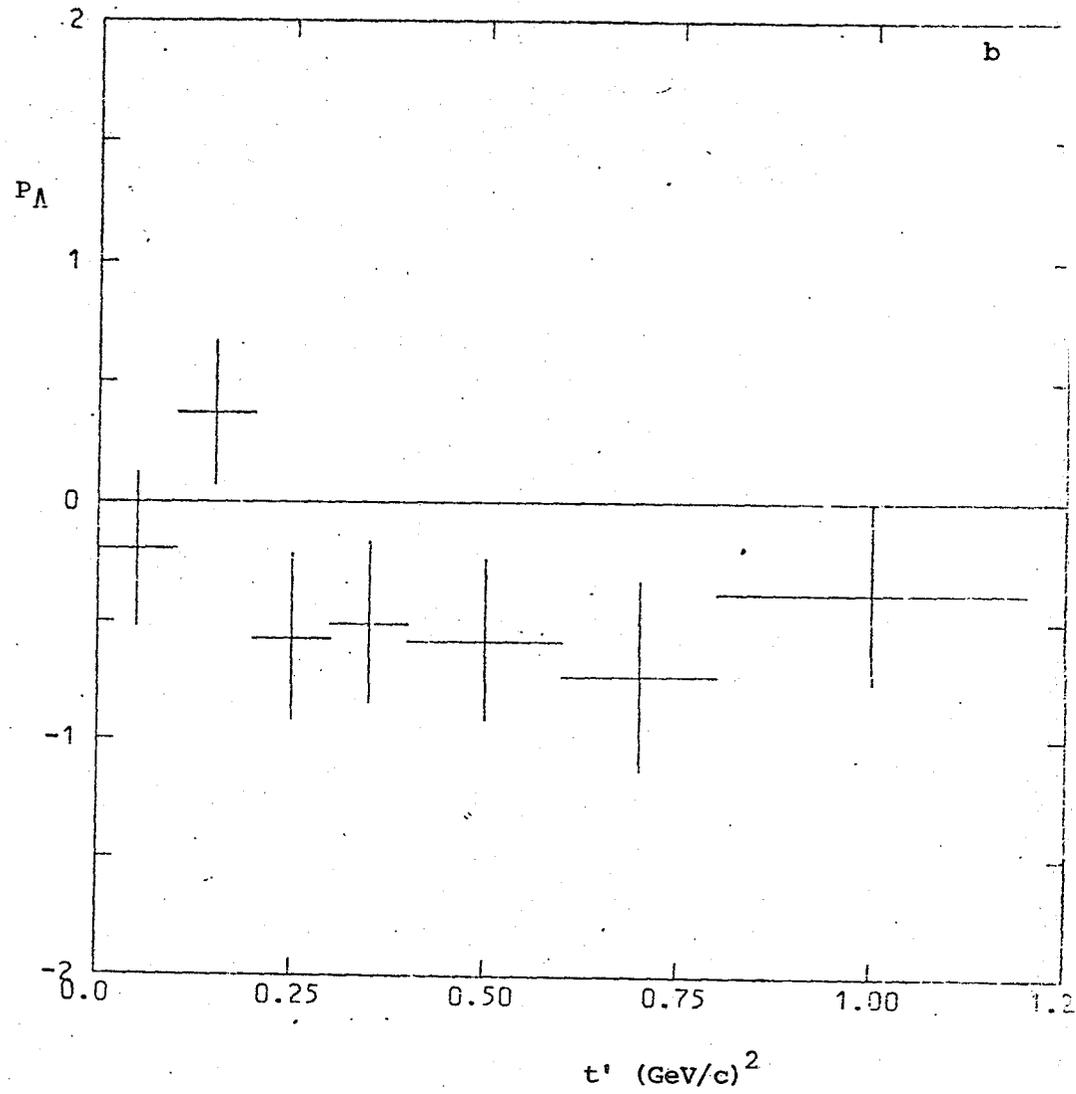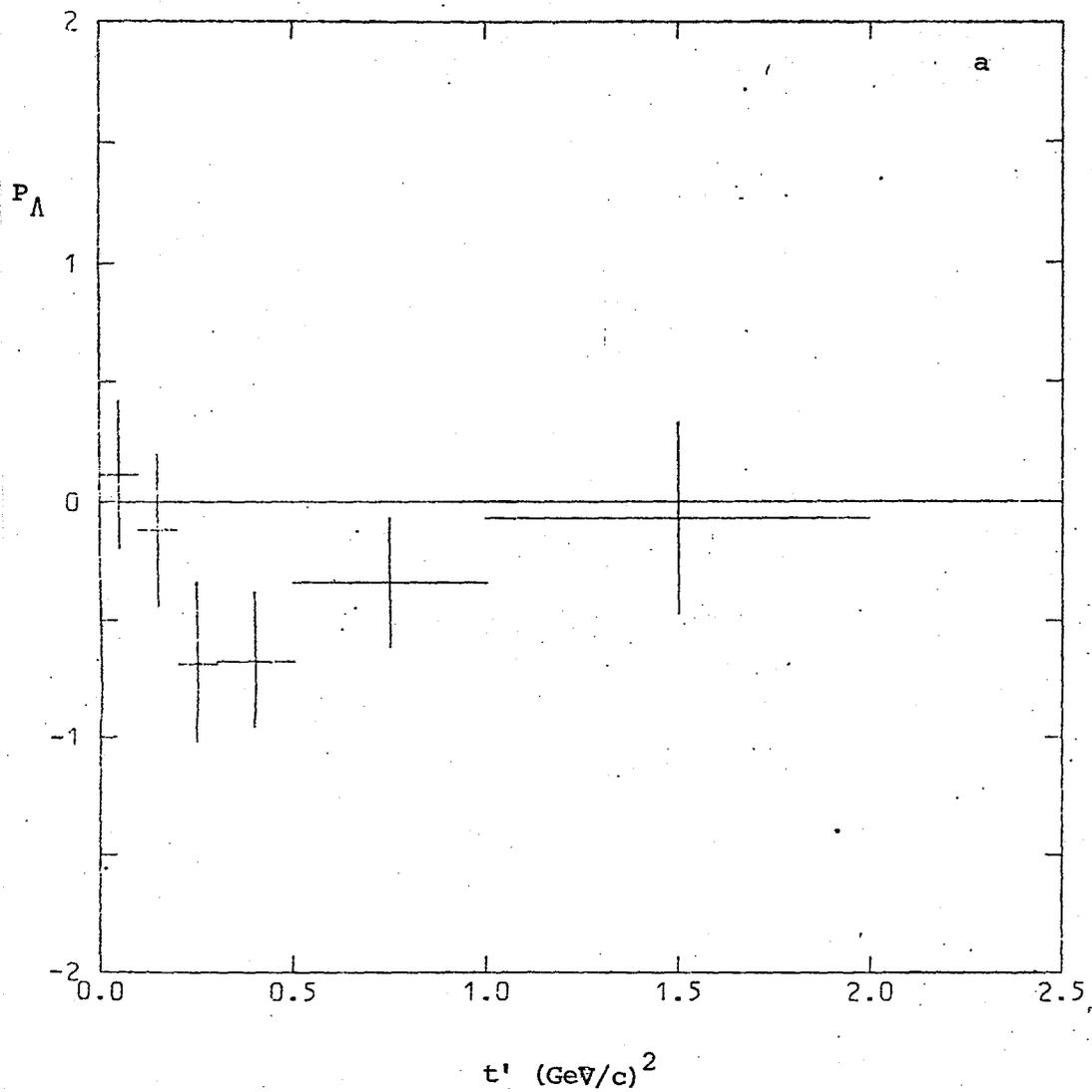| t' range (GeV/c)^2	P_Λ
0 - 0.1	0.11 ± 0.31
0.1 - 0.2	-0.12 ± 0.32
0.2 - 0.3	-0.68 ± 0.34
0.3 - 0.5	-0.67 ± 0.29
0.5 - 1.0	-0.34 ± 0.27
1.0 - 2.0	-0.07 ± 0.40

Fig.Ⅴ.8.　Hyperon polarisation for the reactions　(a) $\pi^+ n \rightarrow K^{*+}(890) \Lambda^0$　at 4 GeV/c (this exprt.)

(b) $\pi^- p \rightarrow K^{*+}(890) \Lambda^0$　at 3.93 GeV/c (ref. I.12)

TABLE V.6

SPIN DENSITY MATRIX ELEMENTS FOR K^{*+} (890)

(a) $\pi^+ n \to K^{*+}(890)\ \Lambda^0$

t' region $(\text{GeV}/c)^2$	ρ_{00}		ρ_{1-1}		Re ρ_{10}	
	s-channel	t-channel	s-channel	t-channel	s-channel	t-channel
< 2.0	0.35±0.03	0.27±0.03	0.13±0.03	0.09±0.03	0.03±0.02	-0.03±0.02
0 - 0.1	0.52±0.08	0.50±0.07	0.09±0.06	0.08±0.06	0.02±0.04	-0.08±0.04
0.1 - 0.2	0.24±0.08	0.21±0.07	0.19±0.07	0.17±0.07	-0.02±0.04	0.01±0.05
0.2 - 0.3	0.30±0.08	0.29±0.09	0.18±0.07	0.18±0.07	0.06±0.05	-0.07±0.04
0.3 - 0.5	0.21±0.06	0.27±0.07	0.15±0.06	0.18±0.05	0.03±0.04	-0.03±0.04
0.5 - 1.0	0.36±0.06	0.21±0.06	0.09±0.06	0.02±0.06	0.01±0.04	0.01±0.04
1.0 - 2.0	0.45±0.10	0.07±0.07	0.06±0.07	-0.13±0.09	0.08±0.06	-0.02±0.06

(b) $\pi^+ n \to K^{*+}(890)\ \Sigma^0$

t' region $(\text{GeV}/c)^2$	ρ_{00}		ρ_{1-1}		Re ρ_{10}	
	s-channel	t-channel	s-channel	t-channel	s-channel	t-channel
< 1.0	0.08±0.07	0.15±0.07	0.34±0.07	0.37±0.07	-0.01±0.04	-0.01±0.04
0 - 0.2	0.19±0.12	0.10±0.12	0.26±0.12	0.22±0.12	-0.05±0.07	-0.04±0.08
0.2 - 0.5	-0.01±0.11	0.19±0.13	0.41±0.12	0.50±0.10	0.09±0.05	-0.05±0.06
0.5 - 1.0	0.06±0.12	0.15±0.10	0.34±0.10	0.38±0.12	-0.08±0.07	0.06±0.06

(c) $\pi^+ p \to K^{*+}(890)\ \Sigma^+$

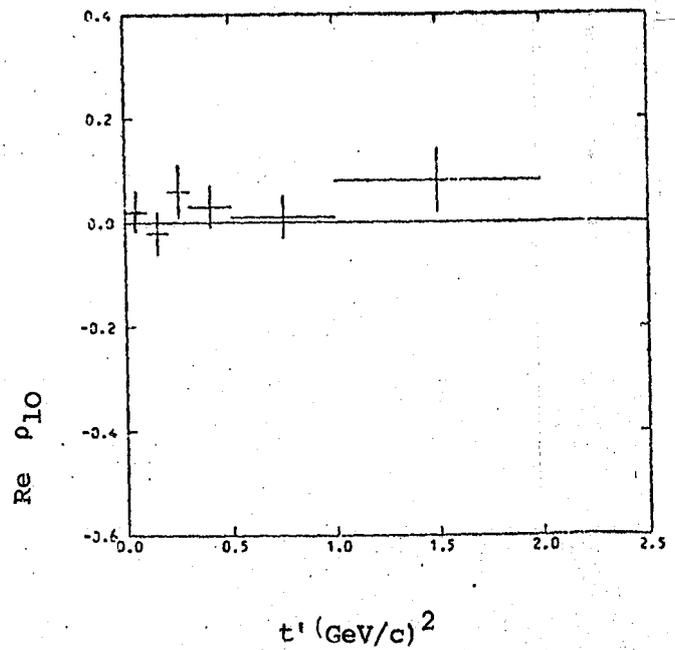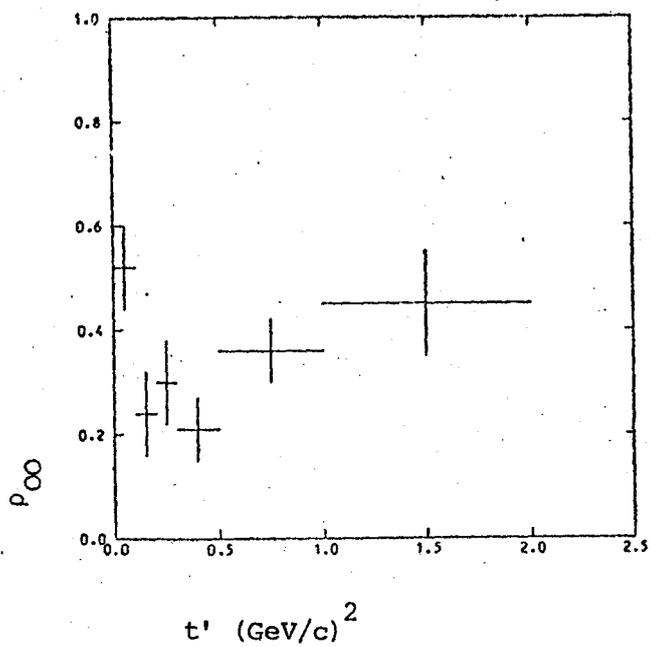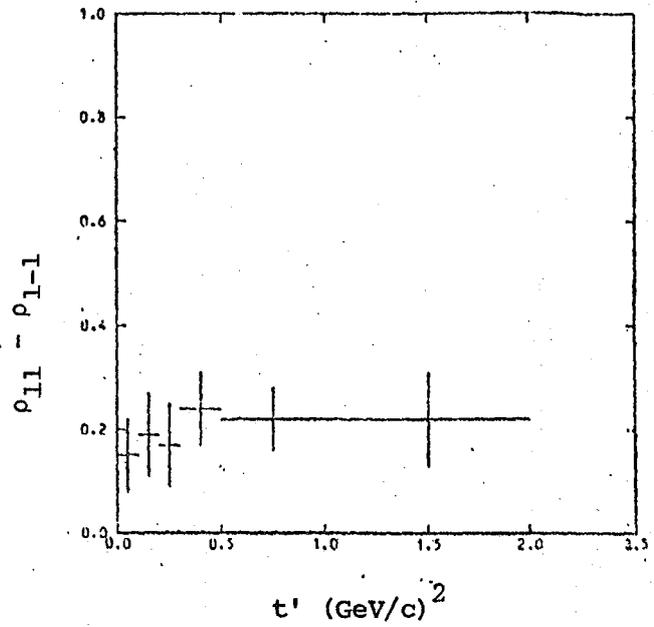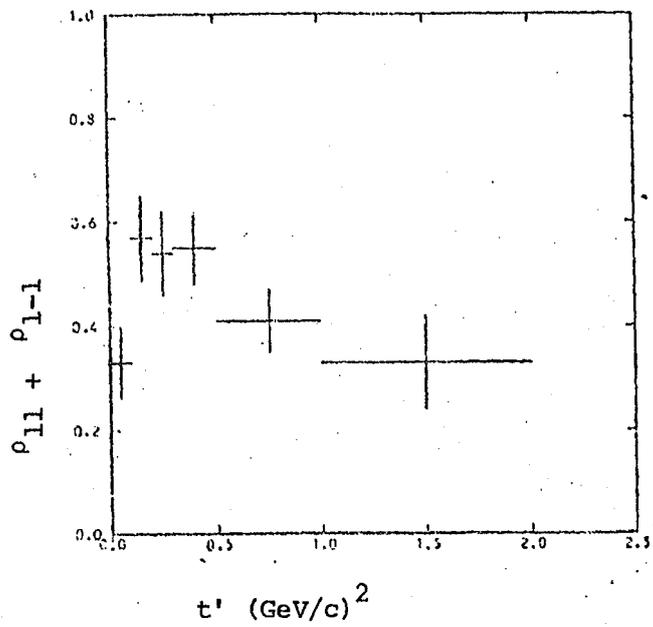| t' region $(\text{GeV}/c)^2$	ρ_{00}		ρ_{1-1}		Re ρ_{10}	
	s-channel	t-channel	s-channel	t-channel	s-channel	t-channel
< 1.0	0.08±0.09	0.20±0.10	0.18±0.09	0.24±0.08	-0.01±0.05	0.05±0.05
0 - 0.2	0.01±0.10	-0.01±0.15	0.11±0.18	0.10±0.16	-0.11±0.11	0.18±0.09
0.2 - 0.5	0.15±0.19	0.33±0.16	0.16±0.14	0.26±0.16	0.07±0.08	-0.04±0.09
0.5 - 1.0	0.05±0.13	0.21±0.18	0.24±0.16	0.32±0.11	-0.01±0.08	0.02±0.08

Fig. V.9   Spin density matrix elements in the s-channel helicity frame
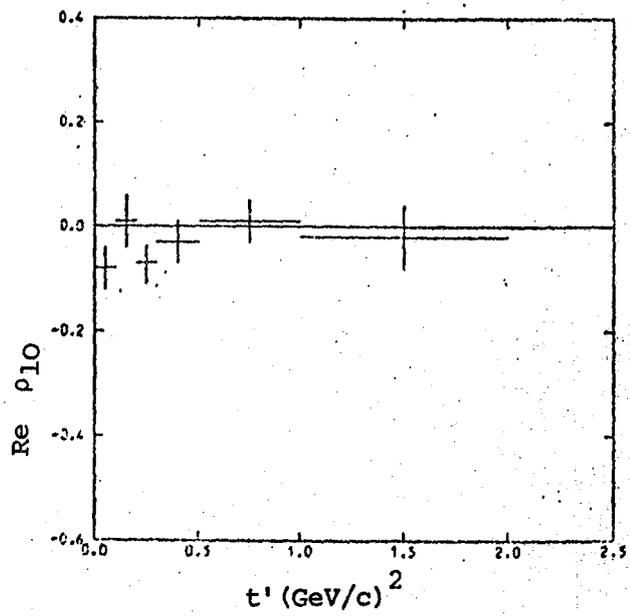   for the reaction $\pi^+ n \rightarrow K^{*+}(890) \Lambda^0$

Fig. V.9 (Cont.) Spin density matrix elements in the t-channel helicity
frame for the reaction $\pi^+ n \to K^{*+}(890) \Lambda^0$
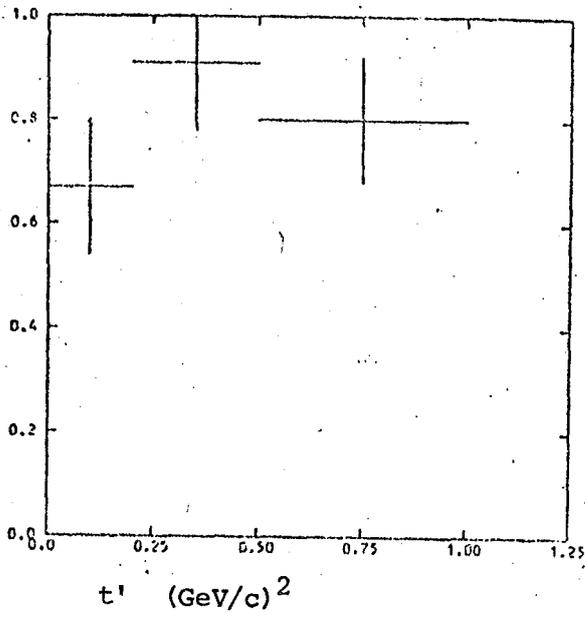
Fig.v.10   Spin   density matrix elements in the s-channel
           helicity frame for the reaction $\pi^+ n \to K^{*+}(890)\ \Sigma^0$
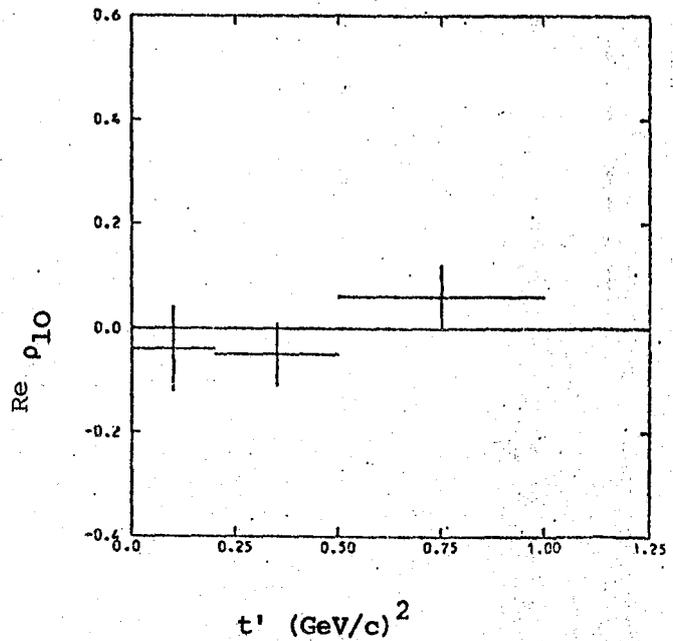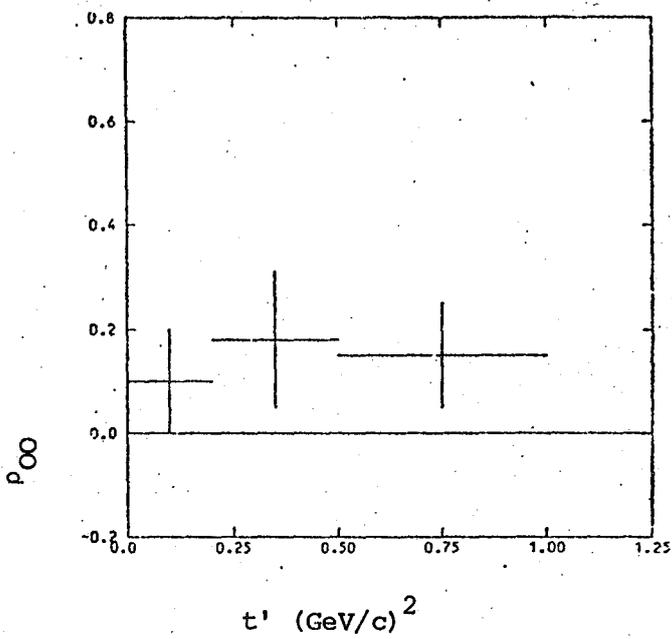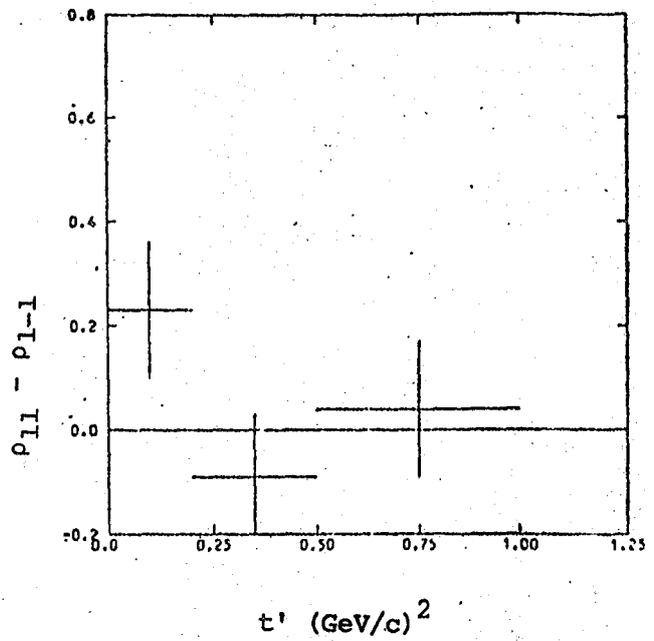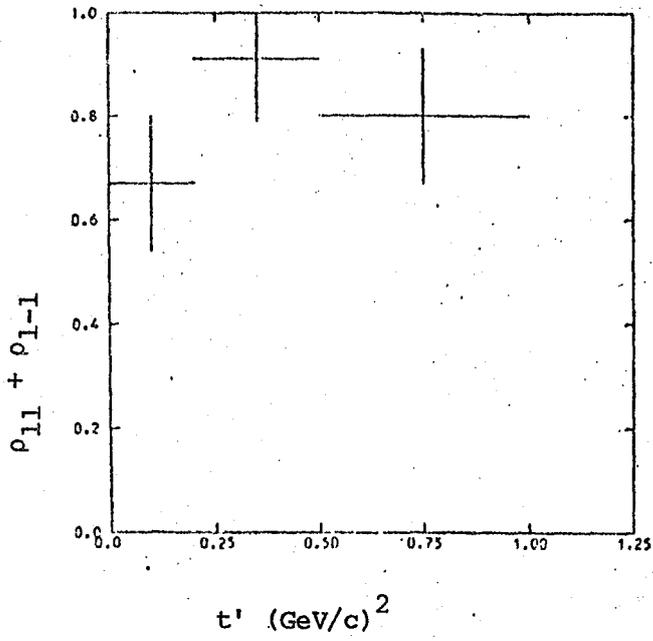
Fig.VI.10 (Cont.) Spin density matrix elements in the t-channel
helicity frame for the reaction $\pi^+ n \to K^{*+}(890)\ \Sigma^0$
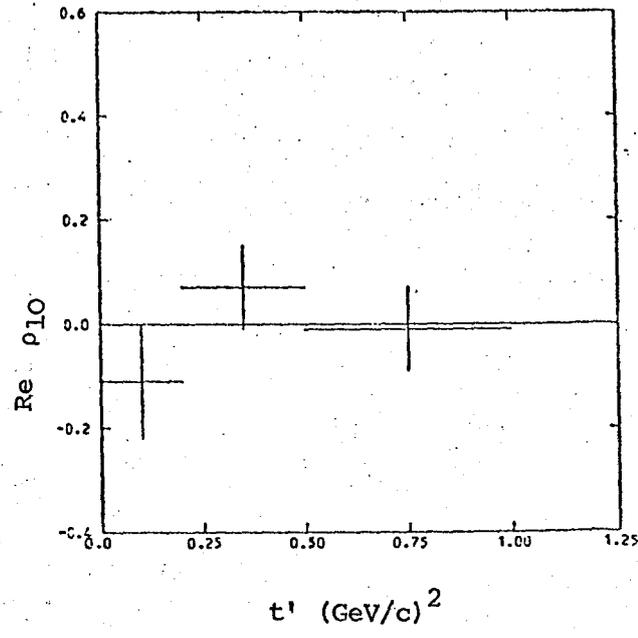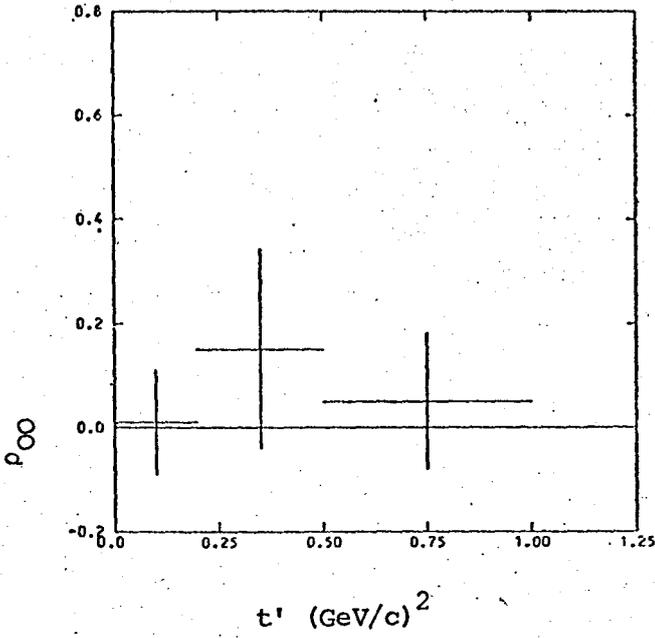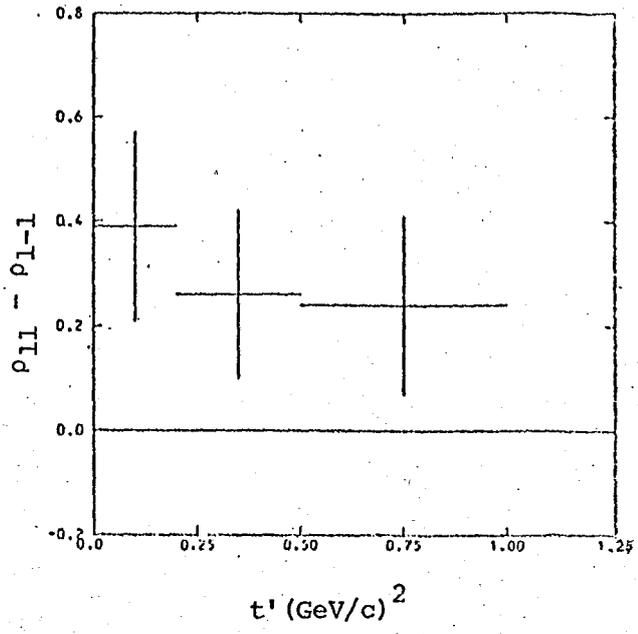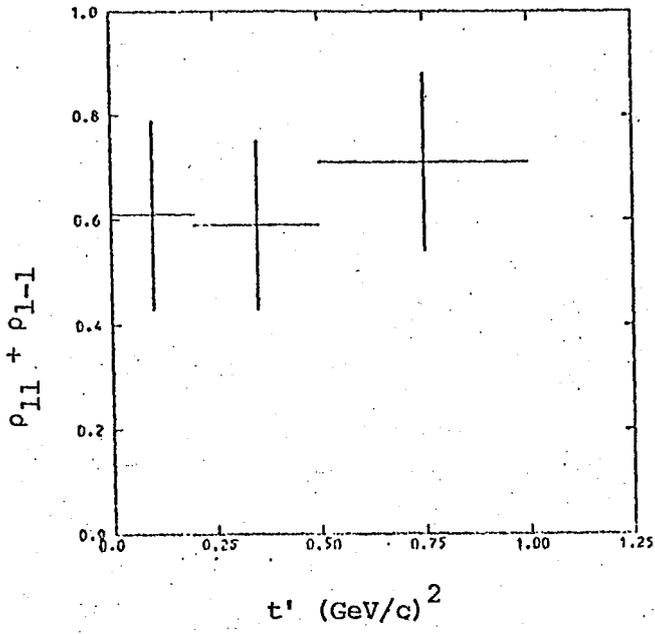
Fig.V.11 Spin density matrix elements in the s-channel helicity
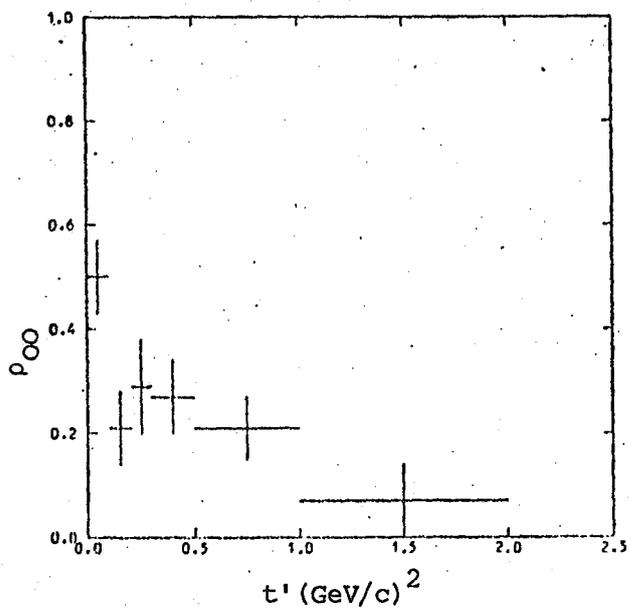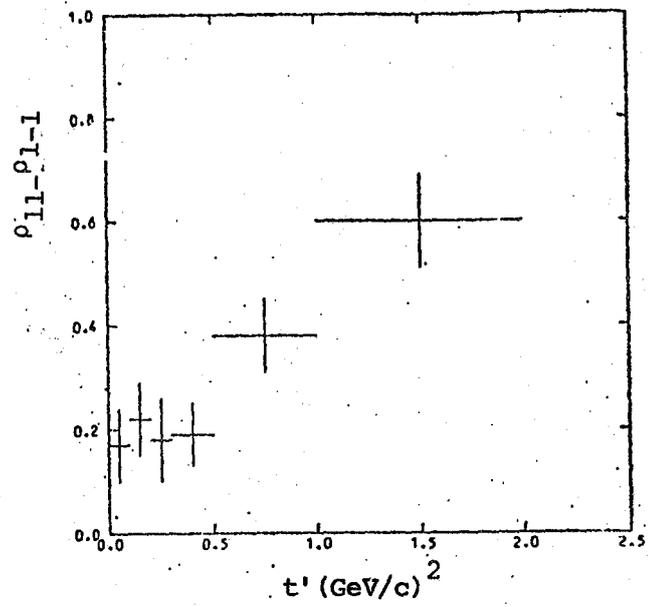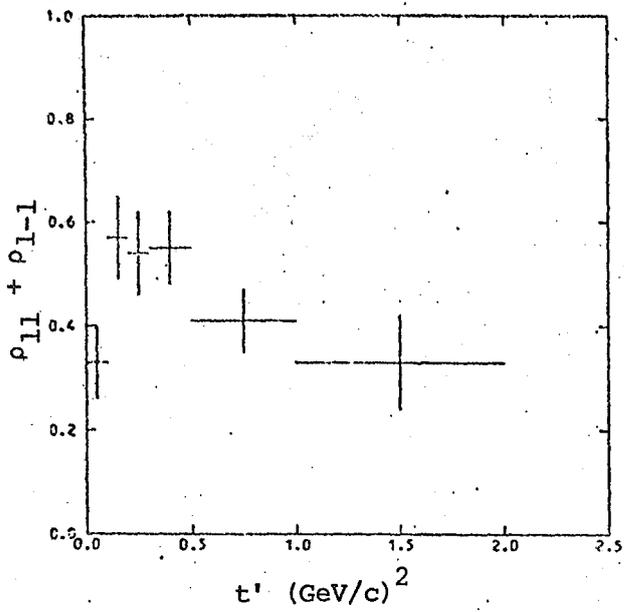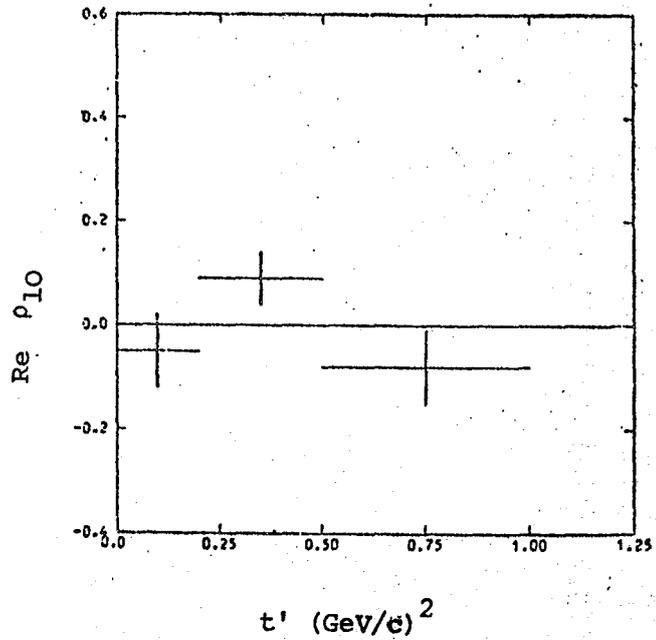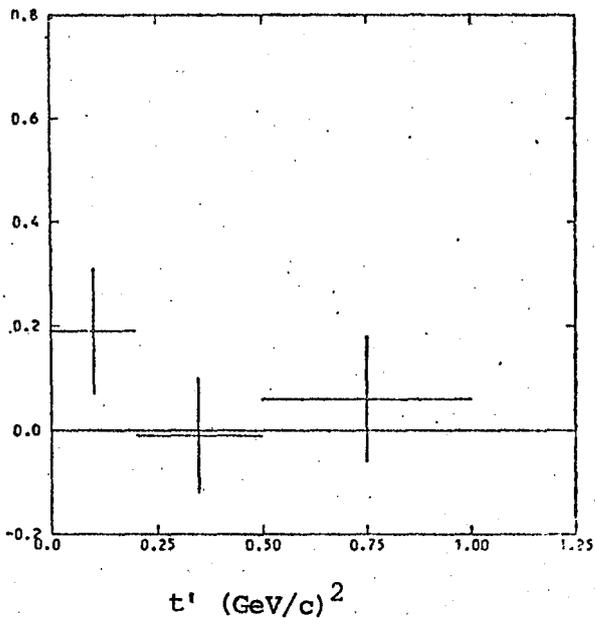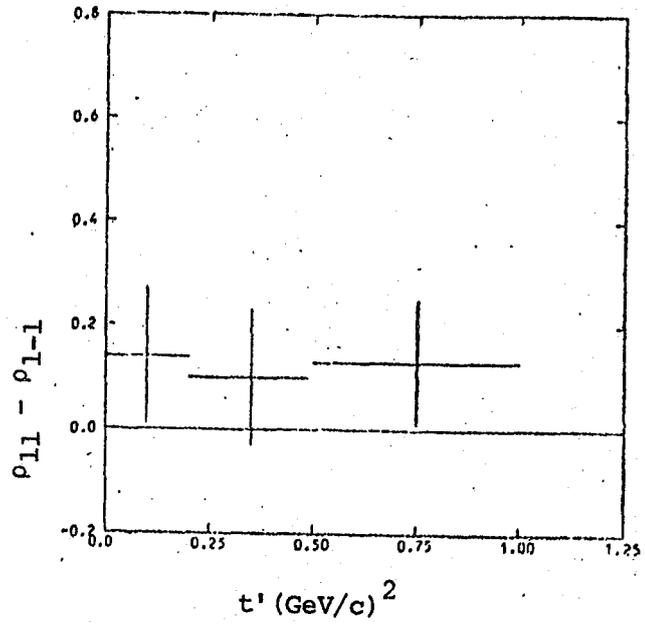frame for the reaction $\pi^+ p \rightarrow K^{*+}(890) \Sigma^+$
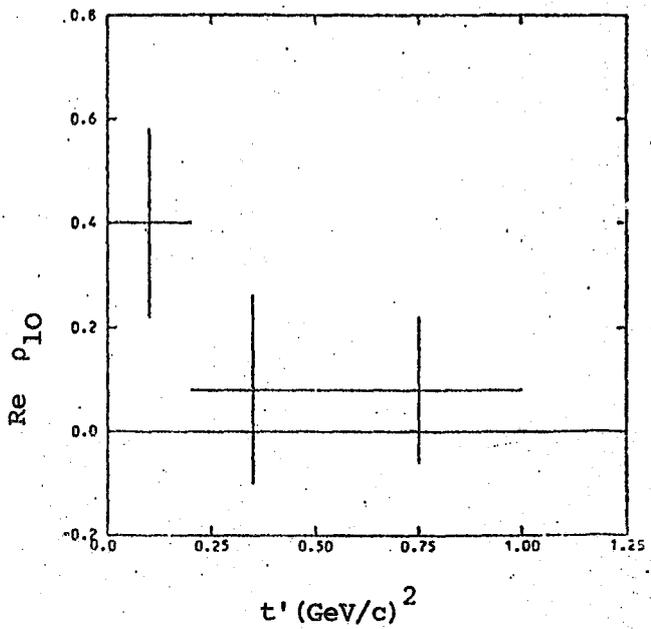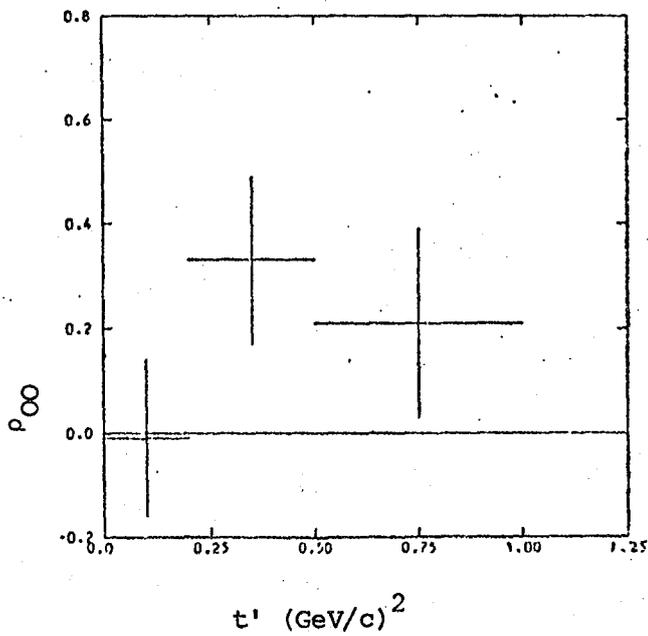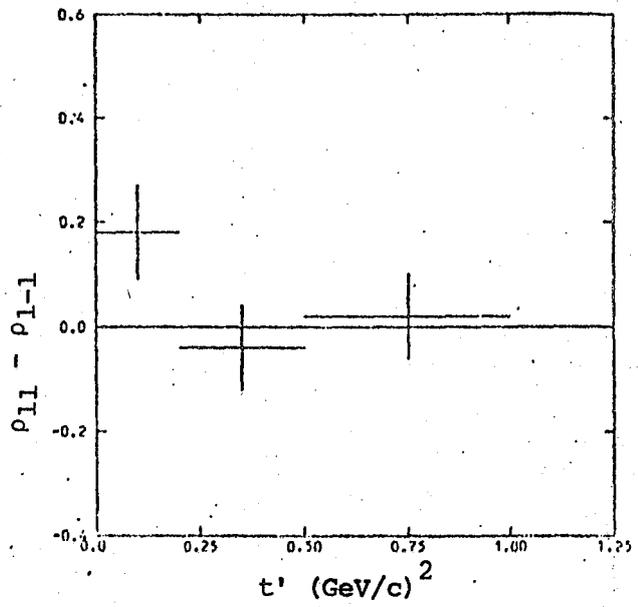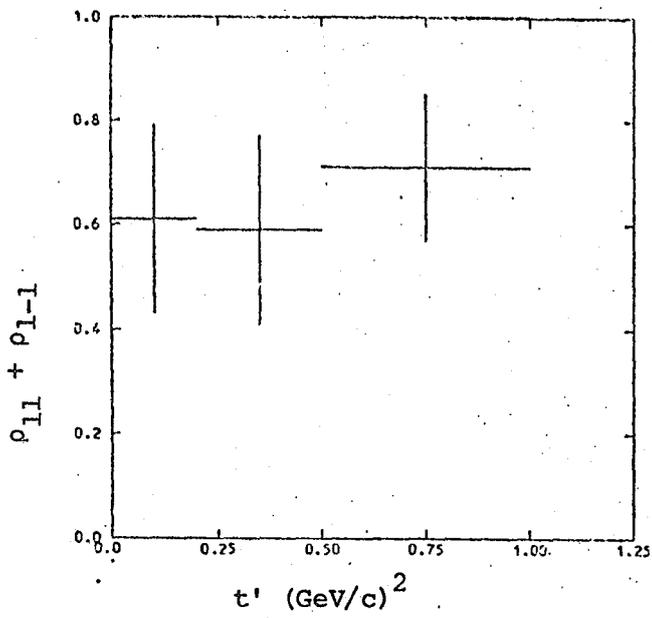
Fig.V.11 (Cont.)   Spin density matrix elements in the t-channel
            helicity frame for the reaction $\pi^+ p \rightarrow K^{*+}(890) \Sigma^+$

reactions are considerably smaller than those for the Λ^{o} reaction.

This may be understood on the basis of the known smallness of the $K \Sigma \bar{N}$

to $K \Lambda \bar{N}$ coupling ratio (ref. V.9). For $t' < 0.2$ $(\text{GeV/c})^2$ the ratio

of :

$$\left[\frac{(\rho_{11} + \rho_{1-1}) \sigma}{}\right]_{K^* \Sigma^{\text{o}}} / \left[(\rho_{11} + \rho_{1-1}) \sigma\right]_{K^* \Lambda^{\text{o}}} = 0.70 \pm 0.22^{(*)}$$

Using equations (V.31) and (V.32) this gives a value for D/F of -0.30

$\pm$ 0.14 in agreement with the value obtained in section V.4.1 for the

reactions $\pi^+ n \rightarrow K^+ \Lambda^{\text{o}}$ and $\pi^+ n \rightarrow K^+ \Sigma^{\text{o}}$ which are also mediated by

K^* (890) and K^* (1420) exchange.

The positivity conditions (equations V.21 and V.22) are satisfied

by the average values of the matrix elements over the t' range considered.

The value of

$$\Delta_{\text{o}} = 2 \frac{\left[\rho_{00} (\rho_{11} - \rho_{1-1}) - 2 (\text{Re } \rho_{10})^2\right]^{\frac{1}{2}}}{\rho_{00} + \rho_{11} - \rho_{1-1}} \qquad (V.34)$$

has been computed as a function of t' for the Λ^{o} reaction. The results

are present in table V.7. The average values for the Σ^{o} and Σ^+

reactions over the interval $0 < t'$ $(\text{GeV/c})^2 < 1.0$ are found to be

$$\Delta_{\text{o}} \ (\pi^+ n \rightarrow K^{*+}(890) \ \Sigma^{\text{o}}) = 0.97 \pm 0.66 \quad \text{(s-channel)}$$

$$0.85 \pm 0.74 \quad \text{(t-channel)}$$

$$\Delta_{\text{o}} \ (\pi^+ p \rightarrow K^{*+}(890) \ \Sigma^{\text{o}}) = 0.82 \pm 0.55 \quad \text{(s-channel)}$$

$$0.95 \pm 0.51 \quad \text{(t-channel)}$$

Δ_{o} measures the unnatural parity exchange contribution to the

(*) The Σ^{o} cross-section has been corrected for the unseen K^* (890) $\rightarrow$ $K^+ \pi^{\text{o}}$ decaymode.

TABLE V.7

Δ_0 AS A FUNCTION OF t' FOR THE REACTION

$$\pi^+ n \rightarrow K^{*+}(890) \Lambda^0$$
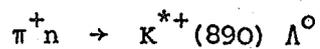
t' range	Δ_0	
$(GeV/c)^2$	s-channel	t-channel
< 2.0	0.95 ± 0.11	0.99 ± 0.10
0 - 0.1	0.83 ± 0.23	0.80 ± 0.24
0.1 - 0.2	0.98 ± 0.34	1.00 ± 0.31
0.2 - 0.3	0.89 ± 0.35	0.88 ± 0.36
0.3 - 0.5	0.98 ± 0.28	0.97 ± 0.26
0.5 - 1.0	0.97 ± 0.20	0.96 ± 0.21
1.0 - 2.0	0.88 ± 0.29	0.61 ± 0.33

polarisation of the vector meson averaged over baryon spin. Its sign cannot be determined from the density matrix alone. The experimental values are close to 1, indicating that the meson helicity 0 and 1 amplitudes for unnatural parity exchange are incoherent and of approximately equal strength.

The weighted average over the interval $0 < t'$ $(GeV/c)^2 < 0.4$ for the ratio of the cross-sections,

$$\sigma(\pi^+ p \rightarrow K^{*+} (890) \Sigma^+)/ \quad \sigma(\pi^+ n \rightarrow K^{*+} (890) \Sigma^0) = 2.0 \stackrel{+}{-} 0.5$$

which is consistent with the absence of any exotic ($I = \frac{3}{2}$, $S = 1$) meson exchange.

The quark model predicts that the reactions $\pi^+ n \rightarrow K^{*+} \Lambda^0$ and $K^- p \rightarrow \phi \Lambda^0$ should have identical cross-sections. Aguilar-Benitez et al. (ref. IV.9) report a total cross-section of $(60 \stackrel{+}{-} 7)$ µb for $K^- p \rightarrow \phi \Lambda^0$ at 3.9 GeV/c, in agreement with the value of $(63 \stackrel{+}{-} 4)$ µb for $\pi^+ n \rightarrow K^{*+} (890) \Lambda^0$ from this experiment. Similarly the cross-sections for $\pi^+ n \rightarrow K^{*+} (890) \Sigma^0$ and $K^- p \rightarrow \phi \Lambda^0$ are expected to be equal. After correcting for the unseen $K^{*+} (890) \rightarrow K^+ \pi^0$ decaymode, the total cross-section for $\pi^+ n \rightarrow K^{*+} (890) \Sigma^0$ is found to be $(32 \stackrel{+}{-} 5)$ µb, in agreement with the value of $(33 \stackrel{+}{-} 7)$ µb for $K^- p \rightarrow \phi \Sigma^0$ from ref. IV.9 .

V.4.3 The reactions $\pi^+ n \rightarrow K^+ \Sigma^O (1385)$ and $\pi^+ p \rightarrow K^+ \Sigma^+ (1385)$

The differential cross-sections for these two processes are shown in table V.8 and figure V.12. In order to reduce any contamination from the strong K^{*+} (890) signal which is also present in the channel $\pi^+ n \rightarrow K^+ \Lambda^O \pi^O$, events have been rejected if 790 Mev/c^2 $<$ M $(K^+ \pi^O)$ $<$ 990 MeV/c^2. Both distributions show a discontinuity in $d\sigma/dt'$ at $t' \sim 0.4$ (GeV/c)^2, which could possibly be interpreted as a nonsense wrong-signature zero for $\alpha(t) = 0$ (cf. $\pi^+ n \rightarrow K^+ \Lambda^O/\Sigma^O$). In view of the t'-dependent corrections applied to the $\Sigma^O(1385)$ reaction in section III.3.2(v), no attempt has been made to determine the slope and intercept of the differential cross-section. The forward differential cross-section (t' $<$ 0.4 (GeV/c)^2) for the $\Sigma^+(1385)$ reaction has been fitted with the empirical form of expression (V.24) and the following values obtained: A $= 41 \pm 6$ μb/(GeV/c)^2 (*), b $= 2.0 \pm 0.5$ (GeV/c)$^{-2}$. The value for the slope parameter, b, is in good agreement with the value of 2.3 ± 0.3 (GeV/c)$^{-2}$ obtained by Ying et al (ref. V.12) for the same beam momentum. For the line-reversed reaction, $K^- p \rightarrow \pi^- \Sigma^+(1385)$, at 5.5 GeV/c Mott et al. (ref. V.13) find a value of 2.7 ± 0.4 (GeV/c)$^{-2}$ for the slope which is consistent with the prediction of weak exchange degeneracy:

$$\frac{d\sigma}{dt'} (\pi^+ p \rightarrow K^+ \Sigma^+ (1385)) = \frac{d\sigma}{dt'} (K^- p \rightarrow \pi^- \Sigma^+ (1385)) \qquad (V.35)$$

assuming both reactions are dominated by K^*(890) and K^*(1420) exchange (cf. equation (V.27)). However, Mott (ref. V.14) has pointed out that the total cross-section for $K^- p \rightarrow \pi^- \Sigma^+ (1385)$ over a range of beam momentum from 2 GeV/c to 8 GeV/c, exceeds that for $\pi^+ p \rightarrow K^+ \Sigma^+ (1385)$ by a factor of ~ 2, in direct contradiction with equation (V.35).

The spin density matrix elements for the $\Sigma(1385)$ decays have been calculated as functions of t' in the s- and t-channel helicity frames.

(*) not corrected for the $\Sigma^+(1385) \rightarrow (\Sigma \pi)^+$ decay mode.

TABLE V.8

DIFFERENTIAL CROSS-SECTIONS

(a) $\pi^+ n \rightarrow K^+ \Sigma^0(1385)$ (*) $\qquad\qquad$ (b) $\pi^+ p \rightarrow K^+ \Sigma^+(1385)$ (*)

t' range $(GeV/c)^2$	Events	$d\sigma/dt'$ $\mu b/(GeV/c)^2$	t' range $(GeV/c)^2$	Events	$d\sigma/dt'$ $\mu b/(GeV/c)^2$
0 – 0.05	9	36 ± 14	0 – 0.1	31	37 ± 7
0.05 – 0.15	26	31 ± 6	0.1 – 0.2	21	25 ± 5
0.15 – 0.25	23	28 ± 6	0.2 – 0.3	21	25 ± 5
0.25 – 0.35	18	22 ± 5	0.3 – 0.4	17	20 ± 5
0.35 – 0.5	11	8.8 ± 2.7	0.4 – 0.5	16	19 ± 5
0.5 – 0.6	11	13 ± 4	0.5 – 0.6	6	7.1 ± 2.9
0.6 – 0.7	11	13 ± 4	0.6 – 0.7	5	5.9 ± 2.6
0.7 – 1.0	10	3.9 ± 1.2	0.7 – 0.8	9	11 ± 4
1.0 – 1.3	5	1.9 ± 0.9	0.8 – 0.9	7	8.3 ± 3.1
1.3 – 1.7	5	1.5 ± 0.7	0.9 – 1.0	5	5.9 ± 2.6
1.7 – 2.2	5	1.2 ± 0.5	1.0 – 1.1	5	5.9 ± 2.6
			1.1 – 1.3	5	3.0 ± 1.3
			1.3 – 1.7	8	2.3 ± 1.0
			1.7 – 2.0	8	3.1 ± 1.1

(*) Not corrected for the $\Sigma(1385) \rightarrow \Sigma\pi$ decay mode.
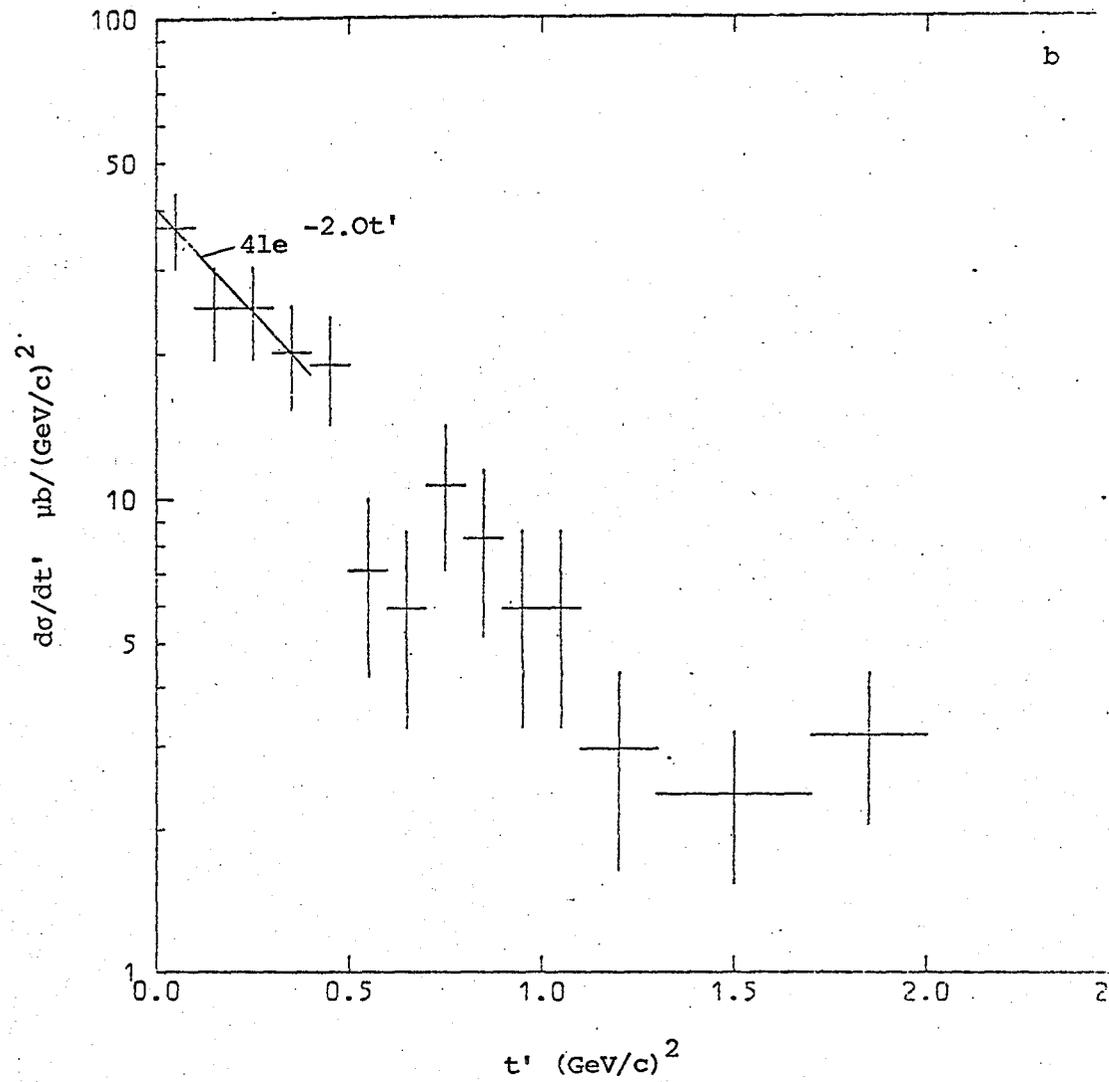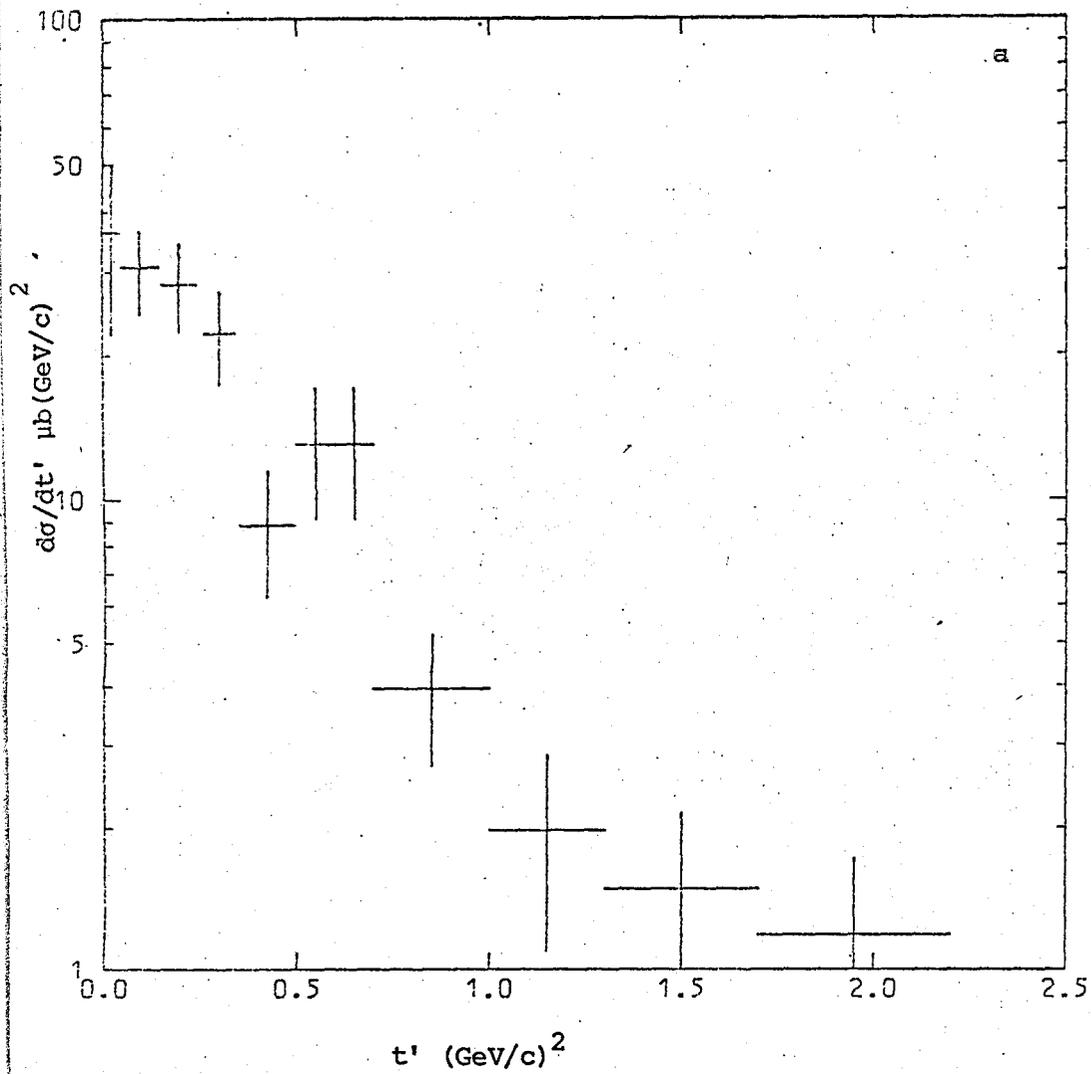
Fig.V.12 Differential cross-section distributions for the reactions (a) $\pi^+ n \to K^+ \Sigma^0 (1385)$
(b) $\pi^+ p \to K^+ \Sigma^+ (1385)$

The results are presented in table V.9 and figures V.13 and V.14. The

average values of the t-channel matrix elements over the interval $0 < t'$

$(GeV/c)^2 < 1.0$ are compared with those of Butler et al. (ref.II.2) in

table V.10. Also shown are the predicted values from a model by Sakurai

and Stodolsky (ref. V.15) based on K^* exchange. The results are in

reasonable agreement with the data.

The positivity condition (equation (V.23)) is satisfied by the

average values of the matrix elements over the t' range considered.

The cross-section ratio for those events with $t' < 0.4$ $(GeV/c)^2$

is

$$\left[\frac{\sigma(\pi^+ p \rightarrow K^+ \Sigma^+ (1385))}{\sigma(\pi^+ n \rightarrow K^+ \Sigma^0 (1385))} \right]_{t' < 0.4} = 1.7 \pm 0.3$$

which is consistent with the absence of any exotic $(I = \frac{3}{2}, S = 1)$ meson

exchange.

V.4.4 The reaction $\pi^+ n \rightarrow K^{*+} (890) \Sigma^0 (1385)$

The study of processes involving the production of two resonances is

known to be difficult because background contamination is usually high.

Of the 68 events which satisfy the effective mass criteria $(1.25 < M(\Lambda^0 \pi^0)$

$GeV/c^2 < 1.35, 0.79 < M (K^0 \pi^+) GeV/c^2 < 0.99)$, only $\sim 70\%$ are

estimated to contribute to the $K^{*+}(890) \Sigma^0 (1385)$ final state, the remain-

ing 30% being largely from single resonance production. In view of this

some caution must be exercised in the interpretation of the results.

The differential cross-section is given in table V.11 and figure V.15.

A marked dip is observed at $t' \sim 0$, although this feature is not apparent

TABLE V.9

SPIN DENSITY MATRIX ELEMENTS FOR Σ (1385)

(a) $\pi^+ n \rightarrow K^+ \Sigma^0$ (1385)

t' range	ρ_{33}		Re ρ_{3-1}		Re ρ_{31}	
(GeV/c)^2	s-channel	t-channel	s-channel	t-channel	s-channel	t-channel
<2.0	0.29 ± 0.05	0.28 ± 0.05	0.14 ± 0.05	0.14 ± 0.05	0.03 ± 0.04	0.03 ± 0.04
0 - 0.1	-0.07 ± 0.15	-0.08 ± 0.14	0.08 ± 0.11	0.09 ± 0.10	-0.02 ± 0.11	-0.05 ± 0.12
0.1 - 0.2	0.35 ± 0.13	0.31 ± 0.13	0.16 ± 0.11	0.15 ± 0.11	0.23 ± 0.09	0.23 ± 0.08
0.2 - 0.3	0.45 ± 0.11	0.46 ± 0.10	0.17 ± 0.11	0.15 ± 0.11	-0.02 ± 0.07	0.01 ± 0.08
0.3 - 0.5	0.24 ± 0.14	0.18 ± 0.13	0.08 ± 0.13	0.08 ± 0.13	0.02 ± 0.12	0.01 ± 0.13
0.5 - 1.0	0.35 ± 0.10	0.31 ± 0.10	0.19 ± 0.11	0.21 ± 0.10	0.03 ± 0.08	0.03 ± 0.09
1.0 - 2.0	0.29 ± 0.18	0.44 ± 0.15	0.11 ± 0.16	0.02 ± 0.19	-0.14 ± 0.16	-0.09 ± 0.17

(b) $\pi^+ p \rightarrow K^+ \Sigma^+$ (1385)

t' range	ρ_{33}		Re ρ_{3-1}		Re ρ_{31}	
<2.0	0.39 ± 0.04	0.36 ± 0.04	0.14 ± 0.04	0.16 ± 0.04	0.05 ± 0.04	0.05 ± 0.04
0 - 0.1	0.36 ± 0.11	0.36 ± 0.11	0.08 ± 0.08	0.08 ± 0.08	0.04 ± 0.08	0.05 ± 0.08
0.1 - 0.2	0.37 ± 0.10	0.28 ± 0.12	-0.05 ± 0.11	0.01 ± 0.11	0.27 ± 0.11	0.30 ± 0.11
0.2 - 0.3	0.49 ± 0.08	0.51 ± 0.08	0.06 ± 0.15	0.04 ± 0.15	-0.13 ± 0.10	-0.04 ± 0.10
0.3 - 0.5	0.50 ± 0.06	0.45 ± 0.07	0.23 ± 0.12	0.26 ± 0.11	0.09 ± 0.07	0.11 ± 0.08
0.5 - 1.0	0.39 ± 0.07	0.32 ± 0.09	0.25 ± 0.09	0.28 ± 0.09	0.10 ± 0.09	0.06 ± 0.08
1.0 - 2.0	0.25 ± 0.10	0.27 ± 0.10	0.20 ± 0.10	0.19 ± 0.10	-0.08 ± 0.09	-0.15 ± 0.09
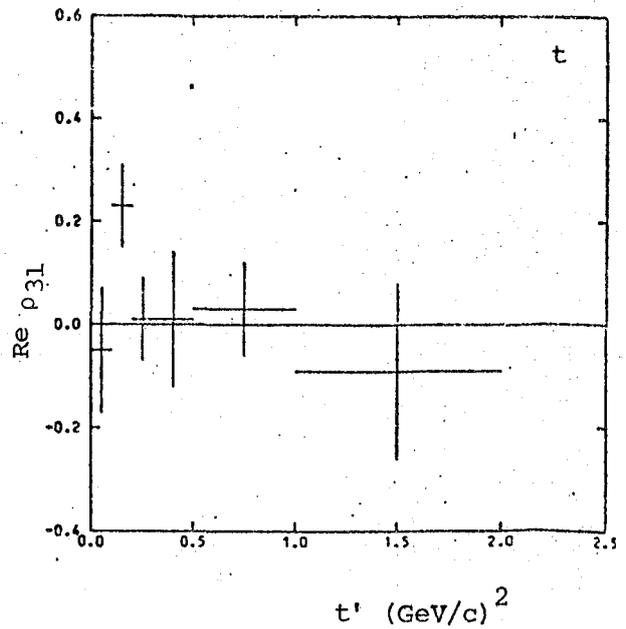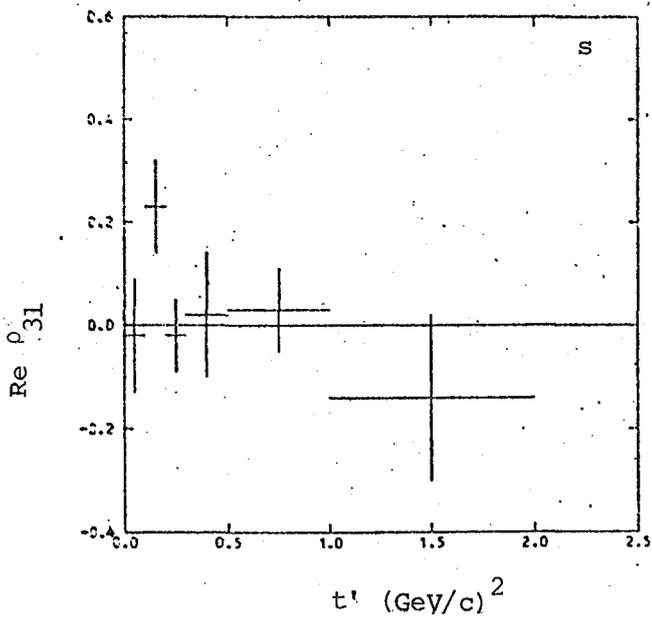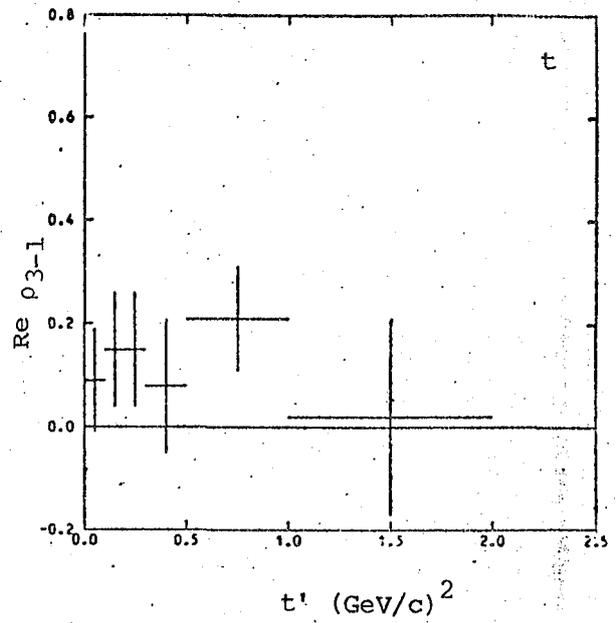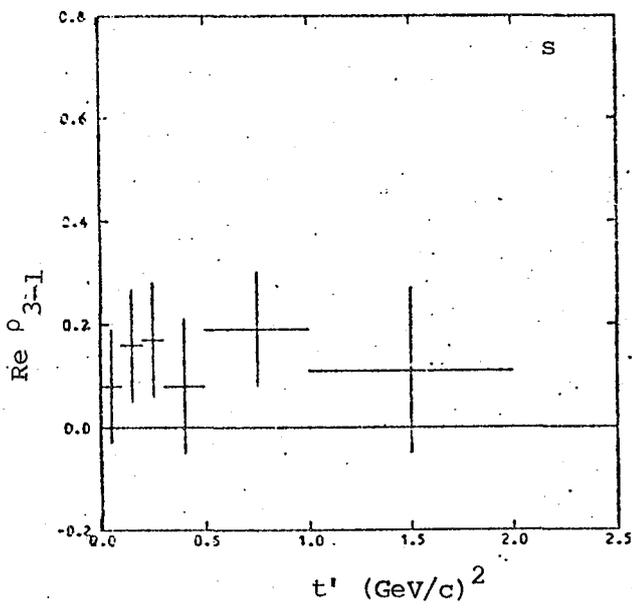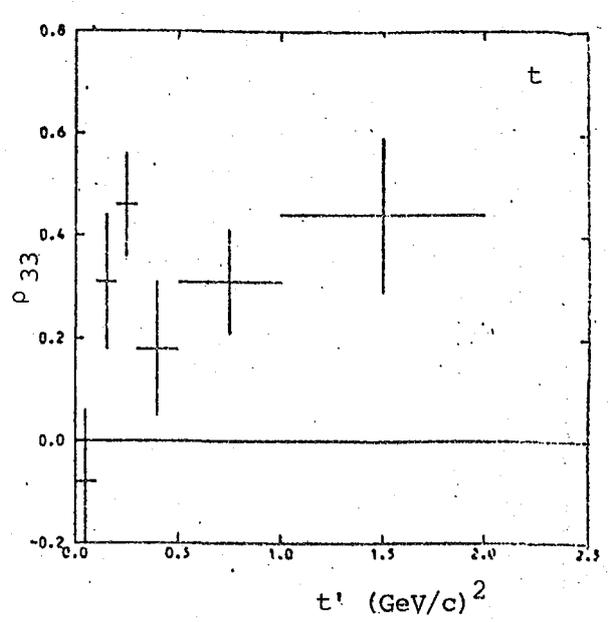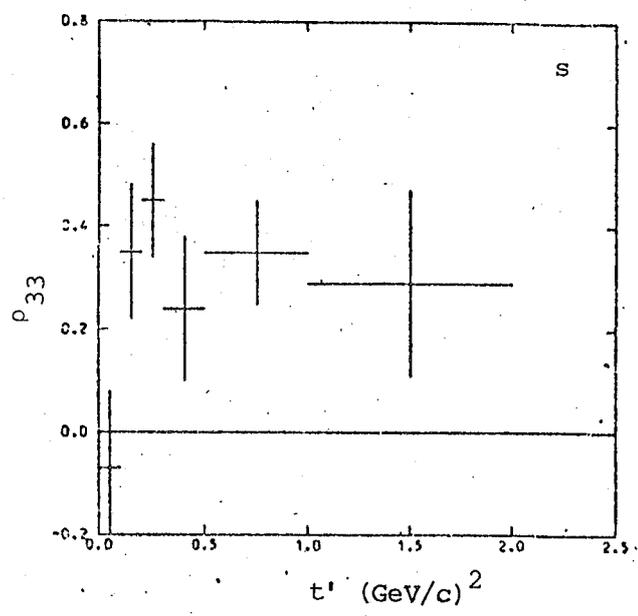
Fig. V.13   Spin density matrix elements for the reaction $\pi^+ n \to K^+ \Sigma^0$ (1385)
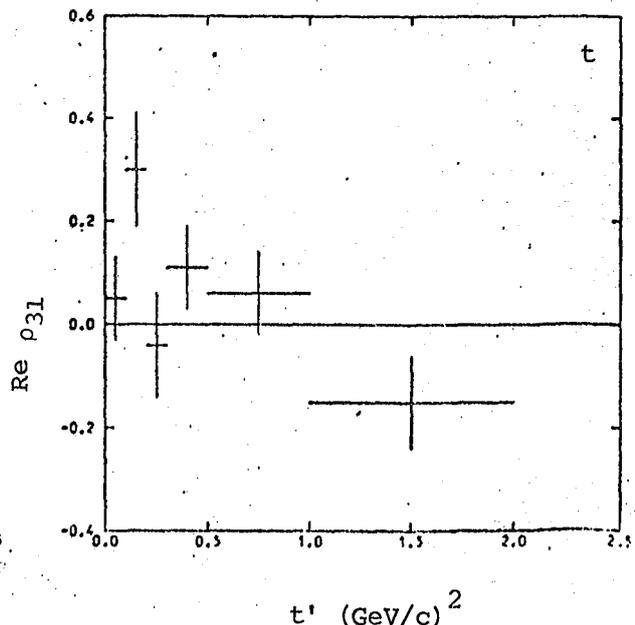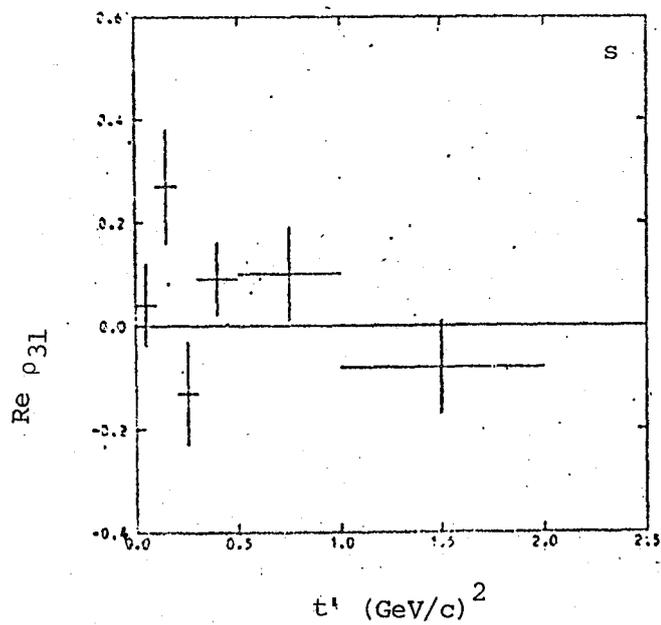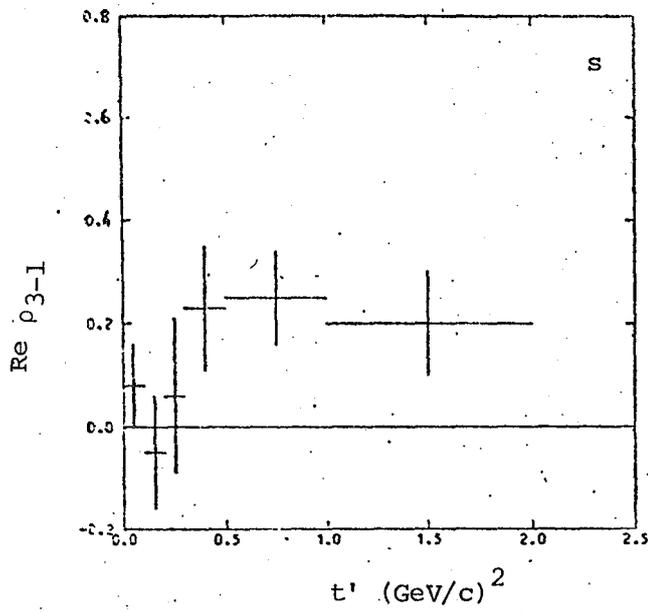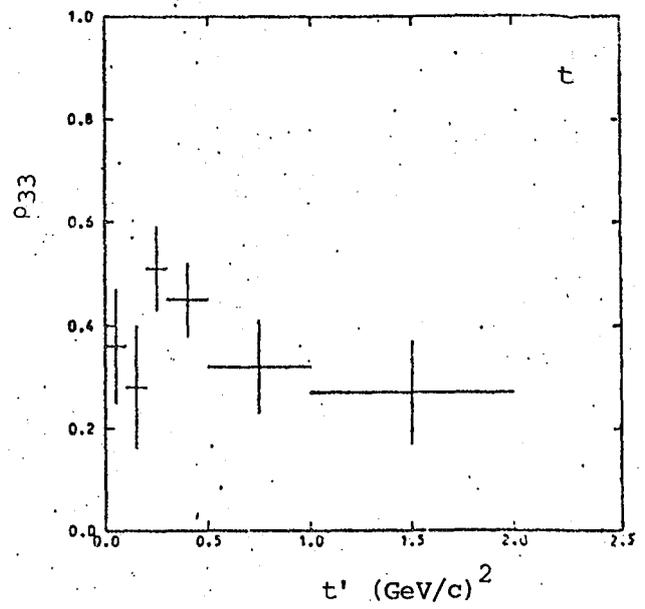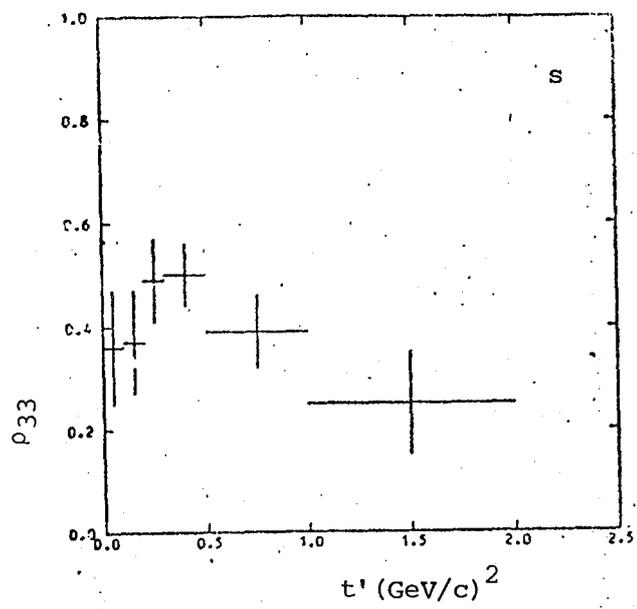
Fig. V.14   Spin density matrix elements for the reaction $\pi^+ p \rightarrow K^+ \Sigma^+ (1385)$

TABLE V.10

AVERAGE SPIN DENSITY MATRIX ELEMENTS OVER THE
INTERVAL $0 < t'$ $(GeV/c)^2 < 1.0$ FOR THE
REACTION $\pi^+ p \rightarrow K^+ \Sigma^+$ (1385)

Beam momentum	ρ_{33}	Re ρ_{3-1}	Re ρ_{31}	Ref
3.7 GeV/c	0.24 ± 0.08	0.19 ± 0.08	0.07 ± 0.06	II.2
4.0 GeV/c	0.26 ± 0.05	0.15 ± 0.05	0.04 ± 0.04	This exp.
Predictions	0.375	0.216	0	$V.1_5$

TABLE V.11

DIFFERENTIAL CROSS-SECTION FOR

$\pi^+ n \rightarrow K^{*+} (890) \ \Sigma^0 (1985)$ (*)

t' range $(GeV/c)^2$	Events	$d\sigma/dt'$ $\mu b/(GeV/c)^2$
0 - 0.1	8	22 ± 8
0.1 - 0.2	12	32 ± 10
0.2 - 0.35	17	30 ± 8
0.35- 0.6	14	15 ± 4
0.6 - 1.0	15	10 ± 3

(*) not corrected for the K^{*+} (890) $\rightarrow K^+ \pi^0$ or

$\Sigma^0 (1385) \rightarrow (\Sigma \pi)^0$ decay modes.
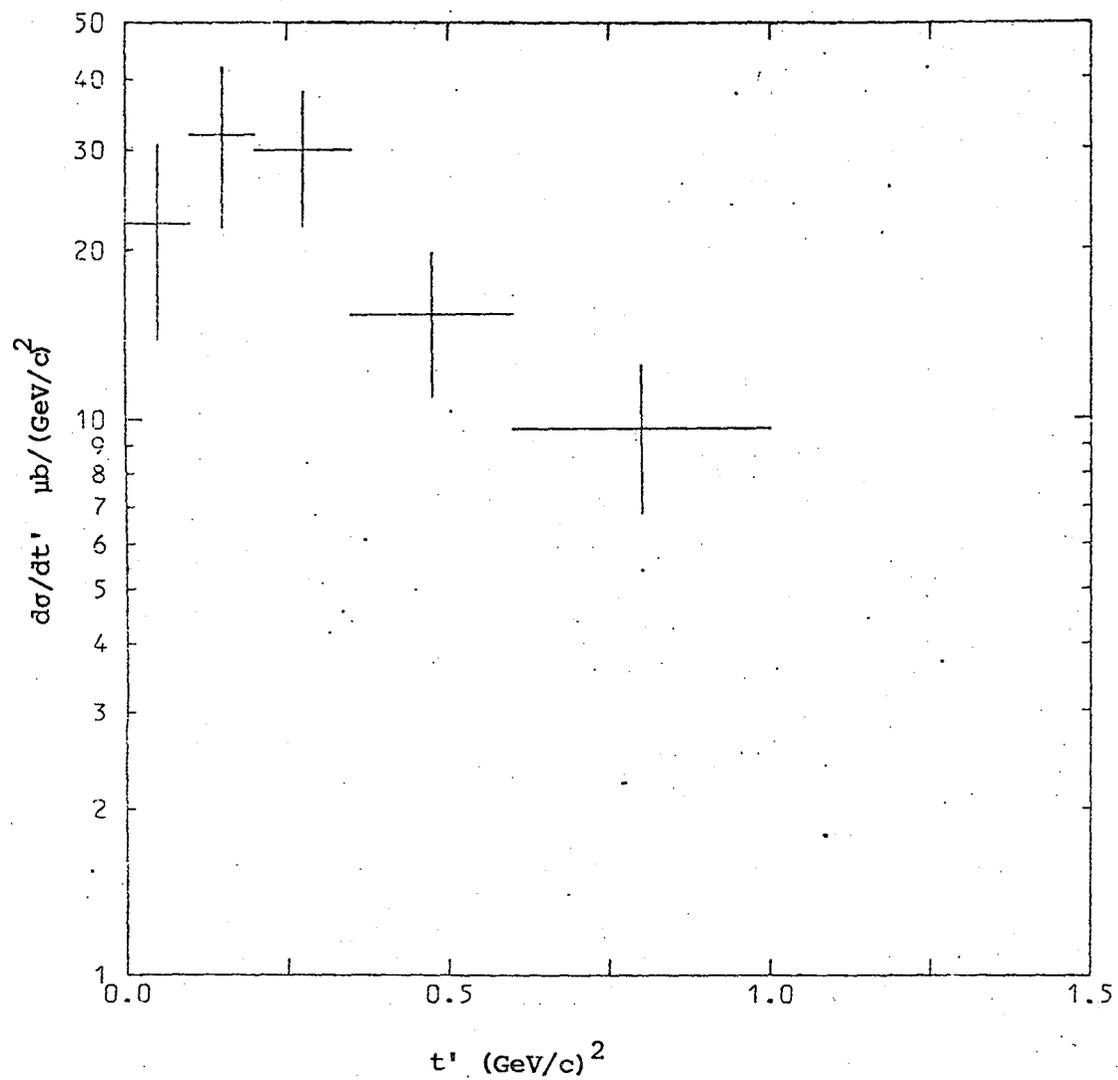
Fig.V.15 Differential cross-section distribution for the reaction $\pi^+ n \rightarrow K^{*+}(890) \, \Sigma^o(1385)$

in Yaffe's data (ref. I.12) for the charge symmetric reaction at 3.93 GeV/c.

The spin density matrix elements for both the K^{*+} (890) and Σ^{0}(1385) decays are given in tables V.12 and V.13 respectively in the s- and t-channel frames. The values obtained by Yaffe (ref. I.12) are also shown for comparison. The positivity conditions (equations (V.21), (V.22) and (V.23) are satisfied by the density matrix elements. From the K^{*} (890) density matrix it appears that both natural and unnatural parity exchange are important.

The quark model predicts the following relations between the density matrix elements for reactions of this type (ref. V.1[6]) ([*]) :

$$\rho_{11} \quad = \quad \tfrac{4}{3} \cdot \rho_{33} \qquad\qquad\qquad (V.36)$$

$$\rho_{1-1} \quad = \quad \tfrac{4}{\sqrt{3}} \ \text{Re} \ \rho_{3-1} \qquad\qquad (V.37)$$

$$\text{Re} \ \rho_{10} \quad = \quad \tfrac{4}{\sqrt{6}} \ \text{Re} \ \rho_{31} \qquad\qquad (V.38)$$

The predicted and observed ratios from this experiment are compared in table V.14 for the s- and t-channel helicity frames. Within the large errors the above relations are satisfied.

The values of Δ_0 have been calculated using expression (V.23) and are found to be (0.86 $\pm$ 0.30) and (0.76 $\pm$ 0.36) in the s- and t-channel helicity frames respectively. The values are close to 1, indicating that the meson helicity 0 and 1 amplitudes from unnatural parity exchange are incoherant

([*])   Kotanski and Zalewski (ref. V.17) have pointed out that these relations can be obtained without involving the quark model.

TABLE V.12
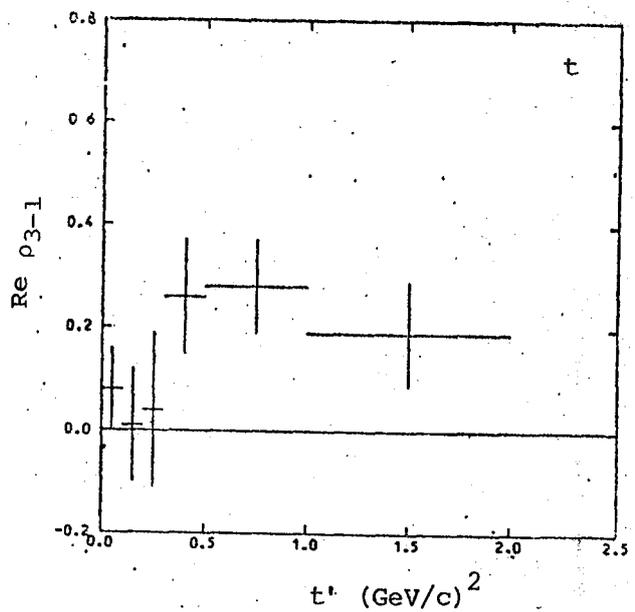
SPIN DENSITY MATRIX ELEMENTS FOR K^* (890)

Reaction	Beam momentum	t' range (GeV/c)^2	ρ_{00} s-channel	t-channel	ρ_{1-1} s-channel	t-channel	Re ρ_{10} s-channel	t-channel	$\rho_{11} + \rho_{1-1}$ s-channel	t-channel	$\rho_{11} - \rho_{1-1}$ s-channel	t-channel	Ref.
$\pi^+ n \to K^{*+}(890)\Sigma^0(1385)$	4.0 GeV/c	0 - 1.0	0.41 $\pm$ 0.09	0.47 $\pm$ 0.11	0.01 $\pm$ 0.09	0.04 $\pm$ 0.08	0.12 $\pm$ 0.06	-0.13 $\pm$ 0.06	0.31 $\pm$ 0.10	0.31 $\pm$ 0.10	0.29 $\pm$ 0.10	0.22 $\pm$ 0.10	this exp.
$\pi^- p \to K^{*0}(890)\Sigma^0(1385)$	3.93 GeV/c	0 - 1.2	0.35 $\pm$ 0.06	0.28 $\pm$ 0.06	-0.03 $\pm$ 0.06	-0.05 $\pm$ 0.06	-0.01 $\pm$ 0.04	-0.03 $\pm$ 0.04	0.30 $\pm$ 0.05	0.30 $\pm$ 0.05	0.33 $\pm$ 0.06	0.40 $\pm$ 0.05	I.12

TABLE V.13

SPIN DENSITY MATRIX ELEMENTS FOR Σ^0 (1385)

Reaction	Beam momentum	t' range (GeV/c)^2	ρ_{33} s-channel	t-channel	Re ρ_{3-1} s-channel	t-channel	Re ρ_{31} s-channel	t-channel	Ref
$\pi^+ n \to K^{*+}(890)\Sigma^0(1385)$	4.0 GeV/c	0 - 1.0	0.24 $\pm$ 0.07	0.15 $\pm$ 0.08	0.04 $\pm$ 0.07	0.10 $\pm$ 0.07	0.07 $\pm$ 0.08	-0.08 $\pm$ 0.07	this exp.
$\pi^- p \to K^{*+}(890)\Sigma^0(1385)$	3.93 GeV/c	0 - 1.2	0.27 $\pm$ 0.05	0.27 $\pm$ 0.05	0.04 $\pm$ 0.05	0.04 $\pm$ 0.05	0.03 $\pm$ 0.05	-0.01 $\pm$ 0.05	I.12

TABLE V.14

TEST OF QUARK MODEL PREDICTIONS FOR

$$\pi^+ n \rightarrow K^{*+} (890) \Sigma^0 (1385)$$

Ratio	Predicted	Observed	
		s-channel	t-channel
ρ_{11}/ρ_{33}	1.33	1.2 ± 0.5	1.8 ± 1.0
$\rho_{1-1}/\text{Re}\rho_{3-1}$	2.31	0.3 ± 2.8	0.4 ± 2.9
$\text{Re}\rho_{10}/\text{Re}\,\rho_{31}$	1.63	1.7 ± 2.1	1.6 ± 1.6

and of approximately equal strength.

The quark model predicts equal cross-sections for the reactions $\pi^+ n \longrightarrow K^{*+}$ (890) Σ^O (1385) and $K^- p \longrightarrow \phi \Sigma^O$ (1385). Aquilar-Benitez et al.(ref. IV.9) report a $K^- p \longrightarrow \phi \Sigma^O$ (1385) cross-section of (20 $\pm$ 5) μb at 3.9 GeV/c after selecting events with t' < 1.0 $(GeV/c)^2$. This is compatible with the value of (24 $\pm$ 7) μb.for $\pi^+ n \longrightarrow K^{*+}$ (890) Σ^O (1385) from this experiment after correcting for the K^{*+} (890) and Σ^O (1385) branching ratios, and imposing the same t' selection.

V.5 Summary

Differential cross-sections and hyperon polarisations have been presented and compared with those for the line-reversed reactions at similar beam momentum. The large values of polarisation which are observed do not support strong exchange degeneracy. Weak exchange degeneracy predicts that the polarisation should change sign between line-reversed partners and that the differential cross-sections should be equal. Neither of these predictions is satisfied by the data.

In general the results from this experiment are consistent with the available data on $\pi^+ p$ and $\pi^- p$ interactions. The only major discrepancies relate to dips in the forward differential cross-section at t' $\sim$ 0, which could possibly arise from t'-dependent losses (see section III.3.2.(v)).

SU(3) related differential cross-sections are in good agreement with quark model predictions. The D/F ratios for helicity non-flip are found to be compatible with previous estimates. Where an exotic exchange contribution can be measured it is found in all cases to be compatible with zero.

The spin density matrix elements have been determined from the decay distributions of the K*(890) and Σ(1385). The K*(890) density matrix has been used to separate natural and unnatural parity exchange. Natural parity exchange appears to dominate in reactions of the type $\pi^+ N \longrightarrow K^*$(890) Λ^0/Σ for t' < 1.0 (GeV/c)^2, whereas for the reaction, $\pi^+ n \longrightarrow K^{*+}$(890) Σ^0(1385), both natural and unnatural parity exchange are important.

CHAPTER VI

AMPLITUDE ANALYSIS

VI.1   Introduction

In this chapter an amplitude analysis is carried out for the reaction

$$\pi^+ n \rightarrow K^{*+} (890) \Lambda^0 \qquad (578 \text{ events})$$
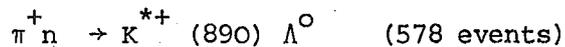
The reaction is described by six (complex) amplitudes giving a total of twelve independent observables. For vector meson production four out of the six amplitudes arise from unnatural parity exchange. Such processes are therefore important for gaining insight into unnatural parity exchange mechanisms. By studying the correlated angular distributions for the decays:

$$K^{*+} (890) \rightarrow (K\pi)^+ \qquad \text{(parity conserving)}$$

$$\text{and} \qquad \Lambda^0 \rightarrow \pi^- p \qquad \text{(parity violating)}$$

ten out of the twelve observables may be determined, since the overall phase of the reaction and the neutron polarisation are unknown.

A model independent analysis of reactions which do not include a subsequent parity violating decay (e.g. $\pi^- p \rightarrow \rho^0 n$) requires a polarised target. It should be stressed that the same amount of information is contained in the reaction $\pi^+ n \rightarrow K^{*+} (890) \Lambda^0$ without the use of polarised targets.

VI.2 Quantisation axes

In the previous chapter the quantisation axis was chosen to be in the production plane (helicity-type quantisation). However in this analysis it is taken to be perpendicular to the production plane (transversity-type quantisation). The resulting transversity amplitudes will therefore transform under parity operation in the production plane in the following way

$$P \; T_{b \; c}^{\; a} \;\; = \;\; (-1)^{a+c-b} T_{b \; c}^{\; a} \qquad\qquad (VI.1)$$

where the indices a, b and c denote the spin projections of the K^*, Λ^0 and n respectively onto the quantisation axis. Parity conservation in the production process requires that the amplitudes vanish for odd values of (a + c - b). This is an important property which greatly simplifies the analysis.

The conventions used to define the axes of the s- and t-channel transversity frames are as follows:

(i) $\hat{z}$ is the normal to the production plane in both frames, $\hat{z} = (\vec{\pi} \; x \; \vec{K})/ \; |\vec{\pi} \; x \; \vec{K}|$, where $\vec{\pi}$ and $\vec{K}$ denote the momenta of the beam and the K^{*+}(890) respectively.

(ii) In the s-channel $\hat{x}$ is the direction of K^{*+}(890) $[\Lambda^0]$ in the C.M. system transformed into the rest frame of the K^{*+}(890) $[\Lambda^0]$

(iii) In the t-channel $\hat{x}$ is the direction of the beam $[n]$ transformed into the rest frame of the K^{*+}(890) $[\Lambda^0]$.

(iv) To obtain a right-handed co-ordinate system, the y axis is then $\hat{y} = \hat{z} \; x \; \hat{x}.$

The angles, θ and ϕ, used to describe the decays are precisely the same as those given in section V.3. The secondary kaon [proton] is used to define the $K^{*+}(890)$ [Λ°] decay direction.

The transversity (T) and helicity (H) quantisation frames are related by simply relabelling the axes: $(x_T, y_T, z_T) \equiv (z_H, x_H, y_H)$

VI.3 The joint spin density matrix

Following the method of moments given by Doncel et al (ref. VI.1) the joint decay angular distribution is expanded in terms of the spherical harmonics, Y_M^L and $Y_{M'}^{L'}$:

$$\omega(\Theta, \phi; \Theta', \phi') = \sum_{L=0}^{2j} \sum_{L'=0}^{2j'} C(L)C'(L') \sum_{M=-L}^{+L} \sum_{M'=-L'}^{+L'} t_{MM'}^{LL'} Y_M^L(\Theta,\phi)^* Y_{M'}^{L'}(\Theta',\phi')^*$$

$$(VI.2)$$

where Θ, ϕ denote the $K^{*+}(890)$ decay distribution,

Θ', ϕ' denote the Λ° decay distribution,

and j, j' are the spins of the $K^{*+}(890)$ and Λ° respectively. $C(L)$ and $C'(L')$ are known coefficients for the decays. For $K^{*+}(890)$:

$$C(0) = \frac{1}{\sqrt{4\pi}}, \quad C(1) = 0, \quad C(2) = \frac{-1}{\sqrt{2\pi}}$$

For Λ°:

$$C'(0) = \frac{1}{\sqrt{4\pi}}, \quad C'(1) = \alpha,$$

where α, the decay asymmetry parameter is taken to be 0.647 (ref. II.3).
Parity conservation in the decay forces the coefficients to vanish for
L odd.

Orthonormality of the spherical harmonics enables the statistical
tensors, $t_{MM'}^{LL'}$, to be projected out (cf. equations V.18 and V.20).
Multiplying equation (VI.2) by $Y_M^L(\theta, \phi)$ $Y_{M'}^{L'}(\theta', \phi')$ and integrating
gives

$$< Y_M^L(\theta, \phi)\; Y_{M''}^{L'}(\theta', \phi') > \;=\; C(L,\; C'(L')\; t_{MM'}^{LL'} \qquad (VI.3)$$

$$\text{with} < Y_M^L(\theta, \phi)\; Y_{M'}^{L'}(\theta', \phi') > \;=\; \frac{1}{N} \sum_{i=1}^{N} Y_M^L(\theta_i,\; \phi_i)\; Y_{M'}^{L'}(\theta'_i,\; \phi'_i) \qquad (VI.4)$$

$\theta_i,\; \phi_i,\; \theta'_i,\; \phi'_i$ denote the decay angles for the i-th event and
N is the total number of events.

The statistical tensors are then used to construct the joint spin
density matrix:

$$\rho_{\lambda\lambda'}^{\mu\mu'} = \sum_{L=0}^{2j} \sum_{L'=0}^{2j'} \frac{(2L+1)\;(2L'+1)}{(2j+1)\;(2j'+1)} \sum_{M=-L}^{+L} \sum_{M'=-L'}^{+L'} t_{MM'}^{LL'} <jL\lambda'M|j\lambda><j'L'\mu'M'|j'\mu> \quad (VI.5)$$

where $<jL\lambda'M|j\lambda>$ and $<j'L'\;\mu'M'|j'\mu>$ are Clebsch-Gordan coefficients.
The single density matrix is recovered by simply summing over the indices:

$$\rho_{\lambda\lambda'} = \sum_{\mu} \rho_{\lambda\lambda'}^{\mu\mu} \qquad (VI.6)$$

A summary of the properties of the statistical tensors and the joint spin density matrix for both helicity- and transversity-type quantisation is given in table VI.1. From these properties the non-vanishing observables in transversity quantization may be identified:

statistical tensors: t^{00}_{00}, t^{20}_{00}, t^{01}_{00}, t^{21}_{00} (real)

$$t^{20}_{20}, \quad t^{21}_{20}, \quad t^{21}_{11}, \quad t^{21}_{1-1} \quad \text{(complex)}$$

density matrix elements (*): ρ^{00}_{++} ρ^{11}_{++} ρ^{-1-1}_{++} (real)

$$\rho^{1-1}_{++} \quad \rho^{10}_{-+} \quad \rho^{0-1}_{-+} \quad \text{(complex)}$$

The observable t^{00}_{00} is simply $1/4\pi$ since the spherical harmonics are normalised (equation (VI.3)).

The relationships between the statistical tensors and the joint spin density matrix elements derived from equation (VI.5) are given in appendix C1. It should be noted that in a model independent analysis the matrix elements ρ^{11}_{++}, ρ^{-1-1}_{++}, ρ^{10}_{-+} and ρ^{0-1}_{-+} can only be determined in the linear combinations $(\rho^{11}_{++} + \rho^{-1-1}_{++})$ and $(\rho^{10}_{-+} - \rho^{0-1}_{-+})$, and not individually. This leaves a total of 12 observables which describe the reaction. Of these only 10 are independent because of the diacritical constraints:

(*) The indices $\pm$ are used to denote $\pm \frac{1}{2}$.

TABLE VI.1

PROPERTIES OF THE STATISTICAL TENSORS
AND THE JOINT SPIN DENSITY MATRIX

Hermiticity	Statistical tensors $t^{LL'}_{MM'}$		Density matrix $\rho^{\mu\mu'}_{\lambda\lambda'}$	
	Helicity	Transversity	Helicity	Transversity
	$t^{LL'*}_{MM'} = (-1)^{M+M'} t^{LL'}_{MM'}$		$\rho^{\mu\mu'}_{\lambda\lambda'} = \rho^{\mu'\mu\,*}_{\lambda'\lambda}$	
Parity conservation in the production process	Real for L+L' even. Pure imaginary for L+L' odd	Zero unless M+M' even	$\rho^{\mu\mu'}_{\lambda\lambda'} = (-1)^{\mu-\mu'+\lambda-\lambda'} \rho^{-\mu-\mu'}_{-\lambda-\lambda'}$	$\rho^{\mu\mu'}_{\lambda\lambda'} = (-1)^{\mu-\mu'+\lambda-\lambda'} \rho^{\mu\mu'}_{\lambda\lambda'}$ $\rightarrow \mu-\mu'+\lambda-\lambda'$ even
Parity conserving decay	L, L' even		—	

$$4 \ \rho_{\substack{++ \\ --}}^{00} \ (\rho_{\substack{-- \\ ++}}^{11} + \rho_{\substack{+\ + }}^{-1-1}) = | \ \Gamma_{\substack{+\\-}} \ \mp \ \sqrt{\Delta} \ |^2 / |\rho_{+-}^{10} - \rho_{+\ -}^{0-1}|^2$$

$$+|\Gamma_{\substack{+\\-}} \ \pm \ \sqrt{\Delta}|^2 / \ |\rho_{-+}^{10} - \rho_{-\ +}^{0\ 1}|^2 \tag{VI.6}$$

with $\Gamma_{\substack{+\\-}} = (\rho_{-+}^{10} - \rho_{-\ +}^{0-1}) \ (\rho_{+-}^{10} - \rho_{+\ -}^{0-1}) \ \mp \ \rho_{++}^{00} \ \rho_{-\ -}^{1-1} \ \pm \ \rho_{--}^{00} \ \rho_{+\ +}^{1-1}$

$$\Delta = \Delta \ \Big[(\rho_{-+}^{10} - \rho_{-\ +}^{0-1}) (\rho_{+-}^{10} - \rho_{+\ -}^{0-1}), \ -\rho_{++}^{00}\rho_{-\ -}^{1-1}, \ -\rho_{--}^{00} \ \rho_{+\ +}^{1-1} \Big]$$

$$\Delta \ \big[x, \ y, \ z \big] = x^2 + y^2 + z^2 - 2 \ (xy + yz + zx)$$

$\sqrt{\Delta}$ = one of the two complex roots, to be fixed by the diacritical constraints.

The matrix elements are also required to obey the positivity conditions:

$$\rho_{\substack{++ \\ --}}^{00} \ \geqslant \ 0 \tag{VI.7}$$

$$\tfrac{1}{2} \ (\ \rho_{\substack{++ \\ --}}^{11} + \rho_{\substack{+\ + \\ -\ -}}^{-1-1}) \ \geqslant \ |\rho_{\substack{+\ + \\ -\ -}}^{1-1}| \tag{VI.8}$$

One further property of the statistical tensors in transversity quantisation is that they transform under rotations ψ, ψ' about the production plane normal in the respective resonance rest frames, in the following simple way:

$$R(\psi,\psi') \ t_{MM'}^{LL'} = e^{-iM\psi \ -iM' \ \psi'} \ t_{MM'}^{LL'} \tag{VI.9}$$

The moduli of the transversity tensors are invariant under such transformations. In particular they will be identical in both the s- and t-channel transversity frames. Observables which depend only on the tensor moduli are known as frame invariants.

VI.4 Amplitude analysis

The transversity amplitudes, $T^{K*}_{\Lambda n}$, are related to the spin density matrix elements in the following way:

$$\rho^{\mu\mu'}_{\lambda\lambda'} = \sum_{\eta} T^{\mu}_{\lambda\eta} \, T^{\mu'}_{\lambda'\eta}{}^{*} \qquad \text{(VI.10)}$$

Parity conservation in the production process requires that only six of these amplitudes are non-vanishing (equation (VI.1)). Their relationships with the spin density matrix elements derived from equation (VI.10) are given in appendix C2. The diagonal matrix elements measure the moduli of the amplitudes, whereas the off-diagonal elements measure interference.

Following the method of Byers and Yang (ref. VI.2) it is useful to construct six amplitudes ($a_{\pm}$, $b_{\pm}$, $c_{\pm}$) defined by:

$$a_{\pm} = T^{0}_{\pm\,\pm} \qquad \text{(VI.11)}$$

$$\frac{-1}{\sqrt{2}} (b_{\pm} - ic_{\pm}) = T^{1}_{-+} \qquad \text{(VI.12)}$$

$$\frac{1}{\sqrt{2}} (b_{\pm} + ic_{\pm}) = T^{-1}_{\mp\,\pm} \qquad \text{(VI.13)}$$

Using these relations and equation (VI.10) it is possible to determine the amplitude moduli and relative phases within the two sets (a_{+}, b_{+}, c_{+}) and ($a_{-} b_{-}, c_{-}$) from the spin density matrix elements.

At high energies the amplitudes $a_{\pm}$ arise from natural parity exchange, whereas $b\pm$ and $c\pm$ respectively describe the unnatural parity exchange contribution to the helicity 0 and 1 states of the K^{*+} (890). This may be understood from their relations to the helicity amplitudes

(see appendix C3). The amplitudes may therefore be used to extract the following observables:

$$N^1 = |a_+|^2 + |a_-|^2 \qquad \text{(VI.14)}$$

$$U^0 = |b_+|^2 + |b_-|^2 \qquad \text{(VI.15)}$$

$$U^1 = |c_+|^2 + |c_-|^2 \qquad \text{(VI.16)}$$

$$P_N^1 N^1 = |a_+|^2 - |a_-|^2 \qquad \text{(VI.17)}$$

$$P_U^0 U^0 = |b_-|^2 - |b_+|^2 \qquad \text{(VI.18)}$$

$$P_U^1 U^1 = |c_-|^2 - |c_+|^2 \qquad \text{(VI.19)}$$

where N and U are the natural and unnatural parity exchange contributions, P_N and P_U are the hyperon polarisations arising from natural and unnatural parity exchange, and the indices denote the helicity state of the K^{*+}(890).

Rotations about the production plane normal will only alter the phase of the transversity amplitudes (cf equation (VI.9)), leaving their moduli unchanged. Using this property together with equations (VI.11) - (VI.13) it is possible to deduce the eight independent frame invariants:

$$|a_\pm|^2, \quad |a_+(b_+ \pm ic_+)^* + a_-^* (b_{-\mp} i c_-|^2$$

$$|b_+ \pm i c_+|^2, \quad |b_\pm i c_-|^2 \qquad \text{(VI.20)}$$

The last two invariants imply that $|b_+|^2 + |c_+|^2$ and $\text{Im} (b_+ c_+^*)$ are also invariant. From equations (VI.14) - (VI.19) it follows that the observables N^1, U, P_N^1 and P_U are frame invariants where

$$U = U^0 + U^1 \quad \text{and} \quad P_U U = P_U^0 U^0 + P_U^1 U^1 .$$

These four invariants are linear combinations of the four real statistical tensors, $t_{00}^{LL'}$. Separation of the unnatural parity contribution and polarisation into helicity 0 and 1 K^{*+}(890) production is not frame invariant.

VI.5   Experimental results

The joint spin density matrix elements are presented as functions of t' in table VI.2 and figure VI.1 for both the s- and t-channel transversity frames. The positivity conditions (equations (VI.7) and (VI.8)) and diacritical constraints (equation (VI.6)) are satisfied within errors.

The Byers and Yang amplitude moduli and relative phases have been determined from the joint spin density matrix and are presented in table VI.3. The relative phases ϕ_{ab}^{+} etc. are defined as arg (a_+) - arg (b_+) in the range $\pm\pi$ radians. The large errors on the phases are due to the large relative errors on the spin density matrix elements. The frame invariants (VI.20) are identical in both frames as expected.

Also shown in table VI.3 and in figure VI.2 are the observables defined in equations (VI.14) - (VI.19). Although the errors are large the polarisation arising from natural parity exchange appears to be negative over the whole t' range, in agreement with the results of Yaffe (ref. I.12) for the charge conjugate reaction at 3.93 GeV/C. This is inconsistent with the prediction of zero polarisation from strong exchange degeneracy (cf section V.4.1). For unnatural parity exchange Yaffe finds the polarisation to be compatible with zero. However, the results of this experiment indicate that the frame invariant quantity, $P_U U = P_U^0 U^0 + P_U^1 U^1$, is positive for t' < 0.2 $(GeV/C)^2$. Non-zero

TABLE VI.2

JOINT SPIN DENSITY MATRIX ELEMENTS FOR THE
REACTION $\pi^+ n \to K^{*+}$ (890) Λ^0

| t' range (GeV/c)^2	0 – 0.1		0.1 – 0.2		0.2 – 0.3		0.3 – 0.5		0.5 – 1.0		1.0 – 2.0	
Events	98		76		69		101		114		54	
	s-channel	t-channel	s-channel	t-channel	s-channel	t-channel	s-channel	t-channel	s-channel	t-channel	s-channel	t-channel
ρ^{00}_{++}	-0.08 ± 0.12		0.14 ± 0.13		0.04 ± 0.17		0.01 ± 0.12		-0.10 ± 0.12		-0.04 ± 0.16	
ρ^{00}_{--}	0.44 ± 0.12		0.48 ± 0.13		0.59 ± 0.17		0.58 ± 0.12		0.59 ± 0.12		0.49 ± 0.16	
$\tfrac{1}{2}(\rho^{11}_{--}+\rho^{-1-1}_{--})$	-0.01 ± 0.07		0.04 ± 0.08		0.11 ± 0.10		0.11 ± 0.07		0.04 ± 0.07		0.08 ± 0.10	
$\tfrac{1}{2}(\rho^{11}_{++}+\rho^{-1-1}_{++})$	0.31 ± 0.07		0.14 ± 0.08		0.08 ± 0.10		0.10 ± 0.07		0.21 ± 0.07		0.20 ± 0.10	
Re $\rho^{1\,-1}_{-\,-}$	0.04 ± 0.10	-0.04 ± 0.10	0.08 ± 0.10	-0.18 ± 0.09	0.02 ± 0.09	-0.09 ± 0.11	0.02 ± 0.08	0.03 ± 0.08	0.02 ± 0.08	0.01 ± 0.08	0.02 ± 0.13	0.18 ± 0.13
Im $\rho^{1\,-1}_{-\,-}$	-0.06 ± 0.09	-0.11 ± 0.09	-0.15 ± 0.10	-0.05 ± 0.10	-0.08 ± 0.11	0.02 ± 0.09	0.14 ± 0.09	-0.11 ± 0.09	-0.01 ± 0.08	-0.02 ± 0.08	-0.18 ± 0.13	0.07 ± 0.12
Re $\rho^{1\,-1}_{+\,+}$	-0.19 ± 0.10	-0.09 ± 0.10	-0.05 ± 0.10	0.16 ± 0.09	0.01 ± 0.09	0.01 ± 0.11	0.05 ± 0.08	-0.12 ± 0.08	-0.01 ± 0.08	0.01 ± 0.08	0.01 ± 0.13	0.03 ± 0.13
Im $\rho^{1\,-1}_{+\,+}$	0.07 ± 0.09	0.22 ± 0.09	0.16 ± 0.10	0.01 ± 0.10	0.01 ± 0.11	0.01 ± 0.09	-0.18 ± 0.09	0.12 ± 0.09	-0.02 ± 0.08	0.03 ± 0.08	0.03 ± 0.13	0.10 ± 0.12
$\tfrac{1}{2}$Re $(\rho^{10}_{-\,+}-\rho^{0\,-1}_{-\,+})$	0.06 ± 0.11	-0.06 ± 0.10	-0.06 ± 0.13	0.04 ± 0.13	-0.03 ± 0.14	0.03 ± 0.14	-0.01 ± 0.12	-0.01 ± 0.11	0.10 ± 0.10	-0.10 ± 0.09	0.09 ± 0.14	-0.10 ± 0.14
$\tfrac{1}{2}$Im $(\rho^{10}_{-\,+}-\rho^{0\,-1}_{-\,+})$	-0.10 ± 0.11	0.10 ± 0.11	0.18 ± 0.13	-0.18 ± 0.13	-0.01 ± 0.14	0.01 ± 0.14	0.01 ± 0.12	0.02 ± 0.11	0.03 ± 0.10	-0.01 ± 0.09	-0.16 ± 0.15	0.15 ± 0.14
$\tfrac{1}{2}$Re $(\rho^{10}_{+\,-}-\rho^{0\,-1}_{+\,-})$	0.07 ± 0.11	-0.04 ± 0.11	0.05 ± 0.13	0.16 ± 0.13	-0.14 ± 0.15	0.33 ± 0.13	0.09 ± 0.12	0.16 ± 0.12	0.29 ± 0.10	0.28 ± 0.10	-0.08 ± 0.14	-0.22 ± 0.14
$\tfrac{1}{2}$Im $(\rho^{10}_{+\,-}-\rho^{0\,-1}_{+\,-})$	-0.03 ± 0.11	0.06 ± 0.11	-0.16 ± 0.14	0.04 ± 0.13	-0.44 ± 0.13	-0.32 ± 0.14	-0.12 ± 0.11	-0.06 ± 0.11	-0.12 ± 0.11	-0.09 ± 0.10	-0.29 ± 0.15	-0.10 ± 0.15
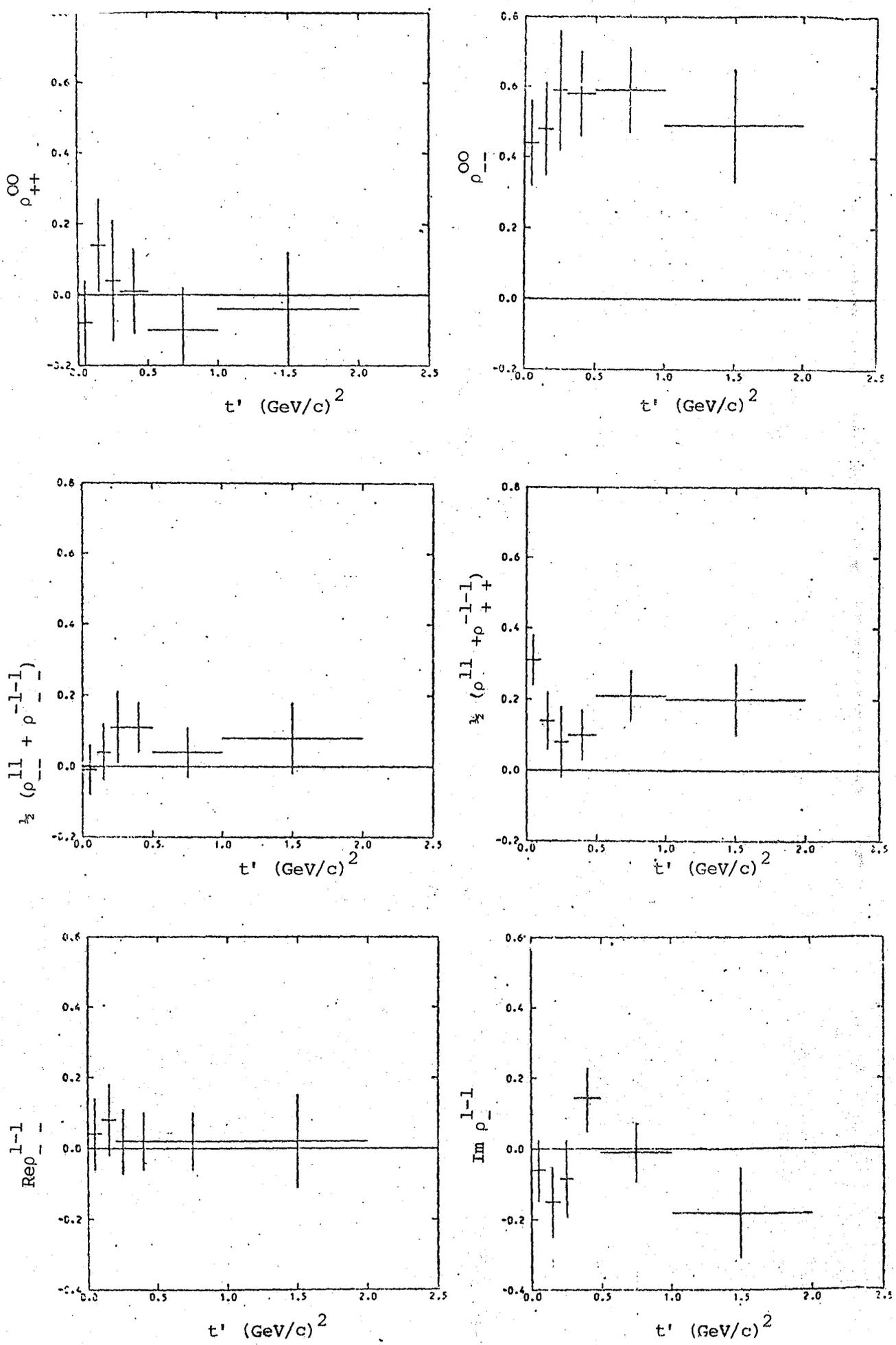
Fig. VI.1 Joint spin density matrix elements in the s-channel transversity Frame.
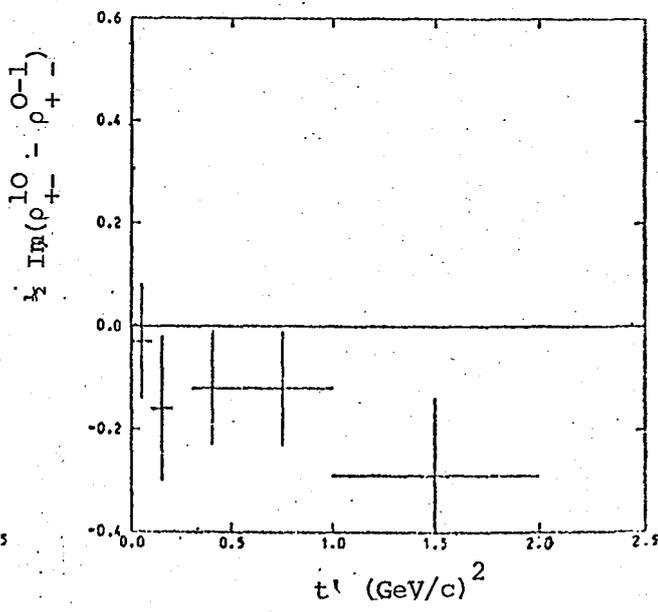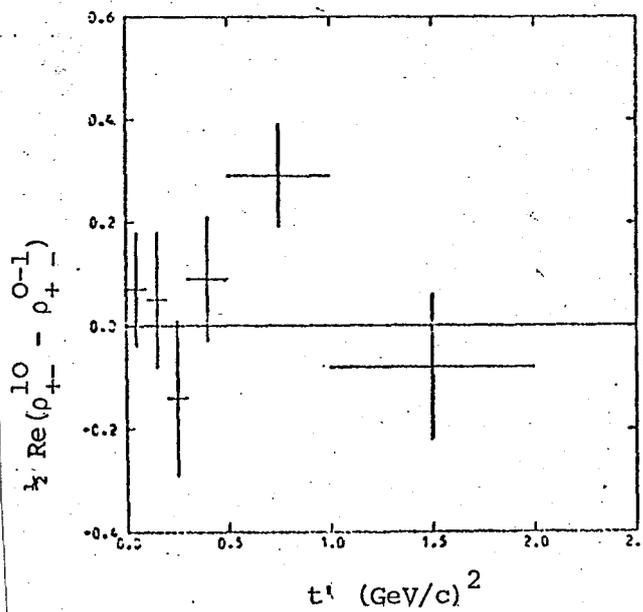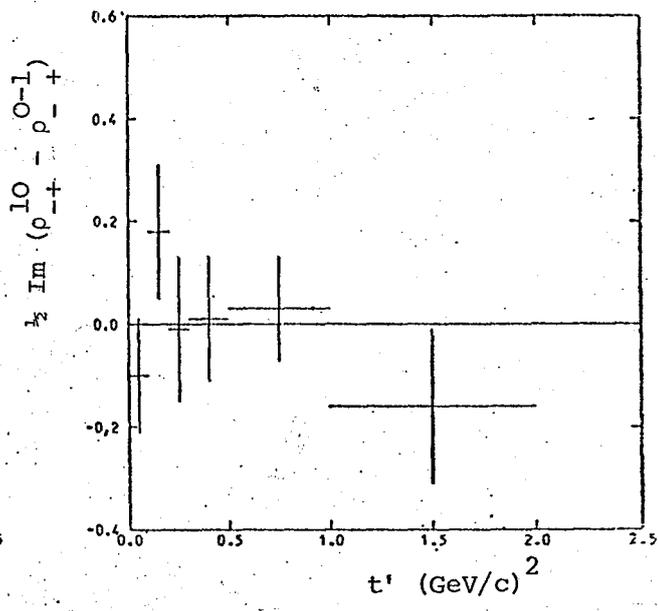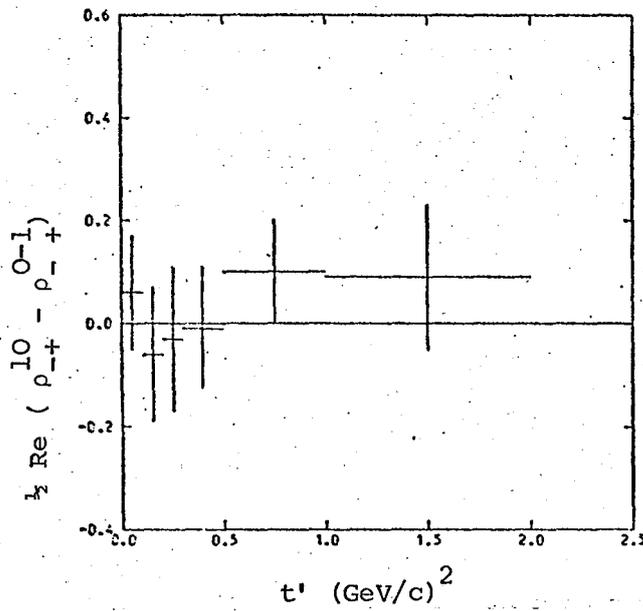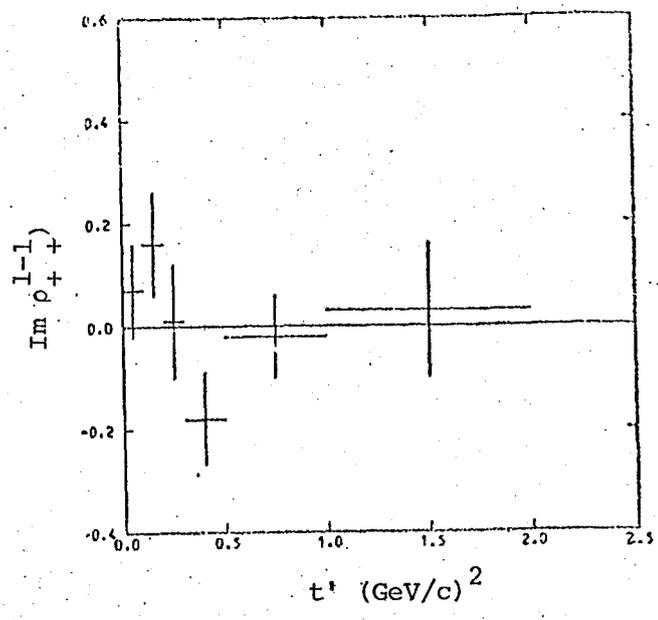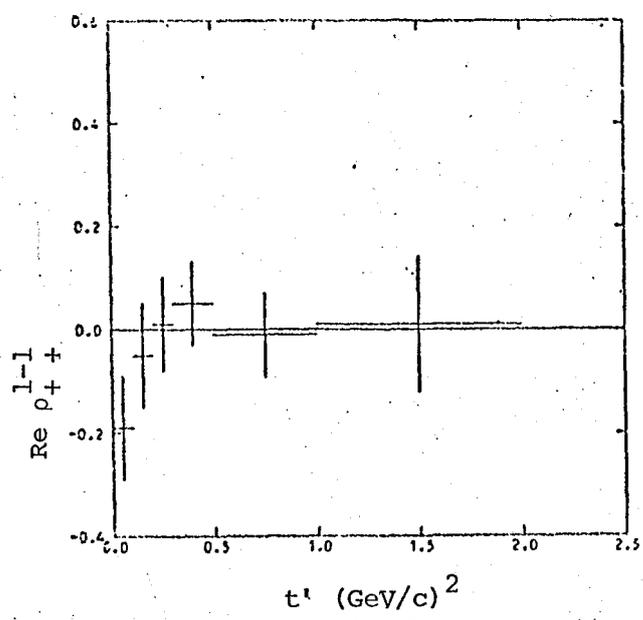
g. VI.1 (cont.) Joint spin density matrix elements in the
s-channel transversity frame.

Figure VI.1 (Cont.)   Joint spin density matrix elements in the t-channel
                      transversity frame.

Fig. VI.1 (Cont.) Joint spin density matrix elements in the t-channel
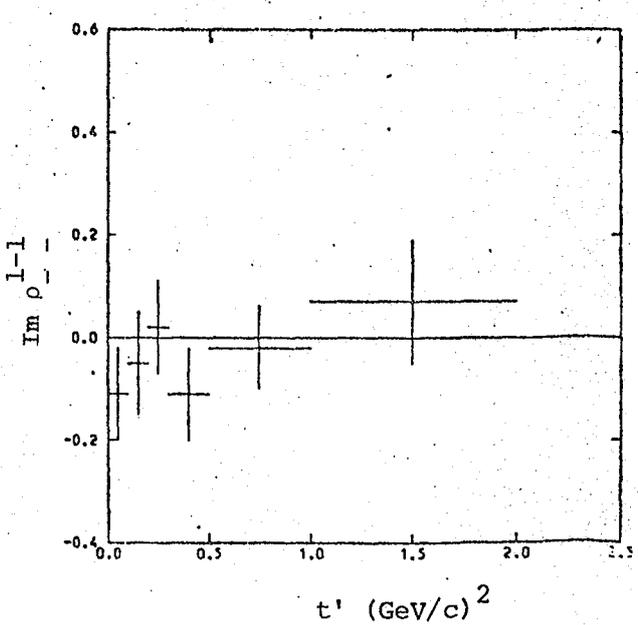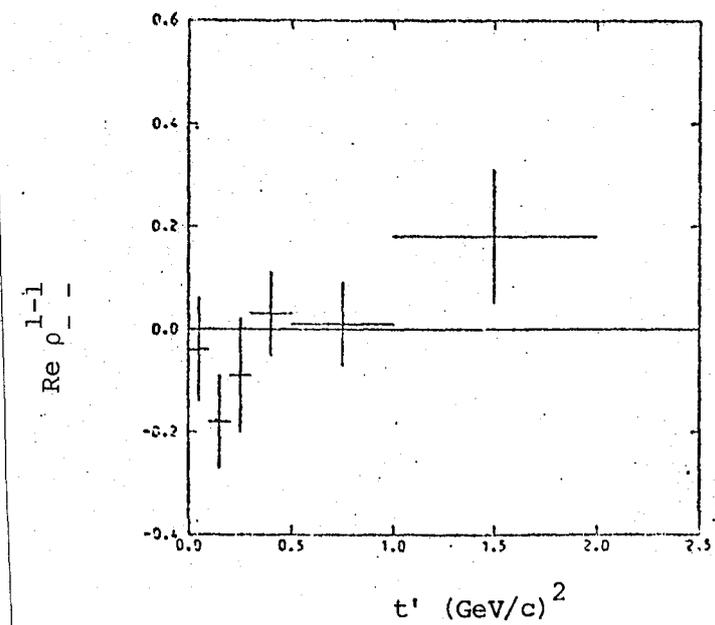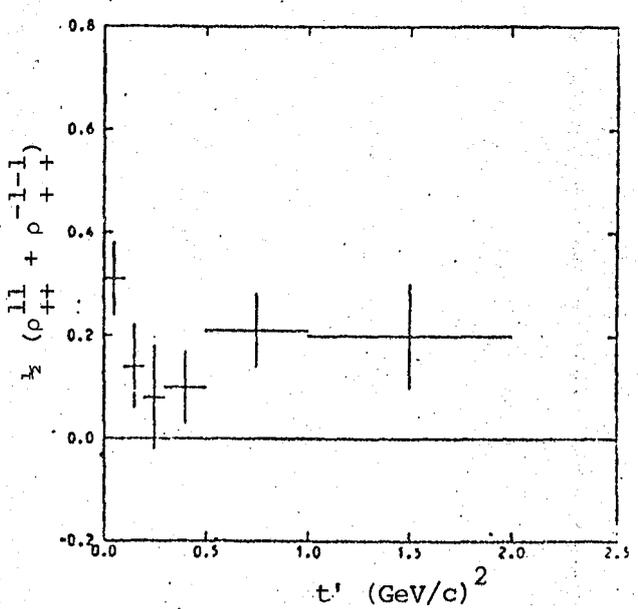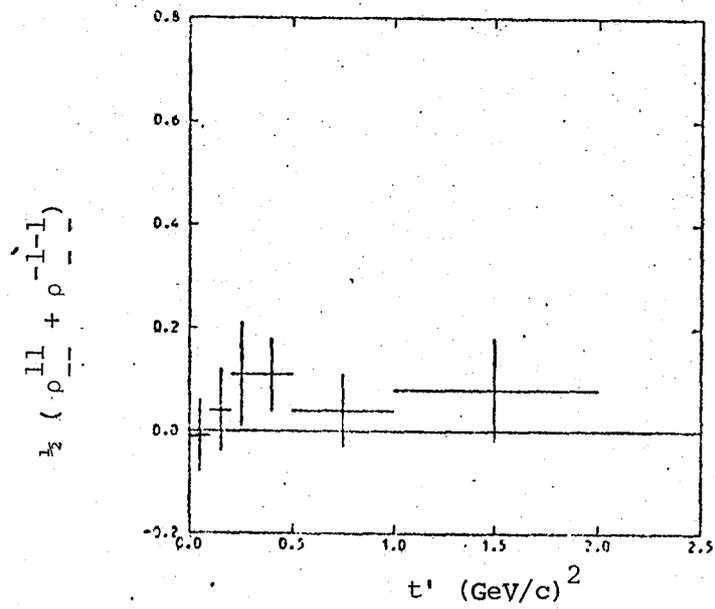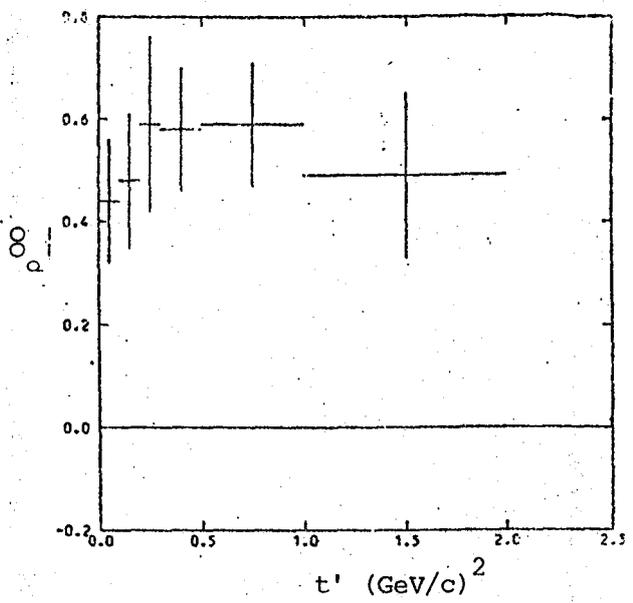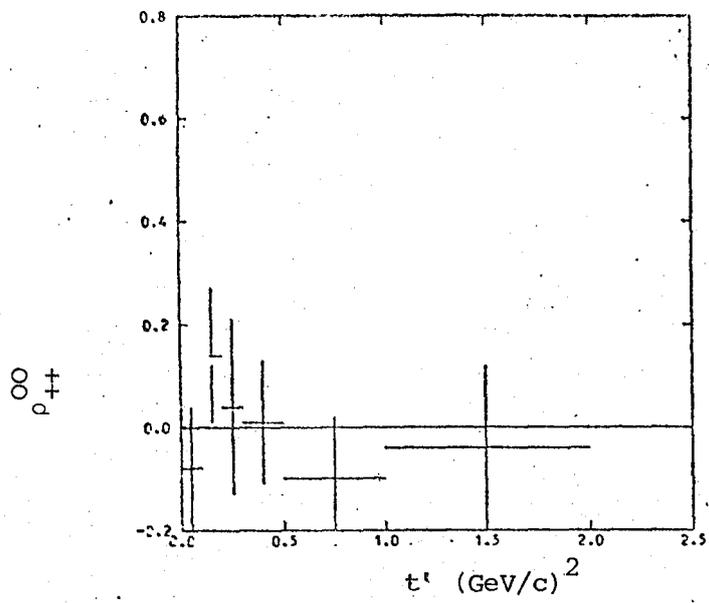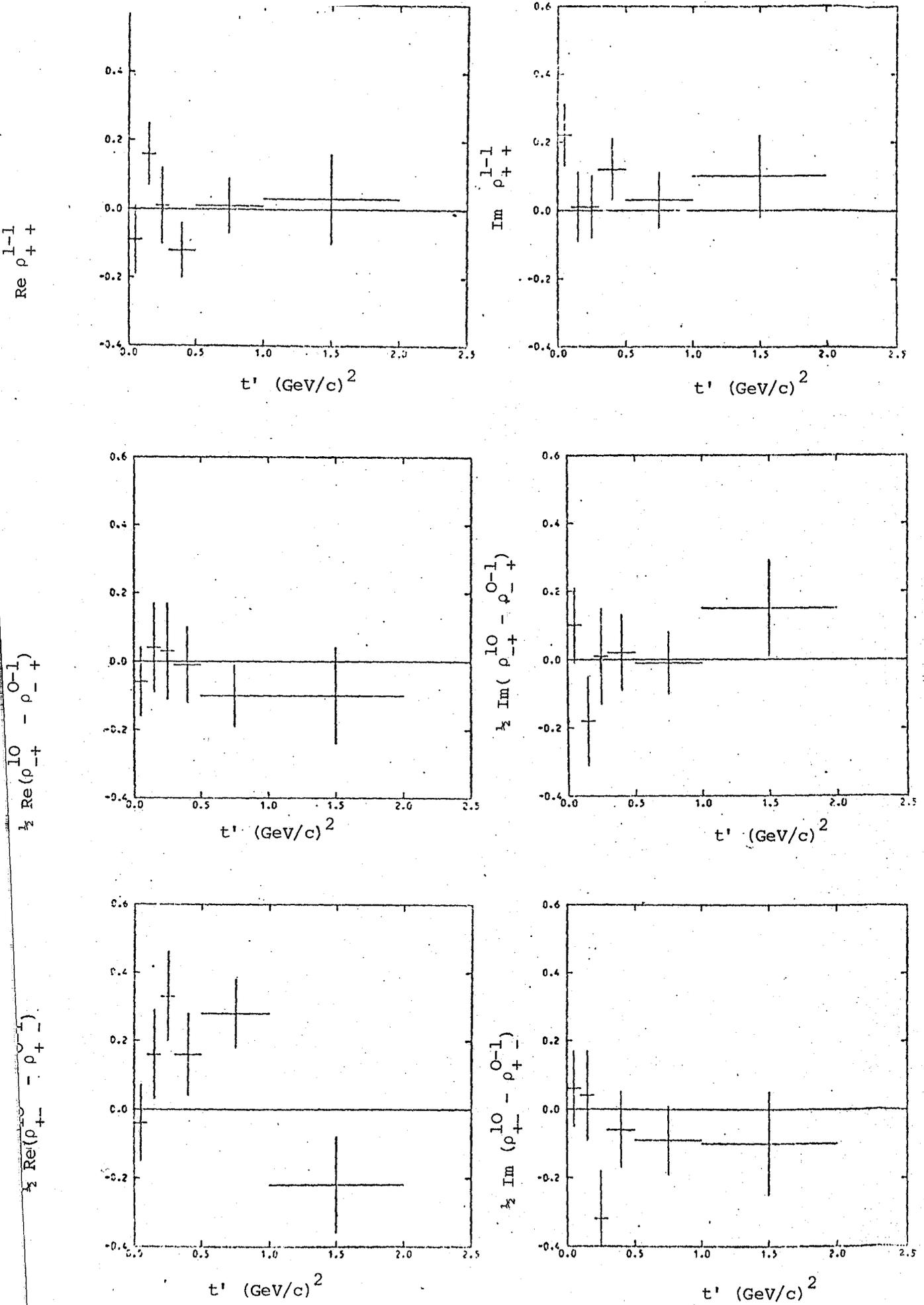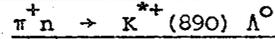transversity frame.

TABLE VI.3

BYERS AND YANG AMPLITUDES FOR THE REACTION
$$\pi^+ n \rightarrow K^{*+}(890)\,\Lambda^\circ$$

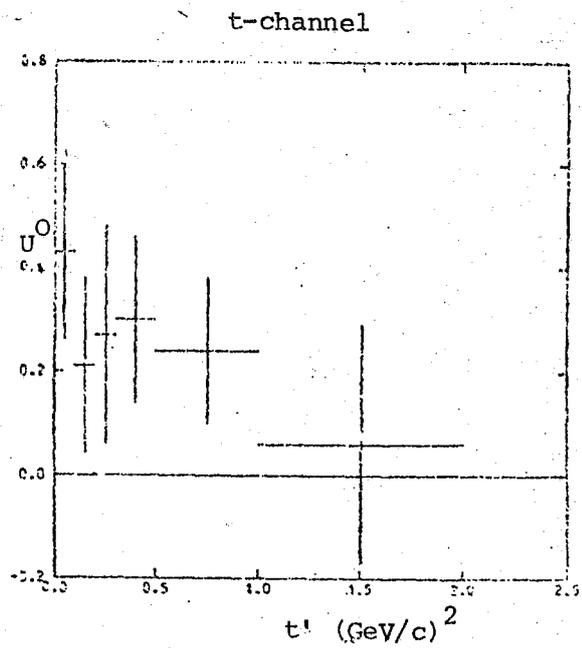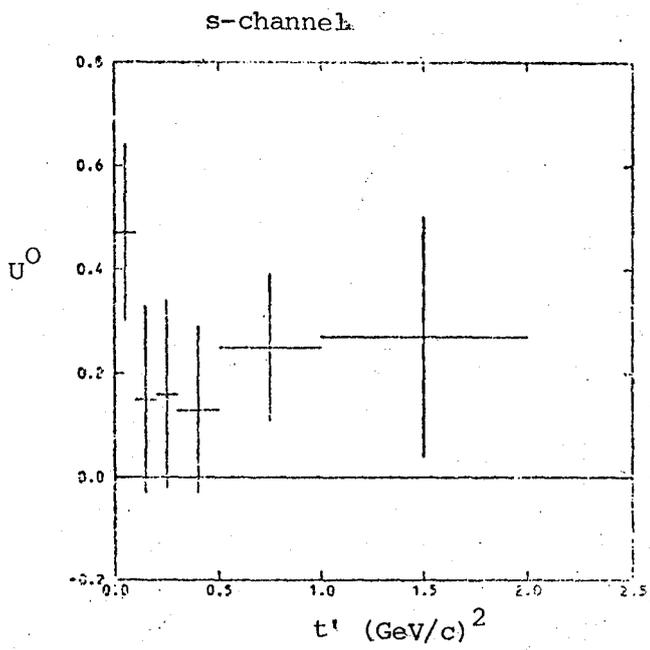| t' range (GeV/c)	0 – 0.1		0.1 – 0.2		0.2 – 0.3		0.3 – 0.5		0.5 – 1.0		1.0 – 2.0	
	s-channel	t-channel	s-channel	t-channel	s-channel	t-channel	s-channel	t-channel	s-channel	t-channel	s-channel	t-channel
$\lvert a_+\rvert^2$	-0.08 ± 0.12		0.14 ± 0.13		0.04 ± 0.17		0.01 ± 0.12		-0.10 ± 0.12		-0.04 ± 0.16	
$\lvert b_+\rvert^2$	-0.04±0.12	0.03±0.12	-0.04±0.13	0.22±0.12	0.09±0.13	0.20±0.15	0.09±0.11	0.08±0.11	0.03±0.10	0.04±0.10	0.07±0.16	-0.10±0.16
$\lvert c_+\rvert^2$	0.04±0.12	-0.04±0.12	0.12±0.13	-0.13±0.12	0.13±0.13	0.02±0.15	0.14±0.11	0.15±0.11	0.06±0.10	0.05±0.10	0.10±0.16	0.27±0.16
$\lvert a_-\rvert^2$	0.44 ± 0.12		0.48 ± 0.13		0.59 ± 0.17		0.58 ± 0.12		0.59 ± 0.12		0.49 ± 0.16	
$\lvert b_-\rvert^2$	0.51±0.12	0.40±0.12	0.19±0.13	-0.01±0.12	0.07±0.13	0.07±0.15	0.04±0.11	0.22±0.11	0.22±0.10	0.20±0.10	0.20±0.16	0.16±0.16
$\lvert c_-\rvert^2$	0.13±0.12	0.23±0.12	0.09±0.13	0.30±0.12	0.08±0.13	0.08±0.15	0.15±0.11	-0.03±0.11	0.20±0.10	0.22±0.10	0.20±0.16	0.23±0.16
ϕ_{a_+b}	-0.1±20.5	2.5±4.3	1.4±7.1	-2.5±1.1	0.2±13.7	2.9±10.9	2.6±13.9	1.4±25.5	3.1±3.1	0.3±5.7	-1.2±4.9	-0.6±4.5
ϕ_{b_+c}	0.0±3.1	0.0±3.1	0.0±3.1	0.0±3.1	0.7±1.6	1.8±12.1	3.1±3.1	0.1±9.5	1.3±1.6	1.0±2.7	0.0±3.1	3.1±3.1
ϕ_{c_+a}	0.1±20.5	-2.5±3.3	-1.4±3.0	2.5±1.3	-0.9±3.6	1.6±104.4	0.5±14.9	-1.5±60.2	1.9±2.4	-1.3±3.2	1.2±4.6	-2.5±4.0
ϕ_{a_-b}	2.3±0.3	-0.6±0.4	-2.4±0.7	1.5±60.1	2.5±1.9	-1.0±1.8	-1.3±3.8	3.1±3.1	-1.6±6.0	1.6±6.5	-2.5±0.9	0.7±1.0
ϕ_{b_-c}	-1.9±1.1	2.4±0.5	3.1±3.1	3.1±3.1	1.7±6.8	1.7±7.9	0.0±3.1	3.1±3.1	-1.5±3.4	-1.7±1.9	1.7±3.1	3.1±1.1
ϕ_{c_-a}	-0.5±1.2	3.0±2.5	-0.8±1.3	1.6±5.9	2.1±1.4	-0.7±1.8	1.3±1.1	0.0±3.1	-3.1±3.1	0.1±3.0	0.8±0.7	-2.8±1.4
N^1	0.36 ± 0.17		0.62 ± 0.18		0.63 ± 0.24		0.59 ± 0.17		0.49 ± 0.17		0.45 ± 0.23	
U^0_1	0.47±0.17	0.43±0.17	0.15±0.18	0.21±0.17	0.16±0.18	0.27±0.21	0.13±0.16	0.30±0.16	0.25±0.14	0.24±0.14	0.27±0.23	0.06±0.23
U_1	0.17±0.17	0.19±0.17	0.21±0.18	0.17±0.17	0.21±0.18	0.10±0.21	0.29±0.16	0.12±0.16	0.26±0.14	0.27±0.14	0.30±0.23	0.50±0.23
$P_N\,^{1}N^{1}$	-0.52 ± 0.17		-0.34 ± 0.18		-0.55 ± 0.24		-0.57 ± 0.17		-0.69 ± 0.17		-0.53 ± 0.23	
$P_U\,^{0}U^{0}$	0.55±0.17	0.37±0.17	0.23±0.18	-0.23±0.17	-0.02±0.18	-0.13±0.21	-0.05±0.16	0.14±0.16	0.19±0.14	0.16±0.14	0.13±0.23	0.36±0.23
$P_U\,^{1}U^{1}$	0.09±0.17	0.27±0.17	-0.03±0.18	0.43±0.17	-0.05±0.18	0.04±0.21	0.01±0.16	-0.18±0.16	0.14±0.14	0.17±0.14	0.10±0.23	-0.04±0.23
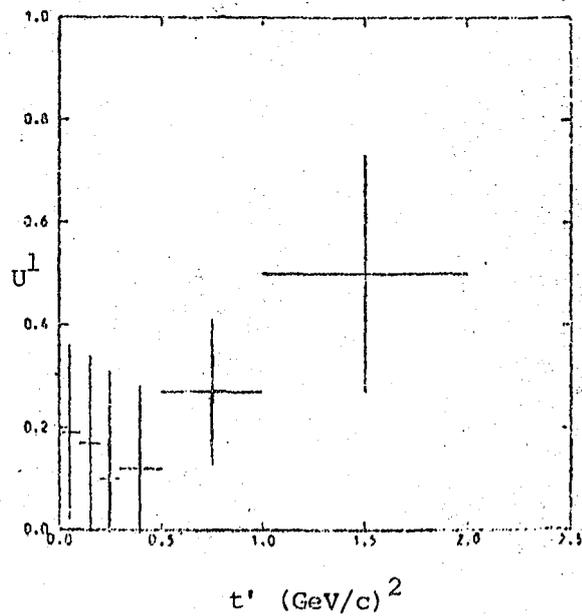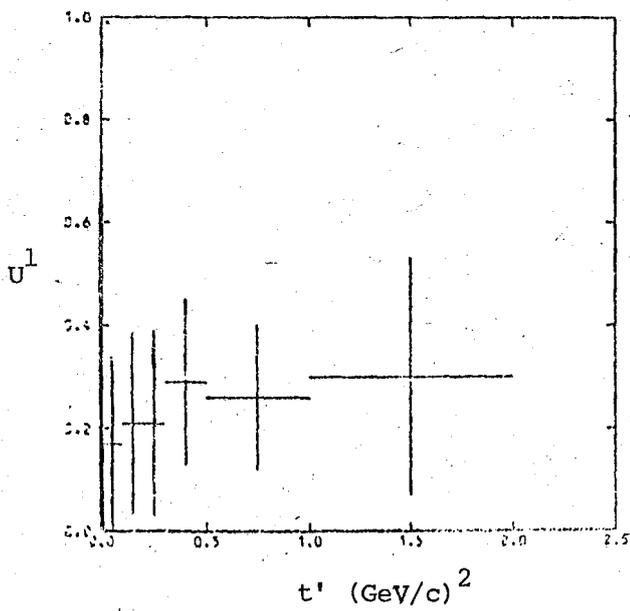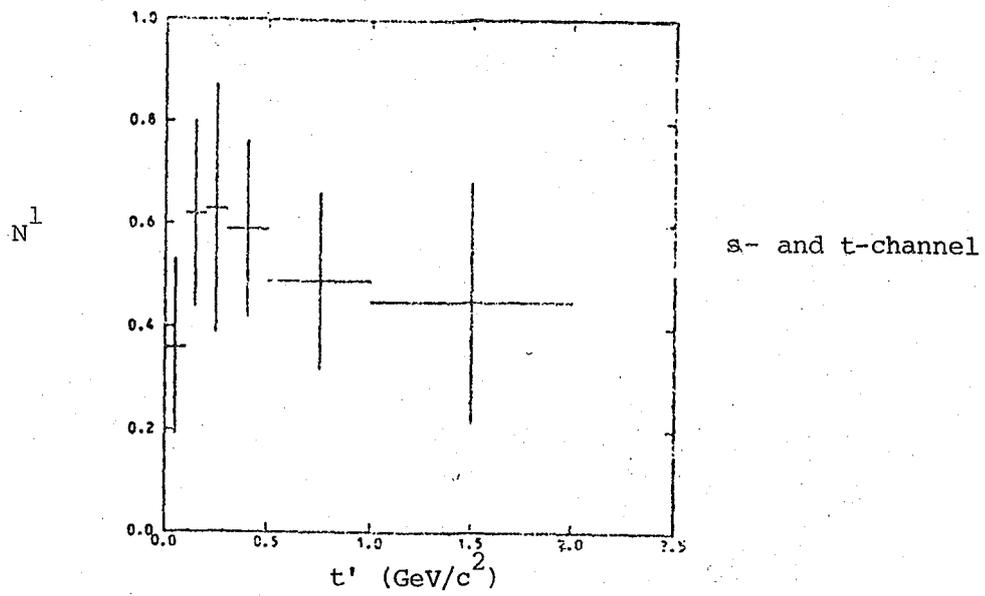
Figure VI.2 Observables defined in equations (VI.14) - (VI.16)
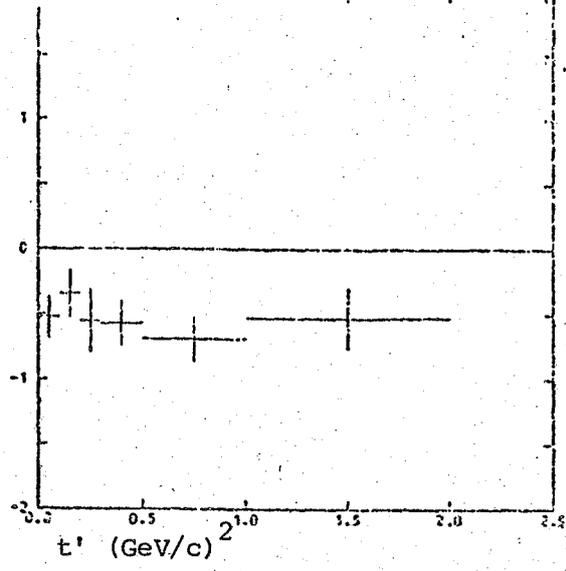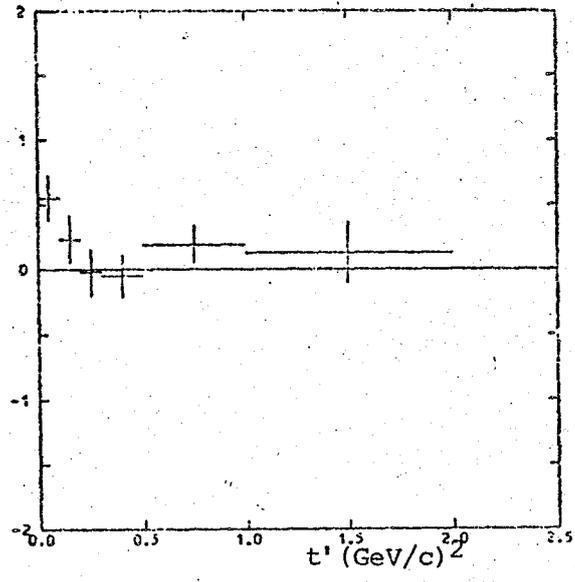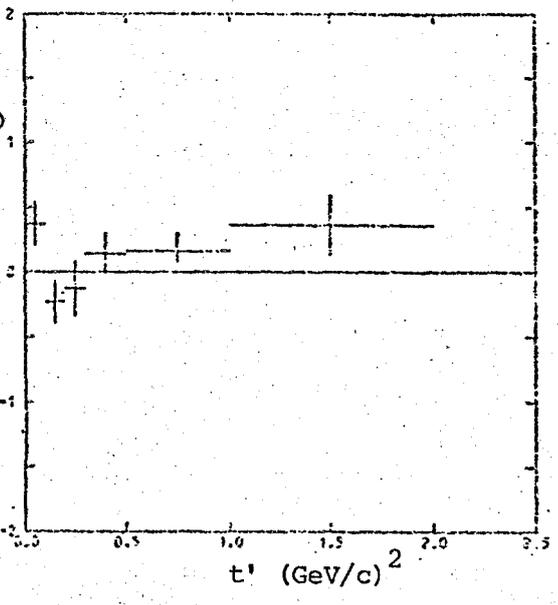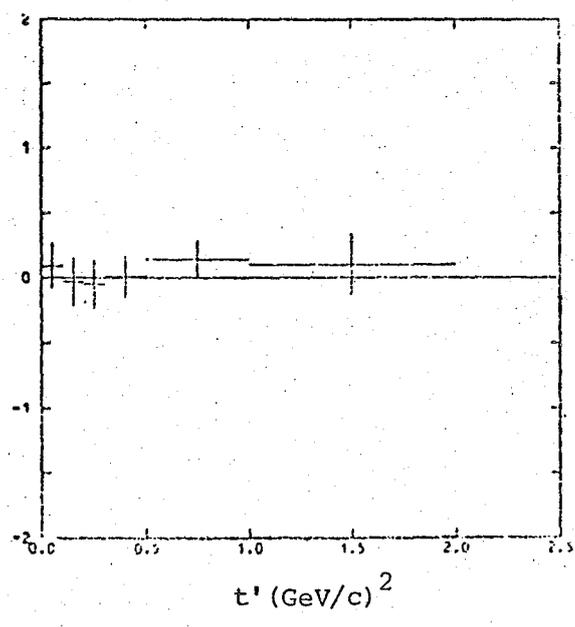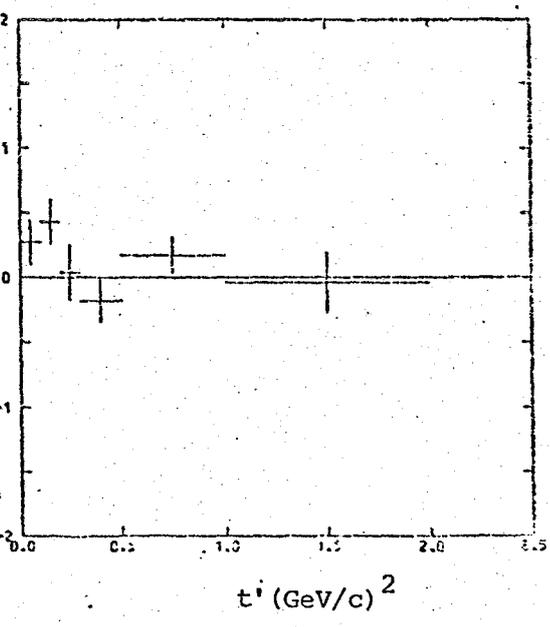
Figure VI.2 (cont)   Observables defined in equations (VI.17) - (VI.19)

polarisation cannot arise from K exchange alone, so that some other

exchange amplitude, possibly the K_A, must be present.

Both the quark model (ref. V,17) and SU(3) plus factorisation

(ref. VI.3) lead to the prediction,

$$T_{bc}^a \ (\pi^+ n \to K^{*+}(890) \Lambda^o) = T_{bc}^a \ (K^- p \to \phi \Lambda^o) \qquad (VI.21)$$

The squared moduli of the transversity amplitudes $\left| T_{bc}^a \right|^2$ for the

reactions $\pi^+ n \to K^{*+}(890) \ \Lambda^o$ (this experiment) and $K^- p \to \phi \ \Lambda^o$ (ref. VI.4)

are compared in the table VI.4. Relation (VI.21) is satisfied within

errors. (An earlier comparison of the reactions $\pi^- p \to K^{*o}(890) \Lambda^o$ and

$K^- p \to \phi \Lambda^o$ is given in ref. I.12).

VI.6 Discussion

From simple exchange model considerations the natural parity contri-

bution to the reaction $\pi^+ n \to K^{*+}(890) \ \Lambda^o$ might be expected to be related

to $\pi^+ n \to K^+ \Lambda^o$ which is also mediated by $K^*(890)$ and $K^*(1420)$ exchange.

However the hyperon polarisation for $\pi^+ n \to K^+ \Lambda^o$ is positive for $t' < 0.4$

$(GeV/_c)^2$ and negative for higher values of t' (see figure V.6a), whereas

P_N for $\pi^+ n \to K^{*+}(890) \ \Lambda^o$ has a consistently negative trend. This could

indicate the presence of multiple scattering or absorptive corrections

which would distort the polarisation.

The non-zero values of P_N and P_U may be explained respectively by

large exchange degeneracy breaking of the $K^*(890)$ and $K^*(1420)$ amplitudes

and a considerable contribution from the K_A pole. Both these features

have been incorporated in a model by R. D. Field et al (Ref. VI.5) to fit

the eight SU(3) related reactions $K^- p \to (\rho, \omega, \phi) \ (\Lambda^o \ \Sigma^o)$ and

$\pi^- p \to K^{*o}(890) \ (\Lambda^o, \Sigma^o)$. If exchange degeneracy is assumed it is

necessary to introduce large Regge cuts, although if these are present it

is difficult to explain the success with SU(3) and factorisation.

TABLE VI.4

A COMPARISON OF THE TRANSVERSITY AMPLITUDES
FOR THE REACTIONS:

(a) $\pi^+ n \to K^{*+}(890)\ \Lambda^0$ (b) $K^- p \to \phi\ \Lambda^0$
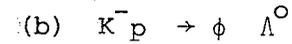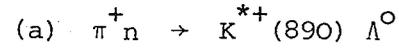
t' range (GeV/c)^2	0 - 0.2	0.2 - 0.5	0.5 - 1.0	0 - 0.2	0.2 - 0.5	0.5 - 1.2
$\left|T^0_{--}\right|^2$	0.46 ± 0.09	0.58 ± 0.10	0.57 ± 0.10	0.32 ± 0.10	0.46 ± 0.09	0.50 ± 0.10
$\left|T^0_{++}\right|^2$	0.02 ± 0.09	0.02 ± 0.10	-0.09 ± 0.10	0.04 ± 0.11	0.02 ± 0.05	0.03 ± 0.07
$\left|T^{-1}_{+-}\right|^2$	0.36 ± 0.09	0.06 ± 0.09	0.40 ± 0.10	0.27 ± 0.18	0.06 ± 0.07	0.06 ± 0.04
$\left|T^1_{-+}\right|^2$	0.02 ± 0.09	0.15 ± 0.09	0.10 ± 0.10	0.07 ± 0.08	0.09 ± 0.04	0.05 ± 0.16
$\left|T^1_{+-}\right|^2$	0.12 ± 0.09	0.12 ± 0.09	0.0 ± 0.10	0.20 ± 0.17	0.35 ± 0.10	0.17 ± 0.09
$\left|T^{-1}_{-+}\right|^2$	0.02 ± 0.09	0.08 ± 0.09	0.02 ± 0.10	0.11 ± 0.10	0.01 ± 0.06	0.19 ± 0.14

CHAPTER VII

GENERAL CONCLUSIONS

The production of strange particles in π^+d interactions has been examined at 4 GeV/c where no previous data exist. Careful attention has been given to the resolution of ambiguous channels and to corrections for losses in a sample of about 22,000 events which have been used to determine channel cross-sections. Where they can be checked, the new results fit well into the observed variation of existing cross-sections at higher and lower energies.

Resonance production has been estimated by fitting the relevant effective mass distribution with an incoherent sum of the Breit-Wigner expression and phase space, or, where statistics are low, by counting the number of events above background within the resonance mass band. The production cross-sections have only been determined for the well-established resonances. Of these the production of $K^*(890)$ and $\Sigma(1385)$ is found to be most dominant, amounting to some 25% and 8% respectively of the strange particle sample considered. Evidence for the Z_O (1865), the E (1420) and the Q(1300) has been investigated, but no firm conclusions can be drawn from the data. Where possible the branching ratios have been determined for the decay modes of the well-established resonances, and are found to be in good agreement with previous estimates or with those predicted from Clebsch-Gordan coefficients.

Exchange mechanisms have been investigated by studying the two body and quasi-two body reactions for which there are adequate statistics. Where an exotic exchange contribution can be measured it is found in all cases to be compatible with zero. The main features of the reactions considered and the conclusions which can be drawn from them are summarised below:

(a) $\pi^+ n \;\rightarrow\; K^+ \; \Lambda^0/\Sigma^0$

Both processes exhibit a break in the differential cross-section

distribution at t' $\sim$ 0.4 (GeV/c)^2, the position of a nonsense wrong-

signature zero for the K^*(890) trajectory. The large values of hyperon

polarisation which are measured do not support strong exchange degeneracy.

However, the opposite behaviour of the Λ^0 and Σ^0 polarisations with

regard to sign is consistent with the prediction of SU(3) and octet

dominance. It should also be noted that the polarisations change sign

in the same t' region as the break in the differential cross-section

distribution.

A comparison with the line-reversed reactions reveals that the

data cannot be explained by the simple concept of weak exchange

degeneracy alone, but requires the introduction of Regge cuts and/or

exchange degeneracy breaking (ref. VII.1).

The D/F ratio for helicity non-flip is found to be -0.30 $\pm$ 0.08,

in good agreement with previous estimates.

(b) $\pi^+ n \;\rightarrow\; K^{*+}$(890) Λ^0
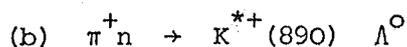
An analysis of the correlated angular distributions for the K^{*+}(890)

and Λ^0 decays enables the hyperon polarisation to be separated into

natural and unnatural parity exchange contributions. The polarisation

arising from natural parity exchange is negative over the t' range con-

sidered, in direct contradiction with the prediction of strong exchange

degeneracy. The unnatural parity exchange contribution to the polarisa-

tion is positive below t' $\sim$ 0.2 (GeV/c)^2. Non-zero polarisation cannot

be produced by single pole exchange alone, so that the presence of an

interfering trajectory, possibly the K_A, is required in addition to

the well-established K exchange.

The spin density matrix for the $K^*(890)$ decay indicates that natural parity exchange tends to dominate below $t' \sim 1.0$ $(GeV/c)^2$. The general features of the density matrix elements in the s-channel helicity frame may be summarised as follows:

(i) ρ_{00} has a sharp peak below $t' \sim 0.1$ $(GeV/c)^2$, falling to a value of ~ 0.2 before rising again above $t' \sim 0.5$ $(GeV/c)^2$.

(ii) $\rho_{11} + \rho_{1-1}$ has a value of ~ 0.6 in the region 0.1 $(GeV/c)^2$ $< t' < 0.5$ $(GeV/c)^2$, falling steadily above 0.5 $(GeV/c)^2$ and displaying a marked dip below 0.1 $(GeV/c)^2$, which can be associated with the peak in ρ_{00}.

(iii) $\rho_{11} - \rho_{1-1}$ remains constant at ~ 0.2

(iv) Re ρ_{10} is consistent with zero.

The transversity amplitudes have been determined from the joint spin density matrix and their moduli have been compared with those of the SU(3) related reaction $K^- p \to \phi \Lambda^0$ (ref. VI.4). The agreement is good, as expected from quark model predictions.

(c) $\pi^+ n \to K^{*+}(890) \Sigma^0$ and $\pi^+ p \to K^{*+}(890) \Sigma^+$
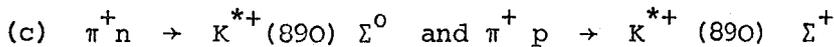
The differential cross-section distribution for the $K^{*+}(890) \Sigma^+$ final state exhibits a dip at $t' \sim 0$ of some 3 standard deviations below that expected from an exponential dependence of the forward differential cross-section. The dip is also present in Toet's data (ref. I.8) and indicates a strong overall helicity flip contribution to the reaction process. On the other hand there is no evidence for a dip at $t' \sim 0$ in the differential cross-section distribution for the $K^{*+}(890) \Sigma^0$ final state. This is in direct contradiction with the results of Yaffe (ref. I.12) who reports a dip of some 8 standard deviations in

the distribution for the charge symmetric reaction. In an attempt to understand the discrepancy, the t' - dependence of the losses discussed in section III.3.2. has been examined. The only loss which was found to affect the t' - distribution of this reaction resulted from assigning true Σ_V^O events to the Λ_V^O reaction. However, it is unlikely that a loss of this type would produce such a marked dip, even if all the Λ^O/Σ^O ambiguities were assigned to the Λ^O reaction.

The spin density matrix elements for both the $K^{*+}(890)$ Σ^O and $K^{*+}(890)$ Σ^+ final states indicate that the natural parity exchange contribution is even more dominant than for the $K^{*+}(890)$ Λ^O final state. This is to be expected from the known smallness of the $K \Sigma \bar{N}$ to $K \Lambda \bar{N}$ coupling ratio, assuming K exchange to be the main unnatural parity exchange contribution. Comparing the $K^{*+}(890)$ Σ^O and $K^{*+}(890)$ Λ^O natural parity exchange contributions to the cross-section below t' = 0.2 $(GeV/c)^2$ yields a value of -0.30 $\pm$ 0.14 for the D/F ratio in agreement with that found from the $K^+ \Sigma^O$ and $K^+ \Lambda^O$ final states.

(d) $\pi^+ n \rightarrow K^+ \Sigma^O (1385)$ and $\pi^+ p \rightarrow K^+ \Sigma^+ (1385)$
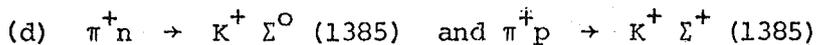
The differential cross-section distributions for both reactions exhibit a dip at t' $\sim$ 0.4 $(GeV/c)^2$, the position of a nonsense wrong-signature zero for the $K^*(890)$ trajectory. The slope of the forward differential cross-section distribution for the $K^+ \Sigma^+ (1385)$ final state is in reasonable agreement with that found for the line-reversed process, $K^- p \rightarrow \pi^- \Sigma^+ (1385)$, at 5.5 GeV/c (ref. V.13). However the total cross-section for $K^- p \rightarrow \pi^- \Sigma^+ (1385)$ over a range of beam momentum from 2 GeV/c to 8 GeV/c is about twice that for $\pi^+ p \rightarrow K^+ \Sigma^+ (1385)$ (ref. V.14) in direct contradiction with the predictions of weak exchange degeneracy. A. Bergland et al. (ref. VII.2) have compared the

line-reversed partners,

$$\pi^+ p \rightarrow K^+ \Sigma^+ ; \quad K^- p \rightarrow \pi^- \Sigma^+$$

$$\text{and} \quad \pi^+ p \rightarrow K^+ \Sigma^+ (1385) ; \quad K^- p \rightarrow \pi^- \Sigma^+ (1385).$$

at 7 GeV/c and 10.1 GeV/c. They report that the prediction of equal cross-sections is only satisfied for the Σ^+ production processes at the higher momentum and low t.

The spin density matrix for the Σ^+ (1385) decay compares favourably with the results of Butler et. al. at 3.7 GeV/c (ref. II.2) and with the predictions based on K^* exchange (ref. V.15), although the errors are too large to discriminate between models.

(e) $\pi^+ n \rightarrow K^{*+} (890) \Sigma^0 (1385)$

The differential cross-section distribution exhibits a dip at $t' \sim 0$ of some 2 standard deviations which is not present in Yaffe's data for the charge symmetric reaction at 3.93 GeV/c (ref. I.12). No t' -dependent losses were found which would affect the differential cross-section distribution. Contamination from processes involving single resonance production may be responsible for the slight discrepancy.

The spin density matrix elements for the K^{*+} (890) and Σ^0 (1385) decays are in reasonable agreement with those of ref. I.12. The quark model predictions for the relationships between the density matrix elements are satisfied within the large errors quoted. From the K^{*+} (890) density matrix both the natural and unnatural parity exchange contributions are important.

The cross-section for the SU(3) related reaction $K^- p \rightarrow \phi \Sigma^0$ (ref. IV.9) is in good agreement with that found for $\pi^+ n \rightarrow K^{*+}$ (890) Σ^0 (1385) from this experiment, as expected from quark model predictions.

APPENDIX A

THE HULTHEN MOMENTUM DISTRIBUTION

The Hulthen wave function for the deuteron in terms of the relative radial co-ordinate, r, may be written as (ref. A.1):

$$U(r) = \left[\frac{2\,\alpha\beta\,(\alpha + \beta)}{(\alpha - \beta)^2}\right]^{\frac{1}{2}} \left[\frac{\exp(-\alpha r) - \exp(-\beta r)}{r}\right] \qquad (A.1)$$

where $\alpha = 0.23$ fm^{-1} and $\beta = 1.27$ fm^{-1}. By applying a Fourier transformation, the wave function may be expressed in momentum space:

$$\psi(p) = A \int_{0}^{\infty} \int_{-1}^{1} \int_{0}^{2\pi} U(r)\,\exp.\,(i\,\vec{p}.\,\vec{r})\,r^2\,dr\,d(\cos\theta)\,d\phi \qquad (A.2)$$

where $\vec{r} \equiv (r, \theta, \phi)$, the relative spherical co-ordinates,

p is the magnitude of the momentum vector, $\vec{p}$, and

A is a normalisation constant.

Performing the angular integration in equation (A.2) gives

$$\psi(p) = A \int_{0}^{\infty} U(r)\,\frac{\sin pr}{pr}\,4\pi r^2\,dr \qquad (A.3)$$

Substituting for $U(r)$ from equation (A.1) and integrating over r:

$$\psi(p) = 4\pi A \left[\frac{2\,\alpha\beta(\alpha+\beta)}{(\alpha-\beta)^2}\right]^{\frac{1}{2}} \left[\frac{1}{\alpha^2 + p^2} - \frac{1}{\beta^2 + p^2}\right] \qquad (A.4)$$

The impulse approximation states that the production amplitude from the deutron is a linear combination of the individual production amplitudes.

The momentum wave function in equation (A.4) will therefore remain unaltered for the spectator nucleon. The momentum distribution of the spectator may then be written, from $P(p) dp \ \alpha \ |\psi(p)|^2 \ 4\pi p^2 \ dp$, as

$$P(p) \ dp \ = \ B \ \frac{\alpha\beta(\alpha+\beta)}{(\alpha-\beta)^2} \left[\frac{1}{\alpha^2+p^2} - \frac{1}{\beta^2+p^2}\right]^2 \ p^2 \ dp \qquad (A.5)$$

where B is a normalisation constant.

APPENDIX B

THE MANDELSTAM VARIABLES AND CROSSING SYMMETRY

Consider the (quasi-) two body process a + b $\rightarrow$ c + d where a, b, c and d are hadronic states. These particles have four-momenta denoted by P_a, P_b, P_c and P_d respectively. The four-momentum, $P_j = (E_j, q_j)$ (*) where E_j is the total energy and q_j is the three-momentum of particle j. Figure B.1 shows the schematic representation of the reaction in the overall centre of momentum (C.M.) system where particles a and b have equal and opposite three-momentum. Kinematically the reaction may be described by the following variables:

q_i = the magnitude of the three-momentum of each initial state
particle in the C.M. system ($q_i = |q_a| = |q_b|$)

q_f = the magnitude of the three-momentum of each final state particle
in the C.M. system ($q_f = |q_c| = |q_d|$)

θ = the C.M. production angle of one of the final state particles.

e.g. $\cos \theta = \dfrac{q_c \cdot q_a}{|q_c||q_a|}$

Because these quantities are not Lorentz invariant, it is often convenient to define the invariant variables s, t and u:

$$s = (P_a + P_b)^2 = (P_c + P_d)^2 \qquad (B.1)$$

$$t = (P_a - P_c)^2 = (P_b - P_d)^2 \qquad (B.2)$$

$$u = (P_a - P_d)^2 = (P_b - P_c)^2 \qquad (B.3)$$

These are the so-called "Mandelstam variables". Combining s, t and u gives

$$s + t + u = m_a^2 + m_b^2 + m_c^2 + m_d^2$$

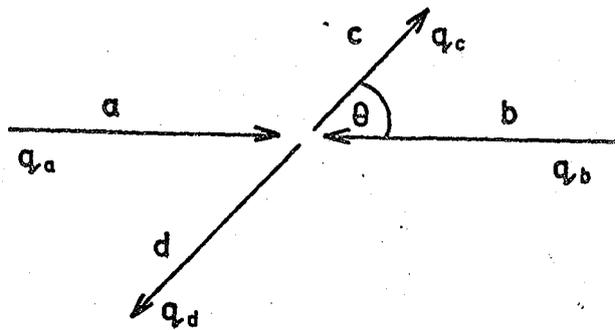The square of the four-momentum is defined by $P_j^2 = E_j^2 - q_j^2$

Fig. B.1   Schematic representation of a
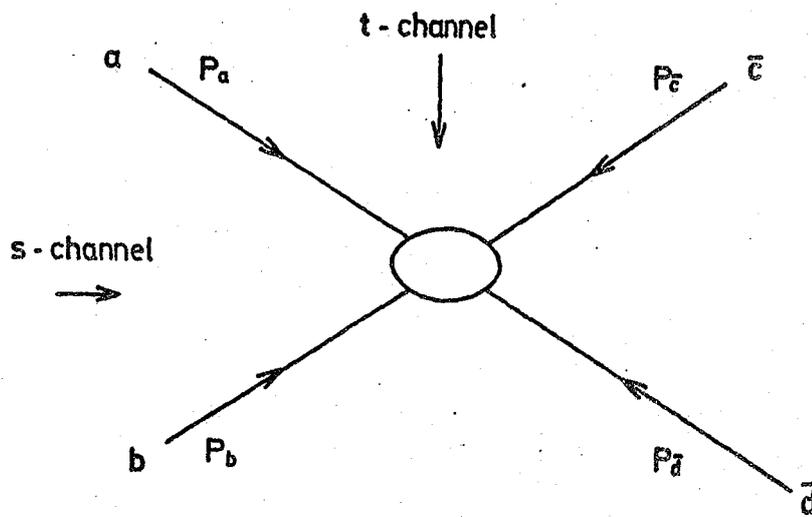two body reaction on the overall
C.M. system.

Fig. B.2   A symmetric description of two body
reactions.

where m_a, m_b, m_c and m_d denote the masses of the particles a, b, c and

d respectively. Because of this relation between the variables, only two

of them are independent. In terms of energy and three-momentum the

expressions (B.1) - (B.3) become

$$s = E_{cM}^2 \quad (> 0) \qquad \text{(B.4)}$$

$$t = m_a^2 + m_c^2 - 2E_a E_c + 2 q_a \cdot q_c$$

$$= m_b^2 + m_d^2 - 2E_b E_d + 2 q_b \cdot q_d \qquad (< 0) \qquad \text{(B.5)}$$

$$u = m_a^2 + m_d^2 - 2E_a E_d - 2 q_a \cdot q_d$$

$$= m_b^2 + m_c^2 - 2E_b E_c - 2 q_b \cdot q_c \qquad (< 0) \qquad \text{(B.6)}$$

where E_{cM} denotes the total energy in the C.M. system. It is apparent that

for fixed values of m_a and m_c, and for given momenta q_a and q_b then there

exists a minimum value of $|t|$, $|t|_{min}$, which is obtained by putting

$q_a \cdot q_c = |q_a| |q_c|$ in equation (B.5). If a resonance is produced, for

example particle c, then its mass, m_c, will have a distribution of values

(i.e. the Breit-Wigner distribution - section IV.2.2). Consequently t_{min}

will vary from event to event depending on the value of m_c. In order to

remove this effect, it is usual to define a new variable

$$t' = |t| - |t|_{min} \qquad (> 0).$$

Using C.M. quantities in equation (B.5) this may be expressed as

$$t' = 2 q_i q_f (1 - \cos \theta) \qquad \text{(B.7)}$$

The differential cross-section is defined as the cross-section per

unit of solid angle. In terms of $\cos \theta$ and azimuthal angle, ϕ, this is

equivalent to $d\sigma / d(\cos \theta) d\phi$. In figure B.1 ϕ is the angle of

rotation of the production plane about q_a. However an unpolarised beam (a)

and target (b) (as is the case in this experiment) implies rotational

symmetry about the beam direction, so that the differential cross-section

may be integrated over ϕ. Since $\cos \theta$ depends linearly on t' (see

equation (B.7)), the differential cross-section is often defined as $d\sigma/dt'$.

By replacing b and c in figure B.1 by their antiparticles $\bar{b}$ and $\bar{c}$,

and reversing their four-momenta, the crossed reaction is obtained:
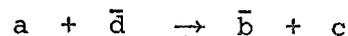
$$a + \bar{c} \rightarrow \bar{b} + d$$

t becomes positive (equation B.2) and has the meaning of an energy

variable:

$$t = (P_a + P_{\bar{c}})^2 = E_{cM}^2 \ (a + \bar{c} \rightarrow \bar{b} + d) \quad (> 0) \quad\quad (B.8)$$

s becomes negative (equation B.1) and is now the square of the four-

momentum transfer between a and $\bar{b}$:

$$s = (P_a - P_{\bar{b}})^2 \quad\quad\quad (< 0)$$

Similarly a third reaction is obtained by replacing b and d by their

anti-particles:

$$a + \bar{d} \rightarrow \bar{b} + c$$

In this case u is the energy variable (equation B.3). The three

reactions may be summarised as follows:

$a + d \rightarrow c + d$ is called the s-channel reaction ($s > 0, \ t < 0, \ u < 0$),

$a + \bar{c} \rightarrow \bar{b} + d$ is called the t-channel reaction ($s < 0, \ t > 0, \ u < 0$),

and $a + \bar{d} \rightarrow \bar{b} + c$ is called the u-channel reaction ($s < 0, \ t < 0, \ u > 0$).

The symmetric description of the three reactions is illustrated in

figure B.2. Each reaction is "physical" in a different region of the

(s, t, u) space. The principal of crossing symmetry states that all three

reactions are described by a single amplitude, $A \ (s, t, u)$. The principle

also requires that the function, $A(s, t, u)$ may be continued into unphysical regions of the (s, t, u) space. For example E_{CM}^2 (t-channel reaction) > 0 corresponds to the unphysical values $t > 0$ (i.e. $\cos \theta > 1$) in the s-channel reaction. Crossing symmetry is of vital importance in seeking to describe high energy processes in the framework of Regge-pole models.

APPENDIX C

C1 - Relationships between the statistical tensors and the joint spin

density matrix elements in transversity quantisation

$$\rho^{00}_{\substack{++\\--}} = \frac{1}{6}\left[1 - \sqrt{10}\ t^{20}_{00} \pm (\sqrt{3}\ t^{01}_{00} - \sqrt{30}\ t^{21}_{00}) \right]$$

$$\frac{1}{2}(\rho^{11}_{\substack{++\\--}} + \rho^{-1-1}_{\substack{+\ +\\-\ -}}) = \frac{1}{6}\left[1 + \sqrt{\frac{5}{2}}\ t^{20}_{00} \pm (\sqrt{3}\ t^{01}_{00} + \sqrt{\frac{15}{2}}\ t^{21}_{00}) \right]$$

$$\rho^{1-1}_{\substack{+\ +\\-\ -}} = \frac{1}{6}\left[\sqrt{15}\ t^{20^*}_{20} \pm \sqrt{45}\ t^{21^*}_{20} \right]$$

$$\frac{1}{2}(\rho^{10}_{-+} - \rho^{0-1}_{-\ +}) = \frac{1}{6} \quad \sqrt{45}\ t^{2\ 1^*}_{1-1}$$

$$\frac{1}{2}(\rho^{10}_{+-} - \rho^{0-1}_{+\ -}) = \frac{1}{6} \quad \sqrt{45}\ t^{21^*}_{11}$$

C2 - Relationships between the transversity amplitudes and the joint spin

density matrix elements.

$$\rho^{00}_{\substack{++\\--}} = \left| T^{0}_{\substack{++\\--}} \right|^2 \qquad \rho^{+1\ 0}_{+\ -} = T^{+1}_{+-}\ T^{0^*}_{--}$$

$$\rho^{11}_{\substack{++\\--}} = \left| T^{1}_{\substack{+-\\-+}} \right|^2 \qquad \rho^{+1\ 0}_{-\ +} = T^{+1}_{-+}\ T^{0^*}_{++}$$

$$\rho^{-1-1}_{\substack{+\ +\\-\ -}} = \left| T^{-1}_{\substack{+-\\-+}} \right|^2 \qquad \rho^{1-1}_{+\ +} = T^{1}_{+-}\ T^{-1^*}_{+-}$$

$$\rho^{-1\ 1}_{-\ -} = T^{-1}_{-+}\ T^{1^*}_{-+}$$

C3 - Relationships between the helicity amplitudes and the Byers and Yang
amplitudes

$$H^1_{++} + H^1_{--} = i(a_+ + a_-)$$

$$H^1_{+-} - H^1_{-+} = -(a_+ - a_-)$$

$$H^0_{++} = \frac{1}{\sqrt{2}}(b_+ + b_-)$$

$$H^0_{+-} = \frac{i}{\sqrt{2}}(b_+ - b_-)$$

$$H^1_{++} - H^1_{--} = -(c_+ + c_-)$$

$$H^1_{+-} + H^1_{-+} = i(c_+ - c_-)$$

REFERENCES

Chapter I

I.1   W. A. Cooper, et al., Phys. Rev. Lett. 20 (1968) 472.

I.2   S. M. Pruss et al., Phys. Rev. Lett. 23 (1969) 189.

I.3   E. Bertolucci et al., Nuov.Cim. Lett. 2 (1969) 149.

I.4   P. Kalbaci et al., Phys. Rev. Lett. 27 (1971) 74.

I.5   M. Abramovich et al., Nucl. Phys. B27 (1971) 477.

I.6   D. J. Crennell et al., Phys. Rev. D6 (1972) 1220.

I.7   M. Abramovich et al., Nucl. Phys. B39 (1972) 189.

I.8   D .Z. Toet et al., Nucl. Phys. B63 (1973) 248.

I.9   D. Mettel and B. Ghidini, Nuov. Cim. Lett. 6 (1973) 437.

I.10   C. E. W. Ward et al., Phys. Rev. Lett. 31 (1973) 1149.

I.11   C. E. W. Ward et al., Phys. Lett. 48B (1974) 471.

I.12   D. Yaffe et al., Nucl. Phys. B75 (1974) 365.

I.13   M. J. Losty et al., Phys. Lett. 56B (1975) 96.

I.14   A. J. Pawlicki et al., Phys. Rev. D12 (1975) 631.

I.15   W. Beusch et al., Nucl. Phys. B99 (1975) 53.

I.16   V. V. Glagolev et al., Sov. J. Nucl. Phys. 21 (1975) 637.

I.17   C. E. W. Ward et al., Argonne preprint ANL-HEP-PR-77-04 (1977).

I.18   I. G. Bell, Ph.D. thesis, Durham (1975).

I.19   M. Dale, Ph.D. thesis, Durham (1975).

I.20   C. Wilkin, Phys. Rev. Lett. 17 (1966) 561.

I.21   V. Flaminio, I. F. Graf, J. D. Hansen, W. G. Moorhead and
        D. R. O. Morrison, CERN/HERA 79-01 (1979).

I.22   E. Keil and W. W. Neale, CERN/TC/02, 63-3 (1963).

I.23   Gordan, Ph.D. thesis, Illinois (1970).

I.24   RHEL Geometry Programme Manual.

I.25   RHEL Kinematics Programme Manual.

I.26   RHEL Judge Programme Manual.

Chapter II

II.1   G. Lynch, UCRL 103355 (1962).

II.2   W. R. Butler et al., Phys. Rev. D7 (1973) 3177.

II.3   Particle Data Group, Phys. Lett. 75B (1978) No. 1.

II.4   D. J. Crennell and D. E. Hall, RL-74-123, journal preprint,
        HEP Division, PRP/H/131.

Chapter III

III.1   D. M. Chew, V. P. Henri, T. A. Lasinski, T. E. Trippe, F. Uchiyama
        and F. C. Winkelman, LBL-53 (1973).

Chapter IV

IV.1   High Energy and Nuclear Physics Data Handbook, edited by W. Galbraith
        and W. S. C. Williams
        (National Institute for Research in Nuclear Science, RHEL, 1963)

IV.2   J. D. Thomas, M.Sc. thesis, Durham (1975).

IV.3   R. H. Dalitz, Ann. Rev. Nucl. Sci. 13 (1963) 339.
        (see also ref. IV.8)

IV.4   J. D. Jackson, Nuov. Cim. 34 (1964) 1644.

IV.5   A. Barbaro-Galtieri, Advances in Particle Physics, edited by
        R. L. Cool and R. E. Marshak (Wiley-Interscience, NY, 1968) Vol. 2,
        p. 175.

        F. von Hippel and C. Quigg, Phys. Rev. D5 (1972) 624.

IV.6   MINUIT (Long write-up), D506, CERN Programme Library.

IV.7   M. J. Emms et al., Nucl. Phys. B96 (1975) 155.

IV.8   N. N. Biswas et al., Phys. Rev. D5 (1972) 1564.

IV.9   M. Aguilar-Benitez et al., Phys. Rev. D6 (1972) 29.

IV.10   Particle Data Group, Phys. Lett. 39B (1972) no. 1.

IV.11   C. Dionisi et al., CERN preprint CERN/EP, 80-1 (1980).

IV.12   B. Conforto and G. Conforto, RHEL preprint RL-77-024/A (1977).

Chapter V

V.1   B. E. Y. Svensson, Proceedings of the 1967 CERN School of Physics
       CERN 67-24 (1967).

       P. D. B. Collins, An Introduction to Regge Theory and High Energy
       Physics, (Cambridge University Press, 1977).

       R. C. Johnson, Proceedings of the School for Young High Energy
       Physicists, RL-78-003-C (1977).

V.2   K. Gottfried and J. D. Jackson, Nuov. Cim. 33 (1964) 309.

       H. Pilkuhn and B. E. Y. Svensson, Nuov. Cim. 38 (1965) 518.

       N. M. Queen, Proceedings of the School for Young High Energy
       Physicists, RL-78-003-C (1977).

V.3   O. I. Dahl et al., Phys. Rev. 163 (1967) 1377.

V.4   S. Ozaki et al., BNL report 15183 (1970).

V.5   D. J. Crennell et al., Phys. Rev. Lett. 23 (1969) 1347.

V.6   W. L. Yen et al., Phys. Rev. Lett. 22 (1969) 963.

V.7   K. W. Lai and J. Louie, Nucl. Phys. B19 (1970) 205.

V.8   C. Michael and R. Odorico, Phys. Lett. 34B (1971) 422.

V.9   G. Ebel, et al., Nucl. Phys. B33 (1971) 317.

V.10   P. Minnaert, Phys. Rev. Lett. 16 (1966) 672.

V.11   P. Minnaert, Phys. Rev. 151 (1966) 1306.

V.12   S. P. Ying et al, Phys. Lett. 30B (1969) 289.

V.13   J. Mott, et al., Phys. Rev. 177 (1969) 1966.

V.14   J. Mott, Nucl. Phys. B13 (1969) 565.

V.15   J. J. Sakurai and R. Stodolsky, Phys. Rev. Lett. 11 (1963) 90.

V.16   A. Bialas and K. Zalewski, Nucl. Phys. B.6 (1968) 465.

V.17   A. Kotanski and K. Zalewski, Nucl. Phys. B13 (1969) 119.

Chapter VI

VI.1   M. G. Doncel, P. Minnaert and L. Michel, CERN preprint CERN/D.Ph.II/
       PHYS 74-7 (1974).

VI.2   N. Byers and C. N. Yang, Phys. Rev. 135 (1964) B796.

VI.3   R. D. Field et al., Phys. Rev. D6 (1972) 1863.

VI.4   R. D. Field et al., Phys. Rev. D7 (1973) 2063.

Chapter VII

VII.1   See for example:

        A. C. Irving, A. D. Martin and C. Michael, Nucl. Phys. B32 (1971) 1.

        H. Navelet and P. R. Stevens, Nucl. Phys. B104 (1976) 171.

VII.2   A. Bergland et al., Nucl. Phys. B166 (1980) 25.